

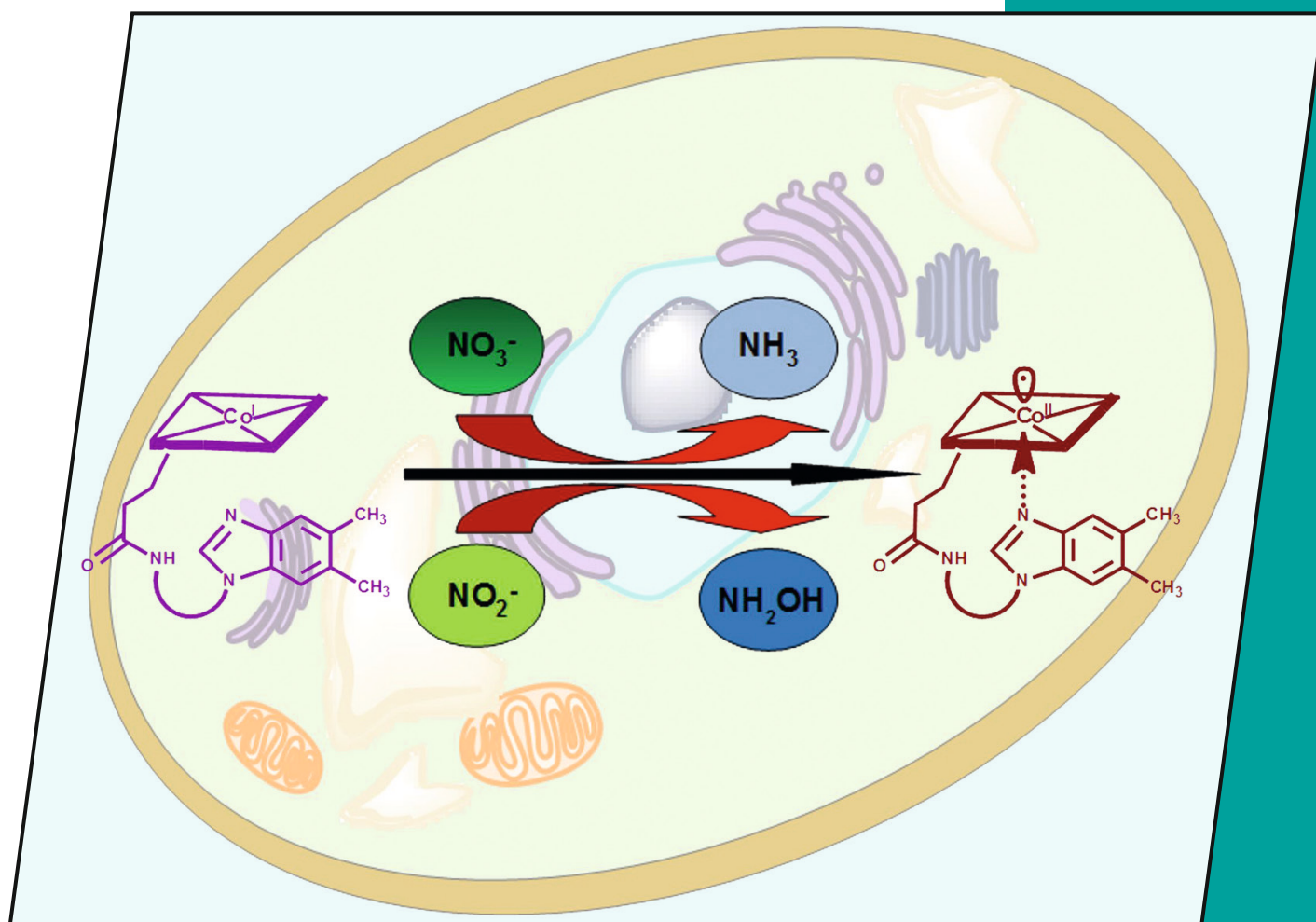


EurJIC

European Journal of
Inorganic Chemistry

6/2012

3rd February Issue



Cover Picture

Nicola E. Brasch et al.

Mechanistic Studies on the Reactions of the Reduced Vitamin B₁₂ Complex

Microreview

Zhong-Xia Wang and Ning Liu

Nickel-Catalyzed Cross-Coupling with Pincer Ligands

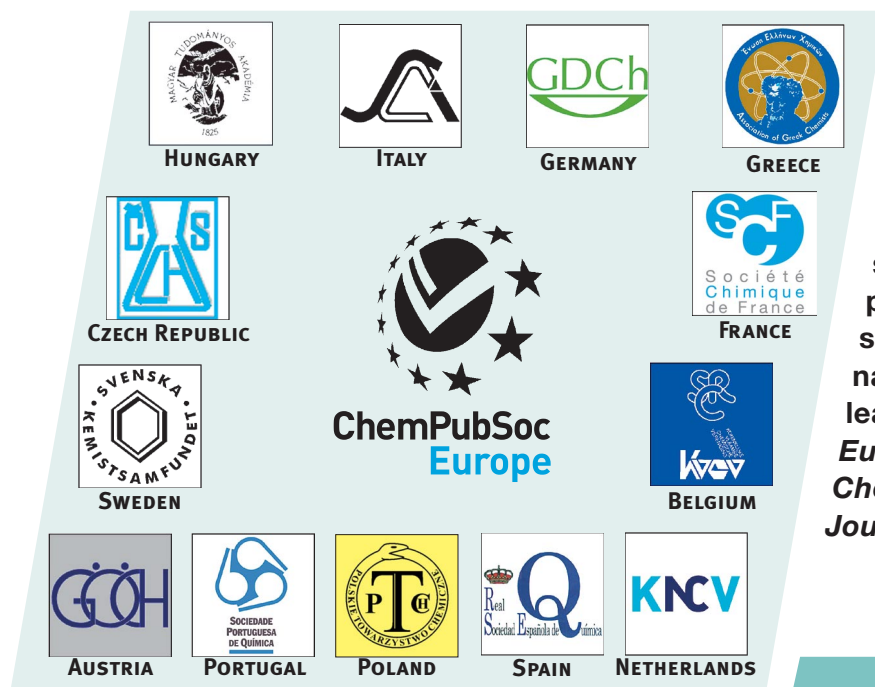
 WILEY-VCH

www.eurjic.org

A Journal of



ChemPubSoc
Europe

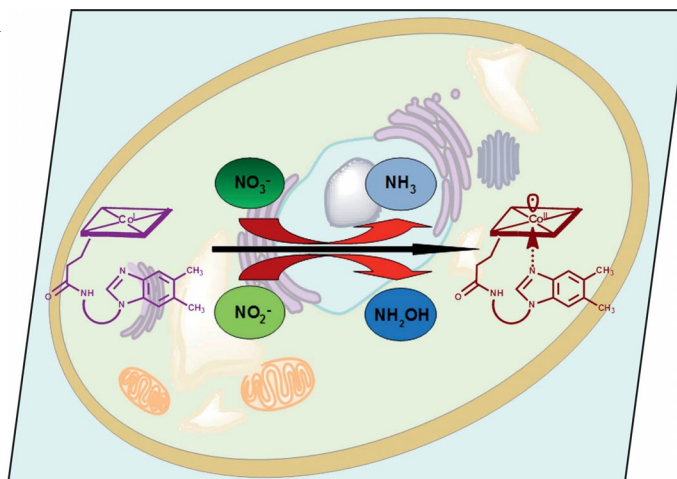


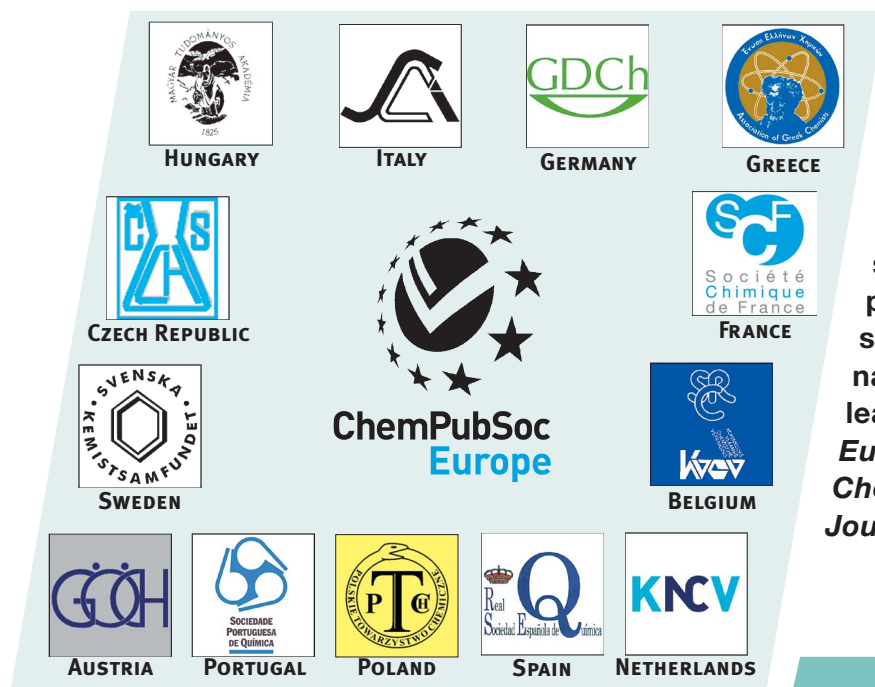
EurJIC is a journal of ChemPubSoc Europe, a union of 16 European chemical societies formed for the purpose of publishing high-quality science. All owners merged their national journals to form two leading chemistry journals, the *European Journal of Inorganic Chemistry* and the *European Journal of Organic Chemistry*.

Other ChemPubSoc Europe journals are *Chemistry – A European Journal*, *ChemBioChem*, *ChemPhysChem*, *ChemMedChem*, *ChemSusChem*, *ChemCatChem*, *ChemPlusChem* and *ChemistryOpen*.

COVER PICTURE

The cover picture shows that nitrate and especially nitrite rapidly oxidize cob(I)alamin to cob(II)alamin. Enzyme-bound cob(I)alamin is a short-lived species whose formation is essential for the activity of both mammalian vitamin B₁₂ dependent enzymes. Nitrite and nitrate, intracellular levels of which are elevated during oxidative/nitrosative stress as a consequence of elevated nitric oxide levels, are generally considered to be benign species. Details are discussed in the article by N. E. Brasch et al. on p. 913ff. The cover picture was designed by Rohan S. Dassanayake.



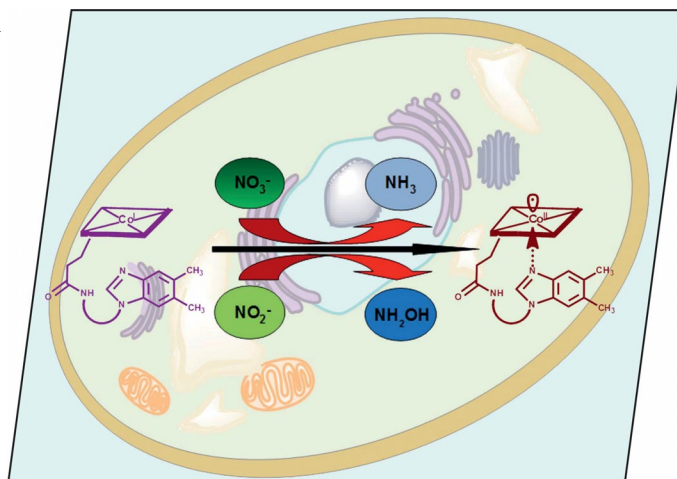


EurJIC is a journal of ChemPubSoc Europe, a union of 16 European chemical societies formed for the purpose of publishing high-quality science. All owners merged their national journals to form two leading chemistry journals, the *European Journal of Inorganic Chemistry* and the *European Journal of Organic Chemistry*.

Other ChemPubSoc Europe journals are *Chemistry – A European Journal*, *ChemBioChem*, *ChemPhysChem*, *ChemMedChem*, *ChemSusChem*, *ChemCatChem*, *ChemPlusChem* and *ChemistryOpen*.

COVER PICTURE

The cover picture shows that nitrate and especially nitrite rapidly oxidize cob(I)alamin to cob(II)alamin. Enzyme-bound cob(I)alamin is a short-lived species whose formation is essential for the activity of both mammalian vitamin B₁₂ dependent enzymes. Nitrite and nitrate, intracellular levels of which are elevated during oxidative/nitrosative stress as a consequence of elevated nitric oxide levels, are generally considered to be benign species. Details are discussed in the article by N. E. Brasch et al. on p. 913ff. The cover picture was designed by Rohan S. Dassanayake.



CONTENTS

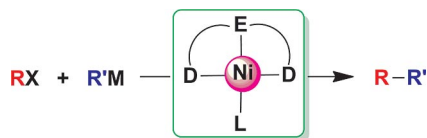
MICROREVIEW

Nickel Catalysts with Pincer Ligands

Z.-X. Wang,* N. Liu 901–911

Nickel-Catalyzed Cross-Coupling with Pincer Ligands

Keywords: Nickel / Pincer ligands / Homogeneous catalysis / Cross-coupling



In this microreview we summarize nickel-catalyzed cross-coupling reactions with pincer ligands. The reactions presented here include Kumada, Negishi, Suzuki, and Sonogashira reactions for the formation of different types of C–C bonds, as well as the thiolation of aryl iodides.

FULL PAPERS

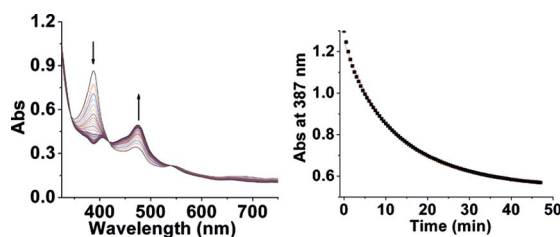
Cobalamins

N. T. Plymale, R. S. Dassanayake,
H. A. Hassanin, N. E. Brasch* ... 913–921



Kinetic and Mechanistic Studies on the Reactions of the Reduced Vitamin B₁₂ Complex Cob(I)alamin with Nitrite and Nitrate

Keywords: Vitamin B₁₂ / Cobalt / Bioinorganic chemistry / Kinetics / Reaction mechanisms



Kinetic studies show that nitrate and especially nitrite react rapidly with cob(I)alamin under biological pH conditions.

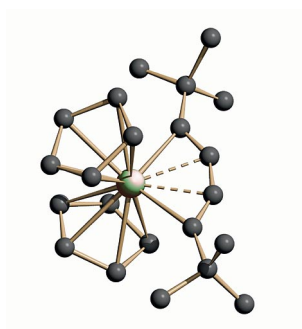
Bonding in Metallacyclocumulenes

R. R. Aysin, L. A. Leites,* V. V. Burlakov,
V. B. Shur, T. Beweries,
U. Rosenthal 922–928

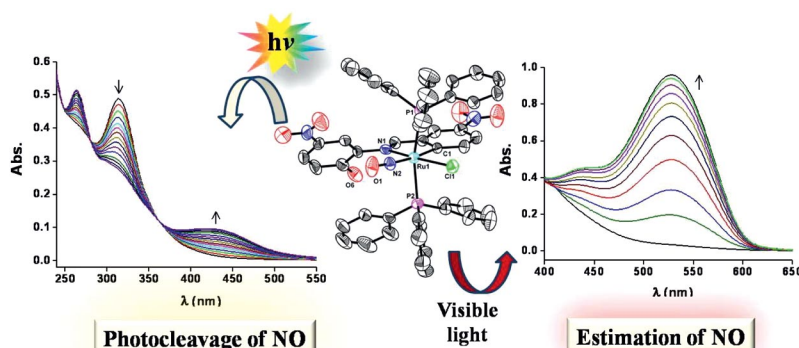


Peculiarities of Vibrational Spectra and Electronic Structure of the Five-Membered Metallacyclocumulenes of the Group 4 Metals

Keywords: Metallacyclocumulenes / Cyclopentadienyl ligands / Electronic structure / Raman spectroscopy / IR spectroscopy / QTAIM analysis



The peculiar bonding pattern of metallacyclocumulenes of the type Cp₂M(η⁴-*t*Bu-C₄tBu) [M = Ti, Zr, Hf] was investigated by experimental and theoretical vibrational spectroscopy and Bader's QTAIM analysis.



K. Ghosh,* S. Kumar, R. Kumar,
U. P. Singh 929–938

Ruthenium(III) Cyclometalates Obtained by Site-Specific Orthometallation and Their Reactivity with Nitric Oxide: Photo-induced Release and Estimation of NO Liberated from the Ruthenium Nitrosyl Complexes

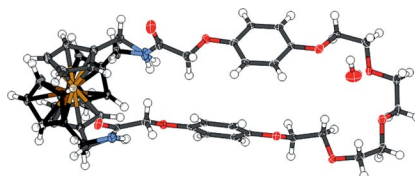
Keywords: Ruthenium / Redox chemistry / Metalation / Photolability

Ruthenium(III) cyclometalates were synthesized by site-specific orthometallation. The reactivity of nitric oxide was investigated and the photolability of nitric oxide in newly synthesized ruthenium nitrosyl

complexes was examined. The amount of photoreleased NO was estimated by using a Griess reagent in UV as well as in visible light. The role of the nitro group in the ligand frame was scrutinized.

Anion Sensing

Two macrocycles that incorporate the redox-active ferrocene motif for anion sensing are presented. The urea macrocycle binds anions more strongly than the amide macrocycle and exhibits greater shifts of the ferrocene/ferrocenium redox couple upon the addition of anions.

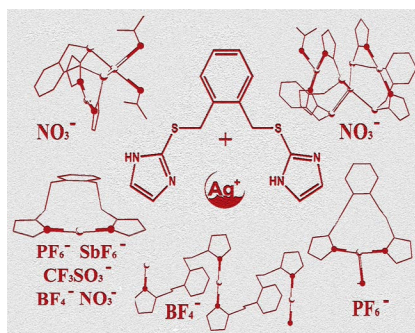


N. H. Evans, C. J. Serpell,
K. E. Christensen, P. D. Beer* ... 939–944

Amide and Urea Ferrocene-Containing Macrocycles Capable of the Electrochemical Sensing of Anions

Keywords: Supramolecular chemistry / Macrocycles / Molecular recognition / Sensors / Anions / Electrochemistry

An XRD structural study of a series of Ag^I coordination compounds with a new flexible ligand, 1,2-bis[(imidazol-2-yl)thiomethyl]benzene, and counterions such as PF₆[−], SbF₆[−], CF₃SO₃[−], BF₄[−] and NO₃[−] prepared in MeOH in a 1:1 metal/ligand ratio, reveals vast structural diversity and highlights the difficulties of solid-state characterisation of bulk materials.

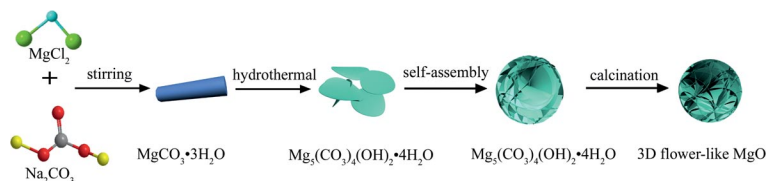


L. Dobrzańska* 945–953

Structural Heterogeneity of Ag^I Complexes with a Flexible 1,2-Bis[(imidazol-2-yl)thiomethyl]benzene Ligand and Issues Regarding the Phase Purity of the Bulk Material

Keywords: Silver / Ligand flexibility / Coordination modes / Phase purity / X-ray diffraction

Coordination Chemistry



A 3D hierarchical flower-like MgO microsphere was formed by a new assembly process from 1D to 3D. The highly crystalline product has cubic symmetry and is assembled from close-packed nanoflakes. Its

large surface area makes it highly favourable for heterogeneous catalysis, particularly in the Claisen–Schmidt condensation reactions for preparing chalcones with benzaldehyde and acetophenone.

Y. Qu, W. Zhou, Z. Ren, K. Pan,
C. Tian, Y. Liu, S. Feng, Y. Dong,
H. Fu* 954–960

Fabrication of a 3D Hierarchical Flower-Like MgO Microsphere and Its Application as Heterogeneous Catalyst

Keywords: Crystal growth / Heterogeneous catalysis / Industrial chemistry / Magnesium

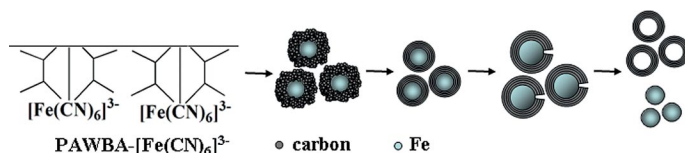
CONTENTS

Graphitic Carbon Nanostructures

L. Wang, C. Tian, H. Zhang,
H. Fu* 961–968

Graphitic Carbon Nanocapsules: Scaled Preparation, Formation Mechanism, and Use as an Excellent Support for Methanol Electro-oxidation

Keywords: Nanostructures / Reaction mechanisms / Carbon / Platinum / Electrochemistry / Oxidation



A simple and high-yielding solid-state pyrolysis route has been used in the large-scale preparation of graphitic carbon nanocapsules (GCNs). Their superb properties, namely high crystallinity and large specific

surface area, allowed the GCNs to be used as an excellent catalyst support for methanol electro-oxidation. The mechanism for the formation of GCNs has been investigated.

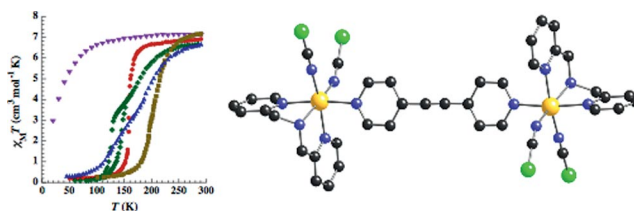
Spin Crossover Complexes

G. S. Matouzenko,* E. Jeanneau,
A. Y. Verat, Y. de Gaetano 969–977



The Nature of Spin Crossover and Coordination Core Distortion in a Family of Binuclear Iron(II) Complexes with Bipyridyl-Like Bridging Ligands

Keywords: Iron / Ligand effects / Magnetic properties / Spin crossover / Binuclear complexes



The structure–property correlations for a family of binuclear spin crossover (SCO) complexes confirm the key role of $[\text{FeN}_6]$ octahedral distortions, which are caused by crystal packing and strain effects from ter-

minal and/or bridging ligands, in the generation of different types of SCO behavior (one-step, two-step, partial 50% transition).

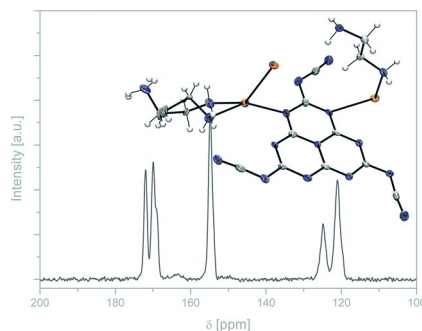
Silver and Nickel Melonates

C. Clauss, U. Böhme, A. Schwarzer,
E. Kroke* 978–986



Silver Melonates and Coordination Modes of the Multidentate $[\text{C}_6\text{N}_7(\text{NCN})_3]^{3-}$ Anion

Keywords: N ligands / X-ray diffraction / Anions / Quantum chemical calculations / Silver



Silver melonates were synthesised, and their spectroscopic, structural and thermal properties were investigated. Theoretical and experimental data that concern the regioselective coordination of the trianion indicate that all four different terminal N atoms are able to interact with metal cations.

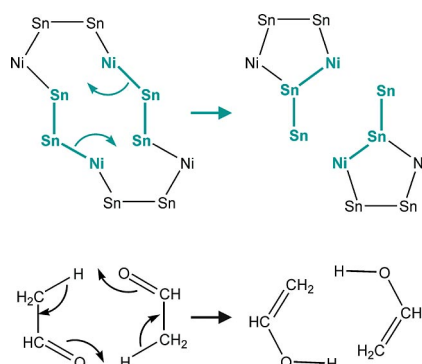
Polymorphic Intermetallic Phase

L. Siggelkow, V. Hlukhyy,
T. F. Fässler* 987–997



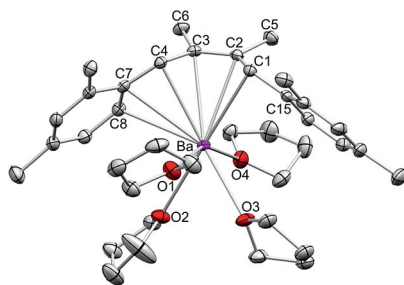
Ca_2NiSn_2 – A Polymorphic Intermetallic Phase: Atomic and Electronic Structure as well as a Topological Description of the Phase Transition by a Sigmatropic-Type Rearrangement of Ni and Sn Atoms

Keywords: Tin / Intermetallic phases / ELF (Electron Localization Function) / Chemical bonding / Phase transitions



The two- and three-dimensional Ni–Sn networks of two new polymorph modifications of Ca_2NiSn_2 exhibit structural similarities. In addition to the syntheses and structural characterizations, two topological descriptions of the phase transition are presented: a conversion by a simple shift of ribbons of atomic layers and a least-motion process through Ni–Sn bond scission and formation.

Barium metal can be efficiently activated by phenyl-substituted 1,3-dienes to afford barium complexes with a unique metallacyclo-2,4-heptadiene bonding motif.



**O. Michel, H. Kaneko, H. Tsurugi,
K. Yamamoto, K. W. Törnroos,
R. Anwender,* K. Mashima* ... 998–1003**

Diene Dissolution of the Heavier Alkaline Earth Metals



Keywords: Alkaline earth metals / Barium / Calcium / Strontium / Structure elucidation / Organometallic complexes / Arenes / Diene ligands

* Author to whom correspondence should be addressed.

Supporting information on the WWW (see article for access details).

This article is available online free of charge (Open Access).

If not otherwise indicated in the article, papers in issue 5 were published online on February 6, 2012

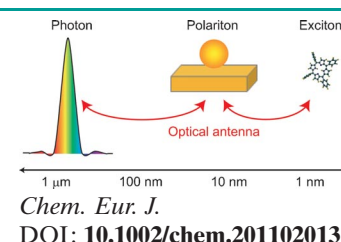


Energy Transfer

K. Ikeda,* K. Uosaki

Optical Antenna for Photofunctional Molecular Systems

Photon manipulation: The interaction efficiency between photons and molecules can be enhanced by a transformation between free-propagating massless photons and “heavy” photons. Although such photon manipulation is realized by metallic optical antennas, chemical interactions at metal–molecule interfaces have to be controlled to increase the overall photochemical reaction efficiency.



Chem. Eur. J.

DOI: 10.1002/chem.201102013

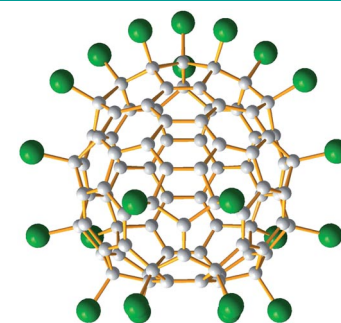


Fullerenes

S. Yang,* T. Wei, E. Kemnitz, S. I. Troyanov*

The Most Stable IPR Isomer of C_{88} Fullerene, C_s-C_{88} (17), Revealed by X-ray Structures of $C_{88}Cl_{16}$ and $C_{88}Cl_{22}$

The most stable IPR isomer of C_{88} fullerene, C_{88} (17), has been captured by chlorination as $C_{88}(17)Cl_{16}$ and $C_{88}(17)Cl_{22}$. X-ray crystallography revealed C_s -symmetrical molecular structures of both compounds, with the former being a substructure of the latter (see picture; C grey, Cl green). The chlorination patterns are characterized by the formation of isolated double C–C bonds, benzenoid rings, and, in $C_{88}(17)Cl_{22}$, a long chain of Cl additions in adjacent positions on the C_{88} fullerene cage.



Chem. Asian J.

DOI: 10.1002/asia.201100759

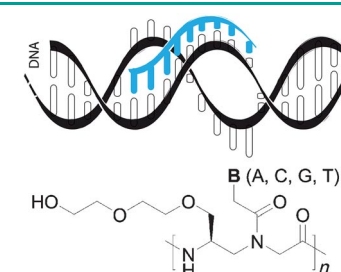


DNA Recognition

R. Bahal, B. Sahu, S. Rapireddy, C.-M. Lee, D. H. Ly*

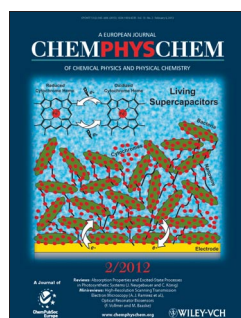
Sequence-Unrestricted, Watson–Crick Recognition of Double Helical B-DNA by (R)-MiniPEG-γPNAs

Invasion of the strand snatchers: We have synthesized chiral γ-peptide nucleic acids containing miniPEG side chains. Using gel shift assays we show that this particular type of nucleic acid mimic can invade any sequence of double helical B-form DNA (see figure), and this recognition occurs through direct Watson–Crick base pairing.



ChemBioChem

DOI: 10.1002/cbic.201100646

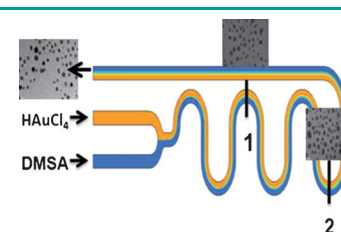


Gold Nanoparticles

Y. Li, A. Sanampudi, V. Raji Reddy, S. Biswas, K. Nandakumar, D. Yemane, J. Goetttert, C. S. S. R. Kumar*

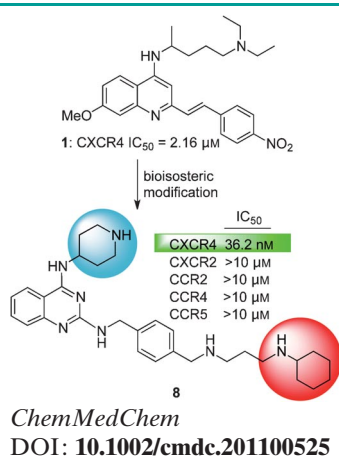
Size Evolution of Gold Nanoparticles in a Millifluidic Reactor

Select your size: The size evolution of gold nanoparticles in a millifluidic reactor (see picture) is investigated through spatially resolved transmission electron microscopy. The experimental data supported by numerical simulations suggests that size and size distributions of the particles formed within the channels are influenced by the mixing zone as well as the residence-time distribution.



ChemPhysChem

DOI: 10.1002/cphc.201100726

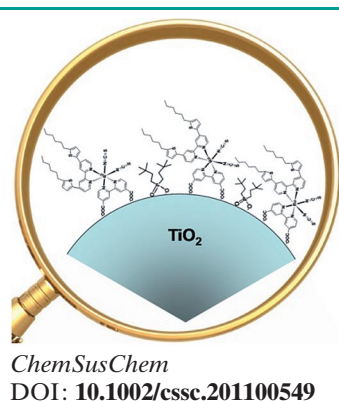
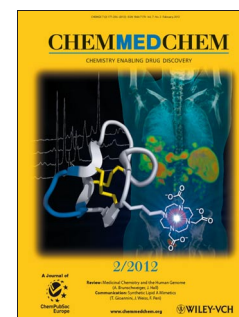


Stem Cell Research

C.-H. Wu, C.-P. Chang, J.-S. Song, J.-J. Jan, M.-C. Chou, S.-H. Wu, K.-C. Yeh, Y.-C. Wong, C.-J. Hsieh, C.-T. Chen, T.-T. Kao, S.-Y. Wu, C.-F. Yeh, C.-T. Tseng, Y.-S. Chao, K.-S. Shia*

Discovery of Novel Stem Cell Mobilizers That Target the CXCR4 Receptor

Going mobile: Based on screening hit **1**, a novel class of polyamine compounds, as represented by compound **8**, were identified as potent and selective CXCR4 antagonists. CXCR4-targeted molecules, as demonstrated by the marketed AMD3100 and **8**, are able to mobilize stem cells from bone marrow effectively and are expected to have broad utility in cell therapy and regenerative medicine.

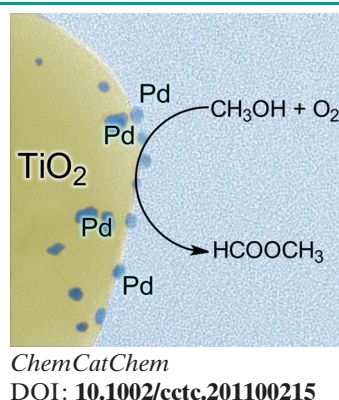
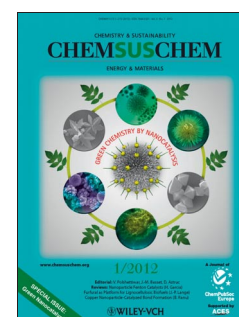


Solar Cells

M. Wang, S. Plogmaker, R. Humphry-Baker, P. Pechy, H. Rensmo,* S. M. Zakeeruddin,* M. Grätzel*

Molecular-Scale Interface Engineering of Nanocrystalline Titania by Co-adsorbents for Solar Energy Conversion

Occupy TiO₂: Co-grafting dyes with amphiphilic molecules containing phosphinic or phosphonic acid end groups can form a more compact monolayer than the adsorption of dye alone. This insulating molecular layer can effectively shield the back electron transfer from the conduction band of TiO₂ to redox electrolytes. Herein coadsorbents are found to not only influence the dye loading, but also the geometry and electronic properties of the system.

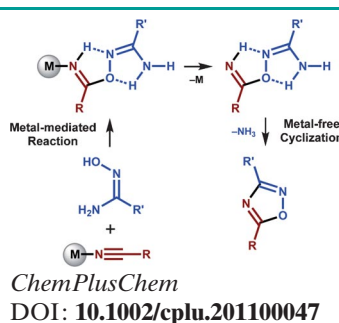
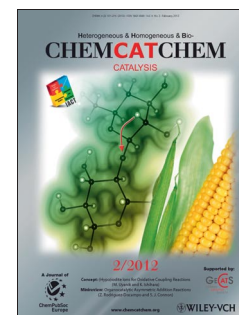


Partial Oxidation

R. Wojcieszak,* E. M. Gaigneaux, P. Ruiz

Low Temperature-High Selectivity Process over Supported Pd Nanoparticles in Partial Oxidation of Methanol

Getting friendly with methanol: The most important challenge in gas phase heterogeneous catalysis is to reach high selectivity in a desired process. Probably the only way to get high selectivity in gas phase heterogeneous catalysis is to work under “friendly temperature conditions”. Methyl formate could be produced directly from methanol with a very high selectivity, over supported palladium nanoparticles at low temperature and under atmospheric pressure.



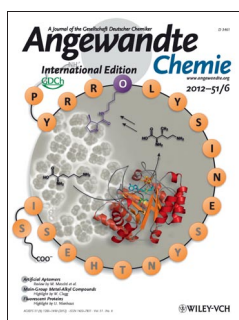
Coordination Chemistry

D. S. Bolotin, N. A. Bokach,* M. Haukka, V. Y. Kukushkin*

Platinum(IV)-Mediated Nitrile–Amidoxime Coupling Reactions: Insights into the Mechanism for the Generation of 1,2,4-Oxadiazoles

Step by step: The stepwise nucleophilic addition of amidoximes to nitrile ligands in platinum(IV) complexes leads to coordinated O-imidoylamidoximes. These newly formed species after de-coordination undergo cyclization (see scheme) to furnish 1,2,4-oxadiazoles. The cyclization is promoted by strong acceptor substituents R' and is not affected by a metal center.



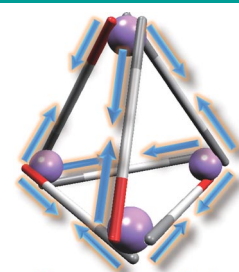


Stereochemistry

N. Ousaka, J. K. Clegg, J. R. Nitschke*

Nonlinear Enhancement of Chiroptical Response through Subcomponent Substitution in M_4L_6 Cages

One for all, all for one: A self-assembled M_4L_6 cage, incorporating small amounts of enantiopure subcomponents at the peripheries, forms predominantly with a one-handed twist at all metal centers. Strong stereochemical coupling between metal centers in the cage amplifies energy differences between the $\Delta\Delta\Delta$ and $\Lambda\Lambda\Lambda$ diastereomers as compared to analogous mononuclear metal complexes (see picture; red and gray bars denote chiral and achiral subcomponents, respectively).



Cooperative effect

Angew. Chem. Int. Ed.
DOI: [10.1002/anie.201107532](https://doi.org/10.1002/anie.201107532)

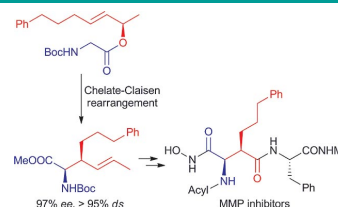


Matrix Metalloprotease Inhibitors

J. L. Burkhardt, B. Diehl, M. J. Schmitt, U. Kazmaier*

A Straightforward Approach to MMP-2 and MMP-9 Inhibitors Based on Chelate Claisen Rearrangements

The chelate Claisen rearrangement allows the stereoselective synthesis of β -substituted γ,δ -unsaturated amino acids, which can be converted into β -substituted aspartates by oxidative cleavage. These are ideal precursors for the synthesis of hydroxamate-type MMP inhibitors.



Eur. J. Org. Chem.
DOI: [10.1002/ejoc.201101318](https://doi.org/10.1002/ejoc.201101318)



Controlling Drug Impurities

Vera Köster

A. Teasdale on Genotoxic Impurities in Drugs

Dr. Andrew Teasdale is the chair of AstraZeneca's internal expert group focused on control of genotoxic impurities. He talks about genotoxic impurities in drugs, what constitutes an acceptable drug risk, and the future of drug development.



ChemViews magazine
DOI: [10.1002/chemv.201200004](https://doi.org/10.1002/chemv.201200004)

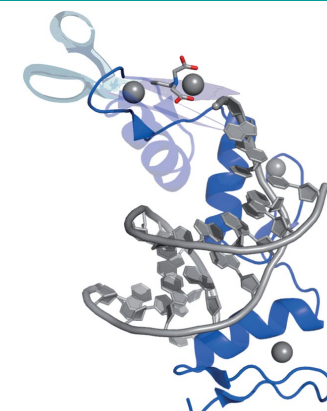


Peptide Chemistry

F. Fehr, A. Nadler, F. Brodhun, I. Feussner, U. Diederichsen*

Semi-Synthesis and Analysis of Chemically Modified Zif268 Zinc-Finger Domains

The entire zinc-finger domain of Zif268 was synthesized by a semi-synthetic pathway using the expressed protein ligation approach. Despite several modifications, for example, attachment of a fluorophore and introduction of a metal-chelating amino acid within the sequence of the third zinc finger, circular dichroism spectroscopic measurements confirmed zinc-induced folding and intact DNA binding ability.



ChemistryOPEN
DOI: [10.1002/open.201100002](https://doi.org/10.1002/open.201100002)

Nickel-Catalyzed Cross-Coupling with Pincer Ligands

Zhong-Xia Wang*^[a] and Ning Liu^[a]

Keywords: Nickel / Pincer ligands / Homogeneous catalysis / Cross-coupling

Transition-metal-catalyzed cross-coupling reactions are powerful tools for constructing carbon–carbon and carbon–heteroatom bonds. In this microreview we summarize the nickel-catalyzed cross-coupling reactions with pincer li-

gands. The reactions presented here include Kumada, Negishi, Suzuki, and Sonogashira reactions for the formation of different types of C–C bonds, as well as the thiolation of aryl iodides.

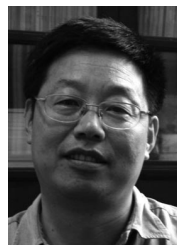
Introduction

Transition-metal-catalyzed cross-coupling reactions of organic halides with organometallic reagents, for example, the Kumada, Negishi, Suzuki, and Stille reactions, are reliable and versatile tools in organic synthesis.^[1,2] Among the cross-coupling reactions, the Negishi, Suzuki, and Stille reactions have been studied in more detail because of the better functional group compatibility.^[1,3] However, the Kumada reaction offers a more direct approach, because the nucleophiles used in the reactions are usually prepared from Grignard reagents.^[4–6] The high reactivity of Grignard reagents leads to poor functional group tolerance in the Kumada reaction but often allows milder reaction conditions. The development of functional-group-tolerant Kumada re-

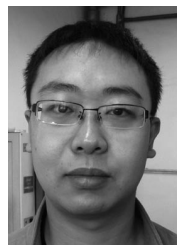
actions is a considerably attractive goal. On the other hand, electrophiles used in the cross-coupling reactions are mainly aryl and alkenyl halides. A number of catalyst systems have been developed to carry out the coupling of the unsaturated substrates. Alkyl halides were still thought to be generally difficult to use as coupling partners until the early 2000s, because of the relatively slow oxidative addition of transition metals to alkyl halides and the facile β -hydrogen elimination.^[8] Significant advances have been made in the past decade, and several reviews have been published on the topic.^[3a,7–9] In addition, organic chlorides are less often employed as the electrophiles than bromides and iodides, because of low reactivity of the C–Cl bond. However, chlorides are more useful substrates, because of their lower cost and the wider diversity of available compounds.^[3b,10]

Both nickel and palladium are most often used as effective catalysts for cross-coupling reactions.^[1] Ancillary ligands play key roles in providing appropriate stereochemical and electronic environments around metal centers and hence controlling catalytic properties. Many effective li-

[a] Department of Chemistry, University of Science and Technology of China, Hefei, Anhui 230026, People's Republic of China
Fax: +86-551-3601592
E-mail: zxwang@ustc.edu.cn



Zhong-Xia Wang was born in 1963 in Anhui, China. He finished his B.S. degree (Chemistry) in 1983 and M.S. degree (Organic Chemistry) in 1986 at Nankai University. He then joined University of Science and Technology of China as a Teaching Assistant, later becoming Lecturer (1988). From August 1993 to October 1996, he studied organometallic chemistry with Prof. Michael F. Lappert at University of Sussex and received a Ph.D. degree in January 1997. He became an Associate Professor at University of Science and Technology of China in December 1996. In October 1999 he joined Prof. W. P. Leung's group at the Chinese University of Hong Kong as a Research Associate. Since October 2000 he has been a Professor at University of Science and Technology of China. His research interests include the design, synthesis, and applications of organometallic compounds as catalysts for activation of inert chemical bonds and the ring-opening polymerization of cyclic esters.

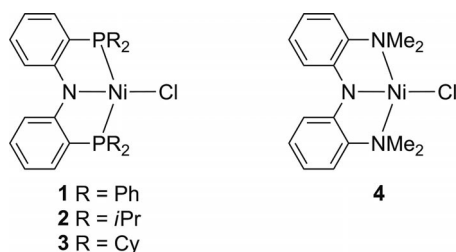


Ning Liu was born in 1984 in Gansu, China. He received his B.S. degree from University of Science and Technology of China in 2007. He is currently a fifth-year graduate student with Prof. Wang at University of Science and Technology of China. His research interest is transition-metal-catalyzed activation of inert carbon–heteroatom bonds.

gands have been employed in transition-metal-catalyzed cross-coupling of saturated and unsaturated substrates. In the last decades, pincer ligands have been recognized to stabilize a lot of metal ions and tune catalytic properties of the complexes.^[11] In 2003, Fu and co-workers reported that a combination of Ni(cod)₂ and a neutral tridentate pyridine–bis(oxazoline) ligand catalyzed the cross-coupling of a range of alkyl bromides and iodides with alkylzinc halides.^[12] Since then, pincer–nickel-catalyzed cross-coupling reactions have been more and more studied. In this review, we will focus our attention on the progress of nickel-catalyzed cross-coupling reactions with pincer-type ligands exclusively, even though, for a specific reaction, some other combination of metal and ligands could be more effective.

Kumada Reactions

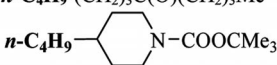
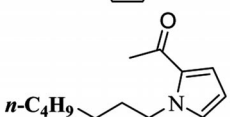
Liang and co-workers reported in 2006 the synthesis of amido-pincer–nickel complexes **1–3** (Scheme 1) and found that these complexes are active catalyst precursors for the Kumada coupling of phenyl iodide or bromide with aryl or alkyl Grignard reagents.^[13] The conversion and selectivity of these catalytic reactions are relatively unsatisfactory. However, it is of interest to note that the catalysis is compatible with alkyl nucleophiles bearing β -hydrogen atoms. Hu et al. found that NN₂-pincer–nickel complex **4** (Scheme 1) is a more widely applicable catalyst for the Kumada coupling of β -hydrogen-containing nucleophiles or electrophiles.^[14] In the reaction of primary alkyl iodides and bromides as well as secondary alkyl iodides with alkyl Grignard reagents 3 mol-% of **4** could drive the cross-coupling to completion. The reactions proceed under very mild conditions (–20 to –35 °C) and hence tolerate a range of functional groups such as ester, amide, keto, ether, thioether, acetal, nitrile, and heterocyclic groups (Table 1).^[15] Recently, a structure–activity study was carried out by the same group, and improved catalysts were developed.^[16] Coupling of alkyl chlorides is ineffective in most cases. However, CH₂Cl₂ can be doubly alkylated by using primary alkyl Grignard reagents catalyzed by **4**. Unfortunately, the reaction can not be extended to other polychloroalkanes; secondary and tertiary alkyl Grignard reagents are also ineffective.^[15b,17] In addition, when bromomethylcyclopropane was coupled to *n*-pentylMgCl in the presence of **4**, 1-nonene was formed as the major product.^[7,15b] The experimental results support a free radical mechanism for the cross-coupling. A proposed catalytic cycle is shown in



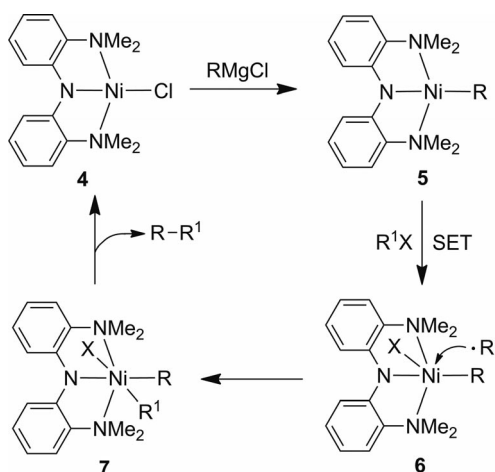
Scheme 1. PNP- and NN₂-pincer–nickel complexes.

Scheme 2.^[15b] Complex **4** reacts with an alkyl Grignard reagent, RMgCl, to form an alkylated nickel complex **5**. Reaction of **5** with an alkyl halide through single-electron transfer generates **6** and an alkyl free radical. The recombination of **6** with the alkyl radical affords six-coordinate nickel complex **7**. Reductive elimination from the metal center of complex **7** leads to coupling product R–R¹ and regeneration of complex **4**. Experimental and DFT studies show that in the reaction β -H elimination of the [(^{Me}N₂N)Ni(alkyl)] complexes is kinetically accessible but thermodynamically unfavorable, which results in achievement of the cross-coupling of the β -H-containing substrates.^[18]

Table 1. Selected examples for the cross-coupling of alkyl halides with alkyl Grignard reagents catalyzed by NN₂-pincer–nickel complex **4**.

$\text{R}^1\text{MgCl} + \text{R}^2\text{X} \xrightarrow[\text{DMA, -35 } ^\circ\text{C}]{\text{4 (3 mol-\%)}} \text{R}^1\text{--R}^2$			
Entry	X	Product	Yield [%] ^[a]
1	Br	<i>n</i> -C ₄ H ₉ –(CH ₂) ₃ COOEt	85
2	Br	Me ₂ CH–(CH ₂) ₃ COOEt	71
3	Br	<i>n</i> -C ₄ H ₉ –(CH ₂) ₃ CONEt ₂	78
4	Br	<i>n</i> -C ₄ H ₉ –(CH ₂) ₃ OC(O)Me	78 ^[b]
5	Br	<i>n</i> -C ₄ H ₉ –(CH ₂) ₂ C(Ph) ₂ CN	99
6	I	<i>n</i> -C ₄ H ₉ –(CH ₂) ₃ C(O)(CH ₂) ₃ Me	75
7	I	<i>n</i> -C ₄ H ₉ – 	86
8	I	<i>n</i> -C ₄ H ₉ – 	93

[a] Isolated yields unless otherwise specified. [b] GC yields.

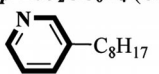
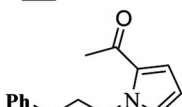


Scheme 2. Catalytic cycle for alkyl–alkyl coupling by NN₂-pincer–nickel complex **4**.

In the presence of a catalytic amount of amine additive tmeda or O-tmeda, complex **4** also catalyzes the cross-coupling of alkyl halides with aryl and heteroaryl Grignard reagents (Table 2). The reactions can be carried out at room temperature. Primary alkyl iodides and bromides as well as

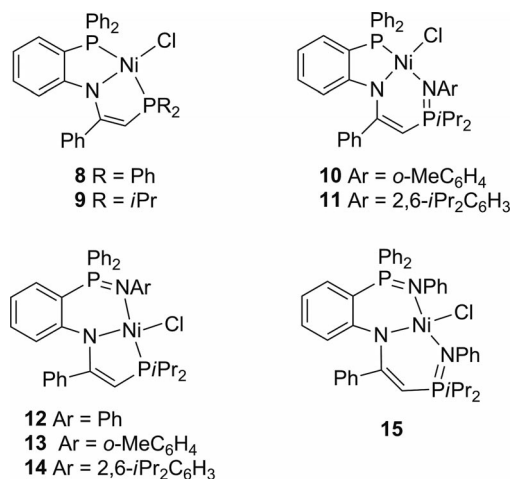
cyclic secondary alkyl iodides give good to excellent yields. However, alkyl chlorides lead to poor results, even at elevated reaction temperature and with higher catalyst loading. The reaction is also compatible with functional groups such as functionalized alkyl halides and functionalized aryl or heteroaryl Grignard reagents. Hence, this catalytic reaction expands significantly the scope of Kumada coupling. The amine additive (tmeda or O-tmeda) was found to suppress the homocoupling of both coupling partners, possibly through coordination to the Mg ion, which stabilizes functionalized Grignard reagents and makes the Grignard reagents more nucleophilic.^[19]

Table 2. Selected examples for the cross-coupling of alkyl halides with aryl Grignard reagents catalyzed by NN₂-pincer–nickel complex **4**.

$\text{ArMgCl} + \text{RX} \xrightarrow[\text{Additive THF, r.t.}]{\textbf{4 (3 mol-\%)}} \text{Ar-R}$				
Entry	X	Additive	Product	Yield [%] ^[a]
1	Br	tmeda	<i>p</i> -FC ₆ H ₄ -(CH ₂) ₂ Ph	78 ^[b]
2	Br	tmeda	Ph-Cy	65 ^[b]
3	Br	tmeda	<i>p</i> -FC ₆ H ₄ -(CH ₂) ₄ Cl	76
4	I	tmeda	Ph-(CH ₂) ₄ CN	80
5	I	tmeda	Ph-CH ₂ CHMe ₂	86 ^[b]
6	I	O-tmeda	Ph-(CH ₂) ₃ COOEt	75
7	I	tmeda	<i>p</i> -NCC ₆ H ₄ -C ₈ H ₁₇	62
8	I	tmeda	<i>p</i> -EtO ₂ CC ₆ H ₄ -(CH ₂) ₂ Ph	88
9	I	tmeda		76
10	I	O-tmeda		62

[a] Isolated yields unless otherwise specified. [b] GC yields.

We synthesized a series of unsymmetrical amido-pincer complexes of nickel (Scheme 3). These complexes are highly active in catalyzing the cross-coupling of aryl iodides with aryl Grignard reagents. The reactions were carried out in



Scheme 3. Unsymmetrical amido-pincer–nickel complexes **8–15**.

toluene at room temperature. A catalyst loading of 0.01–0.5 mol-% almost quantitatively led to cross-coupling products of inactivated and deactivated aryl iodides with *p*-MeC₆H₄MgBr. The activity order of the complexes is approximately **15** > **13** ≈ **10** > **12** > **11** > **14** > **8** ≈ **9**.^[20]

These complexes also efficiently catalyze the cross-coupling of aryl chlorides with aryl Grignard reagents (Table 3). Both inactivated and deactivated aryl chlorides can be coupled. The reactions of PhCl and *o*-MeC₆H₄Cl proceed at room temperature, while the reaction of *p*-MeOC₆H₄Cl often requires elevated temperatures and higher catalyst loading. The activity order of the catalysts in the reaction of aryl chlorides are a little different from that for aryl iodides as the electrophiles.^[20]

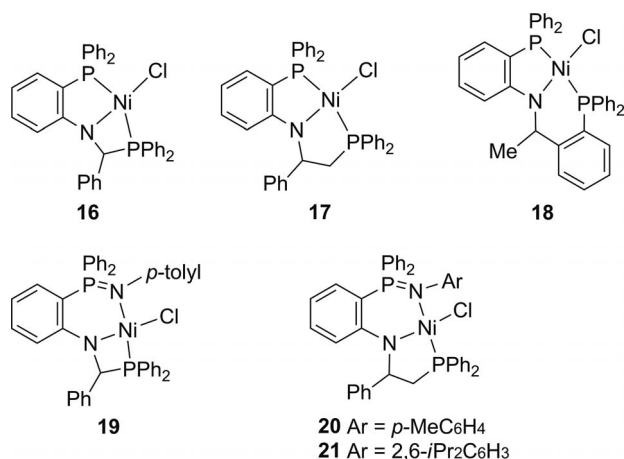
Table 3. Selected examples for the cross-coupling of *p*-MeC₆H₄MgBr with *p*-RC₆H₄Cl catalyzed by complexes **8–15**.^[a]

Entry	Complex (mol-%)	R	Reaction conditions	Yield [%] ^[b]
1	8 (2.5)	H	room temp., 24 h	80
2	9 (2.5)	H	room temp., 24 h	92.8
3	10 (2.5)	H	room temp., 24 h	91
4	11 (2.5)	H	room temp., 24 h	> 99
5	12 (2.5)	H	room temp., 18 h	> 99
6	13 (2.5)	H	room temp., 12 h	98.4
7	14 (2.5)	H	room temp., 24 h	95
8	15 (2.5)	H	room temp., 24 h	94
9	9 (4)	MeO	room temp., 67 h	89
10 ^[c]	9 (4)	MeO	80 °C, 12 h	94
11	10 (4)	MeO	room temp., 66 h	80
12 ^[c]	11 (2.5)	MeO	80 °C, 6 h	92
13	13 (4)	MeO	room temp., 30 h	93
14	14 (4)	MeO	room temp., 40 h	92.3
15	15 (4)	MeO	room temp., 70 h	88
16 ^[c]	15 (2.5)	MeO	80 °C, 6 h	98.6

[a] Reactions were carried out in THF unless otherwise stated. [b] Yields of isolated products. [c] A mixed solvent of THF and toluene (1:1) was used.

Closely related complexes **16–21** (Scheme 4) were also synthesized and evaluated for their catalytic activity in the Kumada reaction (Table 4). Complexes **18** and **21** show low activity in catalyzing the coupling of either aryl iodides or chlorides. Complexes **16**, **17**, **19**, and **20** are highly active in the reaction with aryl iodides as the electrophilic partners. A catalyst loading of 0.005–0.01 mol-% could drive the reaction to completion. Complexes **16**, **17**, **19**, and **20** can also catalyze the coupling of inactivated and deactivated aryl chlorides with aryl Grignard reagents at room temperature. The activity order is approximately **17** ≈ **19** ≈ **20** > **16** > **21** > **18**. The activities of complexes **17**, **19**, and **20** are comparable to those of complexes **13** and **14** in catalyzing the reaction of deactivated aryl chloride and higher than those of **9–11** and **15**. Complexes **17** and **8/9** have similar ligand structural skeletons, but those of **8/9** are more rigid. This rigid skeleton may lead to a lower catalytic activity of **8/9** than that of **17**. However, the difference in the rigidity of the ligand seems not to affect the catalytic activity of **12–14** and **21** very much. These complexes show close catalytic activity in the reaction of aryl chlorides with aryl Grignard

reagents. The size of the metal chelate rings seems to be related to the activity. This was confirmed by the activity difference between complexes **16** and **18**, the former being highly active, whereas the latter shows very low activity.^[21]



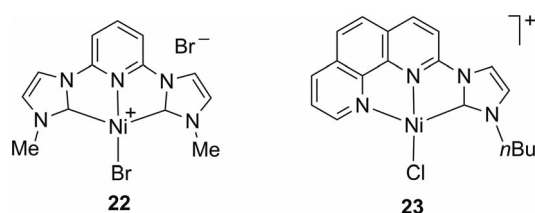
Scheme 4. Unsymmetrical amido-pincer-nickel complexes **16–21**.

Table 4. Selected examples for the cross-coupling of *p*-MeC₆H₄MgBr with *p*-RC₆H₄X catalyzed by complexes **16–20**.^[a]

Entry	X	R	Complex (mol-%)	Yield [%] ^[b]
1	I	MeO	16 (0.005)	98
2	I	MeO	17 (0.01)	89
3	I	MeO	18 (0.01)	43
4	I	MeO	19 (0.005)	97
5	I	MeO	20 (0.005)	96
6	I	MeO	21 (0.01)	48
7	Cl	H	16 (2)	79
8	Cl	H	17 (2)	95
9	Cl	H	18 (2)	3
10	Cl	H	19 (2)	93
11	Cl	H	20 (2)	94
12	Cl	H	21 (2)	9
13	Cl	MeO	16 (4)	75
14	Cl	MeO	17 (4)	94
15	Cl	MeO	19 (4)	98
16	Cl	MeO	20 (4)	97

[a] Reactions were run in toluene (for iodides) or THF (for chlorides) at room temperature for 12 h (for iodides) or 36 h (for chlorides). [b] Yields of isolated products.

Inamoto and co-workers reported an NHC-based CNC-pincer-nickel complex **22** (Scheme 5) and its catalytic action in the cross-coupling of aryl bromides, chlorides, and fluorides with aryl Grignard reagents. The reactions were carried out in THF at room temperature with 5 mol-% catalyst loading. Inactivated and deactivated aryl halides are appli-

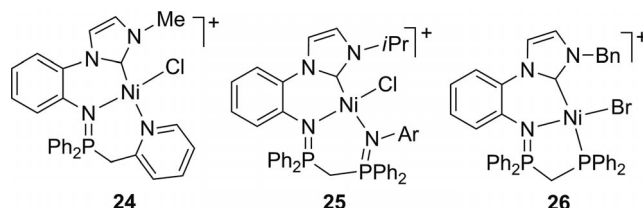


Scheme 5. NHC-based CNC- and NNC-pincer-nickel complexes.

cable as the electrophiles, and most reactions run with moderate to good yields. However, the reactions of fluorides and partial chlorides requires a time of two to six days. This will limit the application of this method.^[22]

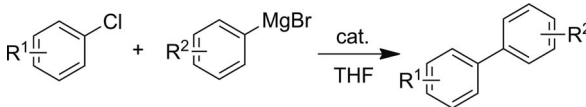
Chen and co-workers reported that unsymmetrical NHC-based pincer-nickel complex **23** (Scheme 5) can catalyze the cross-coupling of aryl chlorides with *p*-tolylmagnesium bromide in THF at room temperature. The activated aryl or heteroaryl chlorides gave good to excellent product yields. However, deactivated aryl chlorides such as 1-chloro-4-methoxybenzene afforded poor results (20% yield).^[23]

Unsymmetrical NHC-based pincer-nickel complexes **24–26** (Scheme 6) are also active catalysts for the cross-coupling of inactivated and deactivated aryl chlorides with aryl Grignard reagents (Table 5). The reactions proceed smoothly in THF at room temperature. However, for 1-chloro-4-methoxybenzene, reactions at elevated temperature result in higher yields. The catalytic activities of complexes **24** and **25** are close to each other, while **26** shows a little lower activity. In the catalytic reactions, the tridentate ligands are assumed to be hemilabile. The carbene group binds to the central nickel atom by a strong σ bond, whereas the terminal nitrogen or phosphorus group is labile. The vacant coordination sites are formed through dissociation of the terminal nitrogen or phosphorus group. Dissociation of the nitrogen group from the nickel center is easier than that of the phosphane group, and hence generation of the active intermediate is easier in the cases of com-



Scheme 6. NHC-based CNC- and NNC-pincer-nickel complexes **24–26**.

Table 5. Selected examples for the cross-coupling of aryl chlorides with aryl Grignard reagents catalyzed by complexes **24–26**.

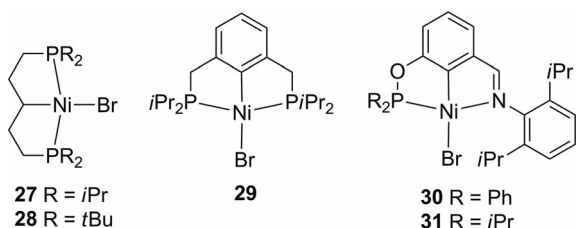


Entry	R ¹	R ²	Complex (mol-%)	Temp. [°C]	Yield [%] ^[a]
1	H	<i>p</i> -Me	24 (1)	room temp.	91
2	<i>o</i> -Me	<i>o</i> -Me	24 (4)	room temp.	88
3	<i>p</i> -MeO	<i>p</i> -Me	24 (4)	room temp.	81
4	<i>p</i> -MeO	<i>p</i> -Me	24 (4)	80	92
5	H	<i>p</i> -Me	25 (1)	room temp.	91
6	<i>o</i> -Me	<i>o</i> -Me	25 (4)	room temp.	90
7	<i>p</i> -MeO	<i>p</i> -Me	25 (4)	room temp.	82
8	<i>p</i> -MeO	<i>p</i> -Me	25 (4)	80	94
9	H	<i>p</i> -Me	26 (1)	room temp.	92
10	<i>p</i> -MeO	<i>p</i> -Me	26 (4)	room temp.	69

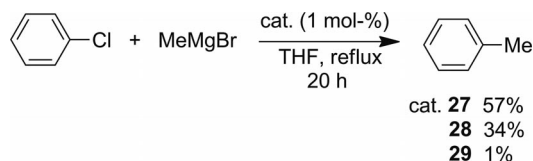
[a] Yields of isolated products.

plexes **24** and **25** than in the case of complex **26**. This difference leads to higher catalytic activity of the former.^[24]

PCP-pincer-nickel complexes **27** and **28** (Scheme 7) catalyze the Kumada coupling in THF heated at reflux. Complex **27** is more active than **28**, whereas complex **29** is nearly inactive (Scheme 8). The authors indicated that there is a direct correlation between the catalytic efficiency of these PCP systems and the respective electron-richness of their Ni centers (**27** > **28** > **29**) on the basis of this activity order and the cyclic voltammetry measurements of the complexes.^[25]



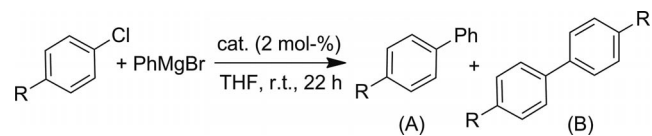
Scheme 7. PCP- and PCN-pincer-nickel complexes **27**–**31**.



Scheme 8. Cross-coupling of PhCl with MeMgBr catalyzed by PCP-pincer-nickel complexes.

PCN-pincer-Ni complexes **30** and **31** (Scheme 7) catalyze the reaction of aryl chloride with PhMgBr in THF at room temperature, forming cross-coupling products and minor homocoupling products of aryl chlorides (Table 6). Complex **31** is more efficient than **30**. This may be attributed to the better donating ability of the diisopropylphosphanyl group than that of the diphenylphosphanyl group.^[26]

Table 6. Cross-coupling of aryl chlorides with PhMgBr catalyzed by PCN pincer-nickel complexes.



Entry	R	Catalyst	Conversion [%] ^[a]	Ratio A/B ^[b]
1	Me	30	71	89:11
2	Me	31	99	90:10
3	OMe	30	69	88:12
4	OMe	31	98	88:12

[a] GC yields based on unreacted aryl chlorides. [b] Calibrated with authentic biphenyl samples.

Negishi Reactions

The Negishi reaction shows better functional group compatibility than the Kumada reaction, and hence it is a valuable tool for the formation of C–C bonds in the presence

of functional groups. Recently Cárdenas et al. reviewed the Ni-catalyzed Negishi cross-coupling reaction.^[9g] Pincer-nickel complexes constitute an important part of Ni catalysts used for the Negishi reaction.

Each of complexes **13**–**15** (Scheme 3) is active for the coupling of aryl chlorides and arylzinc chlorides. Among them, complexes **13** and **15** display the highest catalytic activity. A 1 mol-% loading of **13** or **15** leads to the cross-coupling product of *p*-ClC₆H₄NMe₂ with PhZnCl nearly quantitatively. The activity order is approximately **13** ≈ **15** > **3a** > **2a** ≈ **2b** > **1b** > **3c** > **1a**. For most aryl chlorides, including those inactivated and deactivated, the catalyst loading is extremely low. An amount of 0.02 mol-% **13** or **15** could drive the reaction of *p*-ClC₆H₄OMe with *p*-MeC₆H₄ZnCl to completion. The reaction tolerates a range of functional groups such as keto, ester, trifluoromethyl, cyano, amide, and pyridyl, but it is incompatible with nitro and formyl groups. Chlorobenzonitrile shows much lower reactivity relative to those of other aryl chlorides such as *p*-ClC₆H₄COOEt, *p*-ClC₆H₄COPh, and even *p*-ClC₆H₄OMe. This is ascribed to the coordination of the nitrile group to the catalyst species.^[27] 2-Furylmagnesium bromide is also less reactive than other arylzinc reagents tested. A possible reason is the coordination of the oxygen atom of furyl to a metal center (e.g. zinc or nickel ion), which decreases the nucleophilicity of the furyl anion. In addition, sterically hindered reactants require stronger reaction conditions and often give low product yields (Table 7).^[28]

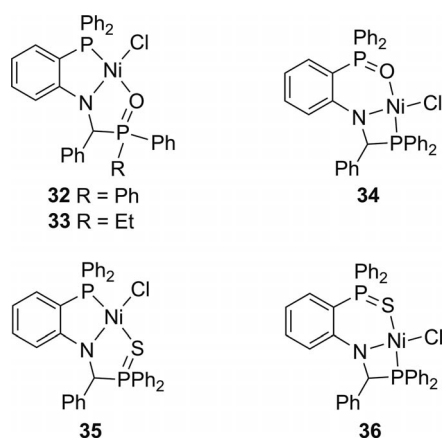
Table 7. Selected examples for the cross-coupling of aryl chlorides with arylzinc chlorides catalyzed by complexes **13** and **15**.^[a]

$\text{Ar}^1\text{ZnCl} + \text{Ar}^2\text{Cl} \xrightarrow[\text{THF/NMP (1:1)}]{\text{cat.}} \text{Ar}^1\text{--Ar}^2$				
Entry	Ar ¹	Ar ²	Complex (mol-%)	Yield [%] ^[b]
1	<i>p</i> -MeC ₆ H ₄	<i>p</i> -Et ₂ NC(O)C ₆ H ₄	13 (0.01)	99
2	<i>p</i> -MeC ₆ H ₄	<i>p</i> -NCC ₆ H ₄	13 (3)	59
3	<i>p</i> -MeC ₆ H ₄	<i>p</i> -MeOC ₆ H ₄	13 (0.02)	97.3
4 ^[c]	<i>p</i> -MeC ₆ H ₄	<i>o</i> -PhC(O)C ₆ H ₄	13 (1.5)	98
5	Ph	<i>p</i> -Et ₂ NC(O)C ₆ H ₄	15 (0.01)	99
6	<i>p</i> -MeC ₆ H ₄	<i>p</i> -MeOC ₆ H ₄	15 (0.02)	99
7 ^[c]	<i>p</i> -MeC ₆ H ₄	<i>o</i> -MeOC ₆ H ₄	15 (2.5)	97
8	<i>o</i> -MeC ₆ H ₄	<i>p</i> -MeOC ₆ H ₄	15 (0.1)	96
9	2-furyl	<i>p</i> -EtOC(O)C ₆ H ₄	15 (0.5)	99
10	2-furyl	<i>p</i> -CF ₃ C ₆ H ₄	15 (0.4)	96
11 ^[c]	2-furyl	Ph	15 (2.5)	58

[a] Reactions were carried out at 70 °C unless otherwise stated. [b] Yields of isolated products. [c] Reactions were run at 100 °C.

NHC-based pincer-nickel complexes **24**–**26** efficiently catalyze the reaction of *p*-MeC₆H₄ZnBr with aryl chlorides. Complex **25** is more active than both **24** and **26**. It catalyzes the cross-coupling reactions in a mixture of THF and NMP at 70 °C in 16 h, giving 55–99% product yields. The catalyst loading is low (0.1–2 mol-%), and the reactions tolerate functional groups such as ester, keto, cyano, and amide.^[24] The catalytic activity of **25** is a little lower than those of **13** and **15** but higher than those of other Ni–NHC systems.^[29]

The Negishi reaction of aryl chlorides often needs elevated temperatures because of the low reactivity of the C–Cl bond. Negishi reactions with aryl chlorides as the electrophilic partners were quite limited at room temperature. Several successful examples employed activated aryl chlorides as the electrophiles. Organ and co-workers reported a Pd-catalyzed reaction of 2,4,6-Me₃C₆H₂ZnCl with 2-chloro-1,3-dimethylbenzene at 23 °C, giving the cross-coupling product in 90% isolated yield.^[30] We found that PNO- and PNS-pincer–nickel complexes **32–36** (Scheme 9) can catalyze reactions of aryl chlorides with arylzinc reagents at room temperature, including those of deactivated aryl chlorides. The PNO-pincer–nickel complexes display excellent catalytic activity, whereas the PNS-pincer–nickel complexes show lower activity (Table 8). Complexes **32** and **34** catalyze room-temperature reactions of a broad spectrum of aryl chlorides and tolerate a range of functional groups. A low catalyst loading can be employed in most cases. *p*-



Scheme 9. PNO- and PNS-pincer–nickel complexes **32–36**.

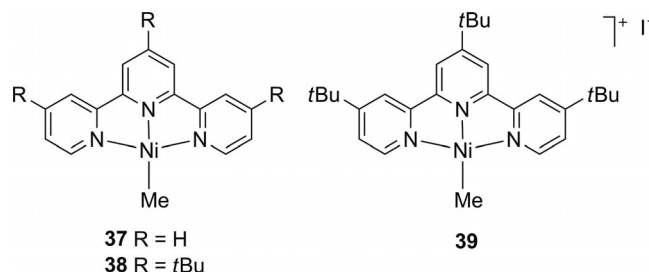
Table 8. Selected examples for the cross-coupling of aryl chlorides with arylzinc chlorides catalyzed by complexes **32–36**.^[a]

$\text{Ar}^1\text{ZnCl} + \text{Ar}^2\text{Cl} \xrightarrow[\text{THF/NMP (1:1), r.t., 24 h}]{\text{cat.}} \text{Ar}^1\text{–Ar}^2$				
Entry	Ar ¹	Ar ²	Complex (mol-%)	Yield [%] ^[b]
1	Ph	<i>p</i> -MeOC ₆ H ₄	32 (0.2)	98
2	Ph	<i>p</i> -MeOC ₆ H ₄	33 (0.2)	97
3	Ph	<i>p</i> -MeOC ₆ H ₄	34 (0.2)	92
4	Ph	<i>p</i> -MeOC ₆ H ₄	35 (0.2)	67
5	Ph	<i>p</i> -MeOC ₆ H ₄	36 (0.2)	62
6	<i>p</i> -MeC ₆ H ₄	Ph	32 (0.05)	99
7	<i>p</i> -MeC ₆ H ₄	<i>p</i> -PhC(O)C ₆ H ₄	32 (0.1)	98
8	<i>p</i> -MeC ₆ H ₄	<i>p</i> -NCC ₆ H ₄	32 (2)	87
9	<i>p</i> -MeC ₆ H ₄	<i>p</i> -CF ₃ C ₆ H ₄	32 (0.05)	95
10	<i>p</i> -MeC ₆ H ₄	2-C ₅ H ₄ N	32 (0.1)	99
11 ^[c]	<i>p</i> -MeC ₆ H ₄	<i>p</i> -Et ₂ NC(O)C ₆ H ₄	32 (0.05)	99
12 ^[c]	<i>p</i> -MeC ₆ H ₄	<i>p</i> -EtOC(O)C ₆ H ₄	32 (0.05)	99

[a] Reactions were carried out under the conditions indicated by the above equation unless otherwise stated. [b] Yields of isolated products. [c] Reactions were run for 12 h.


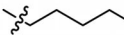

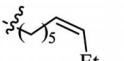

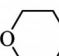
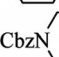
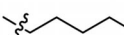
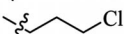
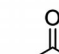

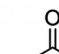
Chlorobenzonitrile and hindered substrates require higher catalyst loadings. In addition, electron-deficient zinc reagents require higher catalyst loadings and afford relatively poor results in the catalytic coupling reaction.^[31]

Vicic and co-workers synthesized several Ni–terpy complexes and found that each of these complexes could catalyze the coupling of alkyl iodides with alkylzinc reagents with good to excellent yields. (Scheme 10).^[32] The reaction tolerates β-hydrogen-containing alkyl halides and alkylzinc compounds. Primary and secondary alkyl iodides are suitable electrophiles. Alkyl bromides are less reactive, achieving low product yields under the same conditions. However, Fu and co-workers found that reaction of propargylic bromides, and even propargylic chlorides, with alkylzinc compounds catalyzed by NiCl₂·glyme/terpy give good to excellent results (Table 9). In the reaction, a bulky group (TIPS, triisopropylsilyl) attached at the C≡C triple bond of the electrophiles is necessary, which prevents the homocoupling of electrophiles.^[33]



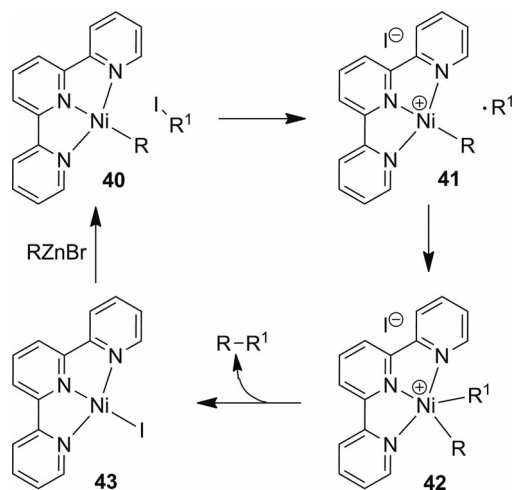
Scheme 10. Ni–terpy complexes **37–39**.

Table 9. Selected examples for the Negishi reactions of alkylzinc reagents with propargylic halides catalyzed by NiCl₂·glyme/terpy.

$\text{TIPS}\text{---}\text{C}\equiv\text{C}\text{---}\text{C}\begin{matrix} \text{R} \\ \text{X} \end{matrix} + \text{R}^1\text{ZnX}^1 \xrightarrow[\text{DMA, r.t.}]{\text{NiCl}_2 \text{ glyme (10 mol-\%)} \text{ terpy (10 mol-\%)}} \text{TIPS}\text{---}\text{C}\equiv\text{C}\text{---}\text{C}\begin{matrix} \text{R} \\ \text{R}^1 \end{matrix}$				
1.6 equiv.				
Entry	X	R	R ¹	Yield [%] ^[a]
1	Br	Bu ⁿ	 ZnI	88
2	Br	 COOMe	 ZnI	72
3	Br	 Et	 ZnI	72
4	Br	Bu ⁿ	 ZnI	70
5	Br	Me	 ZnI	76
6	Br	 COOMe	Me ₂ CHZnI	63
7	Br	 Cl	BnOCH ₂ CH ₂ CH ₂ ZnBr	97
8	Br	H	 ZnBr	90
9	Cl		 ZnI	76

[a] Yields of purified products.

A proposed mechanism for the terpy–Ni-catalyzed alkyl–alkyl cross-coupling is shown in Scheme 11. The reaction of (terpyridyl)Ni(alkyl) complex **40** with an alkyl halide forms **41** and an alkyl free radical. Then, an oxidative radical addition between the alkyl radical and **41** generates Ni^{III}–di-alkyl species **42**. Following reductive elimination of the Ni^{III}–di-alkyl species affords the cross-coupled alkane and (terpyridyl)Ni–I species **43**, which reacts with the organozinc reagent to recycle the catalyst.^[32b,32c,34] Both **40** (R = Me) and **43** have been isolated and characterized, and the former is considered to be a Ni^{II} species coordinated to a methyl and an anionic terpyridyl ligand, according to EPR spectroscopic and DFT studies.^[32,35] (Terpyridyl)NiMe is able to transfer its methyl group to iodocyclohexane to form methylcyclohexane in good yield. It also catalyzes the cross-coupling of alkyl electrophiles with alkylzinc compounds. Several pieces of evidence prove a radical process. Firstly, Vicić et al. found that minor product Ph(CH₂)₃–(CH₂)₃Ph and dicyclohexyl formed as a result of the reactions of Ph(CH₂)₃I and cyclohexyl iodide with *n*-pentylzinc bromide, which may come from the dimerization of the corresponding alkyl radical; secondly, when the radical clock, iodomethylcyclopropane, was used as the electrophile, olefin products were obtained.^[32]

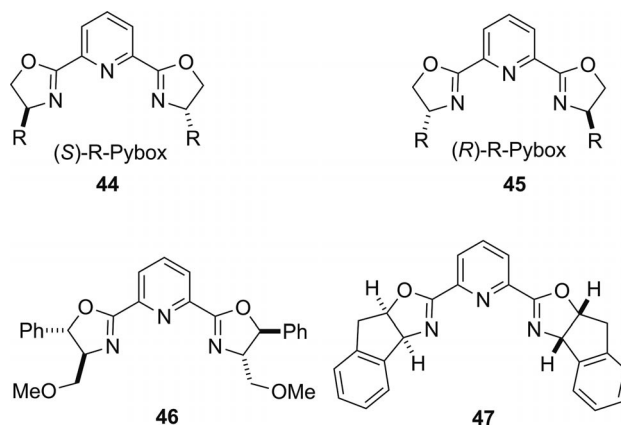


Scheme 11. A mechanism for alkyl–alkyl coupling catalyzed by a Ni–terpy complex.

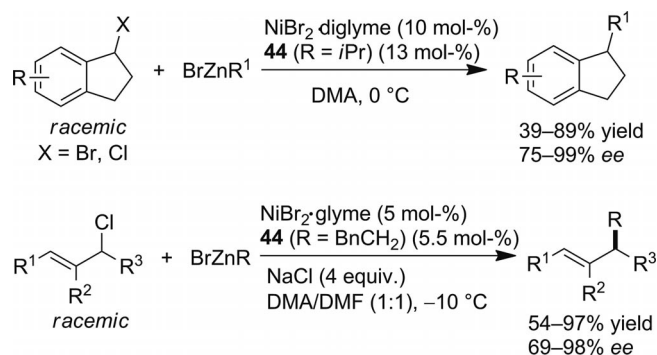
Recently Biscoe and co-workers found that secondary alkylzinc halides can be coupled to aryl/heteroaryl iodides with excellent isomeric retentions by using a terpyridine–NiCl₂ catalyst. This is the first process to overcome the isomerization and β -hydrogen elimination problems that are associated with the use of secondary nucleophiles and that have limited the performance of analogous Pd-catalyzed systems. The presence of LiBF₄ dramatically improves both isomeric retention and yield for challenging substrates.^[36]

Pyridine–bis(oxazoline) (Pybox) ligands (Scheme 12) are structurally closely related to terpyridine. In 2003, Fu and co-workers reported the Ni-catalyzed cross-coupling of primary and secondary alkyl bromides and iodides with alkylzinc reagents by using *s*Bu–Pybox (**44**, R = *s*Bu) as a li-

gand. The reaction was run in DMA at room temperature with 4 mol-% Ni(cod)₂ and 8 mol-% *s*Bu–Pybox loading, affording the cross-coupling products in yields of 62–91%. Pybox ligands with other R groups such as Ph, *t*Bu, and *i*Pr are less effective than *s*Bu–Pybox. Ni(cod)₂ gave better results than NiBr₂.^[12] Fu et al. subsequently reported a series of asymmetric cross-couplings of *racemic* alkyl halides with alkylzinc reagents by using chiral Pybox ligands. A combination of the NiBr₂·diglyme and (*S*)-*i*Pr–Pybox ligands can catalyze the coupling of secondary benzylic bromides and chlorides with alkylzinc compounds, giving 75–99% *ee* and 39–89% yields of the cross-coupling products,^[37] while the combination of NiBr₂·glyme and (*S*)-BnCH₂–Pybox ligands drive the coupling of secondary allylic chlorides with alkylzinc reagents in 69–98% *ee* and yields of 54–97% (Scheme 13).^[38] In an investigation of Ni-catalyzed enantioselective coupling of secondary α -bromoamides with alkylzinc compounds, (*R*)-*i*Pr–Pybox was found to be the best ligand.^[39] For the enantioselective coupling with arylzinc reagents as the nucleophiles, the use of chiral Pybox ligands also depends on the electrophilic substrates. For example, for the Ni-catalyzed reaction of *racemic* α -bromoketones with arylzinc compounds, **46** is the best ligand,^[40] whereas for the reaction of *racemic* propargylic halides with arylzinc compounds, **47** is the best li-



Scheme 12. Pybox ligands.



Scheme 13. Nickel-catalyzed enantioselective coupling of *racemic* secondary benzylic halides and allylic chlorides with alkylzinc reagents catalyzed by (*S*)-R–Pybox ligands.

In addition, Caeiro et al. found that $\text{NiBr}_2 \cdot \text{diglyme} \cdot (S)\text{-}i\text{Pr-Pybox}$ catalyzes the enantioselective coupling of *racemic* secondary benzyl bromides with trialkynylindium. The reaction was performed in a 1:1 mixture of DMA and THF at room temperature with 10% $\text{NiBr}_2 \cdot \text{diglyme}$ and 13% $(S)\text{-}i\text{Pr-Pybox}$ loadings, affording the products in 77–87% *ee* and yields of 30–70%.^[42] Gagné and co-workers reported the coupling of glycosyl halides with alkyl- and arylzinc reagents by using $\text{NiCl}_2 \cdot \text{Pybox}$ (**44**, $R = \text{H}$) as the catalyst.^[43] Lin et al. suggested a $\text{Ni}^{\text{I}}\text{-Ni}^{\text{III}}$ mechanism for the reaction of racemic secondary alkyl electrophiles on the basis of a DFT calculation study.^[44]

In 2007 Cárdenas et al. reported a $\text{Ni}(\text{py})_4\text{Cl}_2 \cdot (S)\text{-}s\text{Bu-Pybox}$ -catalyzed cascade formation of $\text{C}(\text{sp}^3)\text{-C}(\text{sp}^3)$ bonds by cyclization and cross-coupling of alkylzinc reagents with alkyl iodides containing an alkene group (Table 10). The reaction is inhibited by the stable radical TEMPO. The results of the cross-couplings with several radical clock sub-

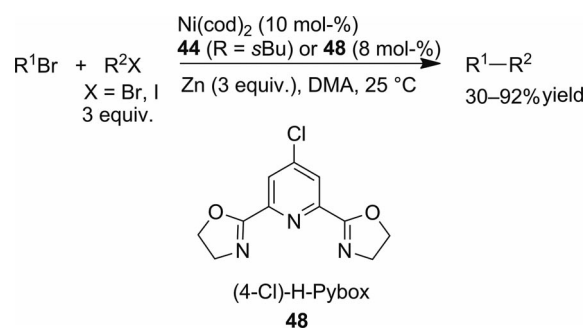
Table 10. Selected examples for cascade formation of two $\text{C}(\text{sp}^3)\text{-C}(\text{sp}^3)$ bonds by cyclization and Negishi coupling catalyzed by $\text{Ni}(\text{py})_4\text{Cl}_2 \cdot (S)\text{-}s\text{Bu-Pybox}$.

$\text{Alkene-I} + \text{RZnBr} \xrightarrow[\text{THF, 23 } ^\circ\text{C}]{\text{Ni}(\text{py})_4\text{Cl}_2 \text{ (10 mol-\%)} \atop (S)\text{-}s\text{Bu-Pybox} \text{ (10 mol-\%)} \atop 4 \text{ equiv.}}$			
Entry	Alkyl iodide	Product	Yield [%]
1			79
2			94 (97:3) ^[a]
3			64
4			81
5			83
6			66

[a] Measured by GC-MS. The minor isomer has the opposite configuration at C3.

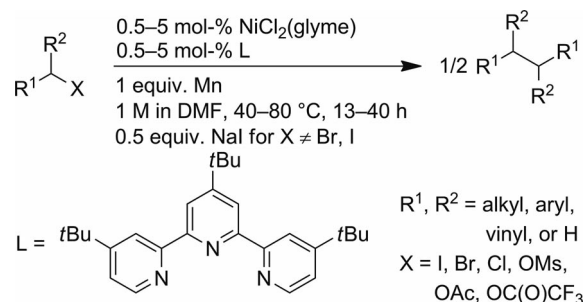
strates also support a radical process. On the basis of experimental results and DFT calculations, it was believed that the catalysis proceeds through a free radical pathway and a Ni^{I} complex is the catalytically active species.^[45]

Recently Gong et al. developed a nickel-catalyzed reductive cross-coupling of two different alkyl halides (Scheme 14). The reaction requires 3 equiv. of zinc and 3 equiv. of one of the reactants when a combination of $\text{Ni}(\text{cod})_2$ and $(S)\text{-}s\text{Bu-Pybox}$ or $(4\text{-Cl})\text{-H-Pybox}$ is used as the catalyst. The mild reaction conditions allow for excellent functional group tolerance. In the case of two alkyl bromides as coupling partners, it was proved that no alkylzinc reagents are formed under the coupling conditions. Hence, it seems that this reaction is a non-Negishi process. However, a Negishi process can not be ruled out when alkyl iodides are employed as the coupling partners.^[46]



Scheme 14. Nickel-catalyzed reductive coupling of alkyl halides.

A related reaction reported by Weix et al. is Ni-catalyzed reductive dimerization of alkyl halides, alkyl pseudohalides, and allylic acetates using Mn^0 as a reducing agent and 4,4',4''-tri-*tert*-butyl-2,2':6',2''-terpyridine as the ligand (Scheme 15). The reaction gave good to excellent yields for the alkyl bromides and iodides as well as for the allylic acetates. However, reaction of alkyl chlorides, alkyl mesylates, and alkyl trifluoroacetates required the addition of 50% NaI. The authors indicated that the role of iodide in these reactions may include: (1) enhancement of the reductive coupling, possibly by facilitating the reduction of the nickel catalyst or the formation of a nickelate species, and (2) generation of reactive alkyl iodides from unreactive alkyl trifluoroacetates in situ by substitution.^[47]

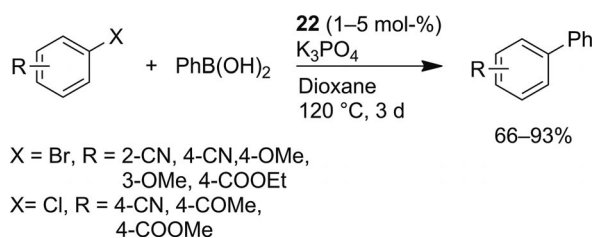


Scheme 15. Reductive dimerization of alkyl halides and pseudohalides.

Suzuki Reactions

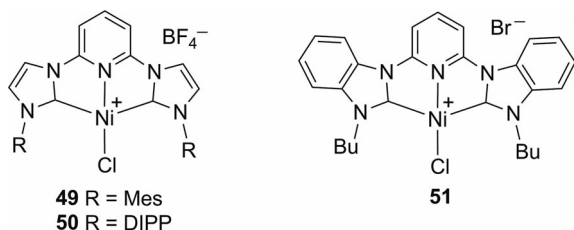
Suzuki reactions are widely used in the laboratory and by the industry, because of their functional group tolerance, regio- and stereoselectivity, ready availability of the boron reagents, nontoxic nature, and air and moisture stability. Numerous catalyst systems have been developed. Recently, several NHC-based pincer–nickel complexes have been applied to this process.

In 2006 Inamoto and co-workers synthesized NHC-based CNC-pincer–nickel complex **22** and reported preliminary results of the cross-coupling of aryl bromides and chlorides with phenylboronic acid (Scheme 16) catalyzed by **22**. Both activated and deactivated aryl bromides led to good to excellent yields. Activated aryl chlorides afforded slightly lower yields with higher catalyst loading.^[48] Further optimization of the reaction conditions led to a much shorter reaction time, and the scope of the electrophilic substrates was extended.^[22]



Scheme 16. Suzuki coupling of phenylboronic acid and aryl halides catalyzed by CNC-pincer–nickel complex **22**.

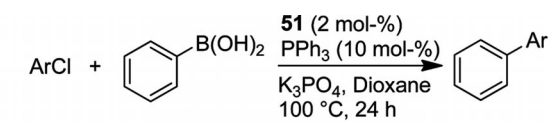
Complexes **49** and **50** (Scheme 17), the structural analogues of complex **22**, also catalyze the cross-coupling of aryl and heteroaryl bromides with aryl and alkenyl boronic acids in *s*BuOH. For the activated substrates, the reactions resulted in good to excellent yields, while for the deactivated substrates lower yields were obtained.^[49] The catalytic activity was improved by employing the modified complex **51** as a catalyst (Scheme 17), which catalyzes the coupling of aryl and heteroaryl halides efficiently: 2 mol-% of **51**, with 10 mol-% PPh₃ as an additive, lead to cross-coupling products in excellent yields (Table 11).^[40]

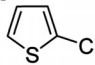
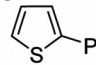
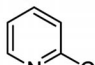
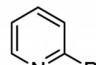


Scheme 17. CNC-pincer–nickel complexes **49–51**.

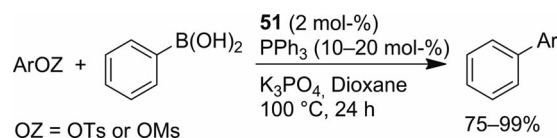
Complex **51** also catalyzes the Suzuki-type coupling of aryl tosylates and mesylates with phenylboronic acid in the presence of catalytic amounts of PPh₃ (Scheme 18). The reaction conditions are almost the same as those for the reaction with aryl halides. Both activated and inactivated aryl tosylates/mesylates are applicable for the coupling. Pyridyl tosylate and mesylate also give excellent results.^[50]

Table 11. Selected examples for the Suzuki coupling of aryl chlorides catalyzed by **51**.



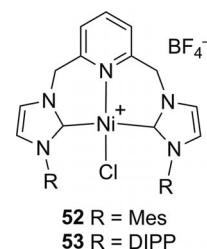
Entry	ArCl	Product	Yield [%] ^[a]
1	PhCl	PhPh	86
2	<i>p</i> -ClC ₆ H ₄ Me	<i>p</i> -MeC ₆ H ₄ Ph	95
3	<i>o</i> -ClC ₆ H ₄ Me	<i>o</i> -MeC ₆ H ₄ Ph	67
4	<i>p</i> -ClC ₆ H ₄ COOMe	<i>p</i> -MeOCC ₆ H ₄ Ph	91
5	<i>p</i> -ClC ₆ H ₄ C(O)Me	<i>p</i> -MeC(O)C ₆ H ₄ Ph	99
6	<i>p</i> -ClC ₆ H ₄ CN	<i>p</i> -NCC ₆ H ₄ Ph	99
7			88
8			98

[a] Yields of isolated products.



Scheme 18. CNC-pincer–nickel-catalyzed cross-coupling of aryl tosylates and mesylates with phenylboronic acid.

CNC-pincer–nickel complexes **52** and **53** (Scheme 19) are also active in catalyzing the cross-coupling of aryl/alkenyl tosylates and mesylates with aryl or alkenylboronic acids. The reactions were carried out in a sealed tube, and the yields were dependent on the properties of the reaction substrates. Yields were very low when the deactivated and hindered coupling partners were employed, and they were excellent when the activated coupling partners were used.^[51]

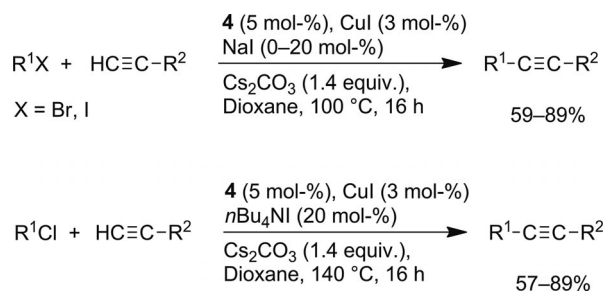


Scheme 19. CNC-pincer–nickel complexes **52** and **53**.

Sonogashira Reactions

The Sonogashira reaction was scarcely explored in the presence of pincer–nickel catalysts. Hu and co-workers reported a NN₂-pincer–nickel-catalyzed cross-coupling of inactivated primary alkyl halides with alkynes. CuI (3 mol-%) was employed as a co-catalyst, and NaI (for bromides) or *n*Bu₄NI (for chlorides) was used as the additive. The reactions were carried out in dioxane in the presence of Cs₂CO₃

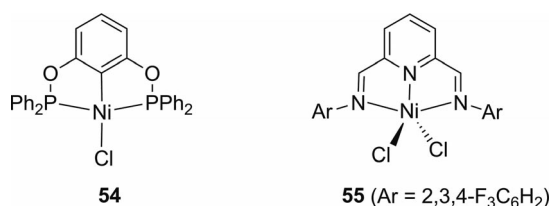
at 100 °C (for bromides and iodides) or 140 °C (for chlorides), affording cross-coupling products in yields of 57–89 % (Scheme 20).^[52]



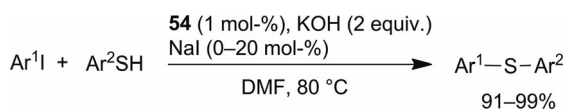
Scheme 20. Sonogashira coupling of inactivated alkyl halides catalyzed by NN₂-pincer-nickel complex **4**.

Carbon–Sulfur Coupling

Diaryl thioethers and alkyl aryl thioethers are important structural motifs in a wide range of molecules with important applications. They are also of significant importance to organic synthesis and the pharmaceutical industry. Catalytic cross-coupling provides a simple and efficient route for the synthesis of organic sulfides. In 2006 Morales-Morales et al. reported cross-coupling of iodobenzene with disulfides catalyzed by both PCP-pincer-nickel (**54**, Scheme 21) and NNN-pincer-nickel (**55**, Scheme 21) complexes. The reaction proceeds in DMF at 110 °C and requires the presence of zinc powder as a reducing agent. The former leads to almost quantitative coupling products, while the latter achieves good to excellent yields.^[53] Guan et al. carried out the reaction of aryl iodides with aryl thiols by employing the same catalyst. The reaction proceeds under milder conditions and affords excellent product yields (Scheme 22).^[54]



Scheme 21. Pincer-nickel complexes **54** and **55**.



Scheme 22. Reaction of aryl iodides with aryl thiols catalyzed by **54**.

Conclusions

From the work discussed above, the pincer-nickel complexes have received increased attention for their catalytic applications in cross-coupling during the past few years.

Significant advances have been made and pincer ligands have been shown to be excellent for a range of nickel-catalyzed coupling processes. Hu et al. developed the NN₂-pincer-nickel catalyst and performed Kumada coupling of β-hydrogen-containing alkyl halides or nucleophiles. Fu et al. and other groups carried out nickel-catalyzed Negishi coupling of β-hydrogen-containing alkyl halides and organozinc reagents by terpy or Pybox ligands. Especially noteworthy is the nickel-catalyzed enantioselective Negishi coupling of alkyl halides employing chiral Pybox ligands. We synthesized a series of nickel complexes bearing unsymmetrical pincer ligands and carried out Kumada and Negishi couplings of aryl chlorides and aryl nucleophiles. The catalysts are especially efficient for the Negishi coupling of aryl chlorides, extremely low catalyst loading and very mild conditions being required. In addition, the mechanisms of alkyl-alkyl coupling catalyzed by NN₂-pincer-nickel and Ni-terpy have been disclosed, which will be helpful for the further development of pincer-nickel catalysts.

Although great progress has been achieved, important challenges remain. It is very rare to see inactivated alkyl chlorides as the electrophiles in pincer-nickel-catalyzed coupling reactions, although the use of alkyl chlorides as the electrophiles would economically benefit a number of large-scale syntheses. The efficiency of most pincer-nickel catalysts is relatively low. Quite some reactions require high catalyst loading, which will limit their application. Hence, the development of more efficient catalyst systems is extremely desirable. Furthermore, the reaction types catalyzed by pincer-nickel complexes are still limited at the present time, mainly for the Kumada and Negishi reactions. It is anticipated that more types of cross-coupling reactions will be carried out by pincer-nickel catalysts in the future.

Acknowledgments

The National Basic Research Program of China (2009CB825300) and the National Natural Science Foundation of China (20772119) are acknowledged for support of this research.

- [1] a) A. de Meijere, F. Diederich (Eds.), *Metal-Catalyzed Cross-Coupling Reactions*, 2nd ed., Wiley-VCH, Weinheim, **2004**; b) J. Tsuji (Ed.), *Transition Metal Reagents and Catalysts: Innovations in Organic Synthesis*, John Wiley & Sons, Chichester, **2000**; c) N. Miyaura (Ed.), *Cross-Coupling Reactions: A Practical Guide*, Springer, Berlin, **2002**.
- [2] a) J. Hassan, M. Sévignon, C. Gozzi, E. Schulz, M. Lemaire, *Chem. Rev.* **2002**, *102*, 1359–1470; b) J.-P. Corbet, G. Mignani, *Chem. Rev.* **2006**, *106*, 2651–2710.
- [3] a) M. R. Netherton, G. C. Fu, *Adv. Synth. Catal.* **2004**, *346*, 1525–1532; b) A. F. Littke, G. C. Fu, *Angew. Chem.* **2002**, *114*, 4350; *Angew. Chem. Int. Ed.* **2002**, *41*, 4176–4211.
- [4] a) E. Negishi (Ed.), *Handbook of Organopalladium Chemistry for Organic Synthesis*, Wiley, New York, **2002**; b) N. Miyaura, A. Suzuki, *Chem. Rev.* **1995**, *95*, 2457–2483.
- [5] a) M. E. Limmert, A. H. Roy, J. F. Hartwig, *J. Org. Chem.* **2005**, *70*, 9364–9370; b) M. G. Organ, M. Abdel-Hadi, S. Avola, N. Hadei, J. Nasielski, C. J. O'Brien, C. Valente, *Chem. Eur. J.* **2007**, *13*, 150–157.
- [6] a) J. Huang, S. P. Nolan, *J. Am. Chem. Soc.* **1999**, *121*, 9889–9890; b) G. Y. Li, W. J. Marshall, *Organometallics* **2002**, *21*,

- 590–591; c) G. Y. Li, *Angew. Chem.* **2001**, *113*, 1561; *Angew. Chem. Int. Ed.* **2001**, *40*, 1513–1516; d) L. Ackermann, C. J. Gschrei, A. Althammer, M. Riederer, *Chem. Commun.* **2006**, 1419–1421; e) A. Fürstner, A. Leitner, M. Méndez, H. Krause, *J. Am. Chem. Soc.* **2002**, *124*, 13856–13863.
- [7] X. Hu, *Chem. Sci.* **2011**, *2*, 1867–1886.
- [8] a) A. Devasagayaram, T. Studemann, P. Knochel, *Angew. Chem.* **1995**, *107*, 2952; *Angew. Chem. Int. Ed. Engl.* **1995**, *34*, 2723–2725; b) D. J. Cárdenas, *Angew. Chem.* **1999**, *111*, 3201; *Angew. Chem. Int. Ed.* **1999**, *38*, 3018–3020; c) N. Kambe, T. Iwasakia, J. Terao, *Chem. Soc. Rev.* **2011**, *40*, 4937–4947.
- [9] a) A. C. Frisch, M. Beller, *Angew. Chem.* **2005**, *117*, 680; *Angew. Chem. Int. Ed.* **2005**, *44*, 674–688; b) A. Rudolph, M. Lautens, *Angew. Chem.* **2009**, *121*, 2694; *Angew. Chem. Int. Ed.* **2009**, *48*, 2656–2670; c) B. D. Sherry, A. Fürstner, *Acc. Chem. Res.* **2008**, *41*, 1500–1511; d) D. J. Cárdenas, *Angew. Chem.* **2003**, *115*, 398; *Angew. Chem. Int. Ed.* **2003**, *42*, 384–387; e) F. Glorius, *Angew. Chem.* **2008**, *120*, 8474; *Angew. Chem. Int. Ed.* **2008**, *47*, 8347–8349; f) J. Terao, N. Kambe, *Acc. Chem. Res.* **2008**, *41*, 1545–1554; g) V. B. Phapale, D. J. Cárdenas, *Chem. Soc. Rev.* **2009**, *38*, 1598–1607; h) R. Jana, T. P. Pathak, M. S. Sigman, *Chem. Rev.* **2011**, *111*, 1417–1492.
- [10] a) B. Cornils, W. A. Herrmann (Eds.), *Applied Homogeneous Catalysis with Organometallic Compounds*, VCH, Weinheim, **1996**; b) C. Dai, G. C. Fu, *J. Am. Chem. Soc.* **2001**, *123*, 2719–2724.
- [11] a) D. Morales-Morales, C. M. Jensen (Eds.), *The Chemistry of Pincer Compounds*, Elsevier, Amsterdam, **2007**; b) N. Selander, K. J. Szabo, *Chem. Rev.* **2011**, *111*, 2048–2076; c) J. I. van der Vlug, J. N. H. Reek, *Angew. Chem.* **2009**, *121*, 8990; *Angew. Chem. Int. Ed.* **2009**, *48*, 8832–8846; d) L.-C. Liang, *Coord. Chem. Rev.* **2006**, *250*, 1152–1177; e) S. T. Liddle, I. S. Edworthy, P. L. Arnold, *Chem. Soc. Rev.* **2007**, *36*, 1732–1744.
- [12] J. Zhou, G. C. Fu, *J. Am. Chem. Soc.* **2003**, *125*, 14726–14727.
- [13] L.-C. Liang, P.-S. Chien, J.-M. Lin, M.-H. Huang, Y.-L. Huang, J.-H. Liao, *Organometallics* **2006**, *25*, 1399–1411.
- [14] X. Hu, *Chimia* **2010**, *64*, 231–234.
- [15] a) O. Vechorkin, X. Hu, *Angew. Chem. Int. Ed.* **2009**, *48*, 2937–2940; b) O. Vechorkin, Z. Csok, R. Scopelliti, X. Hu, *Chem. Eur. J.* **2009**, *15*, 3889–3899.
- [16] P. Ren, O. Vechorkin, K. von Allmen, R. Scopelliti, X. Hu, *J. Am. Chem. Soc.* **2011**, *133*, 7084–7095.
- [17] Z. Csok, O. Vechorkin, S. B. Harkins, R. Scopelliti, X. Hu, *J. Am. Chem. Soc.* **2008**, *130*, 8156–8157.
- [18] J. Breitenfeld, O. Vechorkin, C. Corminboeuf, R. Scopelliti, X. L. Hu, *Organometallics* **2010**, *29*, 3686–3689.
- [19] O. Vechorkin, V. Proust, X. Hu, *J. Am. Chem. Soc.* **2009**, *131*, 9756–9766.
- [20] Z.-X. Wang, L. Wang, *Chem. Commun.* **2007**, 2423–2425.
- [21] K. Sun, L. Wang, Z.-X. Wang, *Organometallics* **2008**, *27*, 5649–5656.
- [22] K. U. Inamoto, J.-I. Kuroda, T. Sakamoto, K. Hiroya, *Synthesis* **2007**, 2853–2861.
- [23] S. Gu, W. Chen, *Organometallics* **2009**, *28*, 909–914.
- [24] C. Zhang, Z.-X. Wang, *Organometallics* **2009**, *28*, 6507–6514.
- [25] A. Castonguay, A. L. Beauchamp, D. Zargarian, *Organometallics* **2008**, *27*, 5723–5732.
- [26] J. Sanford, C. Dent, J. D. Masuda, A. Xia, *Polyhedron* **2011**, *30*, 1091–1094.
- [27] A. Gavryushin, C. Kofink, G. Manolikakes, P. Knochel, *Tetrahedron* **2006**, *62*, 7521–7533.
- [28] L. Wang, Z.-X. Wang, *Org. Lett.* **2007**, *9*, 4335–4338.
- [29] Z. Xi, Y. Zhou, W.-Z. Chen, *J. Org. Chem.* **2008**, *73*, 8497–8501.
- [30] S. Çalimsiz, M. Sayah, D. Mallik, M. G. Organ, *Angew. Chem.* **2010**, *122*, 2058; *Angew. Chem. Int. Ed.* **2010**, *49*, 2014–2017.
- [31] N. Liu, L. Wang, Z.-X. Wang, *Chem. Commun.* **2011**, *47*, 1598–1600.
- [32] a) T. J. Anderson, G. D. Jones, D. A. Vicić, *J. Am. Chem. Soc.* **2004**, *126*, 8100–8101; b) G. D. Jones, J. L. Martin, C. McFarland, O. R. Allen, R. E. Hall, A. D. Haley, R. J. Brandon, T. Konovalova, P. J. Desrochers, P. Pulay, D. A. Vicić, *J. Am. Chem. Soc.* **2006**, *128*, 13175–13183; c) G. D. Jones, C. McFarland, T. J. Anderson, D. A. Vicić, *Chem. Commun.* **2005**, 4211–4213.
- [33] S. W. Smith, G. C. Fu, *Angew. Chem.* **2008**, *120*, 9474; *Angew. Chem. Int. Ed.* **2008**, *47*, 9334–9336.
- [34] X. Lin, D. L. Phillips, *J. Org. Chem.* **2008**, *73*, 3680–3688.
- [35] Recent EPR and DFT studies reveal that (terpy)Ni-Br is a metal-centered, not a ligand-centered, radical. See: J. T. Ciszewski, D. Y. Mikhaylov, K. V. Holin, M. K. Kadirov, Y. H. Budnikova, O. Sinyashin, D. A. Vicić, *Inorg. Chem.* **2011**, *50*, 8630–8635.
- [36] A. Joshi-Pangu, M. Ganesh, M. R. Biscoe, *Org. Lett.* **2011**, *13*, 1218–1221.
- [37] F. O. Arp, G. C. Fu, *J. Am. Chem. Soc.* **2005**, *127*, 10482–10483.
- [38] S. Son, G. C. Fu, *J. Am. Chem. Soc.* **2008**, *130*, 2756–2757.
- [39] C. Fischer, G. C. Fu, *J. Am. Chem. Soc.* **2005**, *127*, 4594–4595.
- [40] P. M. Lundin, J. Esquivias, G. C. Fu, *Angew. Chem.* **2009**, *121*, 160; *Angew. Chem. Int. Ed.* **2009**, *48*, 154–156.
- [41] S. W. Smith, G. C. Fu, *J. Am. Chem. Soc.* **2008**, *130*, 12645–12647.
- [42] J. Caeiro, J. P. Sestelo, L. A. Sarandeses, *Chem. Eur. J.* **2008**, *14*, 741–746.
- [43] a) H. Gong, R. Sinisi, M. R. Gagné, *J. Am. Chem. Soc.* **2007**, *129*, 1908–1909; b) H. Gong, M. R. Gagné, *J. Am. Chem. Soc.* **2008**, *130*, 12177–12183.
- [44] X. Lin, J. Sun, Y. Xi, D. Lin, *Organometallics* **2011**, *30*, 3284–3292.
- [45] V. B. Phapale, E. Buñuel, M. García-Iglesias, D. J. Cárdenas, *Angew. Chem.* **2007**, *119*, 8946; *Angew. Chem. Int. Ed.* **2007**, *46*, 8790–8795.
- [46] X. Yu, T. Yang, S. Wang, H. Xu, H. Gong, *Org. Lett.* **2011**, *13*, 2138–2141.
- [47] M. R. Prinsell, D. A. Everson, D. J. Weix, *Chem. Commun.* **2010**, *46*, 5743–5745.
- [48] K. Inamoto, J.-I. Kuroda, K. Hiroya, Y. Noda, M. Watanabe, T. Sakamoto, *Organometallics* **2006**, *25*, 3095–3098.
- [49] K. Inamoto, J.-I. Kuroda, E. Kwonb, K. Hiroya, T. Doi, *J. Organomet. Chem.* **2009**, *694*, 389–396.
- [50] T. Tu, H. Mao, C. Herbert, M. Xu, K. H. Dötz, *Chem. Commun.* **2010**, *46*, 7796–7798.
- [51] J.-I. Kuroda, K. Inamoto, K. Hiroya, T. Doi, *Eur. J. Org. Chem.* **2009**, 2251–2261.
- [52] O. Vechorkin, D. Barmaz, V. Proust, X. Hu, *J. Am. Chem. Soc.* **2009**, *131*, 12078–12079.
- [53] a) V. Gómez-Benítez, O. Baldovino-Pantaleón, C. Herrera-Álvarez, R. A. Toscano, D. Morales-Morales, *Tetrahedron Lett.* **2006**, *47*, 5059–5062; b) O. Baldovino-Pantaleón, S. Hernández-Ortega, D. Morales-Morales, *Adv. Synth. Catal.* **2006**, *348*, 236–242.
- [54] J. Zhang, C. M. Medley, J. A. Krause, H. Guan, *Organometallics* **2010**, *29*, 6393–6401.

Received: September 30, 2011
Published Online: January 16, 2012

Kinetic and Mechanistic Studies on the Reactions of the Reduced Vitamin B₁₂ Complex Cob(I)alamin with Nitrite and Nitrate

Noah T. Plymale,^[a] Rohan S. Dassanayake,^[a] Hanaa A. Hassanin,^[a,b] and Nicola E. Brasch^{*[a,c]}

Dedicated to the memory of Dr. Edwin S. Gould^[‡]

Keywords: Vitamin B₁₂ / Cobalt / Bioinorganic chemistry / Kinetics / Reaction mechanisms

The kinetics of the reactions between cob(I)alamin [Cbl(I)] and nitrite and nitrate have been studied by UV/Vis and stopped-flow spectroscopy. Enzyme-bound Cbl(I) is an important transient species in several B₁₂-catalyzed enzyme reactions. Levels of nitrite and nitrate are elevated during oxidative stress, as a consequence of elevated nitric oxide levels. Although nitrite and nitrate are generally considered to be benign species, our studies show that nitrate and especially nitrite react rapidly with Cbl(I) at neutral pH conditions (k_{app}

= 6.5×10^{-3} and $1.7 \times 10^3 \text{ M}^{-1} \text{ s}^{-1}$, respectively, at pH 7, 25.0 °C). A reaction pathway is postulated for the reaction between Cbl(I) and (H)NO₂ involving a 2e[−] rate-determining step to form Cbl(III) and HNO. The latter species reacts further with Cbl(I), ultimately resulting in the oxidation of 4Cbl(I) by HNO₂ to yield 4Cbl(II) and NH₂OH. The reaction between Cbl(I) and (H)NO₃ results in the oxidation of 8Cbl(I) by (H)NO₃ to give 8Cbl(II) and NH₄⁺ (pH 5–7).

Introduction

The cob(III)alamins methylcobalamin (MeCbl; X = Me, Figure 1) and adenosylcobalamin (AdoCbl; X = 5'-deoxyadenosyl, Figure 1) are essential cofactors for two enzymes in mammals and multiple enzymes in bacteria.^[1] Insufficient cobalamin is associated with neurological disorders and megaloblastic anemia.^[2]

Reduced cobalamins, cob(II)alamin and cob(I)alamin, are also important intracellular complexes. In the laboratory, free (nonprotein-bound) cob(III)alamins are readily chemically reduced to pentacoordinate cob(II)alamin [$\text{H}_2\text{OCbl}^+/\text{Cbl(II)}$: 0.20 V vs. SHE].^[3] Stronger reducing agents such as excess NaBH₄ or titanium citrate are required to reduce Cbl(II) to Cbl(I) [redox potential Cbl(II)/Cbl(I): −0.61 V vs. SHE^[3]]. Although the X-ray structure of

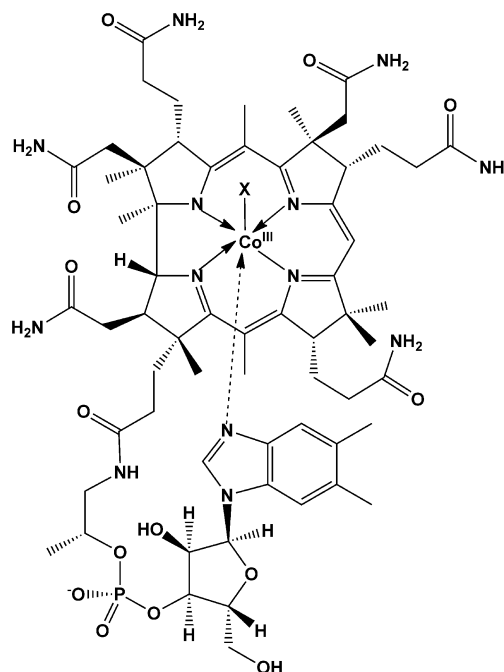


Figure 1. Structure of cob(III)alamins. Biologically relevant Cbl forms include X = CN, CH₃, 5'-deoxyadenosyl, H₂O/HO, NO, or glutathione.^[7]

Cbl(I) has not yet been determined, DFT calculations support the claim that this latter complex is tetracoordinate with essentially a square-planar geometry.^[4]

[a] Department of Chemistry and Biochemistry, Kent State University, Kent, OH 44242, USA

[b] Department of Chemistry, Ain Shams University, Abbassia, Cairo, Egypt

[c] School of Biomedical Sciences, Kent State University, Kent, OH, 44242, USA
E-mail: nbrasch@kent.edu

[‡] In memory of our senior colleague, neighbor, and friend, Dr. Edwin S. Gould, whose deep understanding of inorganic chemistry, and good-humored willingness to share it, will be very much missed.

Supporting information for this article is available on the WWW under <http://dx.doi.org/10.1002/ejic.201100992>.

In mammals, methionine synthase bound Cbl(I) is a transient complex formed in the MeCbl-dependent methionine synthase catalytic cycle.^[1] Synthesis of AdoCbl-bound ATP:cob(I)alamin adenosyltransferase (ATR) also requires transient formation of Cbl(I)-bound ATR.^[5] In mammals, AdoCbl is then sequestered by AdoCbl-dependent methylmalonyl-CoA mutase, which catalyzes the isomerization of L-methylmalonyl-CoA to succinyl-CoA.^[6] Anaerobic bacterial dehalogenases also utilize cob(I)alamin for the dechlorination of aliphatic and aromatic compounds.^[11] There has been much speculation as to how the thermodynamically demanding Cbl(II)/Cbl(I) reduction is achieved within cells given that the redox potential for reduction of free Cbl(II) to Cbl(I) is beyond that achievable by biological reductants.^[5c,6,8] Recent spectroscopic and X-ray structural studies have shed considerable light on how, namely, in Cbl(II)-bound ATR, Cbl(II) is a tetracoordinate “base-off” complex, which lacks a ligand (or perhaps has a weakly bound water molecule) at the lower (*a*) axial site of the Cbl moiety.^[5,9] Loss of the lower axial ligand increases the Co^{II}/Co^I redox potential, because of the decrease in electron density on the Co center. In Cbl(II)-bound methionine synthase, the α -5,6-dimethylbenzimidazole is replaced by a weakly bound water ligand, which, once again, increases the Co^{II}/Co^I redox potential.^[10]

Because of the ease of nucleophilic displacement by Cbl(I), Cbl(I) has frequently been referred to as a supernucleophile.^[4] Cbl(I) dehalogenates or dealkylates a wide range of organic molecules, including alkanes, alkenes, alkynes, aromatics, and phosphotriesters.^[4,11] There is also much interest in using Cbl(I) to trap reactive intermediates such as oxiranes.^[12] Kinetic studies have been reported for the dehalogenation of halogenated alkanes,^[13] alkenes,^[14] and acetic acid^[15] and the dealkylation of phosphotriesters.^[11a] Rate constants have also been reported for the reduction of functionalized pyridine,^[16] transition-metal complexes,^[17] esters,^[18] organic disulfides,^[19] oxyhalogens,^[20] hydroxylamine^[21] and nitrous oxide^[22] by Cbl(I).

We are interested in the reactions of reduced cobalamins with reactive oxygen and nitrogen species (ROS/RNS).^[23] Elevated ROS/RNS levels are implicated in numerous diseases, including septic shock, ischemic/reperfusion injury, atherosclerosis, and asthma.^[24] Both mammalian B₁₂-dependent enzyme reactions are inactivated under oxidative/nitrosative stress conditions.^[25] The reactive nitrogen species nitric oxide (‘NO), a signaling molecule that plays a key role in nerve transmission, vasodilation, and the inflammatory immune response,^[26] is oxidized to nitrite, which can be further oxidized to nitrate in biological systems. Indeed, the production of NO₂[−] and NO₃[−] is used as an indicator of the production of ‘NO.^[27] Megaloblastic anemia is associated with elevated levels of ‘NO, and vitamin B₁₂ supplementation restores ‘NO concentrations to normal levels.^[28] NO₃[−] is also reduced to NO₂[−] by enzymes possessing nitrate reductase activity, including bacterial nitrate reductases in the intestine and mouth.^[26b] Furthermore, it has been suggested that NO₂[−] is a biological signaling molecule and may play an important role in vasodilation and intravascular en-

docrine ‘NO transport.^[29] NO₂[−] concentrations are significant in plasma and tissue, which, under normal conditions, are up to 0.5 and 10 μ M, respectively.^[26b,30] NO₃[−] is present at even higher concentrations.^[31]

In this study we focus on the reaction of Cbl(I) with nitrite and nitrate. Although nitrite and nitrate themselves are generally considered to be benign relative to reactive oxygen and nitrogen species, our studies show that the strong reductant cob(I)alamin reacts with both species at biological pH conditions.

Results and Discussion

Studies on the Reaction of Cob(I)alamin with Nitrite

Determination of the Stoichiometry and the Reaction Products

The Cbl product of the reaction of Cbl(I) with NO₂[−] was identified by UV/Vis spectrophotometry. Figure 2a gives UV/Vis spectroscopic data as a function of time for the reaction of Cbl(I) (50 μ M) with NO₂[−] (9.10 mM) (25.0 °C, phosphate buffer, pH 12.00). The initial and final spectra correspond to that of Cbl(I) and Cbl(II), respectively, Figure 2b. From Figure 2a it can be seen that the reaction exhibits clean isosbestic points at 307, 346, 417 and 543 nm, in agreement with literature values for the conversion of Cbl(I) to Cbl(II),^[32] which indicates a direct and clean conversion of Cbl(I) to Cbl(II) for the rate-determining step of the reaction. Cbl(II) is also the reaction product at lower pH values.

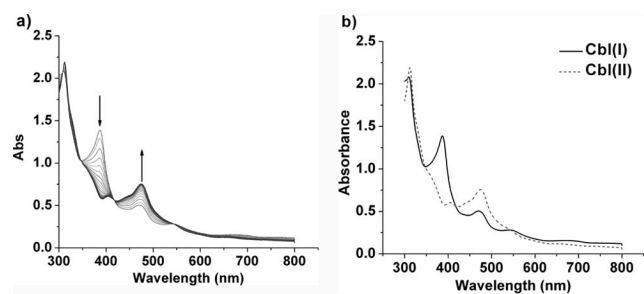


Figure 2. (a) UV/Vis spectra as a function of time for the reaction of Cbl(I) (50 μ M, λ_{max} = 388, 464, 547, and 684 nm^[33]) with NO₂[−] (9.10 mM) at pH 12.00 (25.0 °C, 0.050 M phosphate buffer). Spectra were recorded every 2.5 min for 40 min. (b) Initial and final spectra for the reaction shown in (a). The final spectrum corresponds to Cbl(II) (λ_{max} = 312, 475 nm^[33]).

To determine the stoichiometry of the reaction of Cbl(I) with nitrite, UV/Vis spectra of the product solution obtained upon equilibrating Cbl(I) (200 μ M) with 0–0.50 molequiv. of NO₂[−] under anaerobic conditions were recorded at pH 9.51 (5.0 \times 10^{−3} M CHES buffer, 25.0 °C). The relatively high Cbl(I) concentration was used to enhance its stability in buffered solution. Figure 3 gives a plot of the absorbance at 700 nm vs. molequiv. of nitrite added. From this plot it is clear that the reaction is complete after the addition of \approx 0.25 molequiv. of NO₂[−]. Analysis of the absorbance data at 700 nm gave a mean value of

Table 1. Determination of the stoichiometry of the reaction between Cbl(I) and NO₂[−] at pH 9.51 (5.0 × 10^{−3} M CHES buffer). Absorbances were measured at 700 nm.

10 ⁴ [Cbl(I)] _i (M)	10 ⁵ [NO ₂ [−]] _i (M)	[NO ₂ [−]]/[Cbl(I)] _i	Abs _{Cbl(I)}	Abs _{Cbl(II)}	Abs _{obs}	Fraction Cbl(I) reacted ^[a]	Molequiv. of NO ₂ [−] required ^[b]
2.00	1.00	0.050	0.388	0.104	0.323	0.229	0.22
2.00	2.00	0.10	0.388	0.104	0.262	0.443	0.23
2.00	3.00	0.15	0.388	0.104	0.203	0.651	0.23
2.00	4.00	0.20	0.388	0.104	0.159	0.806	0.25
2.00	5.00	0.25	0.388	0.104	0.119	0.947	0.26
2.00	6.00	0.30	0.388	0.104	0.110	—	—
2.00	7.00	0.35	0.388	0.104	0.103	—	—
2.00	8.00	0.40	0.388	0.104	0.107	—	—
2.00	9.00	0.45	0.388	0.104	0.099	—	—
2.00	10.0	0.50	0.388	0.104	0.100	—	—

[a] Fraction Cbl(I) reacted = [Abs_{Cbl(I)} − Abs_{obs}]/[Abs_{Cbl(I)} − Abs_{Cbl(II)}]. [b] Molequiv. of NO₂[−] required = {[NO₂[−]]/[Cbl(I)]_i}/[fraction Cbl(I) reacted].

0.24 ± 0.02, Table 1. A similar analysis for absorbance data at 500 nm gave a value of 0.25 ± 0.03, Table S1, Supporting Information. A duplicate experiment gave similar results (0.26 ± 0.02 molequiv. of NO₂[−], Tables S2 and S3). The Cbl(I)/NO₂[−] molar ratio is therefore 4:1.

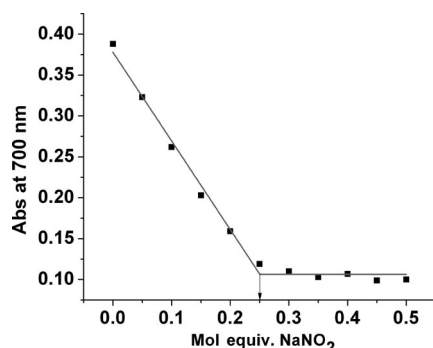
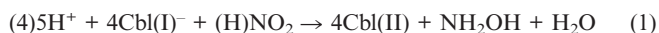


Figure 3. Plot of absorbance at 700 nm vs. molequiv. of NaNO₂ for equilibrated solutions of Cbl(I) (200 ± 9 μM) with 0–0.50 molequiv. of NO₂[−] (5.0 × 10^{−3} M CHES buffer, pH 9.51, 25.0 °C).

The stoichiometry of the reaction of Cbl(I) and NO₂[−] was also determined at pH 7.40 (5.0 × 10^{−3} M phosphate buffer, 25.0 °C), in duplicate, which gave a mean NO₂[−]/Cbl(I) stoichiometry of (0.25 ± 0.04):1 (Tables S4–S7).

Determination of the Amount of Hydroxylamine Product Formed

A NO₂[−]/Cbl(I) reaction stoichiometry of 0.25:1 suggests that the non-Cbl reaction product is NH₂OH, Equation (1).



Whether the reactive species is NO₂[−] and/or HNO₂ will be considered later. The indooxine assay (in which 8-hydroxyquinoline undergoes electrophilic aromatic substitution by NH₂OH and subsequent oxidation by air (O₂) to give 5,8-quinolinequinone-(8-hydroxy-5-quinoyl)-5-imide, “indooxine”) is an established colorimetric procedure to quantify NH₂OH.^[34] Cbl(I) and NO₂[−] were treated in 1:0.27 (near stoichiometric) and 1:0.50 (excess NO₂[−]) molar ratios under anaerobic conditions (5.0 × 10^{−3} M CHES buffer, pH 9.51), and the indooxine test was carried out on

the product mixture at completion of the reaction under aerobic conditions (see Experimental Section). Only the indooxine product, not Cbl(II), absorbs in the 650–750 nm region (λ_{max} of indooxine product = 710 nm^[34]). The NH₂OH concentration was determined from the absorbance at 710 nm of the product mixture by use of a standard calibration curve of absorbance vs. NH₂OH concentration, Figure S1. Given that 200 μM Cbl(I) was treated with sufficient NO₂[−] for the reaction to proceed to completion, 50.0 μM NH₂OH would be expected for both Cbl(I)/NO₂[−] ratios of 1:0.27 and 1:0.50. However, only ≈46% of the NH₂OH product (23 ± 2 μM) was obtained.

The low recovery of NH₂OH determined by the indooxine test was probed further. Control experiments showed that NH₂OH is stable for 1 hr in anaerobic water and in anaerobic and aerobic CHES buffer at pH 9.51 (see Supporting Information) and gave the expected concentration with the indooxine test. Interestingly, NH₂OH is not stable in aerobic water. It was also shown that nitrite does not react with 8-hydroxyquinoline to give a positive indooxine test (see Supporting Information). Others have reported that NH₂OH reacts with HNO₂, albeit under strongly acidic conditions;^[35] however, experiments also showed that the NH₂OH concentration (77 μM) is unaffected by the presence of NaNO₂ (54 μM) (see Supporting Information). As further proof that the indooxine test is functioning reliably, the indooxine test was performed on a Cbl(I) + NO₂[−] product sample that was spiked with NH₂OH. By using the calibration curve, it was determined that the unspiked sample contained 12.1 μM NH₂OH and that the spiked sample contained 32.5 μM NH₂OH (see Supporting Information). The spiked sample gave the expected increase in NH₂OH content based on the amount of NH₂OH added to the product solution.

No observable changes occur in the UV/Vis spectrum for a solution of Cbl(I) (50 μM) or Cbl(II) (50 μM) and NH₂OH (50 μM) (see Supporting Information). Gould et al. reported that Cbl(I) reacts with NH₃OH⁺ in strongly acidic aqueous solution (pH 0.95–2);^[21] however the reaction is slow compared to the reaction between Cbl(I) and nitrite (see later; *k* = 4.1 M^{−1} s^{−1}, 25.0 °C, *I* = 0.11 M) and would be expected to be orders of magnitude slower under the pH conditions of this study since protonation increases the redox potential

of oxyanions [$pK_b(\text{NH}_2\text{OH}) = 7.97$].^[36] Cbl(I) is also stable in the presence of Cbl(III) (hydroxycobalamin) (see Supporting Information). However, in the presence of Cbl(II) (200 μM), only $\approx 70\%$ NH_2OH was observed by the indooxine test (see Supporting Information). The experiments also showed that $\approx 30\%$ of the original NH_2OH is absent from samples containing Cbl(II) regardless of how long the solution was allowed to react (0, 30, or 60 min), while NH_2OH was completely recovered in solutions not containing Cbl(II) (Table S8). Additionally, since the final step in the indooxine test requires oxygen, control experiments were carried out to determine the effect of bubbling air through the Cbl(I) + NO_2^- product solution prior to performing the indooxine test. The bubbling of air for 3 min recovered about 80% of the original NH_2OH concentration, but further bubbling for 10 min was unsuccessful at recovering the remaining NH_2OH (Table S9). Transition-metal-catalyzed disproportionation of NH_2OH has been reported by others.^[37] It is likely that the aqueous reduced products of the disproportionated NH_2OH are re-oxidized to NH_2OH in the presence of oxygen, but the gaseous and oxidized products are not retrieved. Under anaerobic conditions in the presence of transition metals, NH_2OH disproportionates to give N_2 , N_2O , and NO^+ .^[37a]

Finally, an experiment was performed to check that significant amounts of NH_3 are not formed in the reaction. Cbl(I) (200 μM) was treated with NO_2^- (50 μM) under anaerobic conditions (0.050 M CHES buffer, pH 9.51), and the Nessler reagent was added under aerobic conditions to the product solution. The color change indicative of the presence of NH_3 was not observed, which confirms that NH_3 is not produced in the reaction of Cbl(I) with nitrite.

Kinetic Studies on the Reaction of Cbl(I) with Nitrite

The kinetics of the reaction between Cbl(I) and $(\text{H})\text{NO}_2$ were studied in the pH range 6.50–10.80, at 25.0 °C. Data were collected under pseudo-first-order conditions, with the NO_2^- concentration in excess ($\geq 10\times$). Figure 4 gives a typical plot of absorbance vs. time for the reaction of Cbl(I) (50 μM) with NO_2^- (5.00 mM) at pH 10.80. The inset to Figure 4 gives a plot of absorbance vs. time for the identical Cbl(I) solution in the absence of NO_2^- at pH 10.80. Cbl(I) is slowly oxidized to Cbl(II) even under strictly anaerobic conditions;^[38] however, this reaction is significantly slower ($\Delta\text{Abs} = 0.02$ at 388 nm) than the reaction of interest ($\Delta\text{Abs} = 0.45$ at 388 nm for the same time period) at pH 10.80. This was the case under all the pH conditions of this study. Data was collected from 1.00 to 35.0 mM NO_2^- for the reaction between Cbl(I) and NO_2^- at pH 10.80, and the results are summarized in Figure 5. Fitting of the data to a straight line passing through the origin gives an apparent second-order rate constant, $k_{\text{app}} = 0.49 \pm 0.02 \text{ M}^{-1} \text{ s}^{-1}$. Data collected at other pH conditions is shown in Figure S2. Under acidic pH conditions (pH 6.50 and 6.92), Cbl(I) was not sufficiently stable in buffer to mix a buffered solution of Cbl(I) with a buffered solution of nitrite. Therefore, the

Cbl(I) solution was diluted in water and mixed with buffer within the stopped-flow spectrophotometer's tubing itself (see Experimental Section).

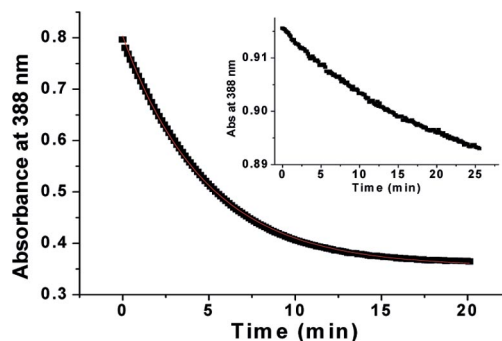


Figure 4. Plot of absorbance at 388 nm vs. time for the reaction of Cbl(I) (50 μM) with NO_2^- (5.00 mM) at pH 10.80 [25.0 °C, 0.050 M CAPS buffer, $I = 0.50 \text{ M}$ (Na_2HPO_4)]. Fitting of the data to a first-order rate equation gives $k_{\text{obs}} = 0.209 \pm 0.001 \text{ s}^{-1}$. Inset: Plot of absorbance vs. time for the spontaneous decomposition of Cbl(I) (50 μM) to Cbl(II) under the same conditions and time period.

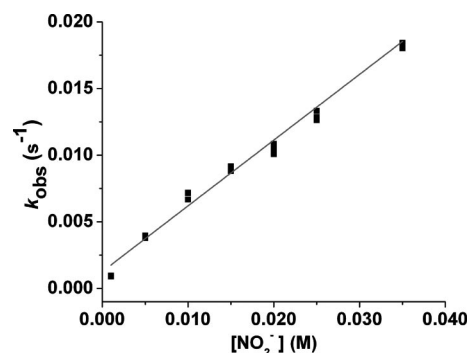


Figure 5. Plot of k_{obs} vs. NO_2^- concentration for the reaction between Cbl(I) and NO_2^- at pH 10.80 (25.0 °C, 0.050 M CAPS, $I = 0.50 \text{ M}$ phosphate buffer). Fitting of the data to a straight line gives a slope, $k_{\text{app}} = 0.49 \pm 0.02 \text{ M}^{-1} \text{ s}^{-1}$ and an intercept of $(1.3 \pm 0.4) \times 10^{-3} \text{ s}^{-1}$.

Figure 6 and Table S10 summarize the dependence of the k_{app} value on pH. Below pH 6.5, the reaction was too rapid to be followed by stopped-flow spectrophotometry. Under acidic conditions, significant intercepts were observed in the plots of k_{obs} vs. $(\text{H})\text{NO}_2$ concentration, and control experiments showed that this arises from partial spontaneous oxidation of Cbl(I) to Cbl(II) [see Table S10 and the accompanying discussion, Supporting Information; the reaction equilibrium lies towards Cbl(I)]. At high pH conditions k_{app} approaches 0; hence, HNO_2 , and not NO_2^- ($pK_a(\text{HNO}_2) = 3.16$ ^[39]), reacts with Cbl(I). It is not unexpected that HNO_2 oxidizes Cbl(I) more rapidly than NO_2^- , since HNO_2 is a stronger oxidant [$E(\text{HNO}_2/\text{N}_2) = 1.45 \text{ V}$, pH 0; $E(\text{NO}_2^-/\text{N}_2) = 0.41 \text{ V}$, pH 14 vs. SHE^[24d]] because of the electron-withdrawing effects of the acidic proton. By assuming that only HNO_2 reacts with Cbl(I), the corresponding rate Equation (2) is:

$$k_{\text{app}} = k_{\text{obs}}/[\text{Cbl(I)}]_{\text{T}} = (k \times 10^{-\text{pH}})/[10^{-\text{pH}} + K_{\text{a}}(\text{HNO}_2)] \quad (2)$$

Fitting of the data in Figure 6 to Equation (2) and by fixing $K_{\text{a}}(\text{HNO}_2) = 6.9 \times 10^{-4}$ gives $k = (1.15 \pm 0.08) \times 10^7 \text{ M}^{-1} \text{ s}^{-1}$. At pH 7, $k_{\text{app}} = 1.7 \times 10^3 \text{ M}^{-1} \text{ s}^{-1}$.

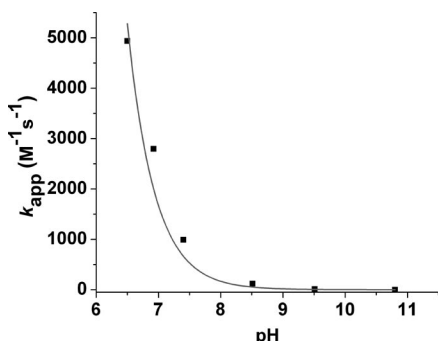
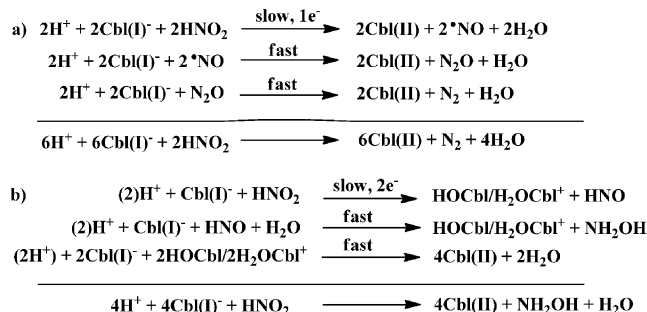


Figure 6. Plot of the second-order rate constant k_{app} vs. pH for the reaction between Cbl(I) and (H)NO₂. The data was fitted to Equation (2) in the text, which gives $k = (1.15 \pm 0.08) \times 10^7 \text{ M}^{-1} \text{ s}^{-1}$.

The two most likely reaction pathways are outlined in Scheme 1a and b. Importantly, complete conversion of Cbl(I) to Cbl(II) is observed in the rate-determining step under all conditions; hence, the first step is slow compared with subsequent reactions. In Scheme 1a, Cbl(I) is oxidized by HNO₂ in a 1e[−] process to form Cbl(II) and ·NO. The subsequent reaction between Cbl(I) and ·NO has been studied by others,^[41] and yields Cbl(II) and N₂O. The latter species oxidizes Cbl(I) to give Cbl(II) and N₂.^[22] Given that NH₂OH is experimentally observed as the reaction product, this reaction pathway is unlikely. In Scheme 1b, Cbl(I) is oxidized by HNO₂ in a 2e[−] process to form Cbl(III) (hydroxycobalamin/aquacobalamin) and HNO in the rate-determining step. Although to the best of our knowledge the reaction between HNO and Cbl(I) has not yet been studied (HNO is a demanding species to work with as it rapidly and spontaneously dimerizes to ultimately form N₂O and H₂O, and requires the use of HNO donor molecules^[42]), there is precedent for HNO acting as a 2e[−] oxidant, being itself reduced to NH₂OH.^[43] The redox potential of (HNO, 2H⁺/NH₂OH) is 0.3 V vs. SHE at pH 7,^[44] which makes it a moderate oxidizing agent capable of oxidizing Cbl(I) { $E^\circ[\text{Cbl(II)}/\text{Cbl(I)}] = -0.61 \text{ V vs. SHE.}^{[3]}$ }. Alternatively, N₂O rather than HNO could be produced in the first step of this pathway. However, others have shown that N₂O reacts with Cbl(I) to give N₂.^[22] Finally, the first step in Scheme 1b must be the rate-determining step since there is no observed accumulation of the HOCbl intermediate. The rate constant for the reaction of Cbl(I) with Cbl(III) is $3.2 \times 10^7 \text{ M}^{-1} \text{ s}^{-1}$.^[22]

To summarize, the stoichiometry of the reaction between Cbl(I) and NO₂[−] was found to be 4:1 Cbl(I)/NO₂[−]. Cbl(II) is the Cbl product (UV/Vis spectroscopy). On the basis of the stoichiometry, the expected non-Cbl product is NH₂OH. The indooxine test for the presence of NH₂OH was positive, albeit nonquantitative. It is likely that partial disproportionation of NH₂OH occurs.



Scheme 1. Possible reaction pathways for the reaction between Cbl(I) and HNO₂. (a) 1e[−] rate-determining step. (b) 2e[−] rate-determining step. $\text{p}K_{\text{a}}(\text{H-}^3\text{NO}) \approx 11.6$.^[40]

Studies on the Reaction of Cob(I)alamin with Nitrate

Determination of the Stoichiometry and the Reaction Products

Studies on the reaction between Cbl(I) and nitrate in strongly acidic solution (pH 1.5–2.5) have been reported;^[32] however it was of interest to determine whether this mechanism is still in operation in the biological pH range. Figure 7 gives typical UV/Vis spectra as a function of time for the reaction between Cbl(I) (50 μM) and NO₃[−] (0.200 M) under anaerobic conditions at pH 6.02 (25.0 °C, 0.10 M phosphate buffer, $I = 1.5 \text{ M}$). Cbl(I) ($\lambda_{\text{max}} = 388, 464, 547$, and $684 \text{ nm}^{[33]}$) is again cleanly oxidized to Cbl(II) ($\lambda_{\text{max}} = 312, 475 \text{ nm}^{[33]}$), with sharp isosbestic points observed at 356, 416 and 539 nm, in agreement with literature values for the oxidation of Cbl(I) to Cbl(II).^[32]

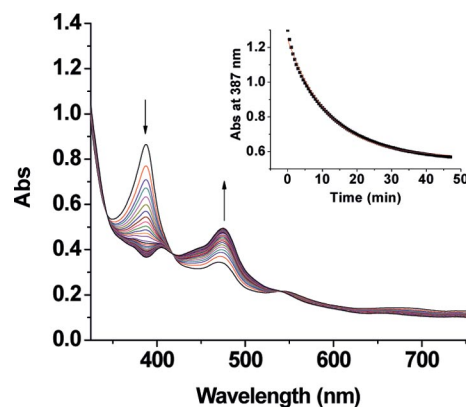
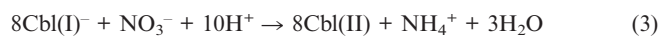


Figure 7. UV/Vis spectra as a function of time for the reaction of Cbl(I) (50 μM) with NO₃[−] (0.200 M) at pH 6.02 (25.0 °C, 0.10 M phosphate buffer, $I = 1.5 \text{ M}$). Selected spectra are shown every 1.0 min. Cbl(I) ($\lambda_{\text{max}} = 388, 464, 547$, and $684 \text{ nm}^{[33]}$) is converted to Cbl(II) ($\lambda_{\text{max}} = 312, 475 \text{ nm}^{[33]}$). Inset: Plot of absorbance at 387 nm vs. time for the data. The data has been fitted to a first-order rate equation, which gives $k_{\text{obs}} = (7.13 \pm 0.07) \times 10^{-2} \text{ min}^{-1}$.

The non-Cbl reaction product was identified as ammonia by using the Nessler's test, consistent with a reaction stoichiometry of 8:1 Cbl(I)/NO₃[−] (see Experimental Section). NH₄⁺ is also produced when Cbl(I) reacts with nitrate under strongly acidic pH conditions.^[32] The overall reaction can therefore be written as Equation (3).



Attempts to confirm this reaction stoichiometry by recording UV/Vis spectra of equilibrated solutions of Cbl(I) containing varying concentrations of nitrate were unsuccessful since considerable Cbl(I) decomposition occurred during the time frame of the reaction even at the lowest pH value of this study (pH 5.02), where the reaction between Cbl(I) and nitrate is the most rapid. The reaction rate was also too slow compared with the rate of Cbl(I) decomposition to accurately determine the stoichiometry at higher pH values.

Kinetic Studies on the Reaction of Cbl(I) with Nitrate

The inset in Figure 7 gives the best fit of the absorbance data at 387 nm vs. time for the reaction between Cbl(I) and nitrate at pH 6.02 to a first-order rate equation, which gives $k_{\text{obs}} = (7.13 \pm 0.07) \times 10^{-2} \text{ min}^{-1}$. The rate of decomposition of Cbl(I) to Cbl(II) is significant under acidic pH conditions and was therefore also independently studied. This latter reaction was found to be over an order of magnitude slower than that of Cbl(I) with nitrate at each pH condition, Table 2.

Table 2. Second-order rate constants (k_{app}) for the reaction of Cbl(I) with NO_3^- , and approximate first-order rate constants (k_{decomp}) for the spontaneous decomposition of Cbl(I) at different pH values. Note that the latter reaction is not strictly first-order, does not proceed to completion, and exhibits considerable variability between experiments.

pH (± 0.02)	k_{app} ($\text{M}^{-1} \text{ min}^{-1}$)	$10^3 k_{\text{decomp}}$ (min^{-1})
5.02	14.92 ± 0.96	$17.1 \pm 0.2, 26.2 \pm 0.7$
6.02	3.15 ± 0.05	$2.84 \pm 0.01, 2.14 \pm 0.02$
7.00	0.39 ± 0.01	$0.65 \pm 0.02, 0.68 \pm 0.06$

The dependence of k_{obs} on the NO_3^- concentration (0.0500–0.500 M) was studied at pH 6.02, and the results are summarized in Figure 8. Fitting of the data to a straight line that passes through the origin gives an apparent second-order rate constant, $k_{\text{app}} = 3.15 \pm 0.05 \text{ M}^{-1} \text{ min}^{-1}$. Data under other pH conditions is shown in Figures S3 and S4, and k_{app} values are summarized in Table 2. From Table 2,

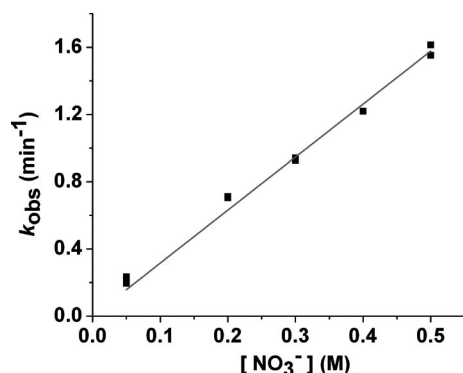


Figure 8. Plot of k_{obs} vs. NO_3^- concentration for the reaction between Cbl(I) and NO_3^- at pH 6.02 ± 0.02 (25.0 °C, 0.10 M phosphate buffer, $I = 1.5 \text{ M}$). The data was fitted to a straight line passing through the origin, which gives a slope of $3.15 \pm 0.05 \text{ M}^{-1} \text{ min}^{-1}$.

it is clear that the rate of the reaction increases with decreasing pH. At pH 8.00, the reaction was too slow relative to the spontaneous decomposition of Cbl(I) to be determined.

The data in Table 2 were fitted to the rate Equation (4):

$$k_{\text{app}} = k_{\text{obs}}/[\text{Cbl(I)}]_{\text{T}} = k^* [\text{NO}_3^-] 10^{-\text{pH}} \quad (4)$$

Fitting of the data to Equation (4) gives $k^* = (2.53 \pm 0.12) \times 10^4 \text{ M}^{-2} \text{ s}^{-1}$. This agrees well with the value obtained elsewhere at pH 1.5–2.5 ($k^* = 2.1 \times 10^4 \text{ M}^{-2} \text{ s}^{-1}$, 25.0 °C, 0.01 M HClO_4 , $I = 0.11 \text{ M}$).^[32] Hence, the mechanism of the oxidation of Cbl(I) by (H)NO₃ is unchanged in the pH range 1.5–7.0. Given that the overall reaction is an 8e⁻ process and therefore involves multiple steps, we are reluctant to propose a reaction scheme for this reaction without carrying out further extensive experimentation. Since NH₃ rather than NH₂OH is produced, this suggests that NO₂⁻ is unlikely to be an intermediate, and the first step of the reaction is therefore most likely a 1e⁻ redox reaction. The first-order dependence of the rate of the reaction on [H⁺] is consistent with the reaction of HNO₃ with Cbl(I).

Summary

The reactions of the strong reductant Cbl(I) with nitrite and nitrate have been studied by UV/Vis spectroscopy and/or stopped-flow spectroscopy. At pH 7, $k_{\text{app}} = 1.7 \times 10^3 \text{ M}^{-1} \text{ s}^{-1}$ for the reaction between Cbl(I) and (H)-NO₂, whereas the apparent rate constant for the reaction between Cbl(I) and (H)NO₃ is five orders of magnitude smaller ($k_{\text{app}} = 6.5 \times 10^{-3} \text{ M}^{-1} \text{ s}^{-1}$). The total Cbl concentration in cells is 30–700 nM in humans,^[6] whereas tissue NO₂⁻ concentrations are as high as 10 μM^[26b,30] under normal conditions and may be significantly elevated during periods of cellular oxidative and nitrosative stress. At 10 μM nitrite, the half-life for oxidation of Cbl(I) by nitrite is ≈40 s. A reaction pathway is postulated for the reaction between Cbl(I) and (H)NO₂ that involves a 2e⁻ rate-determining step to form Cbl(III) and HNO. The latter species reacts further with Cbl(I), which ultimately results in the oxidation of 4Cbl(I) by HNO₂ to yield 4Cbl(II) and NH₂OH. Detailed kinetic and mechanistic studies on the reaction between Cbl(I) and HNO are required, however, to probe this further. The reaction between Cbl(I) and (H)NO₃ results in the oxidation of 8Cbl(I) by (H)NO₃ to give 8Cbl(II) and NH₄⁺.

Experimental Section

Chemicals: Hydroxycobalamin hydrochloride, HOCbl·HCl ($\cdot n\text{H}_2\text{O}$) (≥96%, 10–15% water, batch dependent^[45]) was purchased from Fluka. BIS-TRIS and TAPS buffers were purchased from Sigma. Sodium borohydride (≥98%), CAPS, CHES, and MES buffer, sodium nitrite (99.6%), sodium nitrate (≥99%), and hydroxylamine hydrochloride (NH₂OH·HCl, ≥97%) were purchased from Acros Organics. Disodium hydrogen phosphate, sodium dihydrogen phosphate, sodium carbonate, dipotassium hydrogen phosphate, potassium dihydrogen phosphate, potassium cyanide (≥99.1%), and 8-hydroxyquinoline (≥99%) were purchased from Fisher Scientific.

Nessler's reagent was purchased from RICCA Chemical. Water was purified by using a Barnstead Nanopure Diamond water purification system.

Instrumental and Procedures: For Cbl(I) experiments, anaerobic solutions were degassed by four freeze-pump-thaw cycles under argon gas by using standard Schlenk techniques. Solutions prepared for Cbl(II) work were degassed by bubbling through argon for at least 2 h. Preparation of all anaerobic solutions was carried out in an MBRAUN Labmaster 130 (1250/78) glove box filled with argon, equipped with O₂ and H₂O sensors and a freezer at −24 °C. The pH measurements were carried out at room temperature by using an Orion model 710A pH meter equipped with Mettler-Toledo In-lab 423 or 421 pH electrodes. The electrode was filled with a 3 M KCl/saturated AgCl solution (pH 7.0) and standardized with standard buffer solutions at pH 4.00, 7.00, 10.00, and 12.45. The solution pH was adjusted with H₃PO₄, NaOH, or KOH solutions as necessary.

UV/Vis spectroscopy data were recorded on a Cary 5000 spectrophotometer equipped with a thermostatted (25.0 ± 0.1 °C) cell changer operating with WinUV Bio software (version 3.00). Kinetic data for rapid reactions were collected under strictly anaerobic conditions at 25.0 ± 0.1 °C by using an Applied Photophysics SX20 stopped-flow spectrophotometer equipped with a photodiode array detector in addition to a single wavelength detector, with sequential mixing capabilities. A continuous flow of nitrogen was used to maintain anaerobic conditions. Data were collected with Pro-Data SX (version 2.1.4) and Pro-Data Viewer (version 4.1.10) software, and a 1.0 cm pathlength cell was utilized. All data was analyzed by using Microcal Origin version 8.0.

Synthesis of Cbl(I): Cbl(I) was synthesized under anaerobic conditions according to a modified published procedure.^[46] For a typical synthesis, HOCbl·HCl [≈25 mg, 1.6 × 10^{−5} mol (10–15% H₂O)] was dissolved in anaerobic water (0.75 mL) in a vial. An aqueous, anaerobic stock solution of NaBH₄ (≈10 mg, 2.6 × 10^{−4} mol, 1.00 mL) was prepared, and NaBH₄ (6.0 molequiv.) was added to HOCbl·HCl. The vial was shaken vigorously for ≈1 min, and the reaction was allowed to occur for an additional 15–30 min. After the reaction was complete, the excess NaBH₄ was quenched by addition of acetone (0.200 mL), except when noted otherwise. Note that for all experiments performed with the stopped-flow instrument, the excess NaBH₄ was not quenched in order to provide added stability to the Cbl(I) reagent solution. The product was characterized by UV/Vis spectrophotometry (λ_{max} = 388, 464, 547, and 684 nm^[33]) and stored under anaerobic conditions at −24 °C. Cbl(I) solutions were used within 1 week of preparation.

Synthesis of Cbl(II): Cbl(II) was synthesized under anaerobic conditions according to a modified published procedure analogous to the synthesis of Cbl(I), except that 1.1 equiv. NaBH₄ was used.^[46] Cbl(II) was characterized by UV/Vis spectrophotometry (λ_{max} = 267, 285, 312, 475 nm^[33]), and solutions were stored under anaerobic conditions at −24 °C.

Determining Cobalamin Concentrations: The concentration of cobalamin in stock solutions was determined by converting to dicyanocobalamin, (CN)₂Cbl[−], with 0.1 M KCN [ϵ_{368} = 3.04 × 10⁴ M^{−1} cm^{−1} for (CN)₂Cbl[−]^[47]].

Determining the Stoichiometry of the Reaction between Cbl(I) and Nitrite: The stoichiometry of the Cbl(I) + NO₂[−] reaction was determined in buffer (5.0 × 10^{−3} M; CHES buffer at pH 9.51 and phosphate buffer at pH 7.40) under strictly anaerobic conditions. In a typical experiment, Cbl(I) (200 ± 9 μM, in water) was added to solutions containing varying molequiv. of NO₂[−] (2.96 × 10^{−4} M in

CHES buffer; 0.050, 0.10, 0.15, 0.20, 0.25, 0.30, 0.35, 0.40, 0.45, and 0.50 molequiv. of NO₂[−]). After 30 min (the minimal time required for the slowest reaction to proceed to completion as observed by UV/Vis spectroscopy), the UV/Vis spectrum was recorded. The experiment was completed in duplicate at pH 9.51 and 7.40. At pH 7.40, the reaction was complete in less than 1.5 min (the time required to remove the sample from the glove box to record a UV/Vis spectrum).

Determining the Amount of Hydroxylamine Product Formed in the Reaction between Cbl(I) and Nitrite by using the Indooxine Test: A modified literature procedure^[34] was used to determine the amount of NH₂OH produced by the reaction of Cbl(I) and NO₂[−]. Calibration standards were prepared by the addition of 8-hydroxyquinoline (1.00 mL, 4.0% w/v in ethanol) to a NH₂OH solution (1.00 mL) of a specific concentration in CHES buffer (5.0 × 10^{−3} M), pH 9.51, followed by the addition of Na₂CO₃ (1.00 mL, 1.00 M) under aerobic conditions. The reaction was allowed to proceed for 25 min (room temperature), and UV/Vis spectra recorded. The calibration curve is shown in Figure S1.

The reaction of Cbl(I) (200 ± 7 μM) and NaNO₂ (2.96 × 10^{−4} M) in 5.0 × 10^{−3} M CHES buffer, pH 9.51, was allowed to proceed to completion (1 h) under strictly anaerobic conditions inside the glove box for Cbl(I)/NO₂[−] ratios of 1:0.27 and 1:0.50, each in triplicate. The indooxine test was then performed on each sample by the addition of aerobic 8-hydroxyquinoline solution (1.00 mL, 4.0% w/v in ethanol) and aqueous aerobic Na₂CO₃ solution (1.00 mL, 1.00 M) to the reaction product (1.00 mL) outside the glove box. After standing for 30 min at room temperature, the UV/Vis spectrum was recorded.

Determining whether Ammonia is a Product of the Reaction between Cbl(I) and Nitrite: A Nessler test for the presence of NH₃ was performed on a solution containing the reaction products of 200 μM Cbl(I) with 50 μM NO₂[−] (0.050 M CHES buffer, pH 9.51) under aerobic conditions. Approximately 8 drops of the Nessler reagent were added to the product solution. A positive result for NH₃ is indicated by a yellow or, at high concentrations, brown coloring in the reaction solution.^[48] In this case, no brown or yellow coloring was observed above the pink color of the HOCbl species.

Determining whether Ammonia is a Product of the Reaction between Cbl(I) and Nitrate: Nessler's reagent (2–3 drops) was added to the product mixture (3.00 mL) of the reaction between Cbl(I) (50.0 μM) and NO₃[−] (0.500 M) at pH 5.02 [25.0 °C, 0.01 M acetate buffer, *I* = 1.5 M (K₂HPO₄)] immediately upon the completion of the reaction. The immediate formation of a brown-colored precipitate at the bottom of the vial occurred. In order to check that the formation of the brown precipitate is not due to the reaction of Cbl(II) with Nessler's reagent, a control experiment was carried out in which 2–3 drops of Nessler's reagent was added to Cbl(II) solution (50.0 μM) at pH 5.02 [25.0 °C, 0.01 M acetate buffer, *I* = 1.5 M (K₂HPO₄)]. A cloudy red-colored solution was instead formed.

Kinetic Studies on the Reaction between Cbl(I) and Nitrite: All kinetic experiments for the reaction of Cbl(I) with NO₂[−] were performed by using at least ten times excess NO₂[−] to ensure pseudo-first-order kinetics at a total ionic strength of 0.50 M (Na₂HPO₄/NaH₂PO₄). Buffers (0.050 M; CAPS, CHES, TAPS, phosphate, MES, and BIS-TRIS) were used to maintain the solution pH. Data collected by using the UV/Vis spectrophotometer were obtained by using Schlenk cuvettes equipped with a bulb, which was filled with a concentrated Cbl(I) solution in CHES buffer, to maximize its stability. The solutions were thermostatted at 25.0 °C for at least 10 min before initiating the reaction. Data for the reaction of Cbl(I) with NO₂[−] at pH < 10.80 were collected by using the stopped-flow

spectrophotometer. Experiments at pH < 7.40 required that the Cbl(I) solution (300 μ M, to maximize its stability) be diluted in H₂O and mixed with the nitrite solution in buffer within the tubing of the instrument. Unless otherwise specified, data were analyzed at 388 nm. At pH 6.92 and 6.50, data were collected and analyzed at 500 nm to accommodate the higher Cbl concentrations.

Kinetic Studies on the Reaction between Cbl(I) and Nitrate: All kinetic experiments for the reaction of Cbl(I) with NO₃[−] were performed by using at least ten times excess NO₃[−] at a total ionic strength of 1.50 M (K₂HPO₄/KH₂PO₄). Buffers (0.10 M, phosphate or acetate, 25.0 °C) were used to maintain the solution pH. Data were collected by using the Cary 5000 UV/Vis spectrophotometer. All experiments were carried out by using Schlenk cuvettes equipped with a bulb, which was filled with a concentrated Cbl(I) solution in H₂O. The solutions were thermostatted at 25.0 °C for at least 10 min before mixing the reagents and initiating the reaction. The data were analyzed at 387 nm.

Supporting Information (see footnote on the first page of this article): Determination of the stoichiometry of the reaction between Cbl(I) and NO₂[−] under different conditions, details of the indoxine test experiments, and kinetic plots and details are presented.

Acknowledgments

Funding for this work was provided by the U. S. National Science Foundation (CHE-0848397).

- [1] a) B. Krautler, S. Ostermann, in: *The Porphyrin Handbook* (Eds.: K. M. Kadish, K. M. Smith, R. Guilard), Elsevier Science Oxford, **2003**, pp. 229–276; b) R. Banerjee (Ed.), *Chemistry and Biochemistry of B₁₂*, John Wiley & Sons, New York, **1999**; c) K. L. Brown, *Chem. Rev.* **2005**, *105*, 2075–2150.
- [2] H. P. C. Hogenkamp, in ref.^[1b], p. 3.
- [3] D. Lexa, J. M. Saveant, *Acc. Chem. Res.* **1983**, *16*, 235–243.
- [4] M. D. Liptak, T. C. Brunold, *J. Am. Chem. Soc.* **2006**, *128*, 9144–9156.
- [5] a) T. A. Stich, N. R. Buan, J. C. Escalante-Semerena, T. C. Brunold, *J. Am. Chem. Soc.* **2005**, *127*, 8710–8719; b) T. A. Stich, M. Yamanishi, R. Banerjee, T. C. Brunold, *J. Am. Chem. Soc.* **2005**, *127*, 7660–7661; c) M. St. Maurice, P. Mera, K. Park, T. C. Brunold, J. C. Escalante-Semerena, I. Rayment, *Biochemistry* **2008**, *47*, 5755–5766.
- [6] R. Banerjee, C. Gherasim, D. Padovani, *Curr. Opin. Chem. Biol.* **2009**, *13*, 484–491.
- [7] a) L. Randaccio, S. Geremia, N. Demitri, J. Wuerger, *Molecules* **2010**, *15*, 3228–3259; b) B. Kräutler, *Biochem. Soc. Trans.* **2005**, *33*, 806–810.
- [8] P. Mera, J. Escalante-Semerena, *Appl. Microbiol. Biotechnol.* **2010**, *88*, 41–48.
- [9] a) K. Park, P. E. Mera, J. C. Escalante-Semerena, T. C. Brunold, *Biochemistry* **2008**, *47*, 9007–9015; b) A. K. Park, Y. M. Chi, J. H. Moon, *Biochem. Biophys. Res. Commun.* **2011**, *408*, 417–421.
- [10] a) M. D. Liptak, A. S. Fleischacker, R. G. Matthews, T. C. Brunold, *Biochemistry* **2007**, *46*, 8024–8035; b) M. D. Liptak, S. Datta, R. G. Matthews, T. C. Brunold, *J. Am. Chem. Soc.* **2008**, *130*, 16374–16381; c) M. D. Liptak, A. S. Fleischacker, R. G. Matthews, J. Telser, T. C. Brunold, *J. Phys. Chem. B* **2009**, *113*, 5245–5254.
- [11] a) J. Haglund, A. Rafiq, L. Ehrenberg, B. T. Golding, M. Törnqvist, *Chem. Res. Toxicol.* **2000**, *13*, 253–256; b) S. Kligman, K. McNeill, *Dalton Trans.* **2008**, 4191–4201; c) D. A. Pratt, W. A. van der Donk, *J. Am. Chem. Soc.* **2004**, *127*, 384–396.
- [12] a) H. V. Motwani, C. Fred, J. Haglund, B. T. Golding, M. Törnqvist, *Chem. Res. Toxicol.* **2009**, *22*, 1509–1516; b) J. Haglund, V. Silvani, E. Esmans, M. Törnqvist, *J. Chromatogr. A* **2006**, *1119*, 246–250; c) H. V. Motwani, M. Törnqvist, *J. Chromatogr. A* **2011**, *1218*, 4389–4394.
- [13] a) T. F. Connors, J. V. Arena, J. F. Rusling, *J. Phys. Chem.* **1988**, *92*, 2810–2816; b) G. N. Schrauzer, E. Deutsch, *J. Am. Chem. Soc.* **1969**, *91*, 3341–3350; c) D. Datta, G. T. Sharma, *Inorg. Chem.* **1987**, *26*, 329–332.
- [14] G. Glod, U. Brodmann, W. Angst, C. Holliger, R. P. Schwaizenbach, *Environ. Sci. Technol.* **1997**, *31*, 3154–3160.
- [15] J. F. Rusling, C. L. Miaw, E. C. Couture, *Inorg. Chem.* **1990**, *29*, 2025–2027.
- [16] a) S. K. Ghosh, P. N. Balasubramanian, G. C. Pillai, M. C. Ghosh, E. S. Gould, *Inorg. Chem.* **1991**, *30*, 1043–1045; b) S. K. Ghosh, P. N. Balasubramanian, G. C. Pillai, E. S. Gould, *Inorg. Chem.* **1991**, *30*, 487–491.
- [17] a) G. C. Pillai, S. K. Ghosh, E. S. Gould, *Inorg. Chem.* **1988**, *27*, 1868–1871; b) G. C. Pillai, R. N. Bose, E. S. Gould, *Inorg. Chem.* **1987**, *26*, 3120–3123; c) J. H. Espenson, H. B. Gjerde, *Inorg. Chem.* **1980**, *19*, 3549–3550.
- [18] G. C. Pillai, E. S. Gould, *Inorg. Chem.* **1986**, *25*, 4740–4743.
- [19] G. C. Pillai, E. S. Gould, *Inorg. Chem.* **1986**, *25*, 3353–3356.
- [20] P. N. Balasubramanian, J. W. Reed, E. S. Gould, *Inorg. Chem.* **1985**, *24*, 1794–1797.
- [21] P. N. Balasubramanian, E. S. Gould, *Inorg. Chem.* **1984**, *23*, 824–828.
- [22] R. Blackburn, M. Kyaw, A. J. Swallow, *J. Chem. Soc. Faraday Trans.* **1977**, *73*, 250–255.
- [23] a) E. S. Moreira, N. E. Brasch, J. Yun, *Free Radical Biol. Med.* **2011**, *51*, 876–883; b) E. Suarez-Moreira, J. Yun, C. S. Birch, J. H. H. Williams, A. McCaddon, N. E. Brasch, *J. Am. Chem. Soc.* **2009**, *131*, 15078–15079; c) C. S. Birch, N. E. Brasch, A. McCaddon, J. H. H. Williams, *Free Radical Biol. Med.* **2009**, *47*, 184–188; d) R. Mukherjee, N. E. Brasch, *Chem. Eur. J.* **2011**, *17*, 11723–11727.
- [24] a) N. L. Reynaert, E. F. Wouters, A. van der Vliet, Y. M. Janssen-Heininger, *Antioxid. Redox Signaling* **2005**, *7*, 129–143; b) I. Schulman, M.-S. Zhou, L. Raji, *Curr. Hypertens. Rev.* **2005**, *7*, 61–67; c) Y.-Y. Hsieh, C.-C. Chang, F.-J. Tsai, C.-C. Lin, J.-M. Chen, C.-H. Tsai, *Mol. Hum. Reprod.* **2004**, *10*, 713–717; d) R. W. Schrier, W. Wang, *New Engl. J. Med.* **2004**, *351*, 159–169.
- [25] D. Padovani, R. Banerjee, *Biochemistry* **2009**, *48*, 5350–5357.
- [26] a) L. J. Ignarro (Ed.), *Nitric Oxide: Biology and Pathobiology*, Academic Press, San Diego, **2000**; b) J. Heinecke, P. C. Ford, *Coord. Chem. Rev.* **2010**, *254*, 235–247; c) A. A. Avery, *Environ. Health Perspect.* **1999**, *107*, 583–586.
- [27] a) Y. Misonou, M. Asahi, S. Yokoe, E. Miyoshi, N. Taniguchi, *Nitric Oxide* **2006**, *14*, 180–187; b) G. Zunic, R. Pavlovic, Z. Malicevic, V. Savic, I. Cernak, *Nitric Oxide* **2000**, *4*, 123–128; c) G. Zunic, M. Colic, M. Vuceljic, *Nitric Oxide* **2009**, *20*, 264–269; d) M. Kelm, *Biochim. Biophys. Acta* **1999**, *1411*, 273–280.
- [28] M. A. Erkurt, I. Aydogdu, N. Bayraktar, İ. Kuku, E. Kaya, *Turk. J. Hematol.* **2009**, *26*, 197.
- [29] F. M. Gonzalez, S. Shiva, P. S. Vincent, L. A. Ringwood, L.-Y. Hsu, Y. Y. Hon, A. H. Aletras, R. O. Cannon III, M. T. Gladwin, A. E. Arai, *Circulation* **2008**, *117*, 2986–2994.
- [30] C. Oplander, C. V. Suschek, *J. Invest. Dermatol.* **2009**, *129*, 820–822.
- [31] T. Rassaf, M. Feelisch, M. Kelm, *Free Radical Biol. Med.* **2004**, *36*, 413–422.
- [32] P. N. Balasubramanian, E. S. Gould, *Inorg. Chem.* **1983**, *22*, 2635–2637.
- [33] Z. Schneider, A. Stroiński (Eds.), *Comprehensive B₁₂*, Walter de Gruyter, Berlin, **1987**.
- [34] D. R. Arnelle, J. S. Stamler, in: *Methods in Nitric Oxide Research* (Eds.: M. Feelisch, J. S. Stamler), John Wiley & Sons, New York, **1996**, pp. 541–552.
- [35] T. D. B. Morgan, G. Stedman, M. N. Hughes, *J. Chem. Soc. B* **1968**, 344–349.

- [36] R. Tomat, A. Rigo, R. Salmaso, *J. Electroanal. Chem.* **1975**, 59, 255–260.
- [37] a) G. E. Alluisetti, A. E. Almaraz, V. T. Amorebieta, F. Doctorovich, J. A. Olabe, *J. Am. Chem. Soc.* **2004**, 126, 13432–13442; b) S. E. Bari, V. T. Amorebieta, M. M. Gutiérrez, J. A. Olabe, F. Doctorovich, *J. Inorg. Biochem.* **2010**, 104, 30–36.
- [38] J. M. Pratt, *Inorganic Chemistry of Vitamin B₁₂*, Academic Press, New York, **1972**.
- [39] G. da Silva, E. M. Kennedy, B. Z. Dlugogorski, *J. Phys. Chem. A* **2006**, 110, 11371–11376.
- [40] M. D. Bartberger, W. Liu, E. Ford, K. M. Miranda, C. Switzer, J. M. Fukuto, P. J. Farmer, D. A. Wink, K. N. Houk, *P. Natl. Acad. Sci.* **2002**, 99, 10958–10963.
- [41] D. Zheng, L. Yan, R. L. Birke, *Inorg. Chem.* **2002**, 41, 2548–2555.
- [42] a) J. C. Irvine, R. H. Ritchie, J. L. Favalaro, K. L. Andrews, R. E. Widdop, B. K. Kemp-Harper, *Trends Pharmacol. Sci.* **2008**, 29, 601–608; b) J. M. Fukuto, M. I. Jackson, N. Kaludercic, N. Paolocci, in: *Methods in Enzymology*, Vol. 440 (Eds.: C. Enrique, P. Lester), Academic Press, **2008**, pp. 411–431.
- [43] M. I. Jackson, T. H. Han, L. Serbulea, A. Dutton, E. Ford, K. M. Miranda, K. N. Houk, D. A. Wink, J. M. Fukuto, *Free Radical Biol. Med.* **2009**, 47, 1130–1139.
- [44] V. Shafirovich, S. V. Lymar, *P. Natl. Acad. Sci.* **2002**, 99, 7340–7345.
- [45] N. E. Brasch, R. G. Finke, *J. Inorg. Biochem.* **1999**, 73, 215–219.
- [46] K. L. Brown, J. M. Hakimi, D. M. Nuss, Y. D. Montejano, D. W. Jacobsen, *Inorg. Chem.* **1984**, 23, 1463–1471.
- [47] H. A. Barker, R. D. Smyth, H. Weissbach, J. I. Toohey, J. N. Ladd, B. E. Volcani, *J. Biol. Chem.* **1960**, 235, 480–488.
- [48] P. A. Hansen, *J. Biol. Chem.* **1939**, 131, 309–315.

Received: September 16, 2011

Published Online: December 14, 2011

Peculiarities of Vibrational Spectra and Electronic Structure of the Five-Membered Metallacyclocumulenes of the Group 4 Metals

Rinat R. Aysin,^[a] Larissa A. Leites,^{*[a]} Vladimir V. Burlakov,^[a] Vladimir B. Shur,^[a] Torsten Beweries,^[b] and Uwe Rosenthal^[b]

Keywords: Metallacyclocumulenes / Cyclopentadienyl ligands / Electronic structure / Raman spectroscopy / IR spectroscopy / QTAIM analysis

The vibrational (Raman and IR) spectra of metallacyclic cumulenes of the type $\text{Cp}_2\text{M}(\eta^4\text{-}t\text{BuC}_4t\text{Bu})$ [$\text{M} = \text{Ti}$ (**1**), Zr (**2**), Hf (**3**)] were obtained and analyzed in terms of normal coordinate calculations. The system of three cumulated $\text{C}=\text{C}$ bonds in the five-membered metallacycle was shown to exhibit a peculiar spectral pattern with three normal modes with frequencies at ca. 1900 (ν^s_1), 1650 (ν^{as}_2), and 1280 cm^{-1} (ν^s_3). The ν^s_1 mode is a symmetric stretch of the two equivalent $\text{C1}-\text{C2}$ and $\text{C3}-\text{C4}$ bonds (with simultaneous contraction of the central $\text{C2}-\text{C3}$ bond), the ν^{as}_2 mode is their antisymmetric

combination, while the ν^s_3 mode has a complex eigenvector and involves a “breathing” motion of the metallacycle as a whole along with $\text{C}-\text{C}_{t\text{Bu}}$ bond stretches. Reconstruction of the electron-density distribution in the molecules studied by using Bader’s AIM theory resulted in a specific molecular graph of the metallacycle, that with the so-called “T-shaped” configuration, pointing to topological instability of the system. This is in contrast to analogously calculated “normal” bonding patterns for related cyclopropene complexes $\text{Cp}_2\text{Ti}(\eta^2\text{-RC}_2\text{R})$.

Introduction

A family of novel-type compounds, namely, the smallest metallacyclic cumulenes of the type $\text{Cp}_2\text{M}(\eta^4\text{-}t\text{BuC}_4t\text{Bu})$ [$\text{M} = \text{Ti}$ (**1**), Zr (**2**), Hf (**3**)] has been synthesized and characterized by XRD and NMR spectroscopy.^[1–3] These complexes are of great interest, not only theoretically as aromatic organometallic compounds, but also practically, because some of their derivatives are active catalysts in the polymerization of olefins and ϵ -caprolactone.^[4] The three complexes are isostructural and display bent metallocene structures that contain a planar five-membered metallacycle (Figure 1). The synthesis and X-ray structures of related substituted Zr complexes, $\text{Cp}^*_2\text{Zr}(\eta^4\text{-RC}_4\text{R})$ ($\text{R} = \text{Me}$, Ph , SiMe_3) and $\text{Cp}^*_2\text{Zr}(\eta^4\text{-}t\text{BuC}_4\text{-C}\equiv\text{C}t\text{Bu})$ (**4**), have also been reported,^[5] and their structural features are close to those of **2**.

A comparison of the salient geometric parameters of the metallacycles in **1–3** is presented in Table 1. The endocyclic $\text{C}-\text{C}-\text{C}$ bond angles in the metallacyclocumulative unit of **1–3** strongly deviate from 180° , which seemingly point to a significant angular strain (see below).

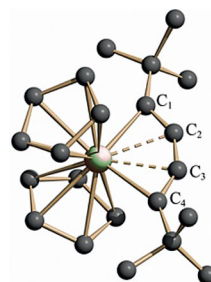


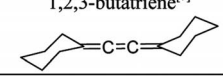
Figure 1. Structure of $\text{Cp}_2\text{M}(\eta^4\text{-}t\text{BuC}_4t\text{Bu})$ ($\text{M} = \text{Ti}$, Zr , Hf).

The lengths of the three $\text{C}-\text{C}$ bonds point to multiple bond orders. From the geometry data of **1–3**, the cumulene structure of the C_4 moiety was inferred.^[1–3] All four ring C atoms possess p orbitals normal to the plane of the cumulene cycle. In addition, the sp -hybridized C2 and C3 atoms possess p orbitals that lie in this plane. The central $\text{C2}-\text{C3}$ bond in **1–3** is longer than the other two bonds. This is in contrast to noncoordinated linear butatrienes, in which their central $\text{C}=\text{C}$ bond is noticeably shorter than the terminal ones.^[7] It is natural that the incorporation of a butatriene moiety into any small five-membered ring should distort the butatriene linearity with concomitant rehybridization of C2 and C3 , which leads to an elongation of the $\text{C2}-\text{C3}$ bond.^[8] However, the elongation observed for the $\text{C2}-\text{C3}$ bonds in **1–3** is far beyond these limits. The $\text{M}-\text{C2}$ and $\text{M}-\text{C3}$ experimental distances in **1–3** and in the Zr complexes described in ref.^[5] are on average shorter than those of $\text{M}-\text{C1}$ and $\text{M}-\text{C4}$; this is in accord with our results on

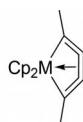
[a] A. N. Nesmeyanov Institute of Organoelement Compounds, Russian Academy of Sciences, 28 Vavilova Street, 119991 Moscow, Russia
E-mail: bukley@ineos.ac.ru

[b] Leibniz-Institut für Katalyse e. V. an der Universität Rostock, Albert-Einstein-Strasse 29a, 18059 Rostock, Germany
Supporting information for this article is available on the WWW under <http://dx.doi.org/10.1002/ejic.201101088>.

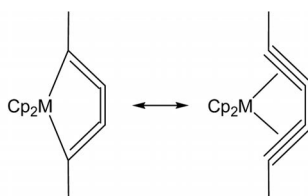
Table 1. Salient geometric parameters in the X-ray structures of $\text{Cp}_2\text{M}(\eta^4\text{-}t\text{BuC}_4t\text{Bu})$ ($\text{M} = \text{Ti}, \text{Zr}, \text{Hf}$) and related free ligands.^[6]

	$\text{M} = \text{Ti}$ (1) ^[2]	$\text{M} = \text{Zr}$ (2) ^[1a]	$\text{M} = \text{Hf}$ (3) ^[3a]	1,4-bis(<i>tert</i> -butyl)- butadiyne ^[6]	1,1,4,4-bis(pentamethylene)- 1,2,3-butatriene ^[7]
					
Interatomic distances [Å]					
M–C1	2.298(10)	2.357(5)	2.281(4)		
M–C2	2.209(9)	2.303(5)	2.294(4)		
M–C3	2.213(9)	2.306(5)	2.297(3)		
M–C4	2.252(9)	2.307(5)	2.308(4)		
C1–C2	1.243(13)	1.28(1)	1.288(5)	C≡C 1.199	(C=C) _{term} 1.324(2)
C2–C3	1.339(13)	1.31(1)	1.334(5)	C–C 1.382	(C=C) _{centr} 1.269(2)
C3–C4	1.276(11)	1.29(1)	1.298(5)	C≡C 1.199	(C=C) _{term} 1.324(2)
Bond angles [°]					
C1–C2–C3	150.0(10)	150.0(5)	146.3(4)		
C2–C3–C4	147.8(10)	147.2(5)	147.1(4)		

the geometry optimization computed for **1–3** at the DFT level (Table S1). These peculiar geometric parameters of **1–3** (especially the C–C bond lengths, which range from the corresponding values for diacetylenes to those for butatrienes, Table 1) suggest π coordination of the central C=C bond to the metal atom with formation of a three-centre, two-electron (3c-2e) bond.^[1–3]



The electronic structure of these metallacycles is sophisticated and difficult to describe unequivocally. Several theoretical DFT studies have been devoted to this matter.^[9–11] Some studies^[9] confirm the strong metal– π interaction in **1** and **2**, which results in substantial cyclic electron delocalization (in-plane aromaticity) and $(\eta^2\text{-}\sigma,\sigma) + (\eta^2\text{-}\pi,\pi)$ coordination of the ligand. Aromaticity is also evidenced by high negative nucleus-independent chemical shift (NICS) values.^[9b] Based on the small hydrogenation energy value for **2**, it has been stated that these molecules are not strained, because interaction with the metal fragment “nearly eliminates the ring strain energy.”^[9b] However, Lam and Lin^[11] cannot accept this point of view; based on a model isodesmic reaction, they have calculated the ring strain energy for the cyclocumulene complex $\text{Cp}_2\text{Zr}(\eta^4\text{-H}_3\text{SiC}_4\text{SiH}_3)$ to be as high as 23.1 kcal/mol. Therefore, they concluded that the structure and high stability of this type of compounds can be adequately described only by a resonance hybrid between a cyclocumulene and a diyne π complex Lewis structure:



The structural and chemical properties of the Ti and Zr complexes in question have been summarized.^[12] The authors concluded that the real bonding situation in metalla-

cyclocumulenes has not yet been fully clarified, especially taking into account their dual reactivity, e.g. their ability to react as η^4 (metallacyclocumulene) and η^2 (metallacyclopentadiene) complexes.

It is of interest to examine how the specific bonding system of **1–3** manifests itself in vibrational spectra, and we report the Raman and IR spectra of **1–3**. In previous studies,^[1a,2] it was mentioned that no features in the regions characteristic of the stretching vibrations of coordinated (1700–1800 cm^{-1}) or free (2050–2200 cm^{-1}) C≡C bonds were found in the IR spectra of **1** and **2**. For **4**,^[5c] IR absorption bands at 1865 and 1653 cm^{-1} along with the free $\nu(\text{C}\equiv\text{C})$ band at 2149 cm^{-1} were reported. We have also carried out quantum chemical DFT PBE/PBE0 calculations of the geometry and vibrational mode frequencies and eigenvectors (normal coordinate analysis) for **1–3**. In addition, to gain a new insight into the cyclocumulene bonding system, the electron-density distribution (EDD) function, $\rho(r)$, has been reconstructed within Bader's atoms in molecules (AIM) theory^[13] based on the optimized geometry obtained. Analogous data for the related metallocene–acetylene complexes have been obtained and are reported for comparison.

Results and Discussion

Vibrational Spectra

The results of the vibrational spectroscopy are presented in Figures 2 and 3, Tables 2 and 3, and the Supporting Information. In Figure 2, the Raman and IR spectra of **3** (as an example) are juxtaposed. Figure 3 presents a comparison of the Raman spectra of **1–3**. Band assignment was made on the basis of the results of normal coordinate analysis (NCA) and by comparison with spectra of related metallocenes.^[14–16] Of particular interest are the vibrations of the metallacyclocumulene unit. In the Raman spectra of **1–3**, an unusual line is observed in the region characteristic of multiple C–C bond stretching vibrations at ca. 1880 cm^{-1} . Its frequency is too low for a “free” C≡C bond and too high for a C=C bond. Its origin can be rationalized by NCA analysis, which showed that the system of three cumulated C=C

bonds in the five-membered metallacycle forms three normal modes with calculated frequencies at ca. 1900, 1650, and 1280 cm^{-1} . These values are in good agreement with those found experimentally, and the effect of the metal atom is most pronounced for $M = \text{Ti}$ (Table 2). Computed eigenvectors of these modes are outlined in Figure 4. The first mode (ν^s_1) is a symmetric stretch of the two equivalent C1–C2 and C3–C4 bonds with simultaneous contraction of the central C2–C3 bond, the corresponding contributions to the potential-energy distribution (PED; $M = \text{Ti}$) are 50 and 35%, respectively. The related experimental Raman line of medium intensity is situated in the 1850–1910 cm^{-1} region and is split into a doublet (Figures 2 and 3), probably due

to Fermi resonance, because the splitting is preserved in the spectra of solutions. This mode appears in the IR spectrum as a very weak feature, which is in accord with its calculated value (Table 2). The second mode (ν^{as}_2) is an antisymmetric stretching vibration of the C1–C2 and C3–C4 bonds (62% in PED) with simultaneous participation of the C–C_{*t*Bu} bonds. The corresponding experimental band is situated in the 1650–1740 cm^{-1} region, and its intensity in both Raman and IR spectra is very weak. The third mode at ca. 1280 cm^{-1} (ν^s_3) is due to a whole-molecule motion; in computer animations it appears as a “breathing” of the metallacycle (with the main contribution from the central C2–C3 bond) and also involves the C–C_{*t*Bu} bond stretches and *t*Bu

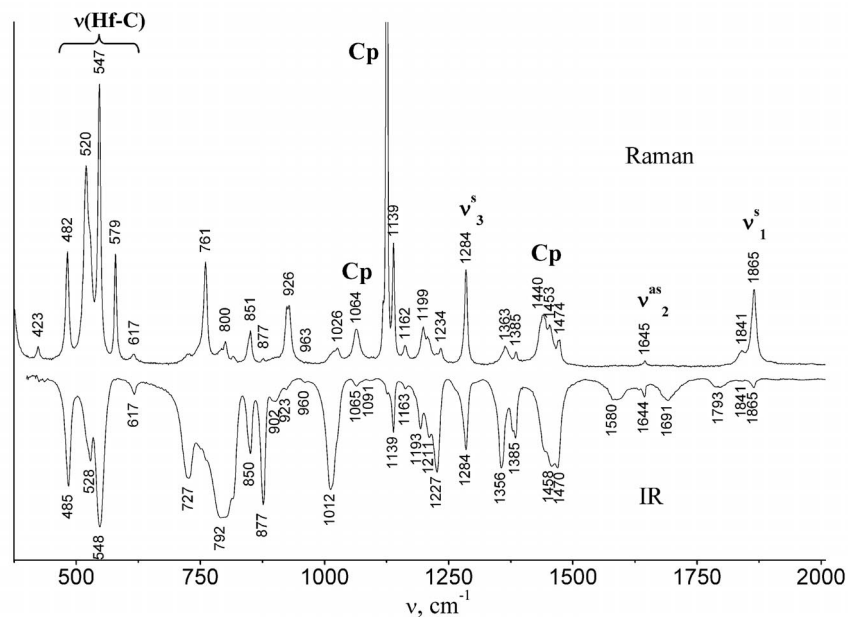


Figure 2. Raman and IR spectra of solid 3.

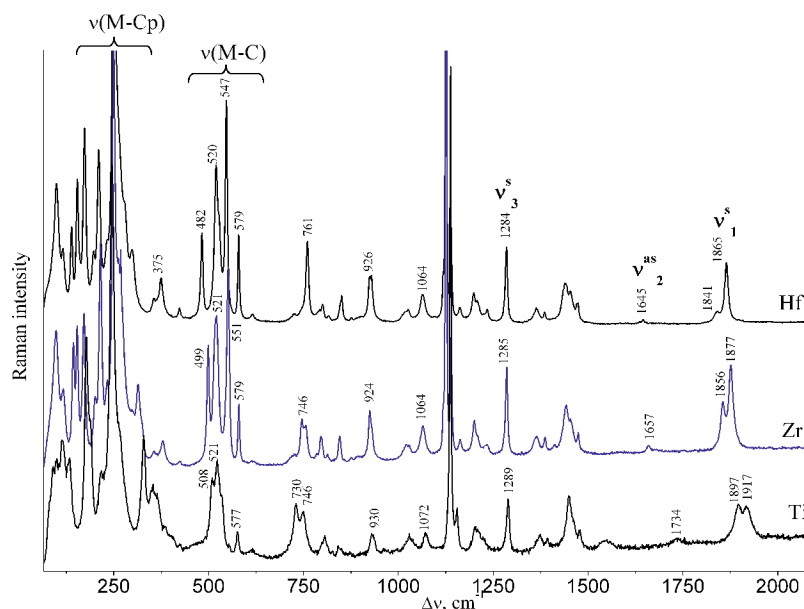
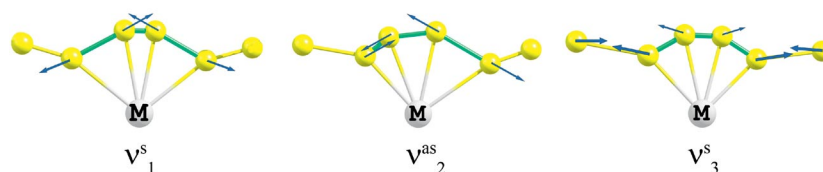


Figure 3. Comparison of the Raman spectra of solid 1–3.

Table 2. Experimental and calculated frequencies [cm^{-1}] of the metallacycle $\nu(\text{C}=\text{C})$ modes in the spectra of **1–4**.

M	ν_1^s	ν_2^{as}	ν_3^s			
	Raman	IR	Raman	IR	Raman	IR
Ti (1)	1897/1917 m	1890/1910 vw	1734 vw	1724 vw	1289 mw	1285 mw
Zr (2)	1856/1877 m	1852/1873 vw	1659 w	1657 w	1285 m	1284 s
$4^{[Sc]}$		1865		1653		
Hf (3)	1841/1865 m	1865 vw	1645 w	1644 w	1284 m	1284 ms
Calculated						
Ti		1943 w		1732 w		1278 m
Zr		1914 vw		1680 vw		1278 m
Hf		1905 vw		1664 vw		1277 m

Figure 4. Outline of the computed eigenvectors for the ν^s_1 , ν^{as}_2 , and ν^s_3 normal modes of the $\text{R}_2\text{C}_4\text{M}$ fragment.

group deformations. The corresponding experimental band is of medium intensity in both spectra (Figures 2 and 3). Another spectral region of interest is $400\text{--}580\text{ cm}^{-1}$ where the bands that correspond to the $\nu(\text{M}=\text{C})$ stretching vibrations are known to be situated.^[15,16] In our case, the features that correspond to normal modes with significant participation of the metallacycle $\text{M}=\text{C}$ bond stretches manifest themselves as intense bands in both the Raman and IR spectra. These vibrations are not localized; they mix with the *t*Bu group vibrations but not with those of the Cp rings. Analysis of the Cp_2M fragment vibrations is beyond the scope of our study and can be found in refs.^[14–16] Some assignments of other spectral bands of **1–3** are given in Table S2.

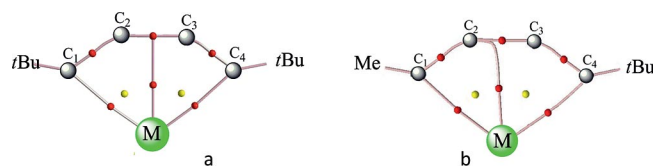
Table 3. Experimental $\nu(\text{C}=\text{C})$ frequencies [cm^{-1}] in the IR and Raman spectra of solid $\text{Cp}^*_2\text{M}(\eta^2\text{-Me}_3\text{SiC}_2\text{SiMe}_3)$ [M = Ti (**6**), Zr (**7**), Hf (**8**)].

	6	7	8
IR	1563/1598 ^[23]	1516 ^[24]	1470 ^[25]
Raman (this work)	1561/1594 m	1518 m	1472 m

It seems pertinent to compare the vibrational mechanics of the bent $\text{C}=\text{C}=\text{C}=\text{C}$ bond system in **1–3** with those of linear free ligands, whose spectra are available in ref.^[17] and firmly assigned based on comparison of the Raman and IR intensities and polarization measurements, namely, butatriene and 1,4-dimethylbutadiyne. In the spectrum of butatriene, the three $\nu(\text{C}=\text{C})$ modes have frequencies at 2079 cm^{-1} (ν^s_1), 1607 cm^{-1} (ν^{as}_2), and 878 cm^{-1} (ν^s_3), and in the spectrum of 1,4-dimethylbutadiyne they are observed at 2265, 2163, and 1228 cm^{-1} , respectively; i.e. the mutual order of frequencies in the spectra, $\nu^s_1 > \nu^{\text{as}}_2 > \nu^s_3$, is the same as for **1–3** but the frequency values differ significantly. It is notable that the ν^{as}_2 frequency of **1–3** is close to that of butatriene, whereas the ν^s_3 frequency of **1–3** is close to that of 1,4-dimethylbutadiyne.

AIM Analysis

AIM analysis is a useful and successful tool in the elucidation of molecular bonding.^[13] Complete molecular graphs, obtained from the reconstruction of EDD functions of **1–3** within Bader's quantum theory (QT)AIM formalism, can be found in Figures S1–S3, and the parts that correspond to the metallacycles are given in Figure 5. The AIM critical point (CP) search for **1–3** revealed the presence of the expected bond paths and corresponding (3,–1) bond (B)CPs for the $\text{C1}=\text{C2}$, $\text{C2}=\text{C3}$, $\text{C3}=\text{C4}$, $\text{C1}=\text{M}$, and $\text{C4}=\text{M}$ bonds. Surprisingly, no bond paths and no BCPs were found between the metal center and the C2 and C3 atoms; however, a BCP on a line that connects the metal atom and the midpoint of the $\text{C2}=\text{C3}$ bond did appear (Figure 5a). The Poincaré–Hopf relationship holds true for the results obtained.

Figure 5. QTAIM molecular graphs of the metallacyclocumulenes studied, which show only the five-membered metallacycle: (a) with a symmetrical *t*Bu C_4 *t*Bu moiety and (b) with an asymmetrical MeC_4 *t*Bu moiety. Red circles = BCPs, yellow circles = ring CPs.

Examination of literature data has shown that analogous T-shaped configurations have been observed previously, e.g. in molecular graphs of $\text{H}\cdots\pi$ complexes formed by HF with symmetrical unsaturated molecules such as acetylene and ethylene.^[18,19] According to Bader,^[13,20] the T-shaped phenomenon corresponds to the so-called “conflict catastrophe structures,” which means that the system is topologically unstable. A break in symmetry of the system should liquidate the catastrophe configuration.^[18] With this in mind, we

carried out the QTAIM calculation for a model asymmetrical complex, $\text{Cp}_2\text{Hf}(\eta^4\text{-MeC}_4\text{tBu})$, and obtained an even stranger molecular graph, that is, with only one bond path, strongly bent, between the metal atom and C2 close to the Me group and no bond path to link M and C3 (Figure 5b). The BCP situated near the center of the five-membered cycle does not shift on going from the graph in Figure 5a to that in Figure 5b. However, both graphs seem to be unable to adequately present the complicated bonding situation in the metallacyclocumulenes studied.

It is of interest to mention here the recent results of an experimental electron-density study on a related and also mysterious 1-metallacyclopent-3-yne complex.^[21] The molecular graph obtained for the metallacycle of $\text{Cp}_2\text{Zr}(\text{H}_2\text{C}-\text{C}_2-\text{CH}_2)$ (**5**) as a result of EDD topological analysis appeared nontrivial but in a slightly different way to those of **1–3**. Similar to **1–3**, no BCPs or bond paths were found between the Zr center and C2 and C3 in **5**. However, in contrast to **1–3**, there was no line to connect the Zr atom and the midpoint of the C2–C3 bond and no BCP along this line, whereas the Zr–C1 and Zr–C2 bond paths appeared strongly bent towards the BCPs of the C1–C2 and C3–C4 bonds to resemble the T-shaped situations. The EDD graph for **5** led to the conclusion that the bonding system of **5** is a resonance hybrid between $\eta^2\text{-}\sigma,\sigma$ and $\eta^4\text{-}\pi,\pi$ coordination, in which the contribution from the latter is small.^[21]

The unusual AIM results obtained for the five-membered metallacycles **1–3** and **5** prompted us to investigate related metallocene-acetylene complexes of the type $\text{Cp}_2\text{Ti}(\eta^2\text{-RC}_2\text{R})$ ^[22] and $\text{Cp}^*_2\text{M}(\eta^2\text{-RC}_2\text{R})$ ($\text{R} = \text{Me}_3\text{Si}$, $\text{M} = \text{Ti}$, Zr , Hf)^[23–25] in the same manner. These molecules contain three-membered metallacycles that are considered^[10,22a] to be aromatic metallacyclopentene moieties with a delocalized 3c-2e π -bond system. This treatment is in accord with the negative NICS values^[10] and experimental $\nu(\text{C}=\text{C})$ frequencies in the IR and Raman spectra (Table 3), where the shift of the initial acetylenic $\nu(\text{C}\equiv\text{C})$ frequency ($\Delta\nu = 500\text{--}650\text{ cm}^{-1}$) is typical for strong complexation.^[15,22]

However, the AIM critical point search for $\text{Cp}^*_2\text{Ti}(\eta^2\text{-Me}_3\text{SiC}_2\text{SiMe}_3)$ (**6**) (Figure 6) and a model complex, $\text{Cp}_2\text{Ti}(\eta^2\text{-tBuC}_2\text{tBu})$, resulted in an ordinary pattern (Figure S4). Part of this molecular graph, which includes the three-membered metallacycle, is presented in Figure 7; it exhibits three (3,–1) BCPs on the two Ti–C bonds and the C=C bond, and no T-shaped situation is observed.

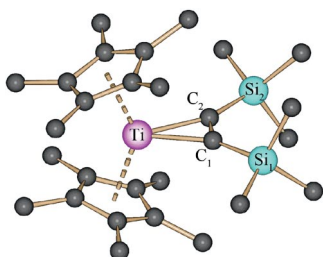


Figure 6. Structure of **6**.^[23]

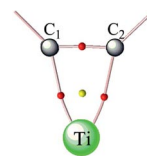


Figure 7. QTAIM molecular graph of **6**, which shows the three-membered metallacycle. Red circles = BCPs, yellow circle = ring CP.

It is notable that the values for the electron density at the BCP (ρ_b), which reflect bond orders, have close values for the central C2–C3 bond in the metallacyclocumulenes and for the C1–C2 bond in the metallacycloprenes (both bonds are considered to participate in 3c-2e π bonding). This is illustrated in Table 4, which shows Ti complexes as an example. Negative values for the Laplacian of the electron density at the bond critical point, $\nabla^2\rho_b$, for the C=C bonds correspond to a covalent nature, whereas positive values for the M–C bonds correspond to “intermediate” type nature.

Table 4. QTAIM topological parameters ρ_b [a.u.], $\nabla^2\rho_b$ [a.u.], and bond ellipticity (ϵ) for the Ti compounds studied.

Cyclocumulene $\text{Cp}_2\text{Ti}(\eta^4\text{-}t\text{BuC}_4t\text{Bu})$ (1)							
	C1–Ti	C2–Ti	C3–Ti	C4–Ti	C1–C2	C2–C3	C3–C4
ρ_b	0.0654		0.0692	0.0655	0.3370	0.3212	0.3336
$\nabla^2\rho_b$	0.1535		0.1970	0.1534	−0.8434	−0.8710	−0.8431
ε					0.099	0.133	0.099
Model cyclopropene $\text{Cp}_2\text{Ti}(\eta^2\text{-}t\text{BuC}_2t\text{Bu})$							
	C1–Ti			C2–Ti		C1–C2	
ρ_b	0.1010			0.1011		0.3481	
$\nabla^2\rho_b$	0.1297			0.1296		−0.9402	
ε						0.188	
Cyclopropene $\text{Cp}^*_2\text{Ti}(\eta^2\text{-Me}_3\text{SiC}_2\text{SiMe}_3)$ (6)							
	C1–Ti			C2–Ti		C1–C2	
ρ_b	0.0915			0.09616		0.3384	
$\nabla^2\rho_b$	0.1347			0.1347		−0.9111	
ε						0.0495	

Thus, in spite of the fact that the three-membered metallacycloprenes and the five-membered metallacyclocumulenes studied are both considered as aromatic and both include 3c-2e π -bond systems,^[9b,9c,10] they exhibit principally different AIM molecular graphs. The reason for the peculiar T-shaped AIM graphs obtained for the five-membered metallacycles **1–3** and **5**, which point to their topological instability, seems to be due to their unique dual, “chameleon” bonding nature that needs resonance structures to be invoked for their adequate description.

Conclusions

The system of three cumulated C=C bonds in the five-membered metallacycles of the complexes $\text{Cp}_2\text{M}(\eta^4\text{-tBuC}_4\text{tBu})$ [$\text{M} = \text{Ti}$ (**1**), Zr (**2**), Hf (**3**)] was shown to exhibit a peculiar pattern in Raman and IR spectra with three normal modes with frequencies at ca. 1850 (ν^s_1), 1650 (ν^{as}_2),

and 1280 cm⁻¹ (ν_{s3}). According to the results of normal coordinate analysis, the ν_{s1} mode is a symmetric stretch of the two equivalent C1–C2 and C3–C4 bonds with simultaneous contraction of the central C2–C3 bond. This mode manifests itself as a band of medium intensity in Raman, which is very weak in IR. The ν_{as2} mode is an antisymmetric stretch of the C1–C2 and C3–C4 bonds, which manifests itself as a weak feature in both Raman and IR. The ν_{s3} mode is a whole-molecule vibration of complex eigenvector and includes the “breathing” motion of the metallacycle with main contribution from the central C2–C3 bond. The corresponding band is rather intense in both spectra. Reconstruction of EDD in the molecules by using the AIM theory resulted in a specific molecular graph of the five-membered metallacycles with a T-shaped configuration, which indicated that the system is topologically unstable. This is in contrast to the ordinary molecular graph obtained for the three-membered cycle of related titanacycloprenes Cp₂Ti(η²-RC₂R).

Experimental Section

Synthesis: Cp₂M(η⁴-tBuC₄tBu)^[1–3] and Cp^{*}₂M(η²-Me₃SiC₂-SiMe₃)^[23–25] were synthesized according to published methods.

Vibrational Spectra: Raman spectra in the region 100–3700 cm⁻¹ were recorded with a Raman spectrometer of last-generation LabRAM with excitation at 632.8 nm from an He-Ne laser with an output power of ca. 5 mW. The samples were solids and saturated solutions in C₆D₆ sealed in capillaries. IR spectra were recorded in the region of 400–4000 cm⁻¹ with a Carl Zeiss M82 spectrophotometer and a Nicolet Magna IR-750 FTIR spectrometer. The samples were nujol mulls placed between KBr plates.

Computational Details: Quantum chemistry calculations of molecular geometry, normal-mode frequencies, eigenvectors in a harmonic approximation, and IR intensities were carried out with Gaussian 03^[26] at the DFT level of theory by using the PBE functional,^[27a] 6-311G(d,p)^[28] valence basis set for C, H, and Ti atoms, and cc-pVTZ-pp^[29] basis set with effective core potentials for Zr and Hf atoms. PED was computed with the NCA-99 program.^[30] QTAIM analysis, based on the results of quantum chemistry calculations at the DFT PBE0^[27b] level with 6-311G(d,p) basis set for C, H, and Ti atoms and UGBS^[31] for Zr and Hf atoms, was performed with the AIM2000 program.^[32]

Supporting Information (see footnote on the first page of this article): Complete QTAIM molecular graphs for **1**, **3**, and **6**; interatomic distances of **1–3** and their complete vibrational (Raman and IR) spectra with approximate assignments.

Acknowledgments

The authors are very grateful to Prof. K. A. Lyssenko for valuable discussions. Partial financial support from the Russian Foundation for Basic Research (project no.09-03-00503) is acknowledged.

- [1] a) U. Rosenthal, A. Ohff, W. Baumann, R. Kempe, A. Tillack, V. V. Burlakov, *Angew. Chem.* **1994**, *106*, 1678; *Angew. Chem. Int. Ed. Engl.* **1994**, *33*, 1605–1607; b) V. V. Burlakov, V. S. Bogdanov, K. A. Lyssenko, L. I. Strunkina, M. Kh. Minacheva,

- B. N. Strunin, U. Rosenthal, V. B. Shur, *Russ. Chem. Bull.* **2010**, *59*, 668–670.
- [2] V. V. Burlakov, A. Ohff, C. Lefebvre, A. Tillack, W. Baumann, R. Kempe, U. Rosenthal, *Chem. Ber.* **1995**, *128*, 967–971.
- [3] a) V. V. Burlakov, V. S. Bogdanov, K. A. Lyssenko, P. V. Petrovskii, T. Beweries, P. Arndt, U. Rosenthal, V. B. Shur, *Russ. Chem. Bull.* **2008**, *57*, 1319–1320; b) V. V. Burlakov, T. Beweries, V. S. Bogdanov, P. Arndt, W. Baumann, P. V. Petrovskii, A. Spannenberg, K. A. Lyssenko, V. B. Shur, U. Rosenthal, *Organometallics* **2009**, *28*, 2864–2870.
- [4] V. V. Burlakov, M. A. Bach, M. Klahn, P. Arndt, W. Baumann, A. Spannenberg, U. Rosenthal, *Macromol. Symp.* **2006**, *236*, 48–53.
- [5] a) P.-M. Pellny, F. Kirchbauer, V. V. Burlakov, W. Baumann, A. Spannenberg, U. Rosenthal, *J. Am. Chem. Soc.* **1999**, *121*, 8313–8323; b) P.-M. Pellny, F. G. Kirchbauer, V. V. Burlakov, W. Baumann, A. Spannenberg, U. Rosenthal, *Chem. Eur. J.* **2000**, *6*, 81–90; c) P.-M. Pellny, V. V. Burlakov, P. Arndt, W. Baumann, A. Spannenberg, U. Rosenthal, *J. Am. Chem. Soc.* **2000**, *122*, 6317–6318.
- [6] W. A. Chalifoux, R. McDonald, R. J. Ferguson, R. R. Tykwinski, *Angew. Chem.* **2009**, *121*, 8056; *Angew. Chem. Int. Ed.* **2009**, *48*, 7915–7919.
- [7] R. E. Bachman, A. Fiseha, S. K. Pollack, *J. Chem. Crystallogr.* **1999**, *29*, 457–462.
- [8] R. O. Angus, R. P. Johnson, *J. Org. Chem.* **1984**, *49*, 2880–2883.
- [9] a) E. D. Jemmis, A. K. Phukan, U. Rosenthal, *J. Organomet. Chem.* **2001**, *635*, 204–211; b) E. D. Jemmis, A. K. Phukan, H. Jiao, U. Rosenthal, *Organometallics* **2003**, *22*, 4958–4965; c) E. D. Jemmis, P. Parameswaran, A. K. Phukan, *Mol. Phys.* **2005**, *103*, 897–903.
- [10] E. D. Jemmis, S. Roy, V. V. Burlakov, H. Jiao, M. Klahn, S. Hansen, U. Rosenthal, *Organometallics* **2010**, *29*, 76–81.
- [11] K. Ch. Lam, Zh. Lin, *Organometallics* **2003**, *22*, 3466–3470.
- [12] a) U. Rosenthal, V. V. Burlakov, P. Arndt, W. Baumann, A. Spannenberg, *Organometallics* **2005**, *24*, 456–471; b) U. Rosenthal, V. V. Burlakov, M. A. Bach, T. Beweries, *Chem. Soc. Rev.* **2007**, *36*, 719–728.
- [13] a) R. F. W. Bader, *Atoms in Molecules: A Quantum Theory*, Clarendon Press, Oxford, **1990**, pp. 438; b) R. F. W. Bader, *Chem. Rev.* **1991**, *91*, 893–928.
- [14] B. V. Lokshin, E. M. Brainina, *Zh. Strukt. Khim.* **1971**, *12*, 1001–1006 (in Russian).
- [15] V. T. Alexanyan, B. V. Lokshin, “Vibrational Spectra of Transition Metal π-Complexes”, in *Molecular Structure and Chemical Bonding*, vol. 5, VINITI, Moscow, **1976** (in Russian).
- [16] E. Maslowsky, *Vibrational Spectra of Organometallic Compounds*, Wiley, New York, London, **1977**.
- [17] L. M. Sverdlov, M. A. Kovner, E. P. Krainov, *Vibrational Spectra of Polyatomic Molecules*, Nauka, Moscow, **1970** (in Russian).
- [18] I. Rozas, I. Alkorta, J. Elguero, *J. Phys. Chem. A* **1997**, *101*, 9457–9463.
- [19] S. J. Grabowski, J. M. Ugalde, *J. Phys. Chem. A* **2010**, *114*, 7223–7229.
- [20] Y. Tal, R. F. W. Bader, T. T. Nguyen-Dang, M. Ojha, S. G. Anderson, *J. Chem. Phys.* **1981**, *74*, 5162–5167.
- [21] a) D. Hashizume, N. Suzuki, T. Chihara, *Chem. Commun.* **2006**, 1233–35; b) N. Suzuki, D. Hashizume, *Coord. Chem. Rev.* **2010**, *254*, 1307–1326.
- [22] a) V. B. Shur, V. V. Burlakov, M. E. Vol’pin, *J. Organomet. Chem.* **1988**, *347*, 77–83; b) U. Rosenthal, V. V. Burlakov, P. Arndt, W. Baumann, A. Spannenberg, *Organometallics* **2003**, *22*, 884–900 and references cited therein.
- [23] V. V. Burlakov, A. V. Polyakov, A. I. Yanovsky, Yu. T. Struchkov, V. B. Shur, M. E. Vol’pin, U. Rosenthal, H. Görls, *J. Organomet. Chem.* **1994**, *476*, 197–206.
- [24] J. Hiller, U. Thewalt, M. Polásek, L. Petrusová, V. Varga, P. Sedmera, K. Mach, *Organometallics* **1996**, *15*, 3752–3759.

- [25] T. Beweries, V. V. Burlakov, M. A. Bach, P. Arndt, W. Baumann, A. Spannenberg, U. Rosenthal, *Organometallics* **2007**, *26*, 247–249.
- [26] M. J. Frisch, G. W. Trucks, H. B. Schlegel, G. E. Scuseria, M. A. Robb, J. R. Cheeseman, J. A. Montgomery Jr., T. Vreven, K. N. Kudin, J. C. Burant, J. M. Millam, S. S. Iyengar, J. Tomasi, V. Barone, B. Mennucci, M. Cossi, G. Scalmani, N. Rega, G. A. Petersson, H. Nakatsuji, M. Hada, M. Ehara, K. Toyota, R. Fukuda, J. Hasegawa, M. Ishida, T. Nakajima, Y. Honda, O. Kitao, H. Nakai, M. Klene, X. Li, J. E. Knox, H. P. Hratchian, J. B. Cross, V. Bakken, C. Adamo, J. Jaramillo, R. Gomperts, R. E. Stratmann, O. Yazyev, A. J. Austin, R. Cammi, C. Pomelli, J. W. Ochterski, P. Y. Ayala, K. Morokuma, G. A. Voth, P. Salvador, J. J. Dannenberg, V. G. Zakrzewski, S. Dapprich, A. D. Daniels, M. C. Strain, O. Farkas, D. K. Malick, A. D. Rabuck, K. Raghavachari, J. B. Foresman, J. V. Ortiz, Q. Cui, A. G. Baboul, S. Clifford, J. Cioslowski, B. B. Stefanov, G. Liu, A. Liashenko, P. Piskorz, I. Komaromi, R. L. Martin, D. J. Fox, T. Keith, M. A. Al-Laham, C. Y. Peng, A. Nanayakkara, M. Challacombe, P. M. W. Gill, B. Johnson, W. Chen, M. W. Wong, C. Gonzalez, J. A. Pople, *Gaussian 03*, Revision E.01, Gaussian, Inc., Wallingford, CT, **2004**.
- [27] a) J. P. Perdew, K. Burke, M. Ernzerhof, *Phys. Rev. Lett.* **1996**, *77*, 3865–3868; b) J. P. Perdew, K. Burke, M. Ernzerhof, *Phys. Rev. Lett.* **1997**, *78*, 1396.
- [28] a) R. Krishnan, J. S. Binkley, R. Seeger, J. A. Pople, *J. Chem. Phys.* **1980**, *72*, 650–654; b) A. D. McLean, G. S. Chandler, *J. Chem. Phys.* **1980**, *72*, 5639–5648.
- [29] a) K. A. Peterson, D. Figgen, M. Dolg, H. Stoll, *J. Chem. Phys.* **2007**, *126*, 124101–124112; b) D. Figgen, K. A. Peterson, M. Dolg, H. Stoll, *J. Chem. Phys.* **2009**, *130*, 164108–164112.
- [30] V. A. Sipachev, *Theochem* **1985**, *121*, 143.
- [31] a) E. V. R. de Castro, F. E. Jorge, *J. Chem. Phys.* **1998**, *108*, 5225–5229; b) F. E. Jorge, E. V. R. de Castro, A. B. F. da Silva, *J. Comput. Chem.* **1997**, *18*, 1565–1569; c) F. E. Jorge, E. V. R. de Castro, A. B. F. da Silva, *Chem. Phys.* **1997**, *216*, 317–321; d) A. B. F. da Silva, H. F. M. da Costa, M. Trsic, *Mol. Phys.* **1989**, *68*, 433–445; e) H. F. M. da Costa, M. Trsic, J. R. Mohallem, *Mol. Phys.* **1987**, *62*, 91–95; f) J. R. Mohallem, M. Trsic, *J. Chem. Phys.* **1987**, *86*, 5043–5044; g) J. R. Mohallem, R. M. Dreizler, M. Trsic, *Int. J. Quantum Chem. Symp.* **1986**, *20*, 45–55; h) D. M. Silver, W. C. Nieuwpoort, *Chem. Phys. Lett.* **1978**, *57*, 421–422; i) D. M. Silver, S. Wilson, W. C. Nieuwpoort, *Int. J. Quantum Chem.* **1978**, *14*, 635–639.
- [32] Update to the AIM2000 – Program for Atoms in Molecules: F. Biegler-König, J. Schonbohm, *J. Comput. Chem.* **2002**, *23*, 1489.

Received: October 10, 2011

Published Online: January 25, 2012

Ruthenium(III) Cyclometalates Obtained by Site-Specific Orthometallation and Their Reactivity with Nitric Oxide: Photoinduced Release and Estimation of NO Liberated from the Ruthenium Nitrosyl Complexes

Kaushik Ghosh,^{*,[a]} Sushil Kumar,^[a] Rajan Kumar,^[a] and Udai P. Singh^[a]

Keywords: Ruthenium / Redox chemistry / Metalation / Photolability

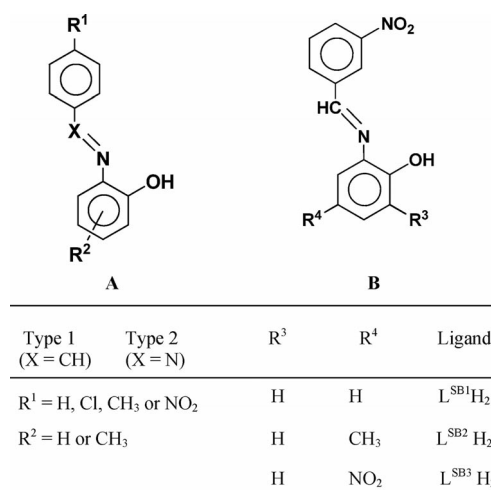
Cyclometalated Ru^{III} complexes [Ru(L^{SB1})(PPh₃)₂Cl] (**1**), [L^{SB1}H₂ = 2-(3-nitrobenzylideneamino)phenol], and [Ru(L^{SB2})(PPh₃)₂Cl] (**2**), [L^{SB2}H₂ = 4-methyl-2-(3-nitrobenzylideneamino)phenol and H = dissociable protons], were synthesized by site-specific orthometallation and characterized by spectroscopic and electrochemical studies. Complexes **1** and **2** were treated with in situ generated nitric oxide (NO), derived from an acidified nitrite solution, which afforded the ruthenium nitrosyl complexes [Ru(L^{SB3}H)(PPh₃)₂(NO)Cl](ClO₄) (**1a**) and [Ru(L^{BOX})(PPh₃)₂(NO)Cl](ClO₄) (**2a**), respectively, [L^{SB3}H₂ = 4-nitro-2-(3-nitrobenzylideneamino)phenol, L^{BOX}H = 5-methyl-7-nitro-2-(3-nitrophenyl)benzoxazole and H = dissociable protons]. Complexes **1a** and **2a** were found to be diamagnetic and were characterized by ¹H

NMR and ³¹P NMR spectral studies. Both **1a** and **2a** exhibited ν_{NO} in the range 1800–1835 cm⁻¹ in the IR spectra. Molecular structures of σ -aryl ruthenium nitrosyl complexes **1a**·CH₃OH·2CH₂Cl₂·H₂O and **2a**·2CH₂Cl₂ were determined by X-ray crystallography. Nitrosylation at the metal centre, oxidative cyclization and ligand nitration were authenticated from the crystal structures. The redox properties of the metal centre were investigated. In both the nitrosyl complexes **1a** and **2a**, coordinated NO was found to be photolabile. The amount of photoreleased NO was estimated by using the Griess reagent and the data was compared with that obtained from sodium nitroprusside (SNP). The role of the nitro group in the ligand frame was discussed with regard to orthometallation, NO reactivity and photolability.

Introduction

Organometallic ruthenium cyclometalates incorporating trivalent ruthenium are scarce.^[1–6] An investigation of the literature of trivalent ruthenium organometallic complexes revealed that the complexes are formed through C–H activation and the concomitant formation of a σ -aryl ruthenium–carbon bond. It has been found that in the case of ruthenium(III) cyclometalates derived from Schiff-base ligands, the metal–carbon bond is established through orthometallation with the phenyl ring that has an aldehyde functional group, see Scheme 1 (A), X = CH, Type 1.^[3] On the other hand, there is another group of structurally similar complexes where instead of azomethine nitrogen, the azo function is bound to the Ru^{III} centre. In these types of complexes, orthometallation is observed with the ring that has been contributed by the aromatic amine during the azo coupling reaction, as shown in Scheme 1 (A), X = N, Type 2.^[4,6] In both cases either *para*-substituted benzaldehyde, during Schiff-base formation, or *para*-substituted aromatic amines were used during the ligand synthesis. Hence, for the synthesis of the ruthenium complexes, a single site for orthometallation was found to be available in both the type

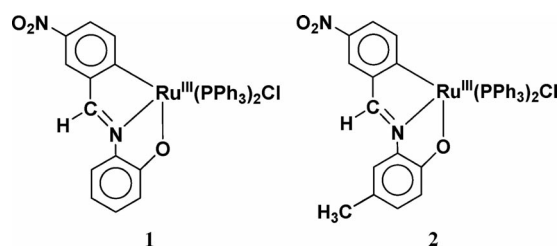
1 and type 2 ligands. To the best of our knowledge, there is no report in the literature where a type 1 or type 2 ligand was used to provide more than one site for the metal centre to establish a ruthenium–carbon bond during the synthesis of ruthenium cyclometalates. Hence, in this endeavour, we have chosen Schiff-base ligands derived from *m*-nitrobenzaldehyde and 2-aminophenol and substituted 2-aminophenol [shown in Scheme 1 (B)] to investigate the mode of σ -aryl ruthenium–carbon bond formation.



Scheme 1.

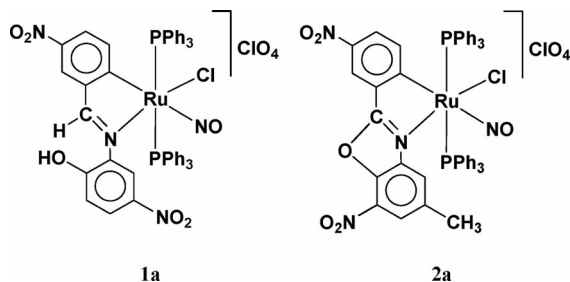
[a] Department of Chemistry, Indian Institute of Technology, Roorkee, Roorkee 247667, Uttarakhand, India
Fax: +91-1332-273560
E-mail: ghoshfey@iitr.ernet.in

Synthesis and characterization of ruthenium nitrosyl complexes and studies on the generation of nitric oxide (NO) on demand have received considerable attention.^[7–9] An investigation of the literature revealed that there is no report on the reactivity of nitric oxide with ruthenium cyclometalates incorporating trivalent ruthenium. To the best of our knowledge, a single report by Crutchley and coworkers^[5] is available in the literature, however, the nitrosyl complex was not utilized for the generation of NO. This work stems from our interest to synthesize novel ruthenium nitrosyl complexes derived from these ruthenium cyclometalates. In recent reports, we have described the role of *trans*-directing carbanion in the coordination and photolability of NO.^[10,11] Moreover, we have observed the effect of substituents on the phenyl ring containing the phenolato function. In our previous reports, we always used *para*-substituted benzaldehydes for the synthesis of Schiff bases and the effect of the substituent on the phenyl ring containing the aldehyde function was not discussed. Hence, *meta*-substituted benzaldehyde has never been used for the synthesis of ruthenium cyclometalates (*vide supra*) as well as ruthenium nitrosyl complexes derived from those cyclometalates. Herein we report on the synthesis and characterization of ruthenium cyclometalates [Ru(L^{SB1})(PPh₃)₂Cl] (**1**) [where L^{SB1}H₂ is 2-(3-nitrobenzylideneamino)phenol] and [Ru(L^{SB2})(PPh₃)₂Cl] (**2**) [where L^{SB2}H₂ is 4-methyl-2-(3-nitrobenzylideneamino)phenol] [H is the dissociable proton, Scheme 1 (B)] derived from Schiff-base ligands L^{SB1}H₂ and L^{SB2}H₂, respectively, and their site-specific orthometallation (Scheme 2).



Scheme 2.

The interaction of NO with these organometallic ruthenium complexes was investigated and the resultant complexes [Ru(L^{SB3}H)(PPh₃)₂(NO)Cl](ClO₄) (**1a**) and [Ru(L^{BOX})(PPh₃)₂(NO)Cl](ClO₄) (**2a**) [L^{SB3}H₂ = 4-nitro-2-(3-nitrobenzylideneamino)phenol, L^{BOX}H = 5-methyl-7-nitro-2-(3-nitrophenyl)benzoxazole and H = dissociable protons] were synthesized and characterized (Scheme 3).



Scheme 3.

Molecular structures of **1a**·CH₃OH·2CH₂Cl₂·H₂O and **2a**·2CH₂Cl₂ were determined by X-ray crystallography. The redox properties of the metal centre in these complexes were investigated in order to better understand the stabilization of the ruthenium oxidation state after orthometallation. The photolability of coordinated NO was authenticated by UV/Vis spectral studies and liberated NO was trapped by reduced myoglobin. Photoreleased NO was not estimated in our previous reports,^[10,11] however, in this report we estimated NO after photodissociation by a Griess reagent using visible as well as UV light. Sodium nitroprusside (SNP), which is utilized for the treatment of cardiovascular disorder and blood pressure regulation through the release of NO,^[12–14] was used as the standard.

The role of the electron-withdrawing –NO₂ group on the phenyl ring, ligated to the metal centre through a σ-aryl bond, will be discussed in the context of light-induced delivery of nitric oxide.

Results and Discussion

Synthesis

The complexes [Ru(L^{SB1})(PPh₃)₂Cl] (**1**) and [Ru(L^{SB2})(PPh₃)₂Cl] (**2**) were synthesized by the reaction of Ru(PPh₃)₃Cl₂ with the Schiff base ligands L^{SB1}H₂ and L^{SB2}H₂, respectively, in ethanol.^[3] Complexes **1** and **2** (Scheme 2) were red-brown in colour and both complexes were isolated in good yield. They were highly soluble in dichloromethane and benzene but were much less soluble in polar solvents like water and methanol. Dichloromethane solutions of **1** and **2** were treated with in situ generated NO derived from an acidified nitrite (NaNO₂) solution with continuous stirring for 2 h.^[10] The red-brown colour of the solution disappeared and the formation of an orange-yellow colour was observed. A methanolic solution of NaClO₄ was added to provide ClO₄[–] ions to stabilize the large cationic ruthenium nitrosyl complexes. [Ru(L^{SB3}H)(PPh₃)₂(NO)Cl](ClO₄) (**1a**) and [Ru(L^{BOX})(PPh₃)₂(NO)Cl](ClO₄) (**2a**) (Scheme 3) were derived from **1** and **2**, respectively. Both the nitrosyl complexes **1a** and **2a** were recrystallized from a dichloromethane/methanol mixture. Complexes **1a** and **2a** were highly soluble in organic solvents like dichloromethane, acetonitrile, dimethylformamide and methanol, however, lower solubility was observed in water.

Description of Structures

The molecular structures of complexes [Ru(L^{SB3}H)(PPh₃)₂(NO)Cl](ClO₄)·CH₃OH·2CH₂Cl₂·H₂O (**1a**·CH₃OH·2CH₂Cl₂·H₂O) and [Ru(L^{BOX})(PPh₃)₂(NO)Cl](ClO₄)·2CH₂Cl₂ (**2a**·2CH₂Cl₂) are depicted in Figure 1 and Figure 2, respectively. The matrix parameters of these complexes are described in Table 4 and the selected bond lengths and bond angles are given in Table 1.

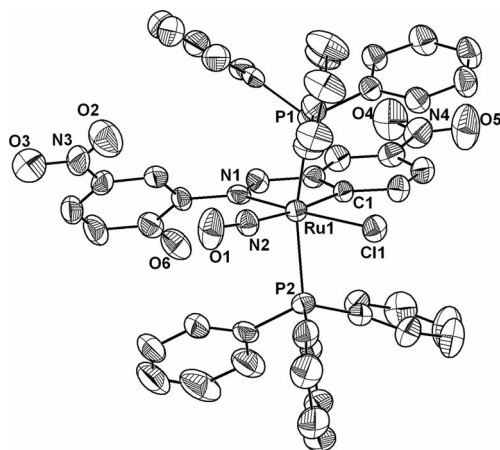


Figure 1. ORTEP diagram (50% probability level) of the cation of the complex $[\text{Ru}(\text{L}^{\text{SB}^3\text{H}})(\text{PPh}_3)_2(\text{NO})\text{Cl}](\text{ClO}_4) \cdot \text{CH}_3\text{OH} \cdot 2\text{CH}_2\text{Cl}_2 \cdot \text{H}_2\text{O}$ (**1a**· $\text{CH}_3\text{OH} \cdot 2\text{CH}_2\text{Cl}_2 \cdot \text{H}_2\text{O}$). All hydrogen atoms and solvent molecules are omitted for clarity.

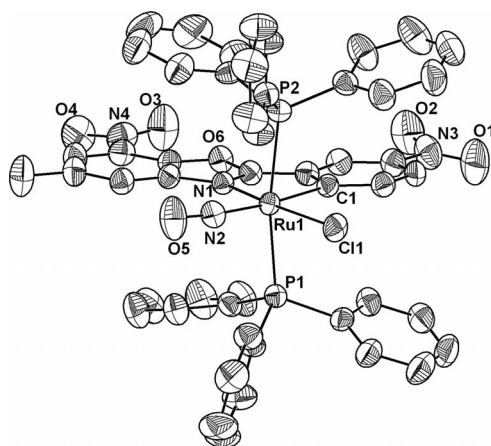


Figure 2. ORTEP diagram (50% probability level) of the cation of the complex $[\text{Ru}(\text{L}^{\text{BOX}})(\text{PPh}_3)_2(\text{NO})\text{Cl}](\text{ClO}_4) \cdot 2\text{CH}_2\text{Cl}_2$ (**2a**· $2\text{CH}_2\text{Cl}_2$). All hydrogen atoms and solvent molecules are omitted for clarity.

In the molecular structure of **1a**· $\text{CH}_3\text{OH} \cdot 2\text{CH}_2\text{Cl}_2 \cdot \text{H}_2\text{O}$, carbanion (C1), Cl(1), NO and the imine nitrogen (N1) constitute the equatorial plane whereas the phosphane groups occupy the axial positions *trans* to each other. So, the geometry around the metal centre is found to be distorted octahedral. Interestingly, in **1a**· $\text{CH}_3\text{OH} \cdot 2\text{CH}_2\text{Cl}_2 \cdot \text{H}_2\text{O}$, the phenolato oxygen is not bound to the metal centre and protonation gave rise to a phenolic –OH function, which was consistent with our ^1H NMR spectroscopic data (vide infra). Hence, in this structure we observed that the tridentate ligand in the precursor complex **1** became bidentate in the σ -aryl ruthenium nitrosyl complex **1a**· $\text{CH}_3\text{OH} \cdot 2\text{CH}_2\text{Cl}_2 \cdot \text{H}_2\text{O}$. The tilting of the phenyl ring containing a phenolato function afforded a dihedral angle of ca. 47° with the ligand binding plane. Moreover, ligand nitration was observed on the phenyl ring containing the phenolato function and the site of nitration was *trans* to the phenolato function.

Table 1. Selected bond lengths and bond angles of complexes $[\text{Ru}(\text{L}^{\text{SB}^3\text{H}})(\text{PPh}_3)_2(\text{NO})\text{Cl}](\text{ClO}_4) \cdot \text{CH}_3\text{OH} \cdot 2\text{CH}_2\text{Cl}_2 \cdot \text{H}_2\text{O}$ (**1a**· $\text{CH}_3\text{OH} \cdot 2\text{CH}_2\text{Cl}_2 \cdot \text{H}_2\text{O}$) and $[\text{Ru}(\text{L}^{\text{BOX}})(\text{PPh}_3)_2(\text{NO})\text{Cl}](\text{ClO}_4) \cdot 2\text{CH}_2\text{Cl}_2$ (**2a**· $2\text{CH}_2\text{Cl}_2$).

Bond lengths [Å]		Bond angles [°]	
1a·CH ₃ OH·2CH ₂ Cl ₂ ·H ₂ O			
Ru(1)–Cl(1)	2.3755(10)	N(2)–Ru(1)–C(1)	170.81(10)
Ru(1)–P(1)	2.4651(11)	N(2)–Ru(1)–Cl(1)	100.64(8)
Ru(1)–P(2)	2.4425(10)	C(1)–Ru(1)–Cl(1)	88.38(8)
Ru(1)–C(1)	2.100(2)	N(2)–Ru(1)–P(1)	93.76(7)
Ru(1)–N(2)	1.799(2)	N(1)–Ru(1)–P(1)	95.66(6)
Ru(1)–N(1)	2.137(2)	C(1)–Ru(1)–P(1)	85.07(7)
N(2)–O(1)	1.152(3)	P(1)–Ru(1)–P(2)	168.04(3)
		O(1)–N(2)–Ru(1)	170.90(2)
2a·2CH ₂ Cl ₂			
Ru(1)–Cl(1)	2.3534(11)	N(1)–Ru(1)–C(1)	77.84(15)
Ru(1)–P(1)	2.4435(12)	N(2)–Ru(1)–Cl(1)	97.47(12)
Ru(1)–P(2)	2.4306(12)	C(1)–Ru(1)–Cl(1)	91.30(12)
Ru(1)–C(1)	2.108(4)	C(1)–Ru(1)–P(1)	86.63(12)
Ru(1)–N(1)	2.105(3)	Cl(1)–Ru(1)–P(2)	90.23(4)
Ru(1)–N(2)	1.786(4)	P(1)–Ru(1)–P(2)	169.78(4)
N(2)–O(5)	1.140(5)	O(5)–N(2)–Ru(1)	170.90(4)

The molecular structure of the nitrosyl complex **2a**· $2\text{CH}_2\text{Cl}_2$ is different from that of **1a**· $\text{CH}_3\text{OH} \cdot 2\text{CH}_2\text{Cl}_2 \cdot \text{H}_2\text{O}$ in certain aspects. Similar to the previous structure, it has been found out that the phenolato function is not attached to the ruthenium centre and that the ligand is chelated in a bidentate fashion, however, in the case of **2a**· $2\text{CH}_2\text{Cl}_2$ oxidative cyclization^[10] was observed.

The carbanion (C1) and imine nitrogen (N1) from the substituted 2-phenylbenzoxazole moiety along with the Cl[–] and NO ligands constitute the equatorial plane whereas the two *trans*-PPh₃ groups are found at the axial positions. The P1–Ru1–P2, N1–Ru1–Cl1 and C1–Ru1–N2 angles indicate a distorted octahedral geometry around the metal centre. On the other hand in **2a**· $2\text{CH}_2\text{Cl}_2$ oxidative cyclization and benzoxazole formation was observed. Hence phenolato –OH is not present in the molecule and the ring with the phenolato function is found to be in the plane with the ligand. For this we did not find any –OH peak in the ^1H NMR spectrum. The presence of *trans*-PPh₃ groups in both the complexes is consistent with the ^{31}P NMR spectroscopic data (vide infra).^[15,16]

In both the nitrosyl complexes, Ru–N_{NO} distances [1.799(2) Å in **1a**· $\text{CH}_3\text{OH} \cdot 2\text{CH}_2\text{Cl}_2 \cdot \text{H}_2\text{O}$ and 1.786(4) Å in **2a**· $2\text{CH}_2\text{Cl}_2$] were found to be longer than those reported,^[17–19] which may be due to the *trans* effect of carbanion (C1).^[4,6] However, this value was close to the value reported by Crutchley and coworkers.^[5] The N–O distance in both the complexes was found to be consistent with the values given in the literature.^[16–18] All these data along with Ru–N–O angles ($\approx 171^\circ$) in **1a**· $\text{CH}_3\text{OH} \cdot 2\text{CH}_2\text{Cl}_2 \cdot \text{H}_2\text{O}$ and **2a**· $2\text{CH}_2\text{Cl}_2$ clearly show a {Ru^{II}–NO⁺}⁶ description^[7] of the {Ru–NO}⁶ moiety.^[20] This is also supported by IR spectroscopic data described in the next section.

The noncovalent interactions are very important in supramolecular chemistry and crystal engineering.^[21] The interactions found in **1a**· $\text{CH}_3\text{OH} \cdot 2\text{CH}_2\text{Cl}_2 \cdot \text{H}_2\text{O}$ and

2a·2CH₂Cl₂ are hydrogen bonding and are described in Table S1 and the interactions are shown in Figure S5–Figure S7 in the Supporting Information.

Molecular structures of **1a**·CH₃OH·2CH₂Cl₂·H₂O and **2a**·2CH₂Cl₂ clearly authenticated that nitrosylation and the ligand nitration were two events that were common in both cases during our NO interaction studies.

The sites for nitration were different in the two cases; this occurs because the preferred *para* position (with respect to the phenolato function)^[22] for nitration was blocked by the methyl group in complex **2a**. However, for complex **2a** the oxidative cyclization and formation of the benzoxazole derivative showed a rare type of reactivity of NO with this family of complexes (vide infra).

Spectroscopic Studies

Complexes **1** and **2** are red-brown in colour and the electronic spectra in dichloromethane are displayed in Figure S8. It has been found^[3,10] that organometallic ruthenium complexes derived from type 1 ligands exhibit different colours from the change of substituents on the phenyl ring containing an aldehyde function. Complex **1** afforded two charge-transfer bands near 475 nm and 585 nm. On the other hand, the electronic spectrum of **2** gave rise to charge-transfer bands near 580 nm and 600 nm. These bands are probably a result of the ligand-to-metal charge transfer (LMCT) transition.^[1–3,6] The electronic absorption spectra of complexes **1a** and **2a** (shown in Figure S9) exhibit one strong band near 312 nm along with a shoulder near 385 nm. These bands are probably from the charge-transfer transitions.^[11]

The infrared spectra of all the complexes exhibit a band near 1590 cm^{–1} corresponding to the azomethine ($\nu_{C=N}$) stretching frequency, which is similar to the value reported by Chakravorty and coworkers.^[3]

The presence of the {Ru–NO}⁶ moiety^[10,11] in both the nitrosyl complexes was also confirmed by the characteristic peaks in the infrared spectra. Complexes **1a** and **2a** have N–O stretching frequencies (ν_{NO}) near 1810 cm^{–1} and 1835 cm^{–1}, respectively. These values clearly indicate the presence of NO⁺ bound to the Ru^{II} centre and a description of {Ru^{II}–NO⁺}⁶ for the {Ru–NO}⁶ moiety present in **1a** and **2a** is proposed.^[7] This is also supported by the data obtained from their crystal structures (vide supra). The peaks around 1090 cm^{–1} and 623 cm^{–1} show the presence of perchlorate ion in the complexes **1a** and **2a**, respectively. These complexes also afforded new bands in the range between 1290 and 1380 cm^{–1} and these bands are probably from the ring nitration (shown in the Supporting Information). In all the complexes, the peaks near 745 cm^{–1}, 695 cm^{–1} and 520 cm^{–1} show the presence of PPh₃ groups.^[1,2,6,11]

The nitrosylation of the metal centre in the ruthenium cyclometalates **1a** and **2a** afforded clean NMR spectra that confirmed the diamagnetic behaviour of complexes with an *S* = 0 ground state. In the ¹H NMR spectrum of **1a** (shown in Figure S10), the peak at δ = 11.84 ppm indicates the pres-

ence of a phenolic O–H proton. This peak disappeared after shaking the NMR sample solution in D₂O, which supported the presence of an exchangeable proton in the –OH functional group (Figure S14).^[11,23] These data supported a dissociation of the Ru–O_{Ph} bond during NO coordination in **1a**.

The ¹H NMR spectrum of **2a** clearly shows the presence of the methyl protons at ca. 2.5 ppm along with other protons present in the complex. Interestingly, no peak was found above 10.0 ppm, which indicates the absence of a phenolic O–H proton in complex **2a**. This data was consistent with our findings from structural calculations by X-ray crystallography and supported oxidative cyclization during the NO interaction. ³¹P NMR spectra of the complexes **1a** and **2a** in CD₃CN indicate a single peak at about 20 ppm and ca. 18 ppm, respectively, confirming the *trans* disposition of the PPh₃ groups.^[15,16]

Site Specific Orthometallation: A Reaction Model

The reaction of Schiff-base ligands with Ru(PPh₃)₃Cl₂ afforded organometallic ruthenium cyclometalates through orthometallation. Considering the orientation of the phenyl ring of *m*-nitrobenzaldehyde (Scheme 1, B), there are two possible sites for orthometallation. A crucial point for this reaction is that we ended up with a single product during the preparation of ruthenium cyclometalates and interestingly, after orthometallation the nitro group was found to be at a *para* position with respect to the Ru–C bond. It is reported in the literature that during orthometallation the metal centre could act as a nucleophile or an electrophile.^[24–26] In the present study, the C–H bond activation seems to proceed by electrophilic attack on the aryl ring by the metal centre. The –I as well as –R effect of the –NO₂ group will decrease the electron density at the *ortho* and *para* positions, however, the effect at the *para* position will be lower compared to that at the *ortho* position. We speculate that the orthometallation occurred at the position *para* to the –NO₂ group, which had better electron density compared with the *ortho* position. Moreover, stability of the resultant complexes **1** and **2** may be obtained by keeping the –NO₂ group at the *para* position with respect to the Ru–C bond (vide infra).

Electrochemistry

The redox property of the metal centre was measured by cyclic voltammetry (Figure 3) in a dichloromethane solution using 0.1 M TBAP as the supporting electrolyte. Complex **1** exhibits quasi-reversible redox couples and *E*_{1/2} values are found to be at –0.42 V and +0.80 V vs. Ag/AgCl. However, these two values for complex **2** are at –0.44 V and +0.72 V vs. Ag/AgCl [Figure 3 (a)]. The redox couples at the negative potential in **1** and **2** are assigned to the Ru^{III}–Ru^{II} couple and those at the positive potential in both the complexes are described as a Ru^{III}–Ru^{IV} couple.^[1–4] The cyclic voltammetric data for the complexes are given in Table 2.

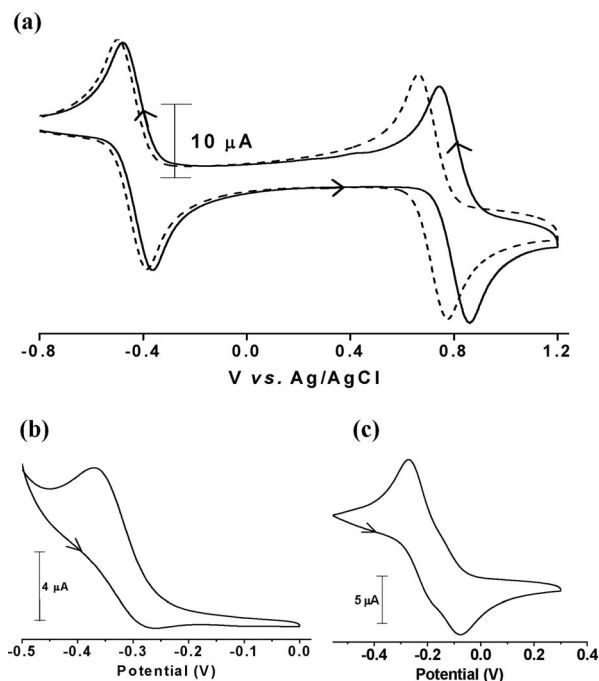


Figure 3. Cyclic voltammograms of 10^{-3} M solutions of (a) complex **1** (solid line) and complex **2** (dashed line). (b) Complex **1a** and (c) complex **2a** in dichloromethane, in the presence of 0.1 M tetrabutylammonium perchlorate (TBAP), using a working electrode (glassy-carbon), reference electrode (Ag/AgCl) and auxiliary electrode (platinum wire), scan rate = 0.1 V s^{-1} .

Table 2. Cyclic voltammetric data for complexes at 298 K. Conditions: solvent dichloromethane; supporting electrolyte TBAP (0.1 M); working electrode glassy carbon; reference electrode Ag/AgCl; scan rate 0.1 V s^{-1} ; concentration 10^{-3} M.

Complex	$E_{1/2}$ [V] ^[a] (ΔE_p [mV]) ^[b]	
	Ru ^{III} –Ru ^{II}	Ru ^{III} –Ru ^{IV}
1	−0.42 (117)	+0.80 (118)
2	−0.44 (109)	+0.72 (114)
1a	−0.32 (102)	—
2a	−0.18 (190)	—

[a] $E_{1/2} = 0.5 (E_{pa} + E_{pc})$ and [b] $\Delta E_p = (E_{pa} - E_{pc})$, where E_{pa} and E_{pc} are the anodic and cathodic peak potentials, respectively.

We have compared these $E_{1/2}$ values with the data reported by Chakravorty and coworkers (especially for complexes **5** and **5a** in that report).^[3] A comparison of the $E_{1/2}$ values for the Ru^{III}–Ru^{II} redox couple clearly indicate better stabilization of the Ru^{II} in complexes **1** and **2**. It is important to note here that in this report because of orthometallation, the nitro group was situated *para* to the carbanion that was involved in Ru–C bond formation. On the other hand, in the above report^[3] the nitro group was found to be at the *meta* position with respect to the carbanion. Hence, the presence of the $-\text{NO}_2$ group in the *para* position with respect to the Ru–C bond is probably responsible for the better stabilization of ruthenium(II) in this class of organometallic ruthenium cyclometalates.

In both the nitrosyl complexes **1a** and **2a**, quasi-reversible cyclic voltammograms are obtained [shown in Figure 3(b) and (c)] with $E_{1/2}$ values of -0.32 V and -0.18 V vs.

Ag/AgCl, respectively. Hence in the nitrosyl complexes we found better stabilization of Ru^{II}. In the precursor complexes (**1** and **2**) we have determined the effect of the position of the nitro group on the phenyl ring, which was attached to the ruthenium centre through a σ -aryl Ru–C bond. This prompted us to examine the stabilization of ruthenium(II) in complexes **1a** and **2a** resulting from the change in position of the $-\text{NO}_2$ group in the ligand frame. A small decrease in the negative potential was obtained for complex **2a** compared with a similar complex reported recently.^[10] After examination of electrochemical data of this report and our previous report,^[10] we found that $E_{1/2}$ values for the Ru^{II}/Ru^{III} couple were near -0.20 V vs. Ag/AgCl for those complexes where oxidative cyclization has occurred. Other complexes, where we did not find the cyclization, afforded the same value in the range -0.30 V to -0.40 V vs. Ag/AgCl.

Photolysis Experiments of Nitrosyls

The photolability of coordinated NO of σ -aryl ruthenium nitrosyl complexes was examined in dichloromethane (for **1a**) and acetonitrile solutions (for **2a**). Solutions of the

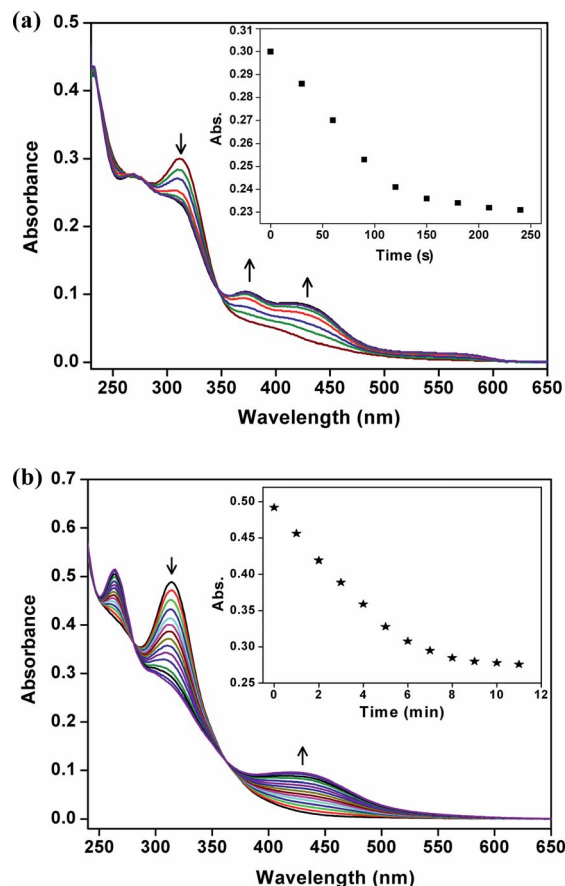


Figure 4. Photodissociation of (a) complex **1a** (ca. $1.1 \times 10^{-5} \text{ M}$) in dichloromethane and (b) complex **2a** (ca. $1.8 \times 10^{-5} \text{ M}$) in CH_3CN under illumination with a 100 W tungsten lamp. Repetitive scans were taken at 30 s intervals for **1a** and at 1 min intervals for **2a**. Inset: Time-dependent changes in absorbance at $\lambda = 311 \text{ nm}$ and $\lambda = 314 \text{ nm}$ for **1a** and **2a**, respectively.

complexes were stable in the dark, however, when these solutions were exposed to visible light (100 W tungsten lamp), a rapid change in colour from orange-yellow to red-brown was observed.

Spectral changes upon irradiation of a solution of **1a** ($\approx 10^{-5}$ M) in dichloromethane with a 100 W tungsten lamp are shown in Figure 4(a) and the spectral changes give rise to three clear isosbestic points near 265 nm, 280 nm and 350 nm. Interestingly we observed that after the photolysis experiment of **1a**, the electronic absorption spectrum of the resulting solution was similar to the spectrum of **1**. This prompted us to characterize the resultant complex after the photocleavage reaction. The resultant complex was characterized by spectroscopic and electrochemical studies (shown in the Supporting Information, Figure S15). The data indicated the formation of ligand nitrated **1** (**1b**). This complex (**1b**) also reacts with nitric oxide and liberates NO under photolytic conditions (Scheme S1). Similar spectral changes were also observed with complex **2a** in an acetonitrile [shown in Figure 4(b)] solution. In this case, the isosbestic points are near 278 nm and 360 nm. A comparison of the data displayed in the inset clearly shows that in the presence of visible light, the release of NO in **2a** is slower than that for **1a**.

Transfer of NO to Myoglobin

The photocleavage of the coordinated NO was also confirmed by trapping the liberated NO by reduced myoglobin (shown in Figure S16). When an acetonitrile solution of complex **1a** was added to a buffer solution of reduced myoglobin under dark conditions no reaction was observed. However, when the same mixture was exposed to a tungsten lamp (100 W) for 2–3 min, its absorption spectrum at 420 nm showed the formation of a Mb–NO adduct.^[11,27]

Determination of the Concentration of NO by Griess Reaction

The amount of NO released by the complexes **1a** and **2a**, synthesized in this report, was determined by using the Griess reagent.^[28] We prepared the standard curve with different concentrations of NaNO₂ (5–50 μ M) in solution (shown in Figure S18). From the molar extinction coefficient of dye (at 540 nm, $\epsilon = 41000 \text{ M}^{-1} \text{ cm}^{-1}$)^[29] the NaNO₂ standard curve predicted that the concentration of NO generated from an acidified nitrite solution was the concentration of NaNO₂ ($\pm 5 \mu$ M). The change in the absorbance of the dye (produced by the Griess reaction) in the dark as well as in the presence of light (UV and visible) clearly expressed the presence of photolabile NO in the nitrosyl complexes and this observation also supported our previous experiments, namely electronic absorption spectral studies (Figure 4) and trapping of NO by reduced myoglobin (Figure S16). The generation of a peak near 538 nm clearly indicates the formation of NO in solution. Hence, we could predict that photolabile coordinated NO was responsible for the change in absorbance at the same wavelength. It is

important to mention here that in the dark we observed little change in absorbance at 538 nm, which indicated the loss of NO from **1a** and **2a**. The loss of NO was found to be ca. 1.5% with respect to the concentration of the complexes (50 μ M) in solution. Using 50 μ M of both of the complexes **1a** and **2a**, we found that in the dark the concentration of

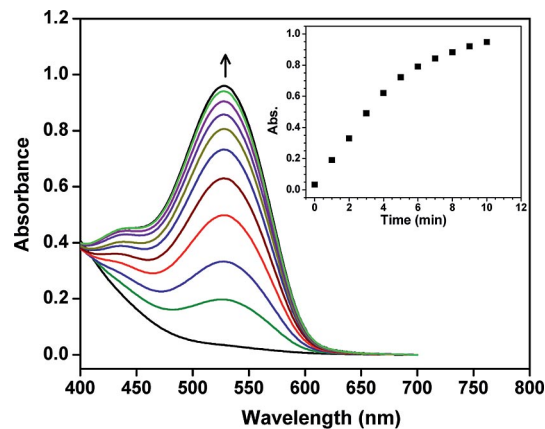


Figure 5. Electronic spectra of the formation of dye when the Griess reagent (100 μ L) was treated with complex **1a** (50 μ M) in the presence of light (100 W tungsten lamp). Repetitive scans were taken at 1 min intervals. Inset: Time-dependent change in absorbance at $\lambda = 538$ nm.

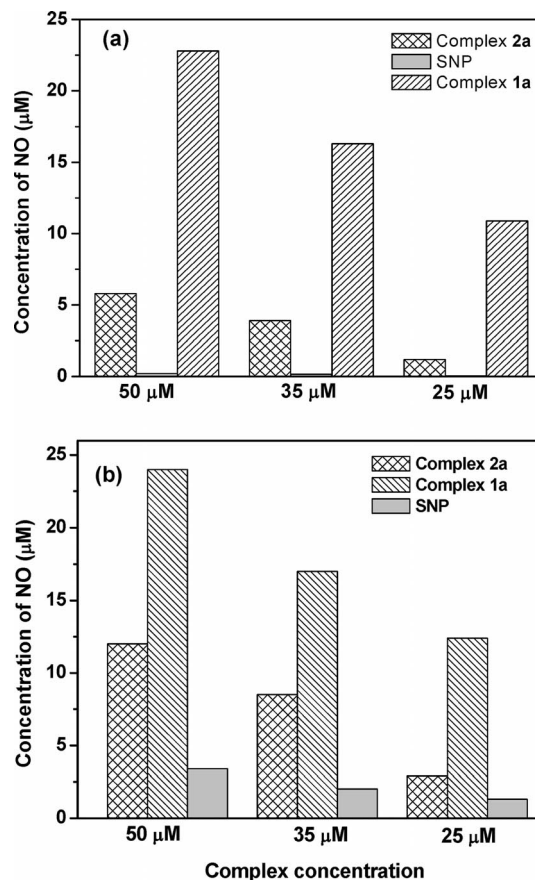


Figure 6. Bar diagrams showing the amount of photoreleased NO (dye formation) from the complexes under exposure to (a) visible light and (b) UV light for 15 min.

produced dye was ca. 0.8 μM . Shining of visible light (100 W tungsten lamp) onto the 50 μM solution of **1a** for 10–15 min gave rise to the formation of about 23.0 μM of dye (Figure 5), however, the solution of **2a** with the same concentration produced only ca. 6 μM of azo dye in visible light [Figure 6(a), Table 3]. We have compared our data with the data obtained from sodium nitroprusside (SNP), a donor of nitric oxide.^[12] In visible light [Figure 6 (a), Table 3], a 50 μM solution of sodium nitroprusside produced a very small amount of nitric oxide (ca. 0.2 μM in 15 min), however, in ultraviolet light [Figure 6 (b), Table 3], the same solution provided about 4.0 μM of nitric oxide.

Table 3. Determination of the amount of dye produced from the complexes **1a**, **2a** and sodium nitroprusside (SNP) on reaction with the Griess reagent in the dark, visible light and UV light.

Complex	Complex conc. [μM]	Concentration of dye produced [μM] ^[a]		
		In the dark	Exposure to visible light	Exposure to UV light
1a	50	0.73	23.00	24.0
2a	50	0.84	5.74	12.0
SNP	50	0.04	0.22	3.4

[a] Average of three experiments.

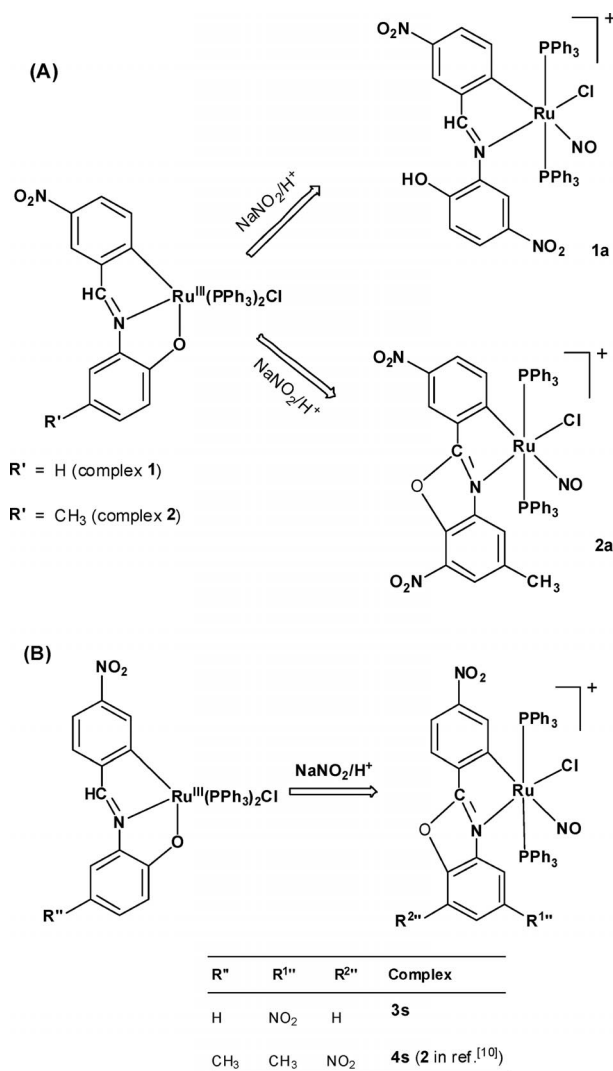
These data afforded the formation of NO in solution and the concentration of photoreleased NO in complexes **1a** and **2a** was found to be greater in comparison with the NO released by SNP.

The quantum yield (ϕ) values for complexes **1a** and **2a** ($\lambda_{\text{irr}} = 365 \text{ nm}$) were found to be 0.017 ± 0.001 and 0.012 ± 0.001 , respectively, in acetonitrile solutions. These data showed a slightly higher NO donor capacity for **1a** than for **2a**.

Role of the $-\text{NO}_2$ Group in Oxidative Cyclization and NO Delivery

It is important to note here that in this study of NO reactivity we have found oxidative cyclization and concomitant formation of the substituted 2-phenylbenzoxazole derivative, only when a methyl group was present in the position *trans* to the phenolato function [described in Scheme 4 (A)]. We have compared these results with our previous observations.^[10] Moreover, to better understand the findings, we studied the synthesis of another ruthenium nitrosyl complex **3s** (described in the Supporting Information, Scheme S2) in order to observe the positional effect of the $-\text{NO}_2$ group. The following points are important in this regard: First, the ^1H NMR spectrum of **3s** (Figure S22) did not afford the characteristic peak for the $-\text{OH}$ function. Second, electrochemical data for **3s** (Figure S23) afforded the $E_{1/2}$ redox couple for $\text{Ru}^{\text{II}}/\text{Ru}^{\text{III}}$ at -0.21 V vs. Ag/AgCl . Third, UV/Vis spectroscopic data (Figure S24) for the photocleavage experiment of NO in **3s** resembles that of **4s** (complex **2** of ref.^[10]). Four, the amount of liberated NO from **3s** and **4s** was similar to that of **2a** (Table S2, Figure S25 and S26). All these data clearly indicate that the presence of the methyl group on the ring containing the

phenolato function was not necessary for the cyclization reaction for the complexes obtained from *p*-nitrobenzaldehyde [described in Scheme 4 (B)].



Scheme 4.

Conclusions

The following are the principle findings of the present study. The organometallic ruthenium(III) cyclometalates **1** and **2** were synthesized by site-specific orthometallation. In these complexes, the metal–carbon bond was established in such a way that the electron-withdrawing $-\text{NO}_2$ group was found to be at the *para* position with respect to the $\text{Ru}-\text{C}$ bond. The interaction of nitric oxide with these complexes was investigated and complexes **1a** and **2a** were obtained from **1** and **2**, respectively. The *trans* effect of carbanion gave rise to dissociation of the phenolato function and NO was coordinated to the metal centre. Molecular structures of **1a**· CH_3OH · $2\text{CH}_2\text{Cl}_2$ · H_2O and **2a**· $2\text{CH}_2\text{Cl}_2$ were determined by X-ray crystallography. Interestingly, structure determination clearly authenticated three important events of

the NO reactivity studies. First, nitrosylation of the metal centre and synthesis of the ruthenium nitrosyl complexes. Second, ligand nitration was observed in both nitrosyl complexes. Third, oxidative cyclization and formation of the benzoxazole ring in **2a**.

Photolability of NO was authenticated by UV/Vis spectral studies and trapping experiments. In **1a**, the ruthenium–phenolato bond was reestablished after the photorelease of coordinated NO. The Ru–N–O angle and N–O bond distances clearly indicated the presence of a {Ru^{II}NO⁺}⁶ moiety in both the nitrosyl complexes. Both **1a** and **2a** exhibited ¹H NMR as well as ³¹P NMR spectra. These findings were supported by the diamagnetic behaviour of **1a** and **2a** and NO stretching frequencies in the IR spectral studies. An electrochemical investigation indicated Ru^{II}–Ru^{III} and Ru^{III}–Ru^{IV} redox couples for **1** and **2**. On the other hand, only a Ru^{II}–Ru^{III} couple was obtained for complexes **1a** and **2a**.

We found that the methyl group was necessary on the ring containing the phenolato function for oxidative cyclization in the complexes described in this report. However, for the ruthenium cyclometalates obtained from *p*-nitrobenzaldehyde^[10] the presence of a methyl group was not important.

We have estimated the amount of available NO in solution during these photolytic reactions and we compared our data with the same obtained from sodium nitroprusside. It has been found that complex **1a** was equally efficient in NO delivery in visible and UV light and that the amount of NO produced by **1a** was higher than that of **2a**. Complexes **3s** and **4s** were similar to **2a** in terms of NO generation in solution. Ruthenium cyclometalates have never been used for photoinduced delivery of nitric oxide^[30] and complexes described in this report demand their application in photodynamic therapy.

A study of the effect of the electron-donating group of the phenyl ring containing an aldehyde function in the coordination and photolability of NO is under progress. Biological applications of these complexes along with the synthesis of substituted benzoxazole are also being investigated.

Experimental Section

Materials: All the solvents used were of reagent grade. The analytical grade reagents; sodium nitrite, (Sigma Aldrich, Steinheim, Germany), RuCl₃·3H₂O, triphenylphosphane (SRL, Mumbai, India), 2-aminophenol, 2-amino-4-methylphenol, 3-nitrobenzaldehyde, sodium perchlorate monohydrate, sulfanilamide, naphthylethylenediamine dihydrochloride (NED) (Himedia Laboratories Pvt. Ltd., Mumbai, India), disodium hydrogen phosphate anhydrous (RFCL Ltd. New Delhi, India) and sodium dihydrogen phosphate (Chemport India Pvt. Ltd. Mumbai, India) were used as obtained. Double-distilled water was used in all of the experiments. Equine skeletal muscle myoglobin was obtained from Sigma Aldrich, Steinheim, Germany.

Physical Measurements: Electronic absorption spectra of all the complexes were recorded in dichloromethane and acetonitrile sol-

vents with an Evolution 600, Thermo Scientific UV/Vis spectrophotometer. Infrared spectra were obtained as KBr pellets with a Thermo Nicolet Nexus FTIR spectrometer, using 16 scans and were reported in cm⁻¹. ¹H and ³¹P NMR spectra were recorded with a Bruker AVANCE, 500.13 MHz spectrometer in the deuterated solvents. Cyclic voltammetric studies were performed with a CH-600 electroanalyser in dichloromethane with 0.1 M tetrabutylammonium perchlorate (TBAP) as the supporting electrolyte. The working electrode, reference electrode and auxiliary electrode were glassy carbon electrode, Ag/AgCl electrode and Pt wire, respectively. The concentration of the compounds was in the order of 10⁻³ M. The ferrocene/ferrocenium couple occurred at *E*_{1/2} = +0.51 (102) V vs. Ag/AgCl (scan rate 0.1 V s⁻¹) in dichloromethane under the same experimental conditions. Quantum yields were determined by actinometry studies using a ferric oxalate solution. The intensity of the light (*λ*_{irr} = 365 nm) was determined using a ferrioxalate actinometer (0.006 M solution of potassium ferrioxalate in 0.1 N H₂SO₄).^[31–33] Quantum yields (*φ*) of the NO photorelease for complexes **1a** and **2a** were determined from the decrease in their absorption bands near 310 nm and 314 nm when irradiated with 365 nm light and were calculated by following the procedure reported earlier.^[7,33,34]

Preparation of Complexes

Caution: Perchlorate salts of metal complexes with organic ligands are potentially explosive. Only a small amount of material should be prepared and handled carefully.

Synthesis of Ligands: The Schiff base ligands L^{SB1}H₂ [2-(3-nitrobenzylideneamino)phenol] and L^{SB2}H₂ [4-methyl-2-(3-nitrobenzylideneamino)phenol] were synthesized by the condensation of 3-nitrobenzaldehyde with 2-aminophenol and 2-amino-4-methylphenol, respectively, in ethanol by following the procedure reported by Chakravorty and his coworkers.^[3]

The precursor complex [Ru(PPh₃)₃Cl₂] was prepared by the procedure reported earlier.^[35]

[Ru(L^{SB1})(PPh₃)₂Cl] (1**):** A batch of L^{SB1}H₂ (0.036 g, 0.15 mmol) and ethanol (5 mL) was added to a warm solution of Ru(PPh₃)₃Cl₂ (0.096 g, 0.10 mmol) in ethanol (30 mL). The mixture was heated under reflux for 2 h and was then allowed to cool to obtain a precipitate of a red-brown colour. The solid was filtered out and was washed thoroughly with ethanol and diethyl ether and was then dried. Complex **1** (0.062 g, 0.069 mmol) was eluted on an alumina column by a dichloromethane/hexane (1:1) mixture; yield 69%. IR (KBr disk): *ν* = 1580 (*ν*_{C=N}), 1482, 1434, 1332, 1310 (*ν*_{NO2}), 1284, 742, 695, 515 (*ν*_{PPh₃}) cm⁻¹. UV/Vis (CH₂Cl₂): *λ*_{max} (*ε*, M⁻¹cm⁻¹) = 267 (38182), 371 (13636), 475 (5636), 585 (2273) nm.

[Ru(L^{SB2})(PPh₃)₂Cl] (2**):** This was prepared by the same procedure as that used for **1**, with Ru(PPh₃)₃Cl₂ (0.096 g, 0.10 mmol) and L^{SB2}H₂ (0.038 g, 0.15 mmol); yield 63%. IR (KBr disk): *ν* = 1595 (*ν*_{C=N}), 1570, 1482, 1433, 1330, 1309 (*ν*_{NO2}), 1298, 1266, 740, 693, 519 (*ν*_{PPh₃}) cm⁻¹. UV/Vis (CH₂Cl₂): *λ*_{max} (*ε*, M⁻¹cm⁻¹) = 270 (39231), 376 (12308), 580 (5385), 598 (2308) nm.

[Ru(L^{SB3}H)(PPh₃)₂(NO)Cl]ClO₄ (1a**):** [where L^{SB3}H₂ = 4-nitro-2-(3-nitrobenzylideneamino)phenol]: A batch of complex **1** (0.016 g, 0.018 mmol) was dissolved in dichloromethane (25 mL) to obtain a brownish-red coloured solution in a round-bottomed flask (100 mL). Acidified distilled water (20 mL) was then layered over this solution. Sodium nitrite (0.19 g, 2.7 mmol) was added to the bilayer solution and the mixture was stirred at room temperature for 1 h to obtain a yellowish-orange coloured solution of complex **1a**. A dichloromethane layer was separated out and NaClO₄ (in excess) with methanol (5 mL) was added to this solution. Stirring

of this solution was continued for another 1 h. A yellowish-orange solid was precipitated out by the evaporation of the solvent. In order to remove the excess NaClO_4 , the compound was further dissolved in dichloromethane and was filtered off. Complex **1a** (0.012 g, 0.011 mmol) was eluted on an alumina column by a dichloromethane/methanol (9:1) mixture. Single crystals of the complex for X-ray crystallography were obtained within 2 d upon slow evaporation of a dichloromethane/methanol mixture; yield 61.11%. IR (KBr disk): $\tilde{\nu}$ = 1811 (ν_{NO}), 1590 ($\nu_{\text{C=N}}$), 1480, 1434, 1345, 1304 (ν_{NO_2}), 1089, 623 (ν_{ClO_4}), 748, 693, 518 (ν_{PPh_3}) cm^{-1} . UV/Vis (CH_2Cl_2): λ_{max} (ϵ , $\text{M}^{-1}\text{cm}^{-1}$) = 385 (5273), 311 (27455) nm. ^{31}P NMR (CD_3CN , 500 MHz): δ = 20.35 ppm. ^1H NMR [$(\text{CD}_3)_2\text{SO}$, 500 MHz]: δ = 11.84 (s, 1 H), 8.83 (s, 1 H), 8.47 (s, 1 H), 8.06 (d, 1 H), 7.46–7.21 (m, 31 H), 6.97 (s, 1 H), 6.95 (d, 1 H) and 6.84 (d, 1 H) ppm.

[Ru(L^{BOX})(PPh₃)₂(NO)Cl]ClO₄ (2a): {where L^{BOX}H = 5-methyl-7-nitro-2-(3-nitrophenyl)benzoxazole}: Complex **2a** was prepared by the same procedure as that used for **1a**. Single crystals of the complex **2a** for X-ray crystallography were obtained within 3 d in the dark upon slow evaporation of a dichloromethane/methanol mixture; yield 59%. IR (KBr disk): $\tilde{\nu}$ = 1837 (ν_{NO}), 1590, 1380, 1350, 1233, 1091, 623 (ν_{ClO_4}), 750, 695, 517 (ν_{PPh_3}) cm^{-1} . UV/Vis (CH_3CN): λ_{max} (ϵ , $\text{M}^{-1}\text{cm}^{-1}$) = 384 (6722), 314 (26667) nm. ^{31}P NMR (CD_3CN , 500 MHz): δ = 18.12 ppm. ^1H NMR [$(\text{CD}_3)_2\text{SO}$, 500 MHz]: δ = 8.49 (d, 1 H), 8.15 (s, 1 H), 7.69 (d, 1 H), 7.37–7.25 (m, 32 H), and 2.45 (s, 3 H) ppm.

Transfer of NO to Myoglobin

Preparation of the Phosphate Buffer Solution: A phosphate buffer solution (50 mM) of pH 6.8 was prepared by adding $\text{NaH}_2\text{PO}_4 \cdot 2\text{H}_2\text{O}$ (0.4192 g) and anhydrous Na_2HPO_4 (0.3283 g) to MilliQ water (50 mL) and making the volume to 100 mL in a volumetric flask.

Preparation of the Myoglobin Stock Solution: Equine skeletal muscle myoglobin (5 mg) was dissolved in the above prepared buffer solution (5 mL).

Binding of the Photoreleased NO with Myoglobin: Electronic absorption spectra were obtained against the phosphate buffer as reference. A myoglobin stock solution (100 μL) was diluted up to 1000 μL in a quartz cuvette with an optical length of 1 cm and sealed with a rubber septum. Its UV/Vis spectrum showed an intense band at 409 nm (Soret band). The UV/Vis spectrum of reduced myoglobin at 433 nm was obtained by the addition of excess sodium dithionite to the same cuvette. When complex **1a** was added to the buffer solution of reduced myoglobin under dark conditions, no reaction was observed. However, when the same mixture was exposed to a tungsten lamp (100 W) for 2 min, its absorption spectrum at 420 nm showed the formation of a Mb–NO adduct.^[11,27]

Estimation of NO Production by the Griess Reaction: The production of NO by complexes **1a** and **2a** was estimated using the Griess reagent (GR).^[28] It was prepared fresh by mixing equal volumes of 1% sulfanilamide in 5% orthophosphoric acid and 0.1% naphthylethylene diamine dihydrochloride (NED) in water. To estimate the production of NO or NO_2 , the absorbance was measured at 538 nm to determine the formation of azo dye. Aqueous solutions of sodium nitrite with different concentrations (5–50 μM) were used to prepare standard curves for the determination of nitrite.

X-ray Crystallography: Orange-red crystals of **1a**· CH_3OH · $2\text{CH}_2\text{Cl}_2$ · H_2O and **2a**· $2\text{CH}_2\text{Cl}_2$ were obtained by slow evaporation of solution of the complexes in a CH_2Cl_2 /methanol mixture. The crystal structures showed the presence of water molecules in the lattice. The X-ray data collection and processing for complexes

were performed with a Bruker Kappa Apex-II CCD diffractometer by using graphite-monochromated Mo- K_α radiation (λ = 0.71073 Å) at 273 K for **1a**· CH_3OH · $2\text{CH}_2\text{Cl}_2$ · H_2O and at 296 K for **2a**· $2\text{CH}_2\text{Cl}_2$ (Table 4). Crystal structures were solved by direct methods. Structure solutions, refinement and data output were carried out with the SHELXTL program.^[36,37] All non-hydrogen atoms were refined anisotropically. Hydrogen atoms were placed in geometrically calculated positions and refined using a riding model. Images were created with the DIAMOND program.^[38]

Table 4. Crystal data and structural refinement parameters for complexes **1a**· CH_3OH · $2\text{CH}_2\text{Cl}_2$ · H_2O and **2a**· $2\text{CH}_2\text{Cl}_2$.

	1a · CH_3OH · $2\text{CH}_2\text{Cl}_2$ · H_2O	2a · $2\text{CH}_2\text{Cl}_2$
Empirical formula	$\text{C}_{52}\text{H}_{48}\text{Cl}_6\text{N}_4\text{O}_{14}\text{P}_2\text{Ru}$	$\text{C}_{52}\text{H}_{42}\text{Cl}_6\text{N}_4\text{O}_{10}\text{P}_2\text{Ru}$
M_r [g mol^{-1}]	1328.65	1258.61
Temperature [K]	273(2)	296(2)
λ [Å] (Mo- K_α)	0.71073	0.71073
Crystal system	triclinic	monoclinic
Space group	$P\bar{1}$	$P2_1/n$
a [Å]	12.505(3)	13.4992(4)
b [Å]	13.488(3)	23.2857(7)
c [Å]	18.220(4)	17.6737(5)
α [°]	93.11(3)	90
γ [°]	101.47(3)	90
β [°]	106.87(3)	101.980(10)
V [Å ³]	2861.5(13)	5434.5(3)
Z	2	4
$\rho_{\text{calcd.}}$ [g cm^{-3}]	1.542	1.538
$F(000)$	1352.0	2552.0
Theta range [°]	1.18–25.00	1.47–28.35
Index ranges	$-14 < h < 14$, $-16 < k < 16$, $-21 < l < 21$	$-18 < h < 18$, $-31 < k < 31$, $-23 < l < 23$
Data / restraints / parameters	10077 / 0 / 719	13337 / 0 / 677
GOF ^[a] on F^2	1.190	1.317
R_1 ^[b] [$I > 2\sigma(I)$]	0.0595	0.0636
R_1 [all data]	0.1394	0.1143
wR_2 ^[c] [$I > 2\sigma(I)$]	0.1574	0.1802
wR_2 [all data]	0.2141	0.2155

[a] GOF = $\{\sum[w(F_o^2 - F_c^2)^2]/M - N\}^{1/2}$ (M = number of reflections, N = number of parameters refined). [b] $R_1 = \sum|F_o| - |F_c|/\sum|F_o|$. [c] $wR_2 = \{\sum[w(F_o^2 - F_c^2)^2]/\sum[w(F_o^2)^2]\}^{1/2}$.

Supporting Information (see footnote on the first page of this article): Characterization of complexes by IR, UV/Vis and NMR spectral studies. The standard curves of NaNO_2 for the Griess reaction. X-ray crystallographic data of complexes **1a**· CH_3OH · $2\text{CH}_2\text{Cl}_2$ · H_2O and **2a**· $2\text{CH}_2\text{Cl}_2$ in CIF format.

Acknowledgments

K. G. is thankful to the Council of Scientific and Industrial Research (CSIR), New Delhi for financial assistance [01(2229)/08/EMR-II, dated 06 March, 2008]. S. K. and R. K. are thankful to the CSIR for financial assistance. U. P. S. is thankful for support by single-crystal X-ray facility of the IIT Roorkee.

- [1] R. Raveendran, S. Pal, *J. Organomet. Chem.* **2009**, *694*, 1482–1486.
- [2] P. Munshi, R. Samanta, G. K. Lahiri, *J. Organomet. Chem.* **1999**, *586*, 176–183.
- [3] P. Ghosh, A. Pramanik, N. Bag, G. K. Lahiri, A. Chakravorty, *J. Organomet. Chem.* **1993**, *454*, 237–241.

- [4] G. K. Lahiri, S. Bhattacharya, M. Mukherjee, A. K. Mukherjee, A. Chakravorty, *Inorg. Chem.* **1987**, *26*, 3359–3365.
- [5] H. Hadadzadeh, M. C. DeRosa, G. P. A. Yap, A. R. Rezvani, R. J. Crutchley, *Inorg. Chem.* **2002**, *41*, 6521–6526.
- [6] S. Kannan, R. Ramesh, Y. Liu, *J. Organomet. Chem.* **2007**, *692*, 3380–3391.
- [7] M. J. Rose, P. K. Mascharak, *Coord. Chem. Rev.* **2008**, *252*, 2093–2114.
- [8] P. C. Ford, J. Bourassa, K. Miranda, B. Lee, I. Lorkovic, S. Boggs, S. Kudo, L. Laverman, *Coord. Chem. Rev.* **1998**, *171*, 185–202.
- [9] M. G. Sauaia, R. G. de Lima, A. C. Tedesco, R. S. da Silva, *J. Am. Chem. Soc.* **2003**, *125*, 14718–14719.
- [10] K. Ghosh, S. Kumar, R. Kumar, U. P. Singh, N. Goel, *Inorg. Chem.* **2010**, *49*, 7235–7237.
- [11] K. Ghosh, S. Kumar, R. Kumar, U. P. Singh, N. Goel, *Organometallics* **2011**, *30*, 2498–2505.
- [12] C. Xin Zhang, S. J. Lippard, *Curr. Opin. Chem. Biol.* **2003**, *7*, 481–489.
- [13] M. J. Rose, P. K. Mascharak, *Curr. Opin. Chem. Biol.* **2008**, *12*, 238–244.
- [14] R. K. Afshar, A. K. Patra, M. M. Olmstead, P. K. Mascharak, *Inorg. Chem.* **2004**, *43*, 5736–5743.
- [15] B. P. Sullivan, J. M. Calvert, T. J. Meyer, *Inorg. Chem.* **1980**, *19*, 1404–1407.
- [16] K. Ghosh, S. Kumar, R. Kumar, *Inorg. Chem. Commun.* **2011**, *14*, 146–149.
- [17] M. J. Rose, A. K. Patra, E. A. Alcid, M. M. Olmstead, P. K. Mascharak, *Inorg. Chem.* **2007**, *46*, 2328–2338.
- [18] M. J. Rose, M. M. Olmstead, P. K. Mascharak, *J. Am. Chem. Soc.* **2007**, *129*, 5342–5343.
- [19] N. Chanda, D. Paul, S. Kar, S. M. Mobin, A. Datta, V. G. Puranik, K. K. Rao, G. K. Lahiri, *Inorg. Chem.* **2005**, *44*, 3499–3511.
- [20] J. H. Enemark, R. D. Feltham, *Coord. Chem. Rev.* **1974**, *13*, 339–406.
- [21] G. R. Desiraju, T. Steiner, *The Weak Hydrogen Bond in Structural Chemistry and Biology*, Oxford University Press, New York, **1999**.
- [22] B. Birkmann, B. T. Owens, S. Bandyopadhyay, G. Wu, P. C. Ford, *J. Inorg. Biochem.* **2009**, *103*, 237–242.
- [23] K. Ghosh, S. Pattanayak, A. Chakravorty, *Organometallics* **1998**, *17*, 1956–1960.
- [24] N. Chitrapriya, V. Mahalingam, M. Zeller, K. Natarajan, *Polyhedron* **2008**, *27*, 1573–1580.
- [25] R. L. Brainard, W. R. Nutt, T. R. Lee, G. M. Whitesides, *Organometallics* **1988**, *7*, 2379–2386.
- [26] R. Cordone, W. D. Harman, H. Taube, *J. Am. Chem. Soc.* **1989**, *111*, 2896–2900.
- [27] S. Maji, B. Sarkar, M. Patra, A. K. Das, S. M. Mobin, W. Kaim, G. K. Lahiri, *Inorg. Chem.* **2008**, *47*, 3218–3227.
- [28] A. Chakraborty, N. Gupta, K. Ghosh, P. Roy, *Toxicol. in vitro* **2010**, *24*, 1215–1228.
- [29] D. Tsikas, *J. Chromatogr. B* **2007**, *851*, 51–70.
- [30] J. P. Djukic, J. B. Sortais, L. Barloy, M. Pfeffer, *Eur. J. Inorg. Chem.* **2009**, 817–853.
- [31] H. J. Kuhn, S. E. Braslavsky, R. Schmidt, *Pure Appl. Chem.* **1989**, *61*, 187–210.
- [32] S. K. Nayak, G. J. Farrell, T. J. Burkey, *Inorg. Chem.* **1994**, *33*, 2236–2242.
- [33] C. F. Works, C. J. Jocher, G. D. Bart, X. Bu, P. C. Ford, *Inorg. Chem.* **2002**, *41*, 3728–3739.
- [34] A. K. M. Holanda, F. O. N. da Silva, J. R. Sousa, I. C. N. Diogenes, I. M. M. Carvalho, I. S. Moreira, M. J. Clarke, L. G. F. Lopes, *Inorg. Chim. Acta* **2008**, *361*, 2929–2933.
- [35] T. A. Stephenson, G. Wilkinson, *J. Inorg. Nucl. Chem.* **1966**, *28*, 945–956.
- [36] G. M. Sheldrick, *Acta Crystallogr., Sect. A* **1990**, *46*, 467–473.
- [37] G. M. Sheldrick, *SHELXTL–NT 2000*, version 6.12, Reference Manual, University of Göttingen, Pergamon, New York, **1980**.
- [38] B. Klaus, University of Bonn, Germany, *DIAMOND*, version 1.2c, **1999**.

Received: September 27, 2011

Published Online: January 23, 2012

Amide and Urea Ferrocene-Containing Macrocycles Capable of the Electrochemical Sensing of Anions

Nicholas H. Evans,^[a] Christopher J. Serpell,^[a] Kirsten E. Christensen,^[a,b] and Paul D. Beer^{*[a]}

Keywords: Supramolecular chemistry / Macrocycles / Molecular recognition / Sensors / Anions / Electrochemistry

Two novel macrocycles that incorporate the redox-active ferrocene motif have been synthesized. The amide-containing macrocycle is capable of sensing basic oxoanions such as dihydrogen phosphate and benzoate despite only exhibiting weak binding of these anions. The second macrocycle, which

incorporates urea functionality, is capable of binding and sensing a greater range of anions with a maximum shift of the ferrocene/ferrocenium redox couple of -170 mV observed upon addition of an excess amount of dihydrogen phosphate.

Introduction

Anions have an immense impact on our world.^[1] They are of exceptional importance in biology, with enzyme substrates and cofactors being typically anionic, whereas the simple monoatomic chloride anion is found extensively in extracellular fluid. The misregulation of this particular anion in the human body is believed to cause the terminal genetic disease cystic fibrosis.^[2] Anions have also been found to have an adverse effect on the environment: the leaching of phosphates and nitrates into waterways through overuse of fertilizers leads to eutrophication.^[3] Pertechnetate (a radioactive byproduct of the nuclear industry)^[4] and perchlorate (which arises from the manufacture of explosives)^[5] are further examples of anionic pollutants.

The sensing of anions is therefore of significant research interest, and a large range of anion sensors that provide either optical or electrochemical responses have been reported.^[6] Among examples of electrochemical anion sensors, hydrogen-bond donor/receptor molecules that incorporate ferrocene have enjoyed considerable popularity. This may be explained by the readily accessible ferrocene/ferrocenium (Fc/Fc^+) redox couple and the extensive chemistry of ferrocene that exists in the chemical literature.^[6c]

1,1'-Bis(aminocarbonyl)ferrocene (see Figure 1a) is a widely used motif in acyclic and macrocyclic anion-sensory receptors.^[7] Whilst exhibiting electrochemical recognition for anions, this motif has a rather positive Fc/Fc^+ potential

value that may be responsible for the commonly encountered irreversible redox behaviour observed in the presence of excess amounts of anions. Reversing the amide as shown in Figure 1b should move the Fc/Fc^+ redox couple to a less positive potential than the 1,1'-bis(aminocarbonyl)-ferrocene motif. An alternative N–H hydrogen-bond donor is urea: examples of two 1,1'-ferrocene bis-urea motifs are depicted in Figure 1 (c and d).^[8,9] Of these, the latter has yet to be included in a macrocycle for anion sensing. Here in this paper we report the synthesis of novel ferrocene-containing macrocycles that incorporate the motifs depicted in Figure 1 (b and d), and the subsequent investigations into their anion recognition and electrochemical sensing properties.

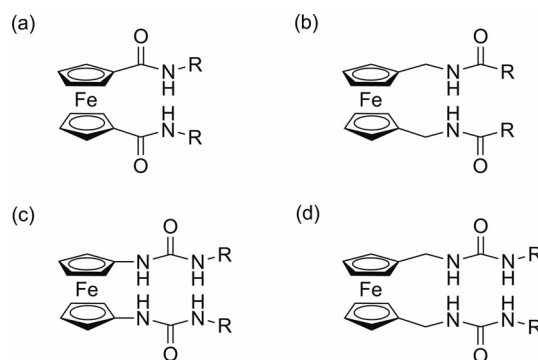


Figure 1. Ferrocene anion-recognition motifs: 1,1'-ferrocene bis-amides (a) and (b) and 1,1'-ferrocene bis-ureas (c) and (d).

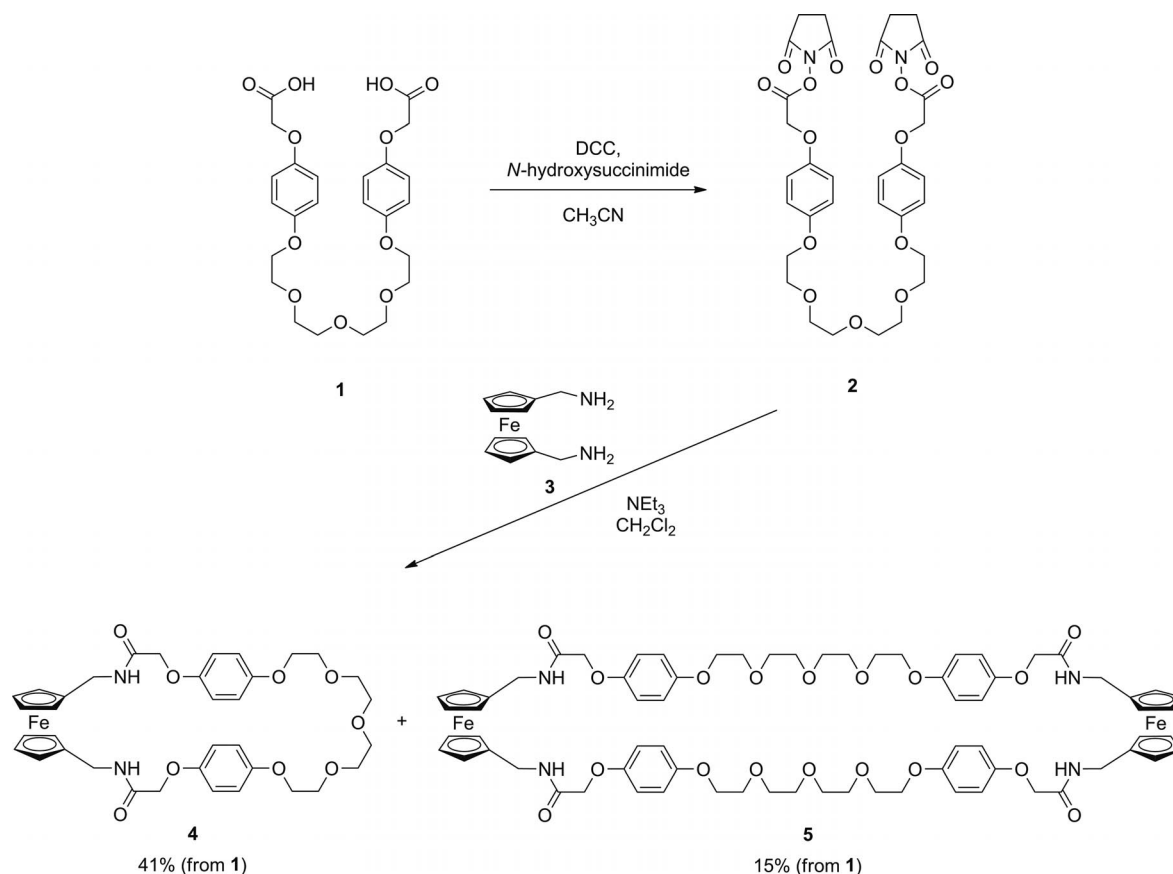
Results and Discussion

“Reverse amide” macrocycle **4** was synthesized as shown in Scheme 1. Dicarboxylic acid **1** was first activated with dicyclohexylcarbodiimide (DCC) and *N*-hydroxysuc-

[a] Chemistry Research Laboratory, Department of Chemistry, University of Oxford, Mansfield Road, Oxford, OX1 3TA, UK
Fax: +44-1865-272690
E-mail: paul.beer@chem.ox.ac.uk

[b] Diamond Light Source Ltd., Chilton, Didcot, Oxon, OX11 0DE, UK

Supporting information for this article is available on the WWW under <http://dx.doi.org/10.1002/ejic.201101257>.



Scheme 1. Synthesis of “reverse amide” macrocycles **4** and **5**.

cinimide to produce bis-succinimide ester **2**.^[10] Treatment of **2** with 1,1'-bis(aminomethyl)ferrocene (**3**)^[11] under high dilution conditions afforded macrocycle **4** in 41% yield after silica gel chromatographic purification. In addition, a dimeric macrocyclic species **5** was isolated in 15% yield. Both macrocycles were characterized by ¹H and ¹³C NMR spectroscopy and high-resolution mass spectrometry.

Single crystals of macrocycle **4** suitable for X-ray crystallography were grown from slow evaporation of a chloroform solution. The determined structure is shown in Figure 2 and confirms the constitution of the macrocycle. The ferrocene unit was found to be disordered in the crystal; it occupies one of two positions with a 1:1 ratio of occupancy of the two sites in the crystal.^[12]

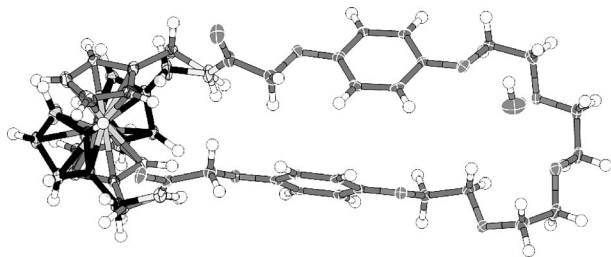
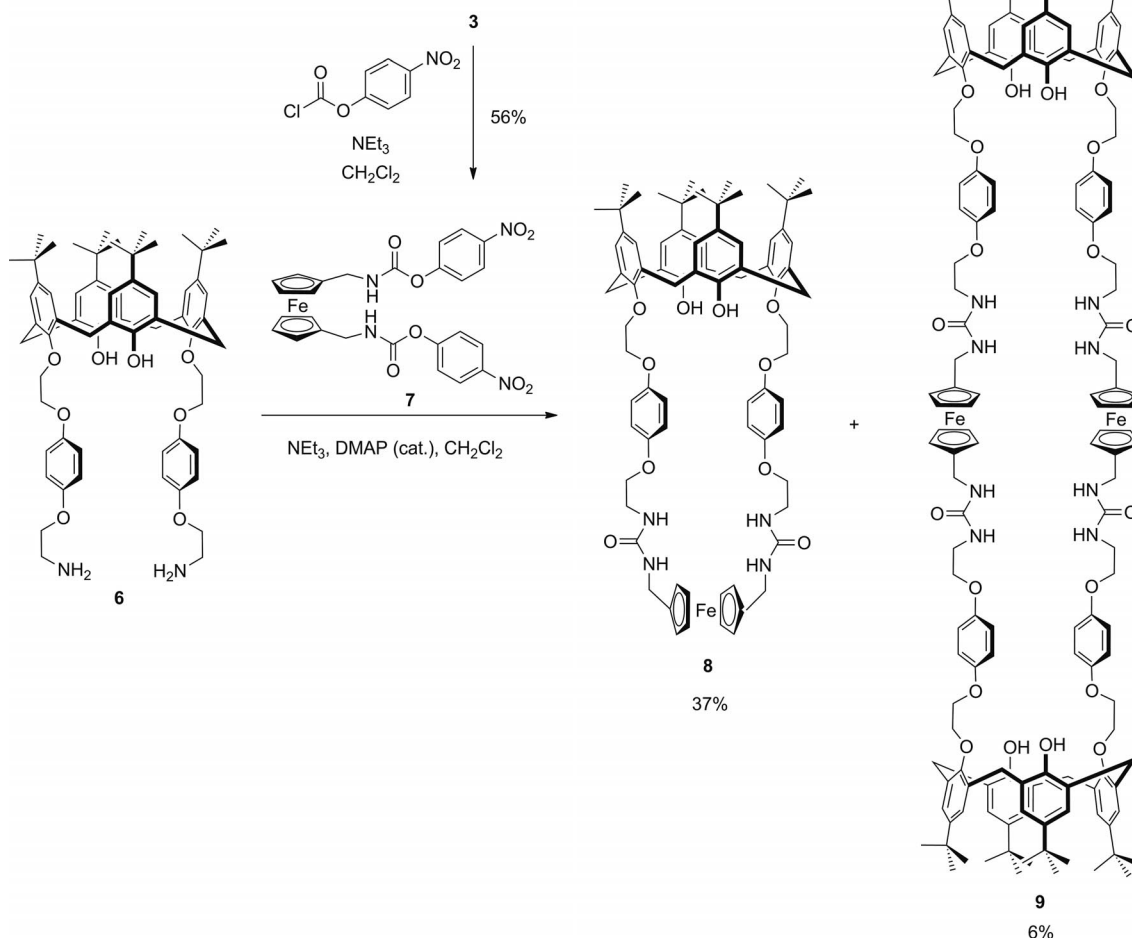


Figure 2. X-ray crystal structure of macrocycle **4**. The ferrocene unit is disordered and occupies two positions with a 1:1 ratio of occupancy of the two sites.

Urea macrocycle **8** was synthesized as depicted in Scheme 2.^[13] In this case, lower-rim-substituted calix[4]-arene bis-amine **6**^[14] was treated with 1,1'-ferrocene bis-carbamate **7** to furnish the desired macrocycle **8** in 37% yield. Once again, a dimeric macrocyclic species **9** was also isolated (in 6% yield); both macrocycles were characterized by ¹H and ¹³C NMR spectroscopy and high-resolution mass spectrometry.

To measure the strength of anion binding of macrocycles **4** and **8**, ¹H NMR spectroscopic titration experiments were undertaken in CD₃CN.^[15] NMR spectroscopy samples of the two macrocycles were prepared, to which aliquots of tetrabutylammonium (TBA) salts of chloride, dihydrogen phosphate, benzoate and hydrogen sulfate were added. The chemical shifts of peaks that arose from the NH protons were monitored. Anion binding events were observed to be fast on the NMR spectroscopic timescale, thereby allowing the use of the computer program winEQNMR2^[16] to calculate association constants with data fitting to a 1:1 stoichiometric binding model (Table 1).

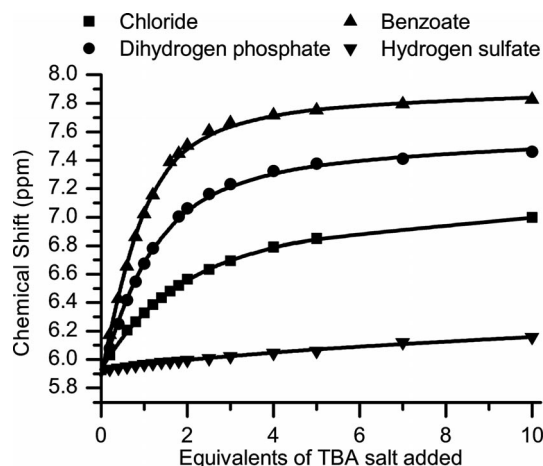
For macrocycle **4**, the addition of anions (apart from HSO₄[−]) caused an appreciable downfield shift of the amide NH resonance. However, plots of the chemical shift of the NH peak against equivalents of anion are almost linear (see the Supporting Information), and values of *K*_a calculated by winEQNMR2 for all four anions were below 25 M^{−1}, thereby implying weak anion binding. For macrocycle **8**, all

Scheme 2. Synthesis of urea macrocycles **8** and **9**.Table 1. Shifts in NH resonances ($\Delta\delta$) and 1:1 anion association constants (K_a) of macrocycles **4** and **8**.^[a]

	Macrocycle 4		Macrocycle 8	
	$\Delta\delta$ [ppm]	K_a [M ⁻¹]	$\Delta\delta$ [ppm]	K_a [M ⁻¹]
Cl ⁻	+0.15	<25	+1.07	4.5×10^2
H ₂ PO ₄ ⁻	+0.35	<25	+1.53	1.1×10^3
BzO ⁻	+0.53	<25	+1.90	2.1×10^3
HSO ₄ ⁻	+0.02	<25	+0.23	<50

[a] Anions added as TBA salts. Shifts are for 10 equiv. of anions added. Association constants are calculated by winEQNMR2, with errors of experimental data fitting to the calculated binding isotherms <10%. Solvent: CD₃CN, concentration of macrocycles: 1.5 mM, $T = 293$ K, peaks monitored: amide NH (macrocycle **4**) and urea NH (macrocycle **8**). Values for macrocycle **8** are averages (see text).

four anions caused much greater downfield shifts of the urea NH resonances (see Figure 3). Apart from chloride, the two NH resonances rapidly merge, and as a consequence, the average of the chemical shifts of the two resonances was therefore used to calculate the association constants reported in Table 1.^[17] The observed increase in binding of all anions by macrocycle **8** compared to macrocycle **4** is attributed to the greater acidity of the urea protons

Figure 3. Plots of the average chemical shift of the urea NH resonances of macrocycle **8** versus equivalents of TBA salt added (solvent: CD₃CN, concentration of macrocycle **8**: 1.5 mM, $T = 293$ K).

than the amide protons. The observed trend of anion binding, BzO⁻ > H₂PO₄⁻ > Cl⁻ > HSO₄⁻, generally follows the basicity of the anion as expected for simple hydrogen-bond donor–acceptor systems. It is proposed that chloride is

bound more strongly than hydrogen sulfate (which is more basic) due to a better geometric complementarity between chloride and the macrocycle cavity than for hydrogen sulfate.

The electrochemical properties of macrocycles **4** and **8** were investigated by cyclic and square-wave voltammetry (CV and SWV) in 0.1 M TBAPF₆ CH₃CN solution. Both macrocycles **4** and **8** exhibit quasi-reversible oxidation waves for the Fc/Fc⁺ redox couple, with $E_{1/2} = +18$ and -12 mV (± 5 mV) respectively, compared to $E_{1/2}(\text{ferrocene}) =$

Table 2. Shifts [mV] of the Fc/Fc⁺ redox couple ($\Delta E_{1/2}$) of macrocycles **4** and **8** upon the addition of anions.^[a]

	Macrocycle 4	Macrocycle 8
Cl [−]	[b]	−45
H ₂ PO ₄ [−]	−75[c]	−170[c]
BzO [−]	[b,c,d]	−90
HSO ₄ [−]	[b]	−25

[a] Anions added as TBA salts. Shifts are for 10 equiv. of anions added. Electrolyte: 0.1 M TBAPF₆ in CH₃CN. Concentration of macrocycles: 1.5 mM. Reference electrode: Ag/AgCl. Values reported to nearest 5 mV. $T = 293$ K. [b] Magnitude of shifts are less than 10 mV. [c] Irreversible behaviour, values reported are perturbations of oxidation peak, ΔE_{pa} . [d] Appearance of a second quasi-reversible redox wave at more anodic potential.

0 V.^[18] Such a small deviation from that of ferrocene itself is attributed to the separation of the electron-withdrawing carbonyl functionalities from the cyclopentadienyl rings by the alkyl CH₂ linkers.

Aliquots of the same anions used in the ¹H NMR spectroscopic investigations were added to electrochemical solution samples of the macrocycles and voltammograms recorded. The shifts in $E_{1/2}$ observed upon the addition of 10 equiv. of anion (as calculated from the CVs) are summarized in Table 2.

A measurable negative shift in the potential of the Fc/Fc⁺ redox couple (attributed to the stabilization of the ferrocenium oxidation state^[19]) was only observed with macrocycle **4** upon addition of dihydrogen phosphate (with a concomitant loss in reversibility; see Figure 4a).^[20] This illustrates that strong binding by the neutral receptor is *not* required for electrochemical sensing of this anion. However, the amide functionality *is* required for this electrochemical behaviour to occur: addition of TBAH₂PO₄ to ferrocene leads only to the development of a cathodic stripping peak,^[21] which is not observed with macrocycle **4**. Macrocycle **4** also demonstrates electrochemical recognition for benzoate: upon addition of this anion, the redox wave becomes irreversible^[20] but does not appreciably shift. Also of

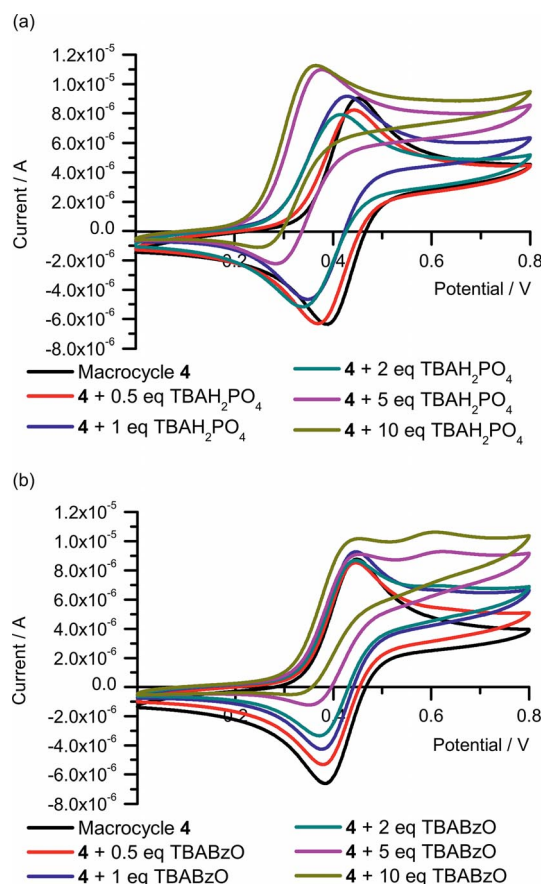


Figure 4. CV of macrocycle **4** upon the addition of aliquots of (a) TBAH₂PO₄ and (b) TBABzO. Electrolyte: 0.1 M TBAPF₆/CH₃CN (concentration of macrocycle **4**: 0.5 mM. $T = 293$ K, potential compared to Ag/AgCl reference).

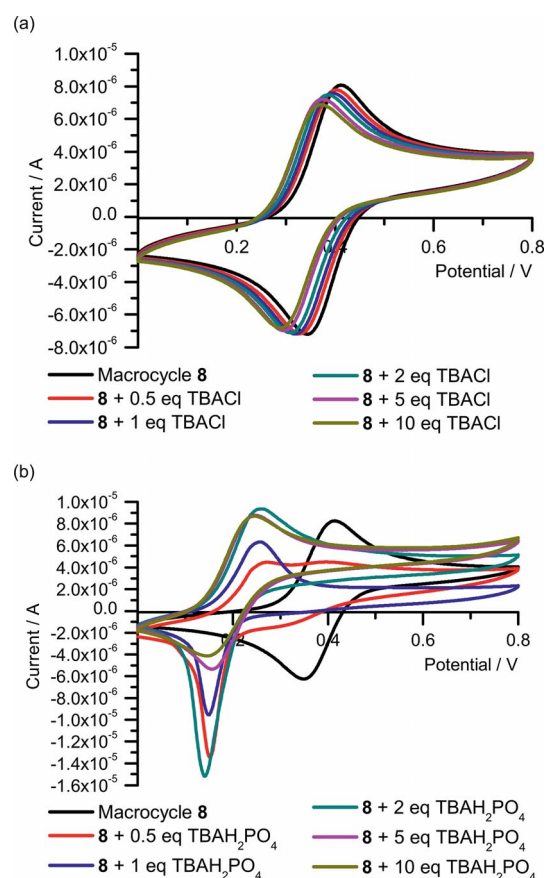


Figure 5. CV of macrocycle **8** upon the addition of aliquots of (a) TBACl and (b) TBAH₂PO₄. Electrolyte: 0.1 M TBAPF₆/CH₃CN (concentration of macrocycle **8**: 0.5 mM. $T = 293$ K, potential compared to Ag/AgCl reference).

note is the appearance of a second quasi-reversible redox wave at a more positive potential (Figure 4b).^[22,23]

With macrocycle **8**, after the addition of chloride, hydrogen sulfate and benzoate the Fc/Fc^+ redox couple remained reversible and shifted to more negative potentials, indicative of anion sensing (see Figure 5a and the Supporting Information).^[19] Upon the addition of dihydrogen phosphate, somewhat different anion electrochemical sensing behaviour was observed (Figure 5b). At substoichiometric equivalents of this anion, a second quasi-reversible wave appears at a more negative potential, to the detriment of the original Fc/Fc^+ redox wave, which upon the addition of a full equivalent of anion disappears. Further addition of anion leads to no shift in potential of the new wave. This behaviour is believed to be due to the binding of the dihydrogen phosphate anion being kinetically slow on the timescale of the experiment.^[24] It should also be noted that between 0.5–2 equiv. of oxoanion there is a reductive stripping peak in the CV, which is lost upon addition of larger excess amounts of anion with the redox wave becoming irreversible. This is consistent with reversible adsorption on the working electrode.^[21]

Conclusion

Novel macrocycles containing amide and urea ferrocene have been synthesized and characterized by NMR spectroscopy, mass spectrometry, and in the case of the amide macrocycle **4** by X-ray crystallography. By means of ^1H NMR spectroscopic titration experiments, it was established that urea macrocycle **8** binds anions much more strongly in acetonitrile than amide macrocycle **4**. This is attributed to the greater acidity of the urea protons of macrocycle **8** than the amide protons of **4**. However, both macrocycles are able to exhibit electrochemical recognition of anions in acetonitrile, even though in the case of macrocycle **4** this is limited to the most basic oxoanions. Greater shifts of the Fc/Fc^+ redox couple were observed with urea macrocycle **8**, thereby reflecting the stronger anion binding affinity of this macrocycle compared to amide macrocycle **4**.

Experimental Section

General Notes: Commercially available solvents and chemicals were used without further purification unless stated. Where dry solvents were used, they were degassed with nitrogen, dried with an MBraun MPSP-800 column and then used immediately. Deionized water was used in all cases. Triethylamine was distilled from and stored over potassium hydroxide. Ferrocene was recrystallized from pentane. NMR spectra were recorded with Varian Mercury 300, Varian Unity Plus 500 and Bruker AVII 500 (with ^{13}C Cryoprobe) spectrometers. Mass spectra were carried out with Waters Micromass LCT, Waters GCT, Bruker micrOTOF and Bruker FT-ICR spectrometers. Melting points were recorded with a Gallenkamp capillary melting-point apparatus and are uncorrected.

Bis-acid **1**,^[9] 1,1'-bis(aminomethyl)ferrocene **3**^[10] and bis-amine **6**^[13] were prepared by literature procedures.

Amide Macrocycle 4: *N*-Hydroxysuccinimide (46 mg, 0.40 mmol) and DCC (76 mg, 0.37 mmol) were added to a suspension of bis-acid **1** (83 mg, 0.17 mmol) in dry CH_3CN (10 mL), and the reaction mixture was then stirred under a N_2 atmosphere for 16 h. The resulting DCC urea was filtered, the solvent removed in vacuo and the isolated activated bis-ester **2**, assumed to have been formed in quantitative yield, was used immediately in the next reaction step. Separate solutions of activated bis-ester **2** in dry CH_2Cl_2 (40 mL) and 1,1'-bis(aminomethyl)ferrocene (**3**) (41 mg, 0.167 mmol) were then added dropwise to NEt_3 (42 mg, 0.06 mL, 0.418 mmol) dissolved in dry CH_2Cl_2 (120 mL). The resulting reaction mixture was stirred under a N_2 atmosphere for 24 h. The volume was reduced to 25 mL and then washed with 10% citric acid (2×25 mL) and H_2O (1×25 mL). The organic layer was dried (MgSO_4) and the solvent was removed in vacuo. The crude material was purified by silica gel preparative TLC plate (97:3 $\text{CH}_2\text{Cl}_2/\text{CH}_3\text{OH}$) to give the amide macrocycle **4** as a yellow solid (48 mg, 41%); m.p. 152–154 °C. ^1H NMR (500 MHz, CDCl_3): δ = 6.79–6.84 (m, 10 H, *NH* and hydroquinone *ArH*), 4.44 [s, 4 H, $\text{C}(\text{O})\text{CH}_2\text{O}$], 4.15 (br. s, 12 H, CH_2 and $2 \times \text{CpH}$), 3.97–3.99 (m, 4 H, CH_2), 3.79–3.81 (m, 4 H, CH_2), 3.65–3.70 (m, 8 H, $2 \times \text{CH}_2$) ppm. ^{13}C NMR (75 MHz, CDCl_3): δ = 168.0, 154.0, 151.4, 115.9, 111.5, 85.5, 70.8, 69.7, 68.6, 68.4, 68.2, 68.1, 37.7 ($1 \times$ aliphatic *C* missing – coincidental) ppm. HRMS (ES, + mode): *m/z* calcd. for $\text{C}_{36}\text{H}_{42}\text{FeN}_2\text{NaO}_9$ 725.2133 [$\text{M} + \text{Na}$] $^+$; found 725.2131.

Amide Macrocycle 5: Isolated from the above reaction as a yellow solid (17 mg, 15%); m.p. 166 °C. ^1H NMR (500 MHz, CDCl_3): δ = 6.81–6.90 (m, 20 H, *NH* and hydroquinone *ArH*), 4.42 [s, 8 H, $\text{C}(\text{O})\text{CH}_2\text{O}$], 4.14 (br. s, 24 H, CH_2 and $2 \times \text{CpH}$), 4.02–4.04 (m, 8 H, CH_2), 3.79–3.81 (m, 8 H, CH_2), 3.65–3.70 (m, 16 H, $2 \times \text{CH}_2$) ppm. ^{13}C NMR (75 MHz, 1:1 $\text{CDCl}_3/\text{CD}_3\text{OD}$): δ = 169.2, 154.5, 152.1, 116.2, 116.2 [sic], 86.0, 71.2, 71.1, 70.2, 69.3, 69.1, 68.6, 68.4, 38.3 ppm. ESMS (ES, + mode): *m/z* calcd. for $\text{C}_{72}\text{H}_{84}\text{Fe}_2\text{N}_4\text{NaO}_{18}$ 1427.4377 [$\text{M} + \text{Na}$] $^+$; found 1427.4372.

Urea Macrocycle 8: Separate solutions of bis-amine **5** (235 mg, 0.233 mol) in dry CH_2Cl_2 (100 mL) and ferrocene bis-carbamate **7** (134 mg, 0.233 mmol) in CH_2Cl_2 (100 mL) were added dropwise to NEt_3 (0.2 mL) and 4-(dimethylamino)pyridine (DMAP; cat.) dissolved in dry CH_2Cl_2 (50 mL). The resulting reaction mixture was stirred under a N_2 atmosphere for 16 h. The solvent was reduced in volume (to 25 mL) and then washed with saturated $\text{NaHCO}_3(\text{aq.})$ until aqueous washes were colourless. The organic layer was dried (MgSO_4), the solvent removed in vacuo and crude material purified by silica gel preparative TLC ($\text{CH}_2\text{Cl}_2/\text{CH}_3\text{OH}$, 98:2) to give a pale yellow solid (112 mg, 39%); m.p. >148 °C (decomp.). ^1H NMR (500 MHz, $[\text{D}_6]\text{acetone}$): δ = 8.49 (s, 2 H, *OH*), 7.24 (s, 4 H, calix *ArH*), 7.22 (s, 4 H, calix *ArH*), 6.90–6.97 (m, 8 H, hydroquinone *ArH*), 6.37–6.41 (m, 4 H, $2 \times \text{NH}$), 4.49 (d, 2J = 12.7 Hz, 4 H, calix CH_2), 4.33–4.38 (m, 8 H, $2 \times \text{CH}_2$), 4.16 (d, 3J = 6.0 Hz, 4 H, CpCH_2NH), 4.12–4.13 (m, 4H CpH), 4.09–4.10 (m, 4 H, CpH), 4.00 (t, 3J = 6.0 Hz, 4 H, $\text{OCH}_2\text{CH}_2\text{NH}$), 3.56–3.59 (app. quartet, 4 H, $\text{OCH}_2\text{CH}_2\text{NH}$), 3.48 (d, 2J = 12.7 Hz, 4 H, calix CH_2), 1.24 [s, 18 H, calix $\text{C}(\text{CH}_3)_3$], 1.06 [s, 18 H, calix $\text{C}(\text{CH}_3)_3$] ppm. ^{13}C NMR (125.8 MHz, $[\text{D}_6]\text{acetone}$): δ = 159.9, 154.4, 154.1, 152.0, 151.1, 148.2, 142.3, 134.6, 128.5, 126.9, 126.4, 116.9, 116.5, 89.8, 75.3, 69.1, 69.1 [sic], 68.5, 68.2, 40.6, 39.4, 34.8, 34.5, 32.7, 32.1, 31.5 ($2 \times$ aliphatic *C* peaks missing) ppm. HRMS (ES, + mode): *m/z* calcd. for $\text{C}_{78}\text{H}_{94}\text{N}_4\text{NaO}_{10}$ 1325.6214 [$\text{M} + \text{Na}$] $^+$; found 1325.6177.

Urea Macrocycle 9: Isolated pure from the above reaction after a second silica gel preparative TLC plate ($\text{CH}_2\text{Cl}_2/\text{CH}_3\text{OH}$, 98:2) as a pale yellow solid (18 mg, 6%); m.p. >160 °C (decomp.). ^1H NMR (500 MHz, $[\text{D}_6]\text{acetone}$): δ = 8.53 (s, 4 H, *OH*), 7.22 (s, 8 H, calix

ArH), 7.21 (s, 8 H, calix ArH), 6.92–6.96 (m, 16 H, hydroquinone ArH), 6.58 (t, $^3J = 5.6$ Hz, 4 H, NH), 6.43 (t, $^3J = 6.1$ Hz, 4 H, NH), 4.47 (d, $^2J = 12.5$ Hz, 8 H, calix CH₂), 4.25–4.27 (m, 8 H, OCH₂), 4.20–4.21 (m, 8 H, OCH₂), 4.11–4.12 (m, 16 H, CH₂Cp and CpH), 4.06–4.07 (m, 8 H, CpH), 4.02 (t, $^3J = 5.4$ Hz, 8 H, OCH₂CH₂NH), 3.57–3.60 (app. quartet, 8 H, OCH₂CH₂NH), 3.44 (d, $^2J = 12.5$ Hz, 8 H, calix CH₂), 1.23 [s, 36 H, calix C(CH₃)₃], 1.05 [s, 36 H, calix C(CH₃)₃] ppm. ¹³C NMR (125.8 MHz, [D₆]-acetone): $\delta = 160.0, 154.4, 154.1, 152.0, 151.0, 148.2, 142.2, 134.7, 128.5, 126.8, 126.4, 117.0, 116.4, 89.4, 75.2, 69.2, 69.1, 68.5, 68.4, 40.6, 39.6, 34.8, 34.5, 32.7, 32.1, 31.5$ (2 \times aliphatic C peaks missing) ppm. HRMS (ES, + mode): m/z calcd. for C₁₅₆H₁₈₈Fe₂N₈-Na₂O₂₀ 1325.6221 [M + 2Na]²⁺; found 1325.6239.

Supporting Information (see footnote on the first page of this article): Syntheses of compounds **3** and **7**; spectral characterization of macrocycles **4**, **5**, **8** and **9**; crystallographic information for structure of macrocycle **4**; protocols and further data from ¹H NMR spectroscopy and electrochemistry experiments.

Acknowledgments

N. H. E. wishes to thank the Engineering and Physical Sciences Research Council (EPSRC) for a DTA studentship. C. J. S. acknowledges the EPSRC and Johnson–Matthey for a CASE-sponsored studentship and the EPSRC for post-doctoral funding (PhD Plus). We express our appreciation to Dr. J. J. Davis (University of Oxford) for use of electrochemical equipment and our gratitude to Diamond Light Source for the award of beamtime on I19 (MT1858) and to the beamline scientists for help and support.

- [1] J. L. Sessler, P. A. Gale, W.-S. Cho, *Anion Receptor Chemistry*, RSC, UK, **2006**.
- [2] S. M. Rowe, S. Miller, E. J. Sorscher, *New Engl. J. Med.* **2005**, *352*, 1992–2001.
- [3] B. Moss, *Chem. Ind.* **1996**, 407–411.
- [4] K. Yoshihara, *Top. Curr. Chem.* **1996**, *176*, 17–35.
- [5] K. Dasgupta, J. V. Dyke, A. B. Kirk, W. A. Jackson, *Environ. Sci. Technol.* **2006**, *40*, 6608–6614.
- [6] For reviews, see: a) P. D. Beer, P. A. Gale, *Angew. Chem.* **2001**, *113*, 502–532; *Angew. Chem.* **2001**, *113*, 502; *Angew. Chem. Int. Ed.* **2001**, *40*, 486–516; b) R. Martínez-Máñez, F. Sancenón, *Chem. Rev.* **2003**, *103*, 4419–4476; c) S. R. Bayly, P. D. Beer, G. Z. Chen, in: *Ferrocenes: Ligands, Materials and Biomolecules* (Ed.: P. Štěpnička), Wiley, UK, **2008**, ch. 8, pp. 281–318; d) S. K. Kim, D. H. Lee, J.-I. Hong, J. Yoon, *Acc. Chem. Res.* **2009**, *42*, 23–31; e) J. W. Steed, *Chem. Soc. Rev.* **2009**, *38*, 506–509; f) R. M. Duke, E. B. Veale, F. M. Pfeffer, P. E. Kruger, T. Gunnlaugsson, *Chem. Soc. Rev.* **2010**, *39*, 3936–3953.
- [7] a) P. D. Beer, Z. Chen, A. J. Goulden, A. Graydon, S. E. Stokes, T. Wear, *J. Chem. Soc., Chem. Commun.* **1993**, 1834–1836; b) P. D. Beer, A. R. Graydon, A. O. M. Johnson, D. K. Smith, *Inorg. Chem.* **1997**, *36*, 2112–2118; c) O. Reynes, F. Maillard, J. C. Moutet, G. Royal, E. Saint-Aman, G. Stanciu, J. P. Dutasta, I. Gosse, J. C. Multatier, *J. Organomet. Chem.* **2001**, *637*–639, 356–363; d) B. Tomapatanaget, T. Tuntulani, O. Chailapakul, *Org. Lett.* **2003**, *5*, 1539–1542; e) C. Suksai, P. Leeladee, D. Jainuknan, T. Tuntulani, N. Muangsinsin, O. Chailapakul, P. Kongsaree, C. Pakavatchai, *Tetrahedron Lett.* **2005**, *46*, 2765–2769.
- [8] F. Otón, A. Tárraga, A. Espinosa, M. D. Velasco, P. Molina, *J. Org. Chem.* **2006**, *71*, 4590–4598.
- [9] M. D. Pratt, P. D. Beer, *Polyhedron* **2003**, *22*, 649–653.
- [10] N. H. Evans, C. J. Serpell, P. D. Beer, *New J. Chem.* **2011**, *35*, 2047–2053.
- [11] 1,1'-Bis(aminomethyl)ferrocene **3** was prepared by modifying a literature procedure: F. Ossola, P. Tomasin, F. Benetollo, E. Foresti, P. A. Vigato, *Inorg. Chim. Acta* **2003**, *353*, 292–300. See Supporting Information for details.
- [12] Additional ordering of the ferrocene moiety in the crystal is implied by the data. The diffuse nature of the scattering, however, prevented a full solution of this at this time. Crystallographic studies on further samples of macrocycle **4** are ongoing.
- [13] Attempts to produce the urea analogue of macrocycle **4** were thwarted by severe insolubility of the macrocycle, thereby preventing purification of the macrocyclization reaction. Hence the use of the solubilizing calix[4]arene in place of the polyether chain in macrocycle **8**.
- [14] M. D. Lankshear, N. H. Evans, S. R. Bayly, P. D. Beer, *Chem. Eur. J.* **2007**, *13*, 3861–3870.
- [15] The estimation of association constants assumes that the TBA salts are completely dissociated in the relatively competitive solvent CD₃CN. For some recent studies on this issue, see: a) C. Roelens, A. Vacca, C. Venturi, *Chem. Eur. J.* **2009**, *15*, 2635–2644; b) H. W. Gibson, J. W. Jones, L. N. Zakharov, A. L. Rheingold, C. Slebodnick, *Chem. Eur. J.* **2011**, *17*, 3192–3206.
- [16] M. J. Hynes, *J. Chem. Soc., Dalton Trans.* **1993**, 311–312.
- [17] To verify the appropriateness of this approach, for chloride it was calculated that the FcCH₂NH urea proton had a $K_a = 4.4 \times 10^2 \text{ M}^{-1}$, whereas that of the other NH had a $K_a = 4.5 \times 10^2 \text{ M}^{-1}$ compared to the average chemical shift giving $K_a = 4.5 \times 10^2 \text{ M}^{-1}$ as stated in Table 1.
- [18] See the Supporting Information for details of the assessment of the reversibility of macrocycles **4** and **8**.
- [19] The shift of the Fc/Fc⁺ redox wave to more negative potentials may be viewed as the binding of an anion that induces a potential shift of the electron transfer of the Fc/Fc⁺ redox couple, or alternatively as the process of electron transfer that changes the anion-binding affinity of the redox-active receptor, see: P. D. Beer, P. A. Gale, G. Z. Chen, *J. Chem. Soc., Dalton Trans.* **1999**, 1897–1909.
- [20] Solubility issues were encountered in the electrochemical titration experiments with dihydrogen phosphate and benzoate anions with macrocycle **4**. This resulted in surface adsorption of material, which led to restrictive diffusive access to the glassy carbon working electrode and accounts for the sigmoidal-shaped voltammograms observed in Figure 4 (a and b).
- [21] Z. Chen, A. R. Graydon, P. D. Beer, *J. Chem. Soc. Faraday Trans.* **1996**, *92*, 97–102.
- [22] Addition of TBABzO to ferrocene leads to no observable changes in the recorded CVs or SWVs.
- [23] See the Supporting Information for further CVs and SWVs of electrochemical anion titration experiments of macrocycle **4**.
- [24] A. J. Evans, S. E. Matthews, A. R. Cowley, P. D. Beer, *Dalton Trans.* **2003**, 4644–4650.

Received: November 10, 2011
Published Online: January 17, 2012

Structural Heterogeneity of Ag^I Complexes with a Flexible 1,2-Bis[(imidazol-2-yl)thiomethyl]benzene Ligand and Issues Regarding the Phase Purity of the Bulk Material

Liliana Dobrzańska*[a,b]

Keywords: Silver / Ligand flexibility / Coordination modes / Phase purity / X-ray diffraction

A series of Ag^I coordination compounds with a new ligand, 1,2-bis[(imidazol-2-yl)thiomethyl]benzene, and counterions such as PF₆[−], SbF₆[−], CF₃SO₃[−], BF₄[−] and NO₃[−] was characterised by powder and single-crystal XRD. Powder XRD revealed the presence of a mixture of crystallographic phases that were further identified by single-crystal XRD. Despite conformational flexibility, 1,2-bis[(imidazol-2-yl)thiomethyl]benzene has a tendency to form *N,N*-chelated Ag^I mononuclear cationic complexes with a linear N–Ag^I–N unit. However, T-shaped geometry (N₂O) around the silver ion was also observed, which involved solvent molecules and/or counterions. The formation of a cationic 1D chain with the *N,N'*-bridging ligand was revealed with the BF₄[−] counterion. Coordination compounds that possess different nuclearity were formed with the NO₃[−] counterion. In the dinuclear and trinuclear complexes, the ligand showed bischelating behaviour with N-donor atoms that interact with one and S-donor atoms with another metal centre. Furthermore, the crystal structure of the trinuclear complex revealed the presence of two crystallographically independent cationic moieties in the asymmetric unit, which only differ by a single O-donor ligand (NO₃[−] vs. H₂O), where both of the moieties possess three different geometries around the constituent silver ions. Argentophilic interactions are present in the majority of the reported structures. Available amine N atoms facilitate hydrogen bond formation and promote the occurrence of solvates.

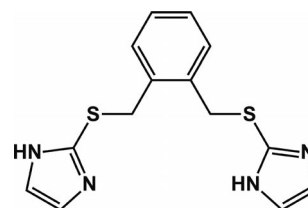
dination compounds that possess different nuclearity were formed with the NO₃[−] counterion. In the dinuclear and trinuclear complexes, the ligand showed bischelating behaviour with N-donor atoms that interact with one and S-donor atoms with another metal centre. Furthermore, the crystal structure of the trinuclear complex revealed the presence of two crystallographically independent cationic moieties in the asymmetric unit, which only differ by a single O-donor ligand (NO₃[−] vs. H₂O), where both of the moieties possess three different geometries around the constituent silver ions. Argentophilic interactions are present in the majority of the reported structures. Available amine N atoms facilitate hydrogen bond formation and promote the occurrence of solvates.

Introduction

During the last three decades, coordination chemistry has increasingly been involved with more elaborate ligands and studies of metal–organic complexes with extended structures of different topologies.^[1] This led to the discovery of new, interesting properties connected with porosity, chirality, magnetism and nonlinear optics, as well as the emergence of related applications for these materials.^[2] Imidazole-based ligands have been investigated for many years. Initially, complexes with simple imidazole rings were studied with focus on detailed spectroscopic and structural characteristics.^[3] When interest shifted to more complicated linkers, the incorporation of imidazole rings was justified by their reputation as effective N-donor building blocks.^[4]

In continuation of our studies on imidazole-based extended linkers,^[5] an investigation of the coordination chemistry of Ag^I complexes with a new ligand, 1,2-bis[(imidazol-2-yl)thiomethyl]benzene (**L**, Scheme 1), was undertaken.^[6] **L** is more flexible than ligands that we have previously studied due to the presence of a thioether linkage.^[7] How-

ever, the *ortho*-position of the thioimidazole substituents on the benzene ring provides some rigidity in **L**. Previously reported Ag^I complexes with a similar ligand, 1,2-bis(2-methylimidazol-1-ylmethyl)benzene (with 2-methylimidazole rings in the *ortho*-position), revealed the formation of 1D chains with PF₆[−], SbF₆[−] and BF₄[−] counterions in a metal/ligand ratio of 1:1 as the 2-methyl groups successfully prevent the formation of mononuclear species.^[8] As will be discussed further, elongation of the linker by the incorporation of an S-donor atom and, even more importantly, the presence of a free NH in the imidazole ring, make the prediction of the final products more complicated.



Scheme 1. 1,2-Bis[(imidazol-2-yl)thiomethyl]benzene (**L**).

Results and Discussion

All metal complexes were prepared similarly in a dark environment with an Ag/**L** ratio of 1:1 (0.2:0.2 mmol). A solution of silver salt (AgPF₆ for **1**, AgSbF₆ for **2**,

[a] Department of Chemistry, Katholieke Universiteit Leuven, Celestijnenlaan 200F, 3001 Heverlee, Belgium
Fax: +32-16-327-990
E-mail: lianger@chem.kuleuven.be

[b] Department of Chemistry and Polymer Science, Stellenbosch University,
Private Bag X1, Matieland 7602, South Africa

Supporting information for this article is available on the WWW under <http://dx.doi.org/10.1002/ejic.201100853>

AgCF₃SO₃ for **3**, AgBF₄ for **4** and AgNO₃ for **5** in MeOH (15 mL) was added to a solution of **L** in MeOH (25 mL). The mixture was stirred for a few minutes and the resulting clear solution was left to stand for ca. four weeks until crystalline material formed. Single crystals of **1–5** were isolated from each vial and XRD measurements were performed to reveal the presence of [AgL]PF₆·CH₃OH (**1a**) in **1**, [AgL]SbF₆ (**2a**) in **2**, [AgL]CF₃SO₃·H₂O (**3a**) in **3**, {[AgL]BF₄}_n (**4a**) in **4** and [Ag₂L(NO₃)₂] (**5a**) in **5**.

Powder XRD Studies

Powder XRD (XRPD) analyses were performed to assess the purity of the phases obtained.^[9a] As there was no agreement between the powder patterns generated from the single-crystal structures (labelled as **a**) and the measured powder patterns of the corresponding bulk material (Supporting Information, Figures S1–S5),^[9b] a further study was performed to identify the remaining crystallographic phases. This way, new crystal structures were revealed (Table S1). PowderCell 2.4 freeware was used to further estimate the percentage of the respective crystallographic phases (Figures S6–S9).^[9c] It is not certain that all the phases were identified, but the results seem to indicate that at the time of the XRPD measurement, the respective compositions were as follows. Complex **1b**, which contains water molecules in the crystal lattice, was the major component of **1** (more than 50%). Complex **2b**, which also contains water molecules, was the dominant phase in **2** (over 80%). In **4**, mononuclear **4b** was the major constituent (ca. 80%) over polynuclear complex **4a**. Complexes **5c** and **5a**, which show bischelating behaviour and have coordinated nitrate ions, were the preferred phases in **5**, and the presence of mononuclear, cationic **5b** was negligible.

Single-Crystal XRD Studies

Crystal Structures of **1a**, **1b**, **1c** and **1d** Formed with PF₆[−] (Bulk Material **1**)

[AgL]PF₆·CH₃OH (**1a**)

Complex **1a** crystallises in the monoclinic space group *P*2₁/*c* and contains one mononuclear cationic Ag^I complex, one PF₆[−] counterion and one molecule of methanol in the asymmetric unit (Figure 1). The silver atom in the complex is linearly coordinated by the two imine N atoms that originate from the chelating imidazole rings of the ligand (for bond lengths, see Table 2). The ligand adopts a folded conformation (Table 3) with a dihedral angle of ca. 34° between the planes of the imidazole rings and the benzene ring. The methanol molecule interacts with the amine N atom of the cationic unit and the counterion by hydrogen bonding.

The solvent molecule acts as a hydrogen bond acceptor and donor simultaneously (Table S2). The distance between neighbouring Ag ions indicates the presence of very weak interactions between the Ag centres from nearby mononuclear units (this conclusion was drawn by comparison with

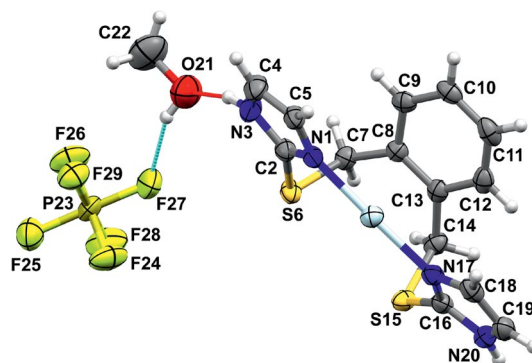


Figure 1. Asymmetric unit of **1a** with displacement ellipsoids drawn at the 50% probability level and hydrogen bonding shown in red and blue.

the results below; see also Table 4)^[10] supported by weak interactions between imidazole rings from corresponding mononuclear complexes with a centroid–centroid distance of 3.507(2) Å (symmetry operation: $-x, 1-y, -z$). Looking down the *b* axis, columns of dimeric cationic complexes stacked above each other are observed. These interact further by C5–H5···S6^{#4} interactions [C5···S6 3.396(4) Å, for symmetry operations, see Table S2]. The dimeric units expand along the *c* axis and are further held together by C–H···π interactions between C10–H10···Cg1^{#6} [where Cg1 is the centroid of the benzene ring belonging to the dimeric unit from a neighbouring column; C10···Cg1 3.545(4) Å] to form layers. These layers are separated by rows of alternating pairs of solvent molecules and counterions (Figure 2). Weak N–H···F and C–H···F interactions support the packing (Table S2).

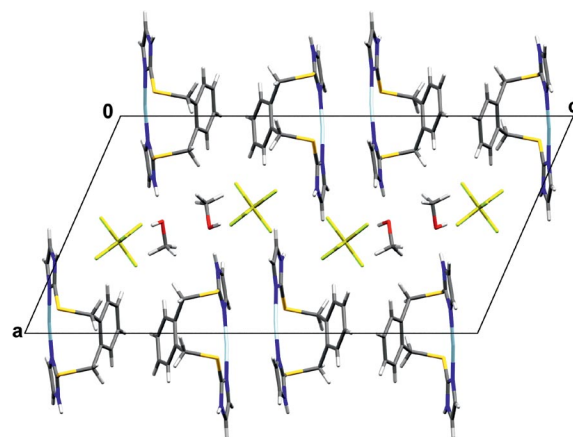


Figure 2. Representation of the packing of **1a** viewed down the *b* axis.

[AgL]PF₆·H₂O (**1b**)

The unit cell parameters of the crystal structure of **1b** are very similar to those of **1a**, as are the main structural features of the compound (the same type of coordination sphere around the metal atom in the monomeric cationic complex). A water molecule takes more or less the same space that was previously occupied by the methanol mole-

cule but it is badly disordered and modelled in four positions. An interaction between the water molecule and the counterions is suspected but is not confirmed due to the disorder present. The smaller size of solvent molecules causes the neighbouring mononuclear cationic complexes to pack closer, which shortens the distance between the silver ions (Table 4). This is also noticeable by a minor decrease of the length of the *c* axis (Table 1). Negligible changes can also be seen in the position of the counterions. The water molecule shows interactions with the amine N atom. It might also interact with the counterions, but the disorder present renders it impossible to make any further assumptions.

[AgL]PF₆·*x*CH₃OH·*x*H₂O (1c)

Complex **1c** crystallises in the monoclinic space group *C2/c* with unit cell parameters different from those of **1a/1b** but very close to those obtained for **2b** (Table S1). Unfortunately, the quality of the crystals was too poor to fully characterise the compound.

[AgLCH₃O(H)_{0.5}](PF₆)_{0.5} (1d)

Complex **1d** crystallises in the same monoclinic space group *P2₁/c* as **1a** and **1b**, but the unit cell parameters, the conformation of the ligand and the packing are completely different. It consists of one mononuclear cationic unit, [AgLCH₃O(H)_{0.5}], and half a PF₆[−] ion (the P atom is lo-

Table 1. Crystal data and details of the refinement parameters for the crystal structures originating from crystalline bulk material **1–5**.

	1a	1b	1d	2a	2b
Formula	C ₁₅ H ₁₈ AgF ₆ N ₄ OPS ₂	C ₁₄ H ₁₆ AgF ₆ N ₄ OPS ₂	C ₃₀ H ₃₅ Ag ₂ F ₆ N ₈ O ₂ PS ₄	C ₁₄ H ₁₄ AgF ₆ N ₄ S ₂ Sb	C ₂₈ H ₃₄ Ag ₂ F ₁₂ N ₈ O ₃ S ₄ Sb ₂
Formula weight	587.29	573.27	1028.61	646.03	1346.11
Crystal system	monoclinic	monoclinic	monoclinic	triclinic	monoclinic
Space group	<i>P2₁/c</i>	<i>P2₁/c</i>	<i>P2₁/c</i>	<i>P</i> $\bar{1}$	<i>C2/c</i>
<i>T</i> [K]	100(2)	100(2)	100(2)	100(2)	100(2)
λ [Å]	0.71073	0.71073	0.71073	0.71073	0.71073
<i>a</i> [Å]	12.9254(13)	12.9855(15)	11.1343(14)	8.7694(11)	28.540(2)
<i>b</i> [Å]	7.1323(7)	7.0940(8)	20.194(3)	10.5672(14)	7.0078(6)
<i>c</i> [Å]	24.719(3)	24.637(3)	8.5647(11)	11.6747(15)	24.697(2)
α [°]	90	90	90	73.364(2)	90
β [°]	113.873(2)	115.260(2)	105.204(2)	70.131(2)	120.7380(10)
γ [°]	90	90	90	80.474(2)	90
<i>V</i> [Å ³]	2083.8(4)	2052.5(4)	1858.3(4)	972.1(2)	4245.6(6)
<i>Z</i>	4	4	2	2	4
<i>D</i> _{calc} [g cm ^{−3}]	1.872	1.855	1.838	2.207	2.106
μ Mo- <i>K</i> α [mm ^{−1}]	1.313	1.330	1.394	2.675	2.459
Crystal size [mm]	0.31 × 0.27 × 0.23	0.27 × 0.17 × 0.13	0.17 × 0.13 × 0.04	0.32 × 0.27 × 0.19	0.31 × 0.28 × 0.20
Unique reflections (<i>R</i> _{int})	4960 (0.0390)	4877(0.0514)	3862 (0.0639)	4419 (0.0185)	4995 (0.0390)
Reflections with <i>I</i> > 2 σ (<i>I</i>)	4699	4007	2998	4194	3965
Refined parameters	275	295	243	253	313
<i>R</i> ₁ ^[a] , <i>wR</i> ₂ ^[b] [<i>I</i> > 2 σ (<i>I</i>)]	0.0470, 0.1236	0.0719, 0.1746	0.0639, 0.1485	0.0228, 0.0544	0.0367, 0.0768
<i>R</i> ₁ ^[a] , <i>wR</i> ₂ ^[b] (all data)	0.0488, 0.1250	0.0892, 0.1834	0.0840, 0.01584	0.0247, 0.0554	0.0525, 0.0829
Goodness-of-fit on <i>F</i> ²	1.099	1.098	1.050	1.075	1.001
	3a	4a	5a	5b	5c
Formula	C ₁₅ H ₁₆ AgF ₃ N ₄ O ₄ S ₃	C ₁₄ H ₁₄ N ₄ S ₂ Ag·BF ₄	C ₁₄ H ₁₄ Ag ₂ N ₆ O ₆ S ₂	C ₁₄ H ₁₄ N ₄ S ₂ AgNO ₃ · <i>x</i> H ₂ O	C ₅₆ H ₆₆ Ag ₆ N ₂₂ O ₂₃ S ₈
Formula weight	577.40	497.09	642.17	472.29	2319.01
Crystal system	triclinic	triclinic	triclinic	triclinic	triclinic
Space group	<i>P</i> $\bar{1}$	<i>P</i> $\bar{1}$	<i>P</i> $\bar{1}$	<i>P</i> $\bar{1}$	<i>P</i> $\bar{1}$
<i>T</i> [K]	100(2)	100(2)	100(2)	100(2)	100(2)
λ [Å]	0.71073	0.71073	0.71073	0.71073	0.71073
<i>a</i> [Å]	9.5218(13)	7.1716(19)	8.0267(8)	9.5430(6)	8.1077(4)
<i>b</i> [Å]	10.1352(14)	11.525(3)	9.8371(10)	11.6976(8)	20.6967(12)
<i>c</i> [Å]	11.6408(16)	12.239(3)	13.6870(14)	17.2051(11)	24.0920(13)
α [°]	72.271(2)	107.444(4)	102.580(2)	84.1350(10)	94.4590(10)
β [°]	74.598(2)	101.474(4)	102.482(2)	82.6390(10)	90.1730(10)
γ [°]	82.707(2)	107.357(4)	105.798(2)	79.7250(10)	98.8550(10)
<i>V</i> [Å ³]	1030.3(2)	873.7(4)	970.30(17)	1868.0(2)	3982.0(4)
<i>Z</i>	2	2	2	4	2
<i>D</i> _{calc} [g cm ^{−3}]	1.861	1.889	2.198	1.679	1.934
μ Mo- <i>K</i> α [mm ^{−1}]	1.340	1.439	2.281	1.325	1.742
Crystal size [mm]	0.34 × 0.19 × 0.17	0.24 × 0.21 × 0.03	0.18 × 0.09 × 0.02	0.23 × 0.11 × 0.03	0.34 × 0.27 × 0.07
Unique reflections (<i>R</i> _{int})	4776 (0.0366)	4024 (0.0628)	4451 (0.0333)	8565 (0.0298)	14825 (0.0513)
Reflections with <i>I</i> > 2 σ (<i>I</i>)	4148	3270	3806	7843	11831
Refined parameters	271	235	271	451	1106
<i>R</i> ₁ ^[a] , <i>wR</i> ₂ ^[b] [<i>I</i> > 2 σ (<i>I</i>)]	0.0415, 0.0915	0.0806, 0.1957	0.0477, 0.1102	0.0583, 0.1367	0.0448, 0.0888
<i>R</i> ₁ ^[a] , <i>wR</i> ₂ ^[b] (all data)	0.0501, 0.0958	0.1013, 0.2079	0.0594, 0.1163	0.0646, 0.1398	0.0612, 0.0945
Goodness-of-fit on <i>F</i> ²	1.040	1.048	1.047	1.167	1.031

[a] $R_1 = \sum ||F_o| - |F_c|| / \sum |F_o|$. [b] $wR_2 = \{\sum [w(F_o^2 - F_c^2)^2] / \sum [w(F_o^2)^2]\}^{1/2}$.

cated on an inversion centre). The methanol molecule is coordinated to the metal centre and, to balance the charge, is partially deprotonated. The cationic complex in this compound is triangular as the result of the conformation adopted by the ligand, with one of the thioether bridges pointing above and the other below the plane of the benzene ring and the imidazole rings tilted towards each other with a dihedral angle between their planes of $42.8(2)^\circ$ (Figure 3).

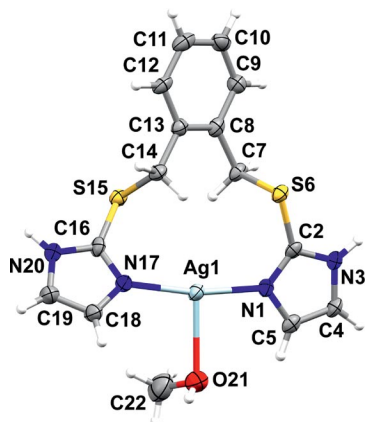


Figure 3. Representation of the cationic complex in **1d** with displacement ellipsoids drawn at the 50% probability level.

The coordinated methanol molecule [Ag1–O21 2.568(6) Å] together with the imine N atoms from the chelating ligand form a T-shaped geometry around the Ag ion. There are no argentophilic interactions present. The amine N atom interacts with the counterions that are additionally involved in interactions with the methanol molecules (Table S2). Hydrogen bonding of the latter probably causes the distortion from linearity of the N–Ag–N unit with an angle of $167.9(2)^\circ$. Furthermore, π – π interactions are present between neighbouring N1–C5 imidazole rings as well as C–H \cdots π interactions between C12–H12 \cdots Cg2^{#6} [where Cg2 is the centroid of the N1–C5 imidazole ring with a C \cdots Cg2 distance of 3.324(6) Å] and C4–H4 \cdots S15^{#5} contacts [C \cdots S 3.774(6) Å], which support the packing.

Crystal Structures of **2a** and **2b** Formed with SbF_6^- (Bulk Material **2**)

$[\text{AgL}]\text{SbF}_6$ (**2a**)

Complex **2a** crystallises in the triclinic space group $P\bar{1}$, with one cationic $[\text{AgL}]^+$ complex and one SbF_6^- counter-

ion in the asymmetric unit. There are no solvent molecules present. The silver ion is linearly coordinated by the two N atoms that originate from the imidazole rings of the chelating ligand (for bond lengths, see Table 2), and the ligand has a folded conformation with both thioether bridges on the same side of the plane of the benzene ring (Table 3). The values of the two C–C–S–C torsion angles are disproportionate, which causes the benzene ring to tilt to one side. Argentophilic interactions are present (Table 4) and form a dimeric species supported by π – π interactions between neighbouring imidazole rings with a distance of 3.632(2) Å between the corresponding centroids.

In the packing motif, cationic silver complexes linked in dimers are stacked above each other (as in **1a** and **1b**) with benzene rings from neighbouring columns in the same row pointing in opposite directions (as they are related by an inversion centre, Figure 4). The rows are separated by counterions. N–H \cdots F and C–H \cdots F hydrogen bonds support the close packing (Table S2).

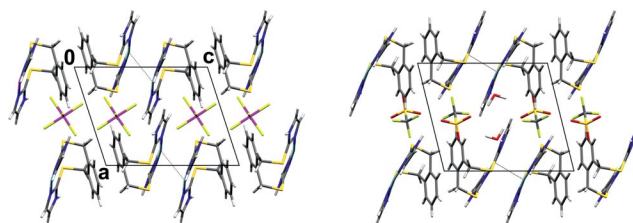


Figure 4. Representation of the packing viewed down the *b* axis for **2a** (left) and **3a** (right); argentophilic interactions are shown as dashed grey lines.

$[\text{AgL}]\text{SbF}_6 \cdot 1.5\text{H}_2\text{O}$ (**2b**)

Complex **2b** crystallises in the monoclinic space group $C2/c$. There is one mononuclear cationic silver complex, one counterion and 1.5 water molecules in the asymmetric unit. The silver ion is linearly coordinated by two imine N atoms from the chelating ligand (see Table 2), and the ligand adopts a folded conformation (see Table 3).

The cationic complex forms dimers that are held together by argentophilic interactions, which are supported by weak interactions between opposite imidazole rings with a centroid–centroid distance of 3.653(3) Å (symmetry operation: $1/2 - x, 1/2 - y, -z$). Looking down the *b* axis, the packing of the cationic complexes resembles that of **1a/1b**, i.e. with the formation of rows that consist of dimeric units with benzene rings from neighbouring columns pointing in the same direction. This enables C–H \cdots π interactions, namely, C11–H11 \cdots Cg1^{#7} (where Cg1 is the centroid of

Table 2. Selected bond lengths [Å] and angles [$^\circ$] for mononuclear **1–5**.

	1a	1b	1d	2a	2b	3a	5b
Ag1–N1	2.088(3)	2.090(6)	2.113(5)	2.108(2)	2.095(3)	2.109(3)	2.133(5)/2.132(5)
Ag1–N17	2.085(3)	2.092(6)	2.133(5)	2.125(2)	2.097(3)	2.107(3)	2.134(4)/2.137(4)
Ag2–O21			2.568(6)				
N17–Ag1–1	173.39(11)	171.9(2)	167.9(2)	170.63(7)	171.74(12)	172.28(11)	163.66(17)/163.39(1)
N1–Ag1–O21			89.20(18)				
N17–Ag1–O21			99.77(19)				

Table 3. Torsion angles [°] that show the flexibility of the ligand in the Ag^I complexes, for corresponding values in **5c**, see main text.

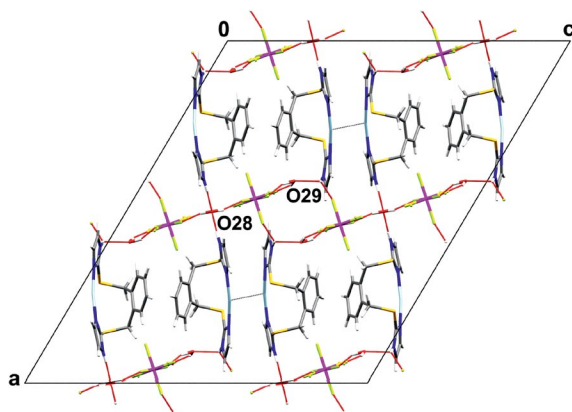
	C8–C7–S6–C2	C13–C14–S15–C16
1a	55.3(3)	–56.6(3)
1b	56.3(6)	–54.2(6)
1d	170.3(4)	–177.6(4)
2a	41.3(2)	–68.6(2)
2b	52.9(4)	–58.6(3)
3a	59.8(3)	–55.3(3)
4a	71.9(7)	–175.0(6)
5a	49.7(4)	–51.0(4)
5b	63.9(5)/64.4(5)	–60.8(6)/–57.1(5)

Table 4. Argentophilic interactions.^[10]

	Silver–silver interaction [Å]
1a	3.4459(6) intermolecular
1b	3.3621(9) intermolecular
1d	–
2a	3.2378(5) intermolecular
2b	3.3418(6) intermolecular
3a	3.2845(6) intermolecular
4a	3.4474(14) intermolecular
5a	2.9558(6) intramolecular
5b	–
5c	3.0919(5) and 3.2082(5) (moiety I) intramolecular 3.1376(5) and 3.1653(5) (moiety II)

benzene ring C8–C13) with a C⋯Cg1 distance of 3.468(5) Å (Table S2). However, the hydrogen bonding net formed is complicated by the presence of a higher number of solvent molecules.

The water molecule with O28 acts as a bifurcated hydrogen-bond acceptor of the amine N–H from two distinct ligands and a hydrogen-bond donor in interactions with counterions, whereas the remaining water molecule (O29) interacts as a hydrogen-bond acceptor of one of the amine N–H groups and as a donor to counterions (Table S2, Figure 5).

Figure 5. Representation of the packing for **2b** viewed down the *b* axis; argentophilic interactions are shown as dashed grey lines, hydrogen bonds that involve water molecules are shown as red lines.

Crystal Structure of **3** Formed with CF₃SO₃[–] (Bulk Material **3**)

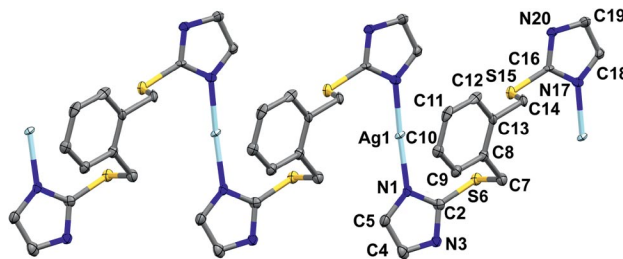
[AgL]CF₃SO₃·H₂O (**3a**)

Complex **3a** crystallises in the triclinic space group *P* $\bar{1}$ with unit cell parameters that are very similar to those observed for **2a**. Likewise, the packing is very similar to that of **2a** (Figure 4). The presence of water molecules and an elongated counterion in the crystal lattice influences the length of the *a* axis, which is ca. 0.75 Å longer than that in **2a**. The *b* axis, however, is slightly shorter, which could be caused by a small difference in the ligand conformation (see Table 3). Interactions between water molecules, triflate and the silver(I) complex further stabilise the packing (see Table S2).

Crystal Structures of **4a** and **4b** Formed with BF₄[–] (Bulk Material **4**)

{[AgL]BF₄}_{*n*} (**4a**)

Complex **4a** crystallises in the triclinic space group *P* $\bar{1}$. The cationic Ag^I complex forms 1D zigzag chains along the *a* axis, with the silver ions coordinated in a linear fashion by imine N atoms that originate from two distinct ligands (bridging mode, Figure 6). The conformation of the ligand facilitates this type of assembly (see Table 3).

Figure 6. Fragment of the cationic chain in **4a**; H atoms are omitted for clarity; displacement ellipsoids drawn at the 50% probability level. Selected bond lengths [Å] and angles [°]: Ag1–N1 2.093(8), Ag1–N17ⁱ 2.065(7), N17–Ag1–N1ⁱ 175.5(3). Symmetry operation: ⁱ: *x* + 1, *y*, *z*.

The bond lengths in the cationic unit are more or less in agreement with the distances observed for similar compounds (vide supra) with a C2–S6 distance of 1.727(9) Å in its shortest range [shorter bonds were reported for a Cd^{II} complex with deprotonated 4-(2-benzimidazolethiomethyl)-benzoic acid]^[11] and a long C16–N17 distance of 1.369(11) Å (for 22 bond lengths of a similar kind found in the crystal structure database, the mean is 1.324 Å).

The chains formed interact by argentophilic interactions with neighbouring chains to result in infinite strands supported by π – π interactions between corresponding imidazole rings (N1–C5) and (C16–N20) with a centroid–centroid distance of 3.722(6) Å and symmetry operation $-x, 2-y, 1-z$. Weak C–H⋯F and N–H⋯F hydrogen bonds between the cationic part and counterions stabilise the packing (see Table S2).

$[AgL]BF_4 \cdot xCH_3OH \cdot xH_2O$ (**4b**)

The quality of the crystals of **4b** was not sufficient to fully characterise the structure (see Table S1). The compound crystallises in the monoclinic space group $P2_1/c$ with unit cell parameters very similar to those obtained for **1a/1b**. The a and c axes are ca. 0.15 and 0.5 Å, respectively, which are shorter than those of the corresponding solvate **1b** and is attributed to the smaller size of the BF_4^- counterion.

Crystal Structures of 5a, 5b and 5c Formed with NO_3^- (Bulk Material 5)

$[Ag_2L(NO_3)_2]$ (**5a**)

Complex **5a** crystallises in the centrosymmetric space group $P\bar{1}$ (triclinic system). It has a 2:1 Ag/L molar ratio even though it was isolated from bulk material prepared with a molar ratio of 1:1. The resulting structure is unique as **L** shows bischelating behaviour (Figure 7). Ag1 is coordinated by imine N atoms to yield a linear geometry around the metal centre, which is distorted from linearity by interactions with nitrate counterions, namely, O24 [Ag–O 2.710(5) Å] and O23 [Ag–O 2.682(5) Å], which come from a symmetry related counterion (symmetry operation: $1 - x, -y, -z$). Defining the above mentioned O atoms with an Ag–O distance of ca. 2.7 Å as bonded, the complex could be described as a dimer with a seesaw geometry around Ag1 and a τ_4 value of 0.59.^[12] Ag2 is chelated by S-donor atoms that participate in its distorted tetrahedral environment (AgS_2O_2), whereby O atoms (O21 and O25) originate from two distinct nitrate counterions ($\tau_4 = 0.71$). Very strong intramolecular argentophilic interactions are present between the two metal centres, with a distance of ca. 2.96 Å, which is only slightly longer than that for metallic silver (2.89 Å).^[13]

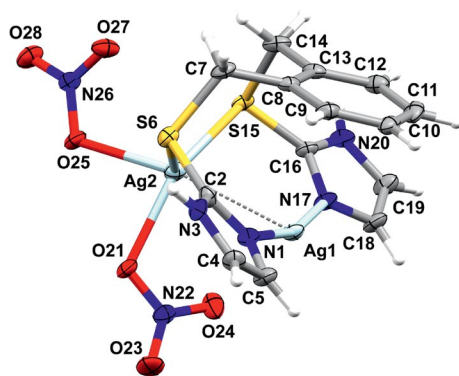


Figure 7. Molecular structure of **5a** with displacement ellipsoids drawn at the 50% probability level; argentophilic interactions are shown as dashed grey lines. Selected bond lengths [Å] and angles [°]: Ag1–N1 2.152(4), Ag1–N17 2.161(4), N17–Ag1–N1 163.56(16), Ag2–O21 2.334(4), Ag2–O25 2.417(4), Ag2–S6 2.539(1), Ag2–S15 2.475(1), O21–Ag2–O25 83.29(12), O21–Ag2–S15 146.52(9), O25–Ag2–S15 98.72(9), O21–Ag2–S6 98.42(10), O25–Ag2–S6 102.93(9), S15–Ag2–S6 113.41(4).

Not taking into account Ag2, the resulting packing (looking down the b axis) is reminiscent of that of **2a** and **3a**. However, intermolecular argentophilic interactions be-

tween neighbouring Ag1 atoms (distance ca. 4.46 Å) are not observed, which is due to the presence of the second silver centre, Ag2. For the same reason, there are no π – π interactions between imidazole rings from neighbouring units. In addition, the unit cell parameters are comparable with those of **2a** and **3a** with a shorter a axis, which is a result of much smaller counterions, and a longer c axis because of an additional silver atom.

The packing is stabilised by weak C10–H10...Cg3^{#3} hydrogen bonds [where Cg3 is the centroid of C16–N20, C10...Cg3 3.558(6) Å], as well as by many other weak C–H...O and N–H...O hydrogen bonding interactions (see Table S2).

$[AgL]NO_3 \cdot xH_2O$ (**5b**)

Complex **5b** crystallises in the centrosymmetric space group $P\bar{1}$ (triclinic system) with two cationic mononuclear metal complexes and two nitrate counterions in the asymmetric unit. The conformation of the ligand differs only slightly in the two cationic complexes. The silver ions are linearly coordinated by imine N atoms that originate from the chelating ligands (Figure 8), and the ligands adopt a folded conformation.

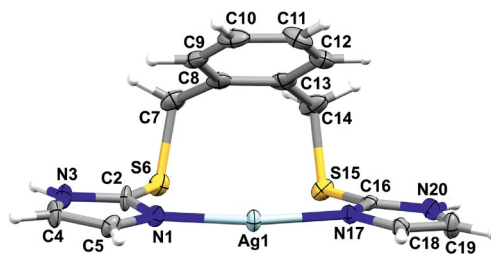


Figure 8. Representation of the cationic complex in **5a** with displacement ellipsoids drawn at the 50% probability level.

There is a noticeable distortion of AgN_2 from linearity (see Table 2), which could be caused by weak interactions with the nitrate O atoms [O23/O22A and O23A that are in the proximity (ca. 3.1 Å) of Ag1/Ag1A, respectively]. Looking down the a axis, columns of cationic complexes that consist exclusively of Ag1 or Ag1A units stacked above each other can be seen. The distance between the nearest Ag1 and Ag1A in those columns is 4.1084(6) Å, which shows the lack of interactions between these metal centres.^[10] Instead, the small nitrate counterions, which are located between the C1–N5/C1A–N5A imidazole rings of the stacked cationic units, form hydrogen bonds with the NH group of these as well as with the NH group from C16–N20/C16A–N20A of the adjacent columns. There are no π – π interactions present in the packing, which is stabilised by weak C–H...S and C–H...O interactions (Table S2). As the solvent molecules could not be modelled, and the final model was refined without them (by applying the SQUEEZE routine of PLATON), full analysis of the resulting packing was impossible.

$[Ag_3L_2NO_3][Ag_3L_2H_2O](NO_3)_5 \cdot 4H_2O$ (**5c**)

Complex **5c** crystallises in the centrosymmetric space group $P\bar{1}$ (triclinic system) and, just as **5a**, it shows an Ag/L

molar ratio of 1.5:1, even though it originated from bulk material prepared with a molar ratio of 1:1. Interestingly, there are two crystallographically independent cationic trinuclear moieties present in the asymmetric unit, as well as five nitrate counterions and four water molecules. Each cationic unit involves two folded **L** molecules with torsion angles C8–C7–S6–C2 –50.7(5)°, C13–C14–S15–C16 48.4(5)°, C28–C27–S26–C22 –45.0(4)°, C33–C34–S35–C36 55.5(4)°, C48–C47–S46–C42 50.3(4)°, C53–C54–S55–C56 –53.4(4)°, C68–C67–S66–C65 52.9(4)°, C73–C74–S75–C78 –53.9(4)°. The ligands show bischelating (*N,N*- and *S,S*-) behaviour as observed in **5a**. Furthermore, in each moiety there are three different geometries around the metal centres present in the structure. Namely, a linear geometry (AgN₂) is formed by one *N,N*-chelating ligand, a distorted tetrahedral environment (AgS₄) is formed by two *S,S*-chelating ligands and a T-shaped (AgN₂O) geometry is built up by the second *N,N*-chelating ligand and, surprisingly, by the counterion in one of the cationic moieties (moiety I) and the water molecule in the other one (moiety II, Figure 9). As a result, these two cationic units have different charges. They interact by hydrogen bonds such as N80–H80⋯O88, which involve the amine N atom from one of the imidazole rings of moiety II and the O atom from the coordinated nitrate anion (N86), and O81–H81B⋯O89^{#1} (for symmetry operation, see Table S2), which involve both

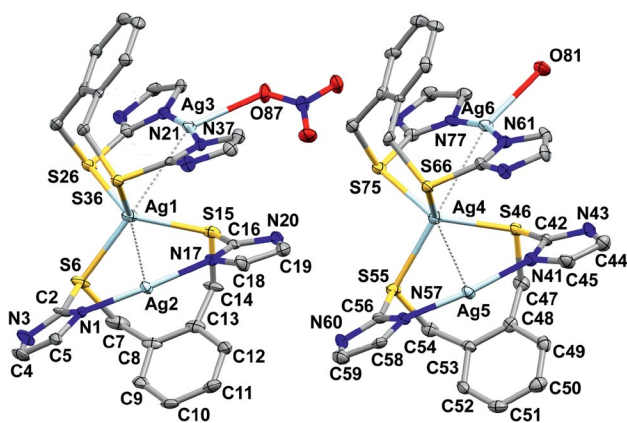


Figure 9. Representation of the two trinuclear cationic moieties with different O-donor ligands coordinated at one of the silver centres present in the asymmetric unit of **5c**. Hydrogen atoms and some labels are omitted for clarity; displacement ellipsoids drawn at the 50% probability level; intramolecular argentophilic interactions are shown as dashed grey lines. Selected bond lengths [Å] and angles [°]: (moiety I) Ag1–S15 2.538(1), Ag1–S35 2.558(1), Ag1–S6 2.603(1), Ag1–S26 2.604(1), N1–Ag2 2.115(4), Ag2–N 17 2.120(4), Ag3–N21 2.120(4), Ag3–N37 2.121(4), Ag3–O87 2.642(3), S15–Ag1–S35 112.77(4), S15–Ag1–S6 110.23(5), S35–Ag1–S6 120.64(5), S15–Ag1–S26 115.85(5), S35–Ag1–S26 106.98(4), S6–Ag1–S26 88.27(4), N1–Ag2–N17 168.35(16), N21–Ag3–N37 167.82(15), O87–Ag3–N21 85.19(13), O87–Ag3–N37 106.91(13); (moiety II) Ag4–S46 2.547(1), Ag4–S66 2.548(1), Ag4–S75 2.619(1), Ag4–S55 2.623(1), Ag5–N57 2.103(4), Ag5–N41 2.121(4), Ag6–N61 2.137(4), Ag6–N77 2.141(4), Ag6–O81 2.467(3), S46–Ag4–S66 113.02(4), S46–Ag4–S75 122.81(4), S66–Ag4–S75 102.82(4), S46–Ag4–S55 104.63(4), S66–Ag4–S55 123.51(4), S75–Ag4–S55 89.40(4), N57–Ag5–N41 169.19(15), N61–Ag6–N77 164.56(15), N61–Ag6–O81 102.26(14), N77–Ag6–O81 93.11(14).

coordinated O-donor ligands to form four-membered units. These are further interlinked by the counterion (N82) with hydrogen bonds O81–H81A...O85 and N23–H23...O83^{#5} into a 1D chain that expands along the *b* axis (Figure 10).

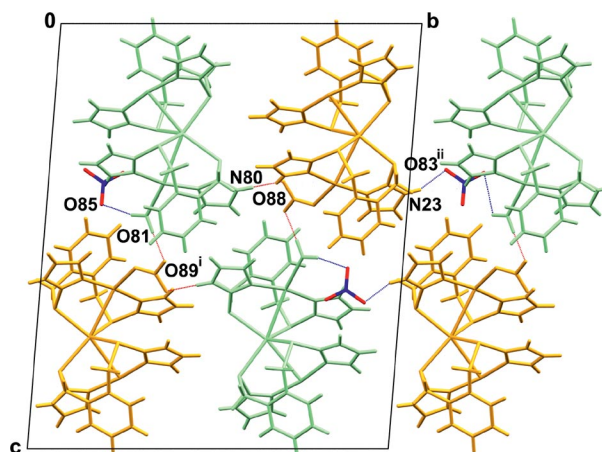


Figure 10. Fragment of the hydrogen bonded 1D chain in **5c** that consists of moieties I (orange) and II (green) shown in capped sticks representation. Symmetry operations: ⁱ: $-x + 1, -y + 1, -z + 1$; ⁱⁱ: $x, y + 1, z$.

There are weak interactions present between Ag2 and O91/O91A and O93/O93A from the disordered nitrate counterion (N90) with distances of 2.70(2)–2.96(2) Å and between Ag5 and O103, O104 from another counterion (N102) with distances of 2.896(4) and 2.722(4) Å, respectively. The counterions N90 and N94 form hydrogen bonds with water molecule O115, which acts as a donor in this case but it is also a bifurcated hydrogen-bond acceptor for amine hydrogen atoms (H20–N20 and H40–N40). The counterions, N98 and N102 and three water molecules, such as O106, O109 and O112, form hydrogen bonded chains, which run along the *a* axis and interact by N–H...O with chains of cationic moieties to result in a 3D assembly. There are also other weak hydrogen bonds that support the packing (Table S2).

It seems that only one of the amine N atoms (N60) is not involved in the net of hydrogen bonds. A methanol molecule might have been present in the neighbourhood, which was lost as the crystals dried, to cause disorder of the N90 nitrate counterion and also yield the small solvent accessible voids nearby in the crystal lattice (PLATON estimates the accessible space to be 2.4% of the total cell volume).^[14]

Intramolecular argentophilic interactions (Table 4) and π - π interactions between imidazole rings (C16–N20 and C37–N40, N41–C45 and N61–C65) with centroid–centroid distances of ca. 3.4 Å are present in both trinuclear units.

Conclusions

This paper tackles the problem of the characterisation of the composition of bulk crystalline material. The presence of mixtures can be easily overlooked by C, H, N elemental analyses. It is still common practice among researchers to select one crystal from the final crystalline material and to

present this specimen as representative for the entire solid fraction. There is no requirement in journals to provide powder patterns as a proof of phase purity for solid samples.^[15] Therefore, the results can actually be very misleading and one might wonder how many papers describe elaborate solid-state studies performed on a mixture of metal–organic complexes. This is especially a risk in instances where research is conducted on extended, flexible (often multidonor) ligands and/or ligands that contain functional groups or atoms that have a tendency to form hydrogen bonds. In the latter case, the presence of solvates, and the replacement of the crystallisation solvent molecules with water upon exposure to air, seem to be very likely.^[16] The coordinating abilities of the counterions complicate matters even further.

1,2-Bis[(imidazol-2-yl)thiomethyl]benzene (**L**) is a good example of a ligand that is difficult to work with due to the heterogeneity of the crystalline material obtained. The amine nitrogen atoms increase the affinity to form different solvates through hydrogen bonding, which is not the case for imidazole-based linkers without an available amine N atom. The presence of additional S-donor atoms makes any structural prediction even more complicated. The ligand generally shows a tendency to form discrete *N,N*-bidentate mononuclear Ag^I complexes with a linear geometry around the metal centre, induced by the chelating imine nitrogen atoms of the folded ligand, with the imidazole rings approximately coplanar. However, other modes of coordination can also take place, such as *N,N'*-bridging, participation of S-donor atoms or a T-shaped geometry around the silver atom, brought about by the chelating N atoms of the ligand in combination with solvent molecules or counterions.

Further studies that aim to control both the conformation of the ligand and the coordination modes, which involve exocyclic S-donor sites as in **5a** and **5c**, are ongoing.

Experimental Section

Reagents: All commercially available chemicals were of reagent grade and were used without further purification. 1,2-Bis[(imidazol-2-yl)thiomethyl]benzene (**L**) was synthesised by the S_N2 reaction of 2-mercaptoimidazole with α,α' -dibromo-*o*-xylol in MeOH. ¹H NMR (300 MHz, [D₆]DMSO): δ = 12.16 (br. s, 2 H), 7.15 (m 4 H), 7.06 (s, 4 H), 4.34 (s, 4 H) ppm. ¹³C NMR (100 MHz, [D₆]DMSO): δ = 138.1, 135.9, 130.1, 127.6, 35.2 ppm. C₁₄H₁₄N₄S₂ (302.41): calcd. C 55.60, H 4.67, N 18.53; found C 55.49, H 4.89, N 18.61.

Crystalline Bulk Materials: Compound **1** was obtained by the reaction of AgPF₆ with **L**. From this batch, four different crystal structures were determined: [AgL]PF₆·CH₃OH (**1a**), [AgL]PF₆·H₂O (**1b**), [AgL]PF₆·xCH₃OH·xH₂O (**1c**) and [AgLCH₃O(H)_{0.5}](PF₆)_{0.5} (**1d**). Compound **2** was obtained by the reaction of AgSbF₆ with **L**. From this batch, two different crystal structures were determined: [AgL]SbF₆ (**2a**) and [AgL]SbF₆·1.5H₂O (**2b**). Compound **3** was obtained by the reaction of AgCF₃SO₃ with **L**. From this batch, one crystal structure was determined: [AgL]CF₃SO₃·H₂O (**3a**). Compound **4** was obtained by the reaction of AgBF₄ with **L**. From this batch, two crystal structures were determined: {[AgL]BF₄}_n (**4a**) and [AgL]BF₄·xCH₃OH·xH₂O (**4b**). Compound **5** was obtained by the reaction of AgNO₃ with **L**. From this batch, three

crystal structures were determined: [Ag₂L(NO₃)₂] (**5a**), [AgL]NO₃·xH₂O (**5b**) and [Ag₃L₂NO₃][Ag₃L₂H₂O](NO₃)₅·4H₂O (**5c**). The water in the crystals can be attributed to the presence of water in the methanol and/or to air moisture, as the crystals were grown by slow evaporation in ambient air (methanol in the crystal lattice was replaced by water over time, as was noted before by the author for similar systems).

Structure Determination: Single-crystal X-ray diffraction data were collected with a Bruker SMART APEX diffractometer equipped with graphite monochromated Mo-K α radiation (λ = 0.71073 Å).^[17a] The crystals were mounted on a glass fibre and coated with Paratone-N oil. Data collection was carried out at 100(2) K to minimise solvent loss, possible structural disorder and thermal motion effects. Cell refinement and data reduction were performed using the program SAINT^[17b] and all empirical absorption corrections were performed using SADABS.^[17c] Each structure was solved by direct methods using SHELXS-97 and refined by full-matrix least-squares methods based on F^2 using SHELXL-97.^[17d] The program Mercury was used to prepare molecular graphics images.^[17e] Hydrogen atoms, excluding those from OH (water, methanol) were positioned geometrically with C–H 0.95 (aromatic), 0.98 (methyl) and 0.99 Å (methylene); N–H 0.88 Å (aromatic) and refined as riding, with $U_{\text{iso}}(\text{H}) = 1.2 U_{\text{eq}}(\text{C}, \text{N})$ and $1.5 U_{\text{eq}}(\text{methyl C})$. The remainder were located in a difference map and refined with restrained O–H bond lengths. Data collection and structure refinement parameters are presented in Table 1. Crystal structures **1a**, **1d**, **2a**, **2b**, **3a**, **5a** and **5c** were deposited with the CCDC. The remaining crystal structures **1b**, **1c**, **4a**, **4b** and **5b** are described briefly in the text (poor data quality for **1c** and **4b** does not allow for in depth discussion). In **1b**, the water molecule was disordered and modelled in four positions. In **4a**, the anisotropic displacement parameters were restrained for C8, C9, C10 and N17. In **5b**, the electron density was subtracted and the SQUEEZE instruction of PLATON was applied^[17f] as it was impossible to find a suitable refinement model because of highly disordered water molecules. From this calculation we can estimate the presence of two water molecules in the asymmetric unit. However, in the tabulated data (Table 1) the molecular formula and weight, $F(0\ 0\ 0)$ and absorption coefficient were not corrected for the presence of solvent molecules. In this crystal structure, the anisotropic displacement parameters were restrained for O43 and O48. In **5c** one of the counterions (N90) is disordered over two positions with refined site occupancies of 0.65(2):0.35(2). As a result, geometrical and displacement-parameter restraints were applied to this anion.

CCDC-839088 (for **1a**), -839089 (for **1d**), -839090 (for **2a**), -839091 (for **2b**), -839092 (for **3a**), -839093 (for **5a**) and -839094 (for **5c**) contain the supplementary crystallographic data for this paper. These data can be obtained free of charge from The Cambridge Crystallographic Data Centre via www.ccdc.cam.ac.uk/data_request/cif.

Supporting Information (see footnote on the first page of this article): Crystal data and details of the refinement parameters for the crystal structures originating from crystalline bulk material **1–5** (Table S1). Parameters for hydrogen bonding in **1–5** (Table S2) as well as figures presenting XRPD patterns for solids **1–5** (experimental and calculated for isolated phases).

Acknowledgments

The author thanks the Research Foundation Flanders (FWO) for financial support and the National Research Foundation (NRF) of South Africa for supporting this work in its initial stage. Special

thanks are directed to Prof. Wim Dehaen and Dr Jo Alen for support during the writing process.

- [1] a) M. B. Duriska, S. M. Neville, S. R. Batten, *Chem. Commun.* **2009**, 5579–5581; b) D. Kim, J. H. Paek, M.-J. Jun, J. Y. Lee, S. O. Kang, J. Ko, *Inorg. Chem.* **2005**, *44*, 7886–7894; c) L. Carlucci, G. Ciani, D. M. Proserpio, *Coord. Chem. Rev.* **2003**, *246*, 247–289; d) G. F. Swiegers, T. J. Malefetse, *Chem. Rev.* **2000**, *100*, 3483–3537.
- [2] a) G. Férey, C. Serre, T. Devic, G. Maurin, H. Jobic, P. L. Llewellyn, G. De Weireld, A. Vimont, M. Daturif, J.-S. Chang, *Chem. Soc. Rev.* **2011**, *40*, 550–562; b) M. Clemente-León, E. Coronado, C. Martí-Gastaldo, F. M. Romero, *Chem. Soc. Rev.* **2011**, *40*, 473–497; c) C. Janiak, J. K. Vieth, *New J. Chem.* **2010**, *34*, 2366–2388.
- [3] a) C. A. Matuszak, A. J. Matuszak, *J. Chem. Educ.* **1976**, *53*, 280–284; b) M. L. Goodgame, M. Goodgame, P. J. Hayward, G. W. Rayner-Canham, *Inorg. Chem.* **1968**, *7*, 2447–2451; c) J. E. Bauman, J. Wang, *Inorg. Chem.* **1964**, *3*, 368–373.
- [4] a) S.-L. Li, Y.-Q. Lan, J.-C. Ma, J.-F. Ma, Z.-M. Su, *Cryst. Growth Des.* **2010**, *10*, 1161–1170; b) H.-Y. Bai, J.-F. Ma, J. Yang, Y.-Y. Liu, H. Wu, J.-C. Ma, *Cryst. Growth Des.* **2010**, *10*, 995–1016; c) L.-P. Zhang, J.-F. Ma, J. Yang, Y.-Y. Liu, G.-H. Wei, *Cryst. Growth Des.* **2009**, *9*, 4660–4673; d) L. Carlucci, G. Ciani, S. Maggini, D. M. Proserpio, *CrystEngComm* **2008**, *10*, 1191–1203.
- [5] a) L. Dobrzańska, *CrystEngComm* **2011**, *13*, 2303–2309; b) L. Dobrzańska, D. J. Kleinhaus, L. J. Barbour, *New J. Chem.* **2008**, *32*, 813–819; c) L. Dobrzańska, G. O. Lloyd, C. Esterhuysen, L. J. Barbour, *Angew. Chem.* **2006**, *118*, 5988; *Angew. Chem. Int. Ed.* **2006**, *45*, 5856–5859.
- [6] Recently, a paper on the treatment of Cd^{II} complexes with 1,3-bis([imidazol-2-yl]thiomethyl)-2,4,6-trimethylbenzene was published. One of the authors was a student working under the supervision of the author of this article (S. V. Potts, L. J. Barbour, *New J. Chem.* **2010**, *34*, 2451–2457). Somehow the name of the senior author was not included in the publication. The nomenclature of the ligand is not correct in this article, where it features as “1,3-bis(1-imidazolyl-2-thione)-2,4,6-trimethylbenzene”.
- [7] For structural studies on metal complexes with extended ligands that contain a benzene core and thioether functionality see: **aniline-based**: a) Ag^I: Y. Zheng, S.-L. Wang, *Acta Crystallogr., Sect. C* **2004**, *60*, m278–m279; **benzene-based**: b) Ag^I: X.-H. Bu, W.-F. Hou, M. Du, W. Chen, R.-H. Zhang, *Cryst. Growth Des.* **2002**, *2*, 303–307. **benzimidazole-based**: c) Ag^I: C. Fan, C. Ma, C. Chen, F. Chen, Q. Liu, *Inorg. Chem. Commun.* **2003**, *6*, 491–494; **imidazole-based**: d) Cd^{II}, Zn^{II}: J. K. Voo, C. D. Incarvito, G. P. A. Yap, A. L. Rheingold, C. G. Riordan, *Polyhedron* **2004**, *23*, 405–412; e) Cu^I J. K. Voo, K. C. Lam, A. L. Rheingold, C. G. Riordan, *J. Chem. Soc., Dalton Trans.* **2001**, 1803–1805; **pyridine-based**: f) Cu^{II}: D. A. McMorran, C. M. Hartshorn, P. J. Steel, *Polyhedron* **2004**, *23*, 1055–1061; g) Co^{II}: Z. Atherton, D. M. L. Goodgame, S. Menzer, D. J. Williams, *Polyhedron* **1999**, *18*, 273–279; h) Ag^I: C. M. Hartshorn, P. J. Steel, *J. Chem. Soc., Dalton Trans.* **1998**, 3935–3940; **pyrimidine-based**: i) Cu^{II}: R. Peng, S.-H. Lin, Y.-Y. Yang, *Acta Crystallogr., Sect. E* **2007**, *63*, m2385; j) Cu^I R. Peng, D. Li, T. Wu, X.-P. Zhou, S. W. Ng, *Inorg. Chem.* **2006**, *45*, 4035–4046; k) Cu^I: R. Peng, T. Wu, D. Li, *CrystEngComm* **2005**, *7*, 595–598; l) Ag^I: L. Han, B. Wu, Y. Xu, M. Wu, Y. Gong, B. Lou, B. Chen, M. Hong, *Inorg. Chim. Acta* **2005**, *358*, 2005–2013; m) Ag^I: R.-H. Wang, M.-C. Hong, W.-P. Su, Y.-C. Liang, R. Cao, Y.-J. Zhao, J.-B. Weng, *Polyhedron* **2001**, *20*, 3165–3170; n) Ag^I: M. Hong, W. Su, R. Cao, M. Fujita, J. Lu, *Chem. Eur. J.* **2000**, *6*, 427–431; **pyridyl-pyrimidine-based**: o) Cd^{II}, Zn^{II}: H. Dong, H. Zhu, T. Tong, S. Gou, *J. Mol. Struct.* **2008**, *891*, 266–271; p) Ag^I, Hg^{II}: H.-Z. Dong, H.-B. Zhu, X. Liu, S.-H. Gou, *Polyhedron* **2008**, *27*, 2167–2174; **thiadiazole-based**: q) Ag^I: Y. Zheng, *Acta Crystallogr., Sect. C* **2004**, *60*, m471–m472; **quino-line-based**: r) Cu^I, Cu^{II}: C.-Y. Su, S. Liao, M. Wanner, J. Fiedler, C. Zhang, B.-S. Kang, W. Kaim, *Dalton Trans.* **2003**, 189–202; s) Cu^I, Cu^{II}: S. Tavecchi, T. A. Miller, R. L. Paul, J. C. Jeffery, M. D. Ward, *Polyhedron* **2003**, *22*, 507–514; t) Ag^I: S. Liao, C.-Y. Su, H.-X. Zhang, J.-L. Shi, Z.-Y. Zhou, H.-Q. Liu, A. S. C. Chan, B.-S. Kang, *Inorg. Chim. Acta* **2002**, *336*, 151–156.
- [8] L. Dobrzańska, E. J. C. de Vries, *Inorg. Chim. Acta* **2007**, *360*, 1584–1592.
- [9] a) XRPD intensities for **1–5** were measured with a Bruker D8 Advance Diffractometer (Cu-K_α, λ = 1.54056 Å) at ambient temperature; b) W. Kraus, G. Nolze, *PowderCell* 2.4, Federal Institute for Materials Research and Testing, Berlin, Germany, **1999**; c) *PowderCell*, v. 2.4 was used for Rietveld refinement (mass-%): the background was approximated with 8th order polynomials; diffraction lines were fitted to pseudo-Voigt profile function; for **1c** assuming the presence of 1.5 H₂O molecules per molecular formula; for **4b** assuming the presence of one MeOH molecule per molecular formula; for **5b** assuming the presence of one H₂O molecule per molecular formula (estimates based on *SQUEEZE*). Due to the assumptions made above and uncertainty whether all crystallographic phases have been identified, the results should be considered “tentative”.
- [10] The majority of the papers refer to a value of 3.44 Å for a cut off for argentophilic interactions, which is twice the van der Waals radius based on a paper by Bondi (a) A. Bondi, *J. Phys. Chem.* **1964**, *68*, 441–451) but he clearly states that the van der Waals values of metallic elements have a purely tentative nature. For more recent values of van der Waals radii (2.05/2.1 Å) see: b) S. S. Batsanov, *J. Mol. Struct.* **2011**, *990*, 63–66; c) S. Nag, K. Banerjee, D. Datta, *New J. Chem.* **2007**, *31*, 832–834; d) S. S. Batsanov, *Inorg. Mater.* **2001**, *37*, 871–885.
- [11] L. Han, Y. Gong, D. Yuan, M. Hong, *J. Mol. Struct.* **2006**, *789*, 128–132.
- [12] For a discussion of Ag–L cut-off values, see: A. G. Young, L. R. Hanton, *Coord. Chem. Rev.* **2008**, *252*, 1346–1386; for geometry index τ₄ (defined as “the sum of angles α and β – the two largest θ angles in the four-coordinate species – subtracted from 360°, all divided by 141°”), see: L. Yang, D. R. Powell, R. P. Houser, *Dalton Trans.* **2007**, 955–964.
- [13] a) B. Cordero, V. Gómez, A. E. Platero-Prats, M. Revés, J. Echeverría, E. Cremades, F. Barragán, S. Alvarez, *Dalton Trans.* **2008**, 2832–2838; b) L. Pauling, *The Nature of the Chemical Bond*, 3rd ed., Cornell University Press, Ithaca, NY, **1980**, p. 403.
- [14] A. L. Spek, *PLATON*, A Multipurpose Crystallographic Tool, Utrecht University, Utrecht, The Netherlands, **2001**.
- [15] It is surprising that in many cases, even though the authors provide powder patterns (experimental and generated from the crystal structures) as proof of phase purity, they differ enough to assume the presence of mixtures.
- [16] a) L. F. Jones, K. D. Camm, C. A. Kilner, M. A. Halcrow, *CrystEngComm* **2006**, *8*, 719–728; b) C.-Y. Su, B.-S. Kang, C.-X. Du, Q.-C. Yang, T. C. W. Mak, *Inorg. Chem.* **2000**, *39*, 4843–4849.
- [17] a) *SMART*, version 5.625, Bruker AXS Inc., Madison, Wisconsin, USA, **2001**; b) *SAINT*, version 6.36a, Bruker AXS Inc., Madison, Wisconsin, USA, **2002**; c) G. M. Sheldrick, *SADABS*, version 2.05, University of Göttingen, Germany, **1997**; d) G. M. Sheldrick, *Acta Crystallogr., Sect. A* **2008**, *64*, 112–122; e) C. F. Macrae, I. J. Bruno, J. A. Chisholm, P. R. Edgington, P. McCabe, E. Pidcock, L. Rodriguez-Monge, R. Taylor, J. van de Streek, P. A. Wood, *J. Appl. Crystallogr.* **2008**, *41*, 466–470; f) *PLATON/SQUEEZE*: P. van der Sluis, A. L. Spek, *Acta Crystallogr., Sect. A* **1990**, *46*, 194–201.

Received: August 16, 2011

Published Online: January 23, 2012

Fabrication of a 3D Hierarchical Flower-Like MgO Microsphere and Its Application as Heterogeneous Catalyst

Yang Qu,^[a] Wei Zhou,^[a] Zhiyu Ren,^[a] Kai Pan,^[a] Chungui Tian,^[a] Yang Liu,^[a] Shanshan Feng,^[a] Youzhen Dong,^[a] and Honggang Fu^{*[a]}

Keywords: Crystal growth / Heterogeneous catalysis / Industrial chemistry / Magnesium

A 3D hierarchical flower-like MgO microsphere was successfully obtained by pyrolysis of the flower-like $\text{Mg}_5(\text{CO}_3)_4(\text{OH})_2 \cdot 4\text{H}_2\text{O}$ microsphere precursor which was itself synthesised by means of a facile and environmentally friendly hydrothermal route from $\text{MgCl}_2 \cdot 6\text{H}_2\text{O}$. The possible formation process of the microsphere precursor was systematically investigated and considered to result from the following steps: (i) forming the 1D pillar-like MgCO_3 ; (ii) cracking to a 2D flake structure; (iii) assembling to the 3D flower-like $\text{Mg}_5(\text{CO}_3)_4(\text{OH})_2 \cdot 4\text{H}_2\text{O}$ microsphere. The obtained close-

packed 3D flower-like MgO microsphere has cubic symmetry and high crystallinity assembled by nanoflake particles with a mean diameter of 10 μm . Moreover, the heterogeneous catalysis of the Claisen–Schmidt condensation reaction between benzaldehyde and acetophenone to synthesise chalcones was also studied. The 3D flower-like MgO microsphere exhibited better catalytic performance than that of commercial MgO and this was attributed to the especially 3D hierarchical flower-like structure and the large surface area.

Introduction

The reserves of magnesium resources are extremely abundant, being mostly in the ocean and in ores or salines inland. Generally, the natural form of magnesium is bischofite ($\text{MgCl}_2 \cdot 6\text{H}_2\text{O}$) which is the precursor of magnesium functional materials such as magnesium oxide (MgO). MgO has been considered to have excellent physical chemical and crystallographic properties, such as a straight-forward rock-salt crystal structure, high ionic character, an insulating nature and the morphology can vary in terms of shape, particle size and surface structure.^[1,2] As a result of the possession of these properties, MgO is widely used as functional material in the field of catalysis, refractory materials, paint, superconductors and toxic waste remediation.^[3–5] In recent years, to further enhance its physical chemistry performance, various MgO materials have been successfully fabricated, such as nanocrystals, nanoparticles, nanocubes, nanowires and nanosheets.^[6–9] However, for surface and interface chemistry, such as heterogeneous catalysis and adsorption, 3D hierarchical structures with micrometer and nanometer dimensions have several advantages due to their high surface area, ability to expedite mass transportation and general robustness.^[10] Therefore, large scale transfor-

mation of nanoscale building blocks into 3D complex architectural microstructures attracts much attention nowadays.^[11,12] However, it is still a great challenge to develop simple and reliable synthetic methods for preparing 3D assembled architectural microstructures with designed chemical components and controlled morphologies. Luckily, the hydrothermal route^[13] has probably provided us with a new idea for facile synthesis of 3D architectural structures in which ordered aggregates can form in a spontaneous process under these special condition. Up to now, significant efforts have been made to design and prepare 3D assembled nanostructures, by the hydrothermal route, such as NiO ,^[14] Fe_2O_3 ,^[15] V_2O_5 ,^[16] TiO_2 ^[17] etc. However, 3D hierarchical MgO has been little studied in the previous works.

As is commonly known, MgO plays an important role in catalysts and catalyst supports, especially in heterogeneous catalysts because of its unique catalytic properties and potential applications. In the past decade, heterogeneous catalysis has aroused people's enthusiasm in industry because it provides a powerful method for the synthesis of optically active molecules that serve as precursors to pharmaceutically important compounds.^[18–20] The Claisen–Schmidt condensation (CSC) as a significant organic reaction is usually used to synthesise some organic compounds and drugs, for example 1,3-diaryl-2-propen-1-ones (chalcones),^[21,22] which are considered as precursors of flavonoids and isoflavonoids. They have also been shown to display a diverse array of pharmacological activities, such as anticancer, anti-inflammatory, nitric oxide regulation and anti-hyperglycemic agents. Traditionally, chalcones could be obtained through the CSC between benzaldehyde and acetophenone

[a] Key Laboratory of Functional Inorganic Material Chemistry, Ministry of Education of the People's Republic of China, Heilongjiang University, Harbin 150080, P. R. China
Fax: +86-451-8667-3647
E-mail: fuhg@vip.sina.com

Supporting information for this article is available on the WWW under <http://dx.doi.org/10.1002/ejic.201100936>.

carried out in basic or acidic media under homogeneous conditions, by utilising bases such as NaOH, KOH, AlCl₃ etc.^[23–25] However, compared with homogeneous catalysis, heterogeneous catalysis is favoured by industry for its easy operation, simple workup and the ability to regenerate or recover the catalyst.^[26,27] Heterogeneous catalysts have also been used for the CSC, including Lewis acids, solid acids, solid bases and so on. Recently, nanocrystalline MgO was used as a heterogeneous catalyst in the CSC reaction due to its good surface chemistry for catalysis and adsorption.^[28] Choudary and coworkers^[29] used different kinds of nanocrystalline MgO to prepare nanoheterogeneous catalysts for the Claisen–Schmidt condensation of benzaldehydes with acetophenones to yield chalcones. Besides, some MgO nanostructures with special morphologies have also been synthesised. For example, Song and his group^[10] synthesised micrometer-sized MgO nanostructures by a solvothermal process using ethylene glycol and PVP. These nanostructures were then used for the CSC between benzaldehyde and acetophenone. However, the process may introduce unwanted impurities into the final MgO product, the latter being obtained by calcining the glycolate intermediate. PVP was used as surfactant which was very hard to remove and this can affect the further applications of the MgO. It is important to synthesise materials without surfactants. So far, most studies of Claisen–Schmidt condensation using MgO as a heterogeneous catalyst used either commercial nanocrystalline or complex synthesised nanostructures. Hierarchical structured MgO synthesised by a nonsurfactant hydrothermal route has been little reported. Although there is some literature focused on hierarchical structured MgO, most reports are limited to synthetic strategies, and the physical chemistry processes of the MgO precursor or the product were not described in detail.^[30–32] Therefore, preparation of 3D hierarchical structured MgO with excellent catalytic performance, by a nonsurfactant hydrothermal method, is a great challenge.

Here, we report a nonsurfactant hydrothermal way to obtain 3D hierarchical structured flower-like MgO microspheres by the hydrothermal route and calcination in air. MgCl₂·6H₂O, the main component of bischofite, which is the natural magnesium resource, was used as a magnesium source. 3D flower-like Mg₅(CO₃)₄(OH)₂·4H₂O microsphere precursors were synthesised by a hydrothermal approach, then the Mg₅(CO₃)₄(OH)₂·4H₂O microspheres were calcined in air to obtain 3D hierarchical structured flower-like MgO microspheres. The possible formation mechanism and heterogeneous catalysis of the CSC between benzaldehyde and acetophenone for 3D flower-like MgO microsphere is also reported in this paper.

Results and Discussion

The Assembly Process of the 3D Flower-Like Mg₅(CO₃)₄(OH)₂·4H₂O Microsphere

SEM images of the samples collected at different time intervals from the reaction mixture after the reaction tem-

perature reached 120 °C are shown in Figure 1. When mixing MgCl₂·6H₂O with Na₂CO₃ solution, a white precipitate was formed immediately.^[33] The SEM image shown in part A of Figure 1 revealed that the white precipitate is a pillar-like structure of about 30 μm in length and 800 nm in diameter. The surface of the pillar is smooth. After the hydrothermal process has lasted for 8 h, 3D flower-like microspheres were observed, see Figure 1 (F). The microspheres were about 10 μm in diameter and assembled with pieces of nanoflakes. In order to understand how the 1D pillar changed to the 3D flower structure, the samples at different hydrothermal time intervals (2 min, 5 min, 30 min and 1 h) from the reaction mixture after the reaction temperature reached 120 °C were collected. SEM images of the collected samples at different times are shown in Figure 1 (B–E). We can see that after a hydrothermal reaction of 2 min, the pillar-like precursor began to crack into flake-like ones which are clearly shown in part B of Figure 1. With the increase of the reaction time, the flakes began to assemble into 3D microspheres (see Figure 1, C–E) and finally into 3D hierarchical flower-like microspheres (Figure 1, F).

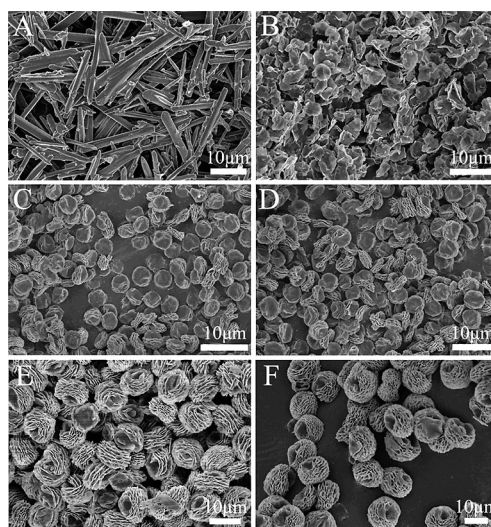


Figure 1. SEM images of the collected samples at different hydrothermal time intervals; (A) before the hydrothermal process and after (B) 2 min, (C) 5 min (D) 30 min, (E) 1 h and (F) 8 h, respectively.

To further characterise the obtained pillars and microspheres, X-ray power diffraction was used to reveal the crystallisation of materials. Figure 2 shows the X-ray diffraction at different time intervals for the collected samples. Figure 2 (a) distinctly indicates that the crystal form of the 1D pillar after mixing the MgCl₂·6H₂O solution with Na₂CO₃ solution before the hydrothermal process was MgCO₃·3H₂O, all peaks in the XRD pattern of the sample are in good agreement with the MgCO₃·3H₂O reference data (JCPDS: 20-0669). After a hydrothermal reaction time of 2 min, MgCO₃·3H₂O began to form Mg₅(CO₃)₄(OH)₂·4H₂O (JCPDS:25-0513) as shown in Figure 2 (b). The above reaction can be described as shown in Equations (1) and (2).

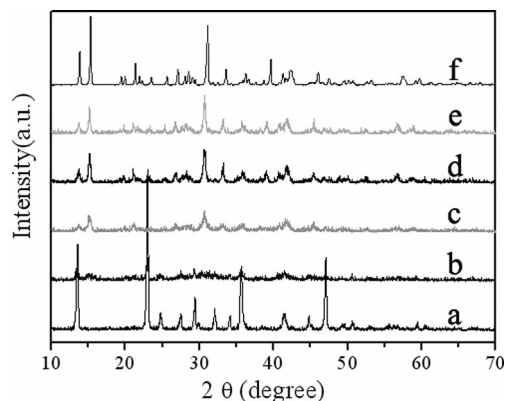


Figure 2. X-ray diffraction of the collected samples at different hydrothermal time intervals; (a) before the hydrothermal process and after (b) 2 min, (c) 5 min, (d) 30 min, (e) 1 h, and (f) 8 h, respectively.

Along with the reaction time, from 5 min to 8 h, the quantity of $\text{MgCO}_3 \cdot 3\text{H}_2\text{O}$ was decreased and, meanwhile, $\text{Mg}_5(\text{CO}_3)_4(\text{OH})_2 \cdot 4\text{H}_2\text{O}$ was increased gradually. Furthermore, the crystallisation of $\text{Mg}_5(\text{CO}_3)_4(\text{OH})_2 \cdot 4\text{H}_2\text{O}$ was clearly improved as shown in Figure 1c–f.

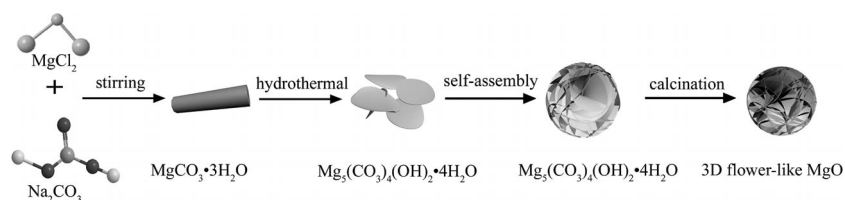
SEM and XRD results give us an exact idea of how the 1D pillar changed to the 3D flower-like structure. This may attribute to the different crystal structures (see Figure S1) of the 1D pillar and the 3D flower-like structures. We know that the 1D pillar is nesquehonite ($\text{MgCO}_3 \cdot 3\text{H}_2\text{O}$) with a hexagonal prismatic crystal structure. During the hydrothermal process, nesquehonite hydrolysed and changed to magnesium carbonate hydrate [$\text{Mg}_5(\text{CO}_3)_4(\text{OH})_2 \cdot 4\text{H}_2\text{O}$]. This was accompanied by the crystal shape changing to a hexagonal flake.^[34] The simulated morphologies of $\text{MgCO}_3 \cdot 3\text{H}_2\text{O}$ and $\text{Mg}_5(\text{CO}_3)_4(\text{OH})_2 \cdot 4\text{H}_2\text{O}$ from the viewpoint of chemical bonding are shown in Figure S1 (see Supporting Information). We can note that in the nesquehonite crystal structure, the density of the (010) lattice plane is low. Based on Bravais' law, the faces most likely to be found on a crystal are those parallel to the lattice planes of greatest point density. In the growth of the $\text{MgCO}_3 \cdot 3\text{H}_2\text{O}$ crystal, the (010) lattice plane continuous to grow until it disappeared, the remnant lattice is the one which has a high density of lattice planes and this led to a rod-like or pillar-like structure. However, in the $\text{Mg}_5(\text{CO}_3)_4(\text{OH})_2 \cdot 4\text{H}_2\text{O}$ crystal structure, the density of the (100) and (001) planes is low

and in the growing process of the crystal, these two lattice planes are the main growth face which produce the flake-like structure. Based on the considerations above, we learn that when the hydrothermal process begins, the crystal structure of the 1D pillar changes from $\text{MgCO}_3 \cdot 3\text{H}_2\text{O}$ to $\text{Mg}_5(\text{CO}_3)_4(\text{OH})_2 \cdot 4\text{H}_2\text{O}$ which leads to the growth of (100) and (001) planes with the result that the 1D pillar structure cracks to form 2D pieces of flake (as shown in Figure 2, A and B). When increasing the reaction time from 5 min to 1 h, we observed that the nanoflakes begin to aggregate into a 3D structure. The resultant 2D flakes can pile up one on top of another to form the final 3D structure by means of hydrogen bonding among the hydroxy groups.^[35,36] During the hydrothermal process, the assembly was complete after 8 h reaction time and the flakes fully transformed to the 3D flower-like structure (Figure 1, F).

Based on the above discussion, in order to show the growth mechanism of the 3D flower-like $\text{Mg}_5(\text{CO}_3)_4(\text{OH})_2 \cdot 4\text{H}_2\text{O}$ microspheres, the possible formation mechanism of the assembly process of the 3D flower-like MgO microspheres can be illustrated in Scheme 1 and Figure S2. A pillar-like $\text{MgCO}_3 \cdot 3\text{H}_2\text{O}$ precursor is firstly formed after mixing MgCl_2 with Na_2CO_3 and this pillar-like MgCO_3 precursor was then transferred to an autoclave to carry out the hydrothermal process. When the hydrothermal process begins, the MgCO_3 pillars begin to crack into flakes of $\text{Mg}_5(\text{CO}_3)_4(\text{OH})_2 \cdot 4\text{H}_2\text{O}$ until all the pillars changed to flakes. Further along in the reaction, the flakes assemble into the 3D flower structure. The 3D flower-like MgO microspheres were obtained by finally calcining the precursor in air.

The Characteristics of 3D Flower-Like MgO Microspheres

MgO has been widely used as a refractory and sorbing material. Generally, MgO was obtained by thermal pyrolysis of different magnesium precursors such as $\text{Mg}_5(\text{CO}_3)_4(\text{OH})_2$ and MgCO_3 . Thus, the obtained 3D flower-like $\text{Mg}_5(\text{CO}_3)_4(\text{OH})_2 \cdot 4\text{H}_2\text{O}$ microspheres are good precursors for F-MgO (3D flower-like MgO). The F-MgO was obtained from calcination of the 3D flower-like $\text{Mg}_5(\text{CO}_3)_4(\text{OH})_2 \cdot 4\text{H}_2\text{O}$ microspheres in air at 500 °C for 2 h. An SEM image of the F-MgO is shown in Figure 3 (A). We can note that after the calcination process, the 3D structure is retained. However, some parts of it are collapsed compared with the $\text{Mg}_5(\text{CO}_3)_4(\text{OH})_2 \cdot 4\text{H}_2\text{O}$ microspheres due to the production of gases during pyrolysis. The pyrolysis gases, such as CO_2 and H_2O can be confirmed by a TG-IR analy-



Scheme 1. An illustration of the possible formation mechanism of the 3D flower-like MgO.

sis (see Figure S3). TEM and HRTEM images of F-MgO are shown in Figure 3 (B and C). F-MgO is too large to obtain a whole microsphere within the TEM image, so we choose a piece of the flakes which assembled to F-MgO in TEM. It can be clearly seen that the F-MgO microsphere is composed of pieces of graphene-like thin flakes with a plicate structure. HRTEM images in Figure 3 (C) show that the 3D F-MgO exhibits the lattice fringe with a lattice distance of 0.21 nm which is in good agreement with the spacing between the (200) planes of MgO. The selected area electron diffraction (SAED) patterns of the calcined materials (inset in Figure 3, B) show circled rings, an indication of the polycrystalline nature of the sample. HRTEM and SAED in Figure 3 also show that the whole structures are polycrystalline due to the anisotropic assembly of the building blocks for F-MgO.

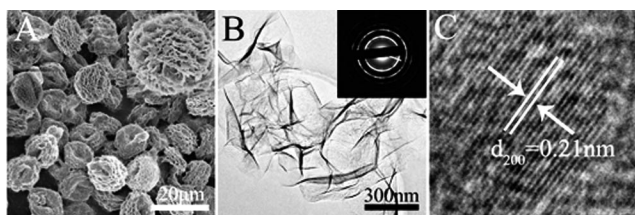


Figure 3. (A) SEM, (B) TEM and (C) HRTEM images of 3D flower-like MgO. (Inside B is selected area electron diffraction pattern).

To investigate the relationship between structure and performance in heterogeneous catalysis, the 1D P-MgO calcined from the pillar-like $\text{MgCO}_3 \cdot 3\text{H}_2\text{O}$ was used as reference sample. Figure S4A show the morphology with different magnification images of P-MgO. We can see that the P-MgO retains both its length and diameter compared with its precursor (Figure 1A). However after being calcined at 500 °C for 2 h, the smooth pillars became rough but the length and diameter are retained. However, we can observe from the high magnification SEM image inside Figure S4A, that the P-MgO is formed by accumulated particles with some cumulate pores. This may be caused by the aggregation and crystallisation in the calcination process of MgO particles. TEM and HRTEM image of P-MgO shown in Figure S4B also confirmed the pores. HRTEM and SAED in Figure S4B and C show that the crystallisation P-MgO is the same as F-MgO. Both of them exhibit the (200) planes of MgO and the whole structures are polycrystalline. Figure 4 shows the XRD patterns of F-MgO and P-MgO. It clearly shows the presence of five Bragg diffraction peaks at $2\theta = 36.8\text{--}78.6^\circ$ which can be observed in the calcined samples and indexed as (111), (200), (220), (311) and (222), respectively, and shows the typical patterns for cubic symmetry (JCPDS: 45-0946). Both the F-MgO and the P-MgO exhibit high crystallinity from the high of the diffraction peaks. In order to confirm whether our obtained material is good or not, commercial MgO (C-MgO) nanocrystals from BASF were used as well. The SEM image and XRD pattern of C-MgO are shown in Figure S5.

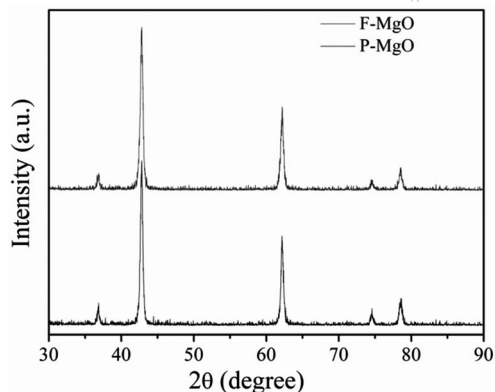


Figure 4. The X-ray diffraction of F-MgO and P-MgO obtained after being calcined at 500 °C for 2 h.

For F-MgO, based on the above analysis, the fully assembled structures with plicate flakes are not only favourable contact with the reactant, but also possess high surface area. The Brunauer–Emmett–Teller (BET) gas sorption analysis is shown in Figure 5. F-MgO has a specific surface area of $43.6\text{ m}^2\text{ g}^{-1}$, However P-MgO has a specific surface area of $18.7\text{ m}^2\text{ g}^{-1}$ and C-MgO has $25.4\text{ m}^2\text{ g}^{-1}$. The high surface area of F-MgO may be ascribed to the intersheet spacing, the thin plicate flakes and the pores in the thin flake (Figure S7). The high surface area and special 3D flower-like structure of F-MgO are favourable for absorption and mass transport, which is beneficial for high catalytic performance.

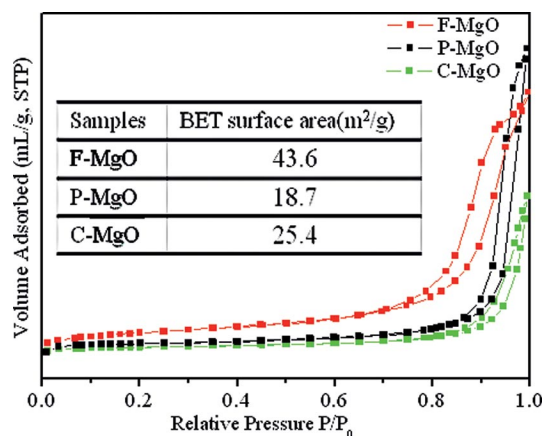
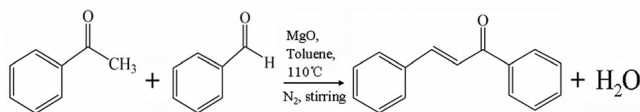


Figure 5. The BET surface areas and N_2 adsorption isotherms of F-MgO, P-MgO and C-MgO.

Heterogeneous Catalysis with 3D Flower-Like MgO Microspheres

Sufficient and effective contact between two phase and an abundant reaction interface is beneficial for heterogeneous catalysis. Focussing on the previous report, MgO showed good basic catalytic properties such as in the Claisen–Schmidt condensation reaction for synthesising chalcones from benzaldehyde and acetophenone. The equa-

tion of the reaction is shown in Scheme 2. The basic catalytic activity of the CSC between benzaldehyde and acetophenone at 110 °C using MgO (F-MgO, P-MgO and C-MgO) as a heterogeneous catalyst is shown in Figure 6. We can clearly note that F-MgO shows a substantially higher activity in the reaction than P-MgO and C-MgO under the same conditions. F-MgO was synthesised without a surfactant and the catalytic activity is comparable under the same reaction conditions. We believe that this promising activity is not due to impurities. It is pure and has no impurities (Figure S8). Some of the previous studies indicated that MgO can be used as heterogeneous catalyst. In MgO, the Mg^{2+} site is a Lewis-acid type ion and the O^{2-} site is a Lewis-base for MgO. The Claisen–Schmidt condensation between benzaldehyde and acetophenone could be accelerated by the Lewis-basic O^{2-} sites.^[10,28,37,38] The O^{2-} sites of these oxides are necessary to trigger the Claisen–Schmidt condensation reaction. This means MgO with various structures has been shown to be active for aldol condensation reactions.^[39] Figure 6 shows that the conversion of benzaldehyde reached 95% after 8 h, whereas during the same period of time the experiment using P-MgO gave a conversion of about 50% and C-MgO only 25% benzaldehyde conversion was observed. The GC and GC–MS data of benzaldehyde, acetophenone and chalcone are shown in Figure S9, S10 and S11. The high activity of F-MgO may be ascribed to the fast mass transfer in the well assembly 3D structure in the inter-sheet spaces of the MgO nanoflakes.



Scheme 2. Claisen–Schmidt condensation reaction of benzaldehyde and acetophenone.

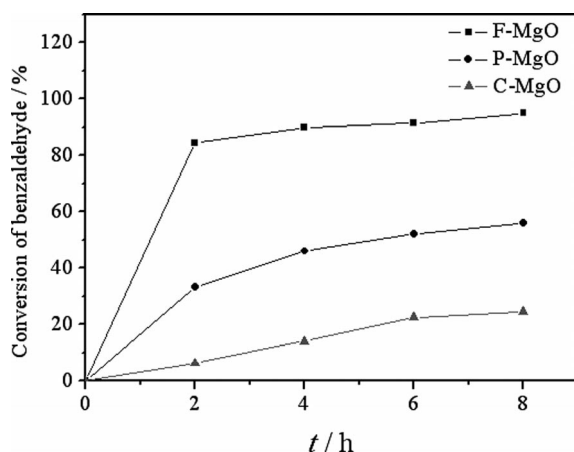


Figure 6. Claisen–Schmidt condensation of benzaldehyde with acetophenone using different magnesium oxides at 110 °C.

The 3D structures provide a large surface area and the MgO sheet can favour mass transport. Usually, four-coordinate hydroxy groups and low coordinate oxide ions are

favourable for the CSC reaction. In order to confirm this hypothesis, FTIR spectroscopy was performed (as shown in Figure S6). The bands at 3725 cm^{-1} of F-MgO (Figure S6-I-a) and at 3723 cm^{-1} of P-MgO (Figure S6-I-b) can be attributed to the multi- and monocoordinate hydroxy groups, respectively. The band at 3653 cm^{-1} in C-MgO (Figure S6-I-c) can be attributed to the interaction of the four coordinate hydroxy groups with the surface defects. The band at 3427 cm^{-1} (observed mainly in Figure S6-I-a and S6-II-a) correlates with the interaction of four-coordinate hydroxy groups with the low coordinate oxide ions.^[40] Hence the FTIR pattern supports the presence of the low coordinate oxide anions in the F-MgO. The reason for the low coordinate oxide anions may ascribed to the very thin flakes of F-MgO (as shown in Figure 3, B). The presence of some low coordinate oxide sites may be another reason for the high catalytic activities.^[41,42] On the basis of the above consideration, the excellent catalytic properties of F-MgO was attributed to the large surface area, the special 3D flower-like structures, the abundant O^{2-} sites and the presence of the low coordinate oxide anions. It was also observed that coking as mentioned in the previous report is also one of the potential problems with 3D flower-like MgO microspheres. After the catalytic reaction, the catalyst became yellow, possibly from coking. In this regard, the ability to catalyse the reaction at lower temperatures will lead to less coking and prolong the catalyst's life.

Conclusions

In conclusion, 3D hierarchical flower-like MgO microspheres were obtained using a nonsurfactant hydrothermal route and a cheap magnesium resource. The evolution of the microspheres was investigated and found that a new assembly process from 1D to 3D was exhibited. The microspheres show excellent chemical and physical properties, which made them exhibit favourable heterogeneous catalysis of the CSC reaction for synthesising chalcones. The result of catalytic experiments showed that the catalytic properties are related to the morphology of the catalyser. The 3D flower-like MgO microspheres had a conversion of 95% at 8 h which is better than that of 1D MgO and commercial MgO. This facile and active catalytic 3D flower-like MgO material will have promising applications in heterogeneous catalysis for obtaining special organic molecules.

Experimental Section

Preparation of 3D Flower Like $\text{Mg}_5(\text{CO}_3)_4(\text{OH})_2 \cdot 4\text{H}_2\text{O}$ Microspheres:

A typical synthesis of 3D flower-like $\text{Mg}_5(\text{CO}_3)_4(\text{OH})_2 \cdot 4\text{H}_2\text{O}$ is as follows. All of the chemicals were analytical grade and used without further purification. Firstly, 0.5 M Na_2CO_3 solution (20 mL) was added to 0.5 M MgCl_2 solution (20 mL) dropwise to form a mixture with a white precipitate. The mixture was then transferred into a 40 mL Teflon®-lined stainless-steel autoclave which was sealed and heated at 120 °C for various times. The precipitate formed after the hydrothermal process was purified by three centrifuge and redispersion cycles with deionised water and

it was then dried under vacuum at 60 °C for 12 h. Moreover, a series of control experiments was done from which products were collected at different time intervals (2 min, 5 min, 30 min, 1 h and 8 h) from the reaction mixture after the reaction temperature reached 120 °C.

Preparation of MgO with Different Morphology: The 3D flower-like MgO microsphere which was denoted F-MgO was obtained by calcining the $\text{Mg}_5(\text{CO}_3)_4(\text{OH})_2 \cdot 4\text{H}_2\text{O}$ microsphere precursor at 500 °C for 2 h in air. For investigating the relationship between structure and performance, a pillar-like MgO was used for contrast in this paper. The pillar-like MgO was obtained by separating the mixture with the white precipitate before transferring into a Teflon®-lined stainless-steel autoclave mentioned above by centrifugation and washing with deionised water three times and drying at 60 °C for 12 h in a vacuum oven. The product was calcined at 500 °C for 2 h in air to obtain the pillar-like MgO which was denoted to P-MgO. To compare the catalytic performance of our obtained materials, commercial MgO (which was denoted to C-MgO) nanocrystals from BASF were also used and these were activated at 250 °C before being used.

Characterisation: X-ray powder diffraction (XRD) patterns were obtained by using a Rigaku D/max-III B diffractometer using $\text{Cu-K}\alpha$ radiation ($\lambda = 1.5406 \text{ \AA}$). Scanning electron microscopy (SEM) micrographs were taken using a Hitachi S-4800 instrument operating at 15 kV. The transmission electron microscopy (TEM) experiment was performed on a JEM-2100 electron microscope (JEOL, Japan) with an acceleration voltage of 200 kV. Carbon coated copper grids were used as the sample holders. The pyrolysis experiments of the 3D flower-like MgO precursor $[\text{Mg}_5(\text{CO}_3)_4(\text{OH})_2 \cdot 4\text{H}_2\text{O}]$ were carried out in TG (TA, Q600) coupled to FTIR (Nicolet, IS10) under a stream of air at a heating rate of $10 \text{ }^\circ\text{C min}^{-1}$. The specific surface area was determined according to the Brunauer–Emmett–Teller (BET) method using a Tristar II 3020 surface area and porosity analyser (Micromeritics).

Catalytic Reactions: For the test of catalytic activity, a traditional procedure for the preparation of chalcone by using CSC reaction was used.^[28,29] A mixture of acetophenone (3 mmol), benzaldehyde (2.5 mmol), dry toluene (10 mL) and catalyst (0.175 g) was put into a 50 mL round bottomed flask and the mixture was stirred under a nitrogen atmosphere (to avoid benzaldehyde oxidation to benzoic acid) at 110 °C. Samples were taken periodically and analysed by gas chromatography (GC) using an Agilent 6890NGC instrument equipped with a flame-ionisation detector and a HP-5 capillary column. The reaction products were identified by using a GC–MS instrument (Shimadzu 2010).

Supporting Information (see footnote on the first page of this article): TG-IR of $\text{Mg}_5(\text{CO}_3)_4(\text{OH})_2 \cdot 4\text{H}_2\text{O}$, TEM images of P-MgO, SEM images of C-MgO, FT-IR curve of F-MgO, P-MgO and C-MgO and GC-MS analysis of the CSC reaction.

Acknowledgments

We gratefully acknowledge the support of this research by the Key Program Projects of the National Natural Science Foundation of China (No. 21031001), the National Natural Science Foundation of China (No. 20971040, 51102082, 21101060, 21001042 and 20703015), the Cultivation Fund of the Key Scientific and Technical Innovation Project, Ministry of Education of China (No. 708029), the Program for New Century Excellent Talents in Heilongjiang Provincial University of China (No. 1154-NCET-010), the Excellent Youth of Common Universities of Heilongjiang Prov-

ince of China (No. 1251G045), the Harbin Youth Foundation (No. 2009RFQXG202) and the Scientific Research Fund of Heilongjiang Provincial Education Department (No. 12511376, 11541283).

- [1] S. Stankic, M. Müller, O. Diwald, M. Sterrer, E. Knözinger, J. Bernardi, *Angew. Chem.* **2005**, *117*, 4996; *Angew. Chem. Int. Ed.* **2005**, *44*, 4917–4920.
- [2] K. Zhu, J. Hu, C. Kübel, R. Richards, *Angew. Chem.* **2006**, *118*, 7435; *Angew. Chem. Int. Ed.* **2006**, *45*, 7277–7281.
- [3] Y. Kawaguchi, *Solid State Commun.* **2000**, *117*, 17–20.
- [4] a) H. B. Lu, L. Liao, H. Li, D. F. Wang, Y. Tian, J. C. Li, Q. Fu, B. P. Zhu, Y. Wu, *Eur. J. Inorg. Chem.* **2008**, *17*, 2727–2732; b) N. Sutradhar, A. Sinhamahapatra, S. K. Pahari, P. Pal, H. C. Bajaj, I. Mukhopadhyay, A. B. Panda, *J. Phys. Chem. C* **2011**, *115*, 12308–12316.
- [5] B. Q. Xu, J. M. Wei, H. Y. Wang, K. Q. Sun, Q. M. Zhu, *Catal. Today* **2001**, *68*, 217–225.
- [6] A. Subramania, V. G. Kumar, A. R. S. Priya, T. Vasudevan, *Nanotechnology* **2007**, *18*, 225601–225605.
- [7] X. S. Fang, C. H. Ye, L. D. Zhang, J. X. Zhang, J. W. Zhao, P. Yan, *Small* **2005**, *1*, 422–428.
- [8] S. Makhlof, R. Dror, Y. Nitzan, Y. Abramovich, R. Jelinek, A. Gedanken, *Adv. Funct. Mater.* **2005**, *15*, 1708–1715.
- [9] M. Zhao, X. L. Chen, W. J. Wang, Y. J. Ma, Y. P. Xu, H. Z. Zhao, *Mater. Lett.* **2006**, *60*, 2017–2019.
- [10] S. W. Bain, Z. Ma, Z. M. Cui, L. S. Zhang, F. Niu, W. G. Song, *J. Phys. Chem. C* **2008**, *112*, 11340–11344.
- [11] R. F. Service, *Science* **2005**, *309*, 95.
- [12] a) S. Park, J. H. Lim, S. W. Chung, C. A. Mirkin, *Science* **2004**, *303*, 348–351; b) D. H. Gracias, J. Tien, T. L. Breen, C. Hsu, G. M. Whitesides, *Science* **2000**, *289*, 1170–1172.
- [13] J. Zhao, X. Liu, D. Cui, Y. Sun, Y. Yu, Y. Yang, C. Du, Y. Wang, K. Song, K. Liu, S. Lu, X. Kong, H. Zhang, *Eur. J. Inorg. Chem.* **2010**, *12*, 1813–1819.
- [14] X. Song, L. Gao, *J. Phys. Chem. C* **2008**, *112*, 15299; X. Song, L. Gao, *J. Phys. Chem. C* **2008**, *112*, 15299–15305.
- [15] L. S. Zhong, J. S. Hu, H. P. Liang, A. M. Cao, W. G. Song, L. J. Wan, *Adv. Mater.* **2006**, *18*, 2426–2431.
- [16] A. M. Cao, J. S. Hu, H. P. Liang, L. J. Wan, *Angew. Chem.* **2005**, *117*, 4465; *Angew. Chem. Int. Ed.* **2005**, *44*, 4391–4395.
- [17] C. Wang, L. Yin, L. Zhang, Y. Qi, N. Lun, N. Liu, *Langmuir* **2010**, *26*, 12841–12848.
- [18] T. Hayashi, K. Yamasaki, *Chem. Rev.* **2003**, *103*, 2829–2844.
- [19] T. Ireland, K. Tappe, G. Grossheimann, P. Knochel, *Chem. Eur. J.* **2002**, *8*, 843–852.
- [20] L. Pu, H. B. Yu, *Chem. Rev.* **2001**, *101*, 757–824.
- [21] J. R. Dimmock, D. W. Elias, M. A. Beazely, N. M. Kandepu, *Curr. Med. Chem.* **1999**, *6*, 1125–1149.
- [22] D. N. Dhar, *Chemistry of Chalcones and Related Compounds*, John Wiley & Sons, New York, **1981**.
- [23] A. Corma, H. García, *Chem. Rev.* **2003**, *103*, 43074–365.
- [24] F. D. Cheng, J. Fei, Z. Gong, K. Z. Liu, *Catal. Commun.* **2008**, *9*, 1924–1927.
- [25] N. O. Calloway, L. D. Green, *J. Am. Chem. Soc.* **1937**, *59*, 809–811.
- [26] C. E. Song, S. G. Lee, *Chem. Rev.* **2002**, *102*, 3495–3524.
- [27] R. A. Brown, P. Pollet, E. McKoon, C. A. Eckert, C. L. Liotta, P. G. Jessop, *J. Am. Chem. Soc.* **2001**, *123*, 1254–1255.
- [28] a) T. Selvamani, A. Sinhamahapatra, D. Bhattacharjya, I. Mukhopadhyay, *Mater. Chem. Phys.* **2011**, *129*, 853–861; b) T. Qiu, X. L. Wu, F. Y. Jin, A. P. Huang, P. K. Chu, *Appl. Surf. Sci.* **2007**, *253*, 3987–3990; c) N. Sutradhar, A. Sinhamahapatra, S. K. Pahari, P. Pal, H. C. Bajaj, I. Mukhopadhyay, A. B. Panda, *J. Phys. Chem. C* **2011**, *115*, 12308–12316.
- [29] a) B. M. Choudary, K. V. S. Ranganath, J. Yadav, M. Lakshmi Kantam, *Tetrahedron Lett.* **2005**, *46*, 1369–1371; b) B. M. Choudary, M. L. Kantam, K. V. S. Ranganath, K. Mahendar, B. Sreedhar, *J. Am. Chem. Soc.* **2004**, *126*, 3396–3397.
- [30] C. Gao, W. Zhang, H. Li, L. Lang, Z. Xu, *Cryst. Growth Des.* **2008**, *8*, 3785–3790.

- [31] a) G. Wang, L. Zhang, H. Dai, J. Deng, C. Liu, H. He, C. T. Au, *Inorg. Chem.* **2008**, *47*, 4015–4022.
- [32] Z. Zhang, Y. Zheng, Y. Ni, Z. Liu, J. Chen, X. Liang, *J. Phys. Chem. B* **2006**, *110*, 12969–12973.
- [33] C. M. Janet, B. Viswanathan, R. P. Viswanath, T. K. Varadara-jan, *J. Phys. Chem. C* **2007**, *111*, 10267–10272.
- [34] X. X. Yan, Y. F. Li, D. F. Xue, C. L. Yan, L. J. Wang, *J. Synth. Cryst.* **2007**, *5*, 991–999.
- [35] S. M. Zhang, H. C. Zeng, *Chem. Mater.* **2009**, *21*, 871–883.
- [36] H. Yan, M. Wei, J. Ma, D. G. Evans, X. Duan, *J. Phys. Chem. A* **2010**, *114*, 7369–7376.
- [37] M. T. Drexler, M. D. Amiridis, *J. Catal.* **2003**, *214*, 136–145.
- [38] P. Jeevanandam, K. J. Klabunde, *Langmuir* **2002**, *18*, 5309–5313.
- [39] M. J. Climent, A. Corma, S. Iborra, M. Mifsud, *J. Catal.* **2007**, *247*, 223–230.
- [40] J. Hu, K. Zhu, L. Chen, C. Kübel, R. Richards, *J. Phys. Chem. C* **2007**, *111*, 12038–12044.
- [41] T. Selvamani, T. Yagyu, S. Kawasaki, I. Mukhopadhyay, *Catal. Commun.* **2010**, *11*, 537–541.
- [42] M. Sterrer, T. Berger, O. Diwald, E. Knözinger, *J. Am. Chem. Soc.* **2003**, *125*, 195–199.

Received: September 5, 2011

Published Online: January 16, 2012

Graphitic Carbon Nanocapsules: Scaled Preparation, Formation Mechanism, and Use as an Excellent Support for Methanol Electro-oxidation

Lei Wang,^[a,bl] Chungui Tian,^[bl] Hongxing Zhang,^[al] and Honggang Fu^{*[a,bl]}

Keywords: Nanostructures / Reaction mechanisms / Carbon / Platinum / Electrochemistry / Oxidation

Graphitic carbon nanocapsules (GCNs) with high crystallinity and a large specific surface area (SSA) have been prepared in high yield by a solid-state pyrolysis route using a polyacrylic weak-base anion-exchange resin (PAWBA) as the carbon source. A possible mechanism for the formation of the GCNs is proposed based on a series of experiments, including TG, FTIR, Raman, and TEM analyses, as well as on the structure of PAWBA: The catalytic iron particles are surrounded by the active carbon atoms derived from PAWBA during the pyrolytic process, which then escape from the carbon nanocapsules as the pyrolytic temperature is further

increased to finally yield the GCNs. The synthesized GCNs were used as an excellent support of platinum nanoparticles (3–5 nm) for methanol electro-oxidation. The Pt/GCN electrocatalyst exhibited a higher catalytic activity and better durability towards methanol electro-oxidation than Pt/C (Vulcan XC-72R support) and commercial Pt/C(JM) catalysts. The current density of the Pt/GCN catalyst for methanol electro-oxidation is as high as 275 A/g Pt, whereas for the Pt/C and Pt/C(JM) catalysts the values are only 190 and 184 A/g Pt, respectively.

Introduction

The interest in carbon nanomaterials was aroused after the discovery of carbon nanotubes in 1991 because of their special structure and unique electrical properties.^[1–3] Soon afterwards, the properties of novel carbon nanostructures such as nanocapsules,^[4] nanofibers,^[5] and nanobelts were also studied.^[6] Of these structures it has emerged that graphitic carbon nanocapsules (GCNs) have a wide range of potential applications, for example, in lithium-ion batteries,^[7] supercapacitors,^[8] hydrogen storage,^[9] and drug delivery.^[10] Notably, the GCNs have attracted growing research interest for their use as catalyst supports of direct methanol fuel cells (DMFCs) due to their outstanding properties, such as low density, high specific surface area, superb corrosion resistance, excellent electronic transport properties as well as high thermal resistance, high chemical stability, and high rigidity.^[11–15] Therefore, great effort has been made to fabricate GCNs.

The traditional synthetic methods, including arc discharge,^[16] pulsed laser irradiation,^[17] and metal-catalyzed chemical vapor deposition (CVD),^[18] require complex and

expensive production steps. To synthesize GCN materials that are suitable for use as electrocatalytic supports in DMFCs it is essential to develop facile and low-cost synthetic methods. Recently, the solid-state pyrolysis route, which involves the carbonization of carbon precursors containing transition-metal (e.g., Fe, Co, and Ni) graphitization catalysts, has attracted considerable attention for its advantages of easy handling, medium temperatures, and high yields.^[15,19–22] In previous studies we had developed an effective strategy for the synthesis of highly crystalline GCNs in high yields by a solid-state pyrolysis route using polyacrylic weak-base anion-exchange resin (PAWBA) and $K_3[Fe(CN)_6]$ as the carbon source and catalyst precursor, respectively.^[23] Shen and co-workers have subsequently used a similar method for the preparation of graphitic carbon.^[24] However, the mechanism for the formation of GCNs has not been clarified. Herein we report on an investigation into the formation of nanostructures of GCNs based on the structures of ion-exchange resin PAWBA and the results of a series of experiments, including TG, FTIR, Raman, and TEM analyses. The synthesized GCNs are very suitable for use as a catalyst support for Pt nanoparticles in fuel cells due to their high crystallinity and large specific surface area (SSA). Therefore, the application of GCNs as a support for platinum nanoparticles (3–5 nm) in methanol electro-oxidation has also been studied. The results indicate that the Pt/GCN electrocatalyst exhibits a higher catalytic activity and better durability towards methanol electro-oxidation than Pt/C (Vulcan XC-72R support) and commercial Pt/C(JM) catalysts.

[a] State Key Laboratory of Theoretical and Computational Chemistry, Jilin University, Changchun 130023, P. R. China
Fax: +86-451-8666-1259
E-mail: fuhg@vip.sina.com

[b] Laboratory of Functional Inorganic Materials Chemistry, Ministry of Education of the People's Republic of China, Heilongjiang University, Harbin 150080, P. R. China

Results and Discussion

Characterization of GCNs

A typical transmission electron microscopy (TEM) image of GCNs derived from PAWBA- $[\text{Fe}(\text{CN})_6]^{3-}$ after carbonization at 1100 °C and removal of the catalyst is shown in Figure 1. It can be seen that the sample consists of homogeneous hollow capsules with inner diameters of around 15 nm and outer diameters in the range of 30–40 nm (Figure 1a). The synthesized GCNs have a high crystallinity, as demonstrated by the high-resolution transmission electron microscopy image (Figure 1b), which displays highly defined (002) graphite lattice fringes of 0.34 nm. The carbon nanocapsules were dispersed by refluxing in nitric acid at 140 °C for 8 h and TEM images of the sample obtained are shown in Figure 1c,d. It can clearly be seen that the separated carbon nanocapsules are well dispersed and have high crystallinity, which further indicates that the as-prepared GCNs consist of individual carbon nanocapsules. Moreover, the X-ray diffraction (XRD) pattern of the GCNs exhibit well-resolved XRD peaks at $2\theta = 26.4, 42.5, 54.6,$ and 77.4° , which have been assigned to the (002), (100), (004), and (110) diffractions, respectively, of the graphitic framework (Figure 2a). The XRD results further confirm the high crystallinity of the synthesized GCNs. Raman spectroscopy is a useful technique for providing information on the structure of GCNs. For comparison, the Raman spectra of the GCNs and activated carbon and Vulcan XC-72R were recorded. A G-band peak at around 1580 cm^{-1} is associated with sp^2 vibrations of a perfect graphite crystal, whereas a D-band peak at around 1360 cm^{-1} is related to

vibrations at the crystal “edges”. As shown in Figure 2b, the G- and D-band peaks of the GCNs are located at 1567 and 1360 cm^{-1} , respectively. For activated carbon and Vulcan XC-72R, the two peaks are located at 1593 and 1357 cm^{-1} , and 1595 and 1357 cm^{-1} , respectively. The ratio of the intensities of the G and D bands (I_G/I_D) is generally used to estimate the degree of graphitization. The intensity ratios of I_G/I_D for the GCNs, activated carbon, and Vulcan XC-72R are around 2.1, 1.0, and 1.1, respectively, which indicates high crystallinity of the as-prepared GCNs, consistent with the results of the TEM and XRD analyses. Moreover, the yield of the resulting GCN material was about 1.1 g, which could be used in further applications.

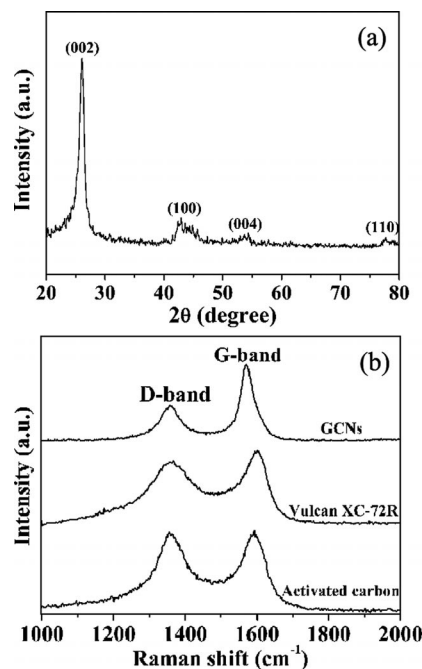


Figure 2. (a) XRD pattern of the GCNs. (b) Raman spectra of the GCNs activated carbon and Vulcan XC-72R.

The N_2 sorption isotherm for the synthesized GCNs is shown in Figure 3; a typical type-IV isotherm similar to H_2 hysteresis is observed. The pore-size distribution of the

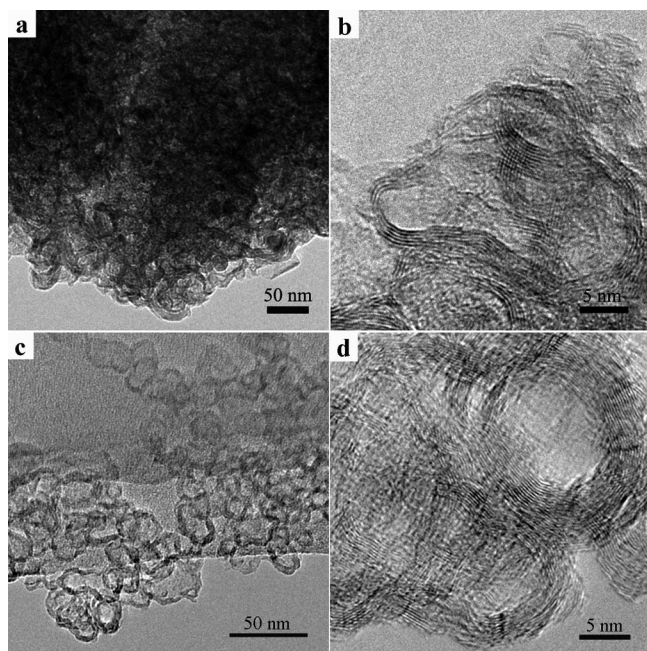


Figure 1. (a) TEM and (b) HRTEM images of the as-prepared GCNs. (c) TEM and (d) HRTEM images of the as-prepared GCNs after treatment with nitric acid; well-dispersed individual carbon nanocapsules can be observed.

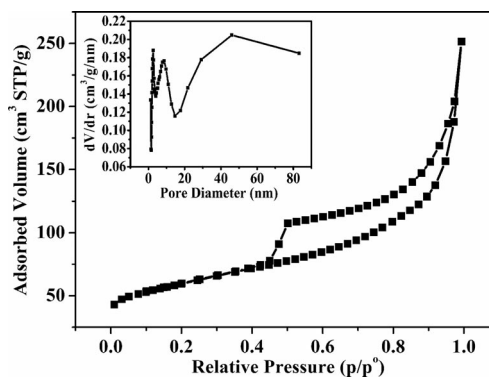


Figure 3. N_2 adsorption/desorption isotherm of the synthesized GCNs. The inset displays the corresponding pore-size distribution obtained by the BJH method.

synthesized GCNs, obtained by the BJH method, is mainly in the range of 20–90 nm. The SSA calculated from the Brunauer–Emmett–Teller (BET) equation and the total pore volume of the GCNs are 208.4 m²/g and 0.39 cm³/g, respectively. The SSA is much higher than that of the GCNs synthesized by a solid-state pyrolysis route using saccharides as the carbon source reported previously.^[15]

Mechanism for the Formation of GCNs

Investigating the mechanism for the formation of GCNs is very important to give an insight into the synthetic design of GCNs, which is also beneficial for its further applications. The GCNs were synthesized by pyrolysis of the PAWBA–[Fe(CN)₆]^{3−} composite. A TG analysis was performed to provide information on the pyrolysis of the PAWBA–[Fe(CN)₆]^{3−} composite (Figure 4). The weight loss observed below 200 °C has been attributed to the loss of H₂O from the PAWBA–[Fe(CN)₆]^{3−} composite. When the temperature was raised further, the weight loss increased rapidly until all the groups in the PAWBA resin had decomposed (about 700 °C). Finally, residues accounting for around 20 wt.-% of the starting material were obtained, which included GCNs and the remaining catalyst.

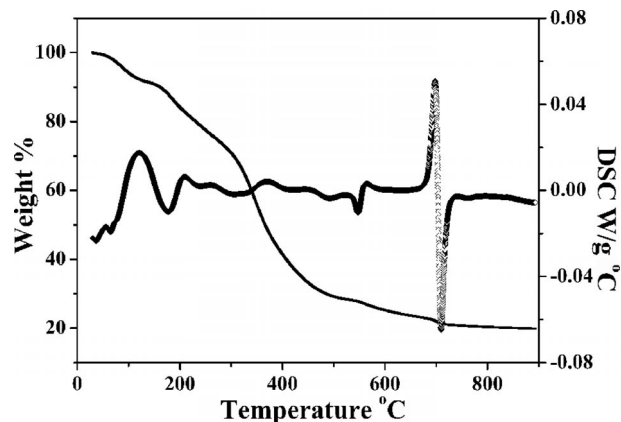


Figure 4. TG analysis of the carbon precursor PAWBA–[Fe(CN)₆]^{3−}.

IR spectroscopy provided information on the changes to the organic functional group in the ion-exchange resin during the synthesis. Figure 5 shows the IR spectra of samples derived from the PAWBA–[Fe(CN)₆]^{3−} composite after carbonization at different temperatures. It can clearly be seen that the characteristic peaks of organic groups between 2000 and 3000 cm^{−1} disappear almost completely as the temperature is raised to 500 °C, which indicates that the functional groups in PAWBA had decomposed and that the resin had been completely converted into amorphous carbon. The amorphous carbon gradually is graphitized as the temperature is raised.

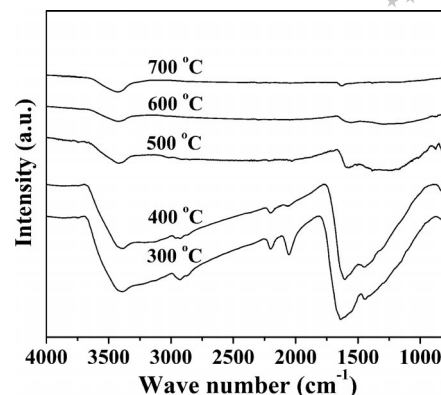


Figure 5. IR spectra of samples derived from the PAWBA–[Fe(CN)₆]^{3−} composite after carbonization at different temperatures.

Raman spectroscopy also provided evidence for the formation of GCNs. Figure 6 shows the Raman spectra of samples derived from PAWBA–[Fe(CN)₆]^{3−} after carbonization at different temperatures. It is well known that the D band is closely related to the disorder-induced scattering that results from imperfections or the loss of hexagonal symmetry in the structure, whereas the G band arises from the vibration of sp²-bonded carbon atoms in a two-dimensional hexagonal lattice. It can be seen that the intensity ratio *I*_G/*I*_D increases gradually with increasing carbonization temperature for the samples derived from PAWBA–[Fe(CN)₆]^{3−}. Notably, the G bands gradually shift from 1580 to 1567 cm^{−1} as the reaction temperature is increased from 700 to 1100 °C, which indicates an increase in the curvature of the carbon nanostructure and the formation of GCNs.^[25]

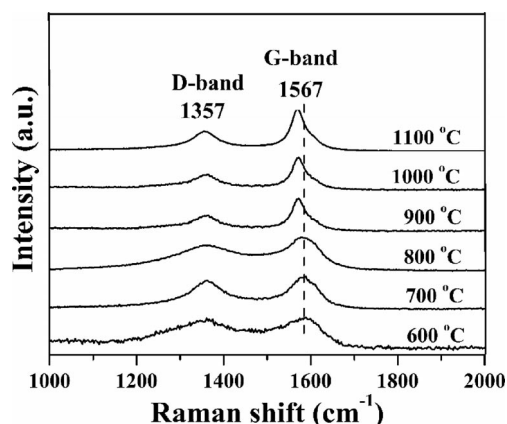


Figure 6. Raman spectra of samples derived from the PAWBA–[Fe(CN)₆]^{3−} composite after carbonization at different temperatures.

TEM analysis provided more detailed information about the formation and transformations of the GCNs. The formation processes were systematically studied by analyzing the samples at different stages of formation. The carbon nanocapsules were synthesized by pyrolysis of a PAWBA–[Fe(CN)₆]^{3−} composite. Figure 7 displays the TEM images of the samples derived from PAWBA–[Fe(CN)₆]^{3−} after car-

bonization at different temperatures without removal of the catalyst particles. At a carbonization temperature of 600 °C, the PAWBA- $[\text{Fe}(\text{CN})_6]^{3-}$ structure decomposes into carbon and catalyst particles (see Figure 7a). At 700 °C, the catalyst forms cores that can be encapsulated by carbon particles, as shown in Figure 7b. The catalyst particles escape from the carbon nanocapsules at higher temperatures, and the GCN nanostructures are finally obtained (Figure 7c,d).

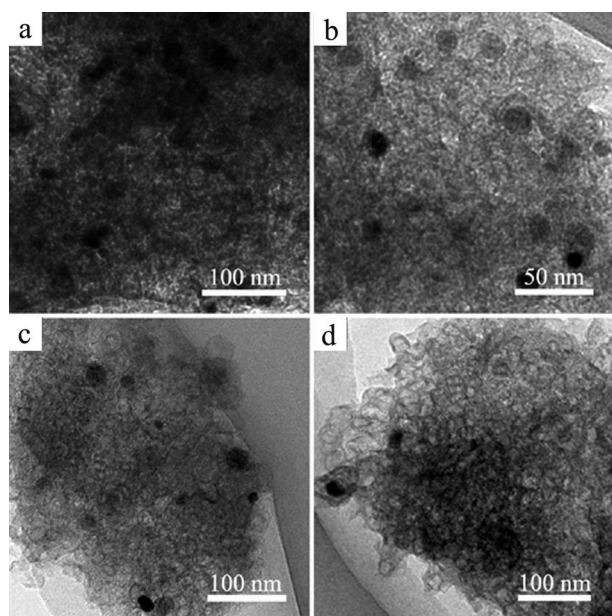


Figure 7. TEM images of samples derived from carbonization of PAWBA- $[\text{Fe}(\text{CN})_6]^{3-}$ at different temperatures: (a) 600, (b) 700, (c) 900, and (d) 1100 °C.

The structure of the ion-exchange resin is an important factor in the formation of GCNs. The structures of the ion-exchange resin PAWBA and the corresponding resin-metal-ion composite PAWBA- $[\text{Fe}(\text{CN})_6]^{3-}$ are shown in Figure 8. It can be seen that the exchange group of PAWBA has a large steric hindrance and the $[\text{Fe}(\text{CN})_6]^{3-}$ ion has a large

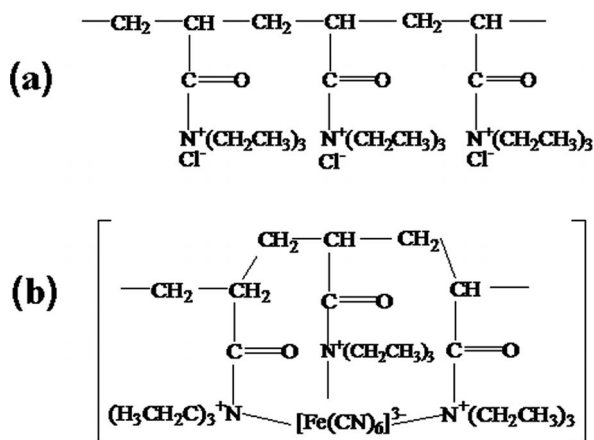
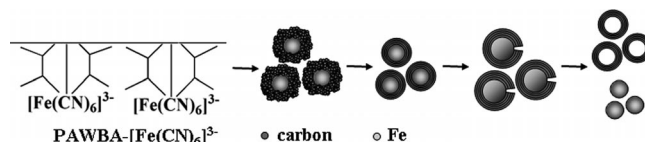


Figure 8. Structures of (a) the ion-exchange resin PAWBA and (b) the corresponding resin-metal-ion composite PAWBA- $[\text{Fe}(\text{CN})_6]^{3-}$.

volume. Therefore, it is proposed that the catalytic particles derived from the PAWBA- $[\text{Fe}(\text{CN})_6]^{3-}$ complex cannot easily come into contact with each other during the pyrolytic process due to steric hindrance, and thus the catalytic particles are generally separated by the active carbon atoms formed in the pyrolysis of PAWBA. The iron particles are then surrounded by carbon atoms at a high carbonization temperature so the carbon nanocapsules can be formed. When the carbonization temperature is further increased, the coated iron particles can escape from the carbon nanocapsules, which leads to the formation of hollow carbon nanocapsules. Based on the above analyses, a possible mechanism for the formation of GCNs has been proposed (Scheme 1).



Scheme 1. Proposed mechanism for the formation of GCNs.

Electrocatalytic Activity of Pt/GCN

Direct methanol fuel cells (DMFCs), with high energy conversion efficiency, high energy density, low noise, and no pollution for the environment, are new power sources to replace conventional sources. The electrocatalytic supports for DMFCs require materials to be highly crystalline and to have large SSAs. Because our synthesized GCNs exhibit these characteristics and can be prepared in high yields, they are anticipated to be excellent catalyst support materials for DMFCs. The traditional borohydride reduction method was adopted to prepare the Pt/GCN catalyst with 20 wt.-% Pt. The TEM images of the Pt/GCN catalyst in Figure 9 show that small aggregated Pt nanoparticles, with a diameter of about 3–5 nm, are dispersed over the GCNs.

X-ray photoelectron spectroscopy (XPS) was used to examine the composition of the GCNs and Pt/GCN catalyst. Figure 10a shows the C1s XPS of the GCNs; the main peak at around 284.6 eV has been attributed to the graphitic sp^2 carbon atom. The peaks at 285.1, 285.3, and 288.1 eV have been attributed to the carbon atom connected to oxygen groups, namely C–O–C and O–C=O (both resulting from the process of treatment with 10 wt.-% HCl at 90 °C to remove catalyst particles); the total oxygen content was about 4.63%.^[26] The oxygen groups in the Pt/GCN catalyst account for 3.25% of the weight, as shown in Figure 10b, which is clearly lower than that of the GCNs, which suggests that the oxygen groups of the GCNs could be reduced by borohydride during the loading of Pt nanoparticles onto the GCNs. The binding energies of the Pt(4f_{7/2}) and Pt(4f_{5/2}) electrons in the high-resolution EPS spectrum of the Pt(4f) line are 71.2 and 74.6 eV, respectively, as shown in Figure 10c, which indicates that the oxidation state of platinum in the Pt/GCN catalyst is platinum(0).^[15] In gene-

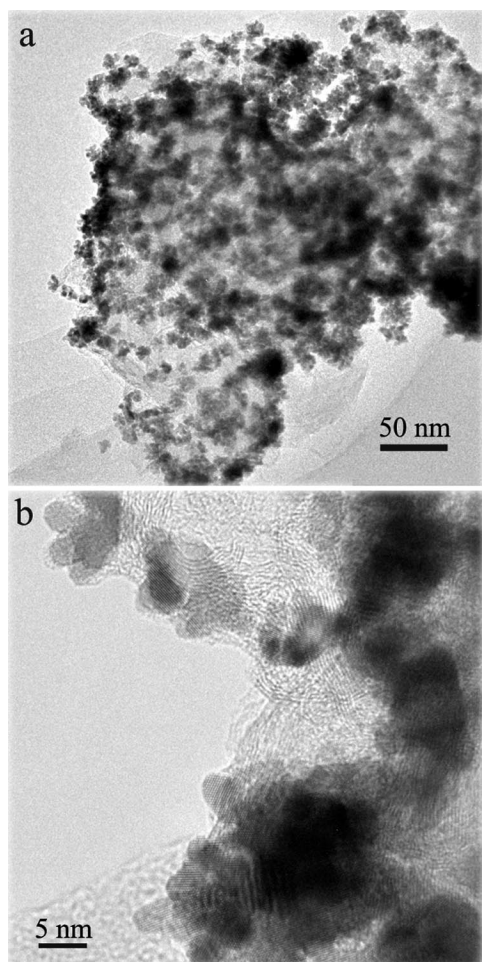


Figure 9. (a) TEM and (b) HRTEM images of the Pt/GCN catalyst synthesized by a borohydride reduction method.

ral, the oxidation state of the Pt nanoparticles deposited on the carbon surface is directly related to the hydrophilic nature of the carbon material.^[27] It can be concluded from the XPS analyses that the abundant oxygen groups (C–O–C and O–C=O) are present on the surfaces of the GCNs. Hence, GCNs with a hydrophilic nature may disperse uniformly in water, which allows the Pt nanoparticles to be evenly deposited on the surfaces of the GCNs.

To determine the weight percents of Pt in the Pt/GCN, Pt/C (Vulcan XC-72R), and Pt/C(JM) catalysts, TG tests were performed on the three catalysts under oxygen, and the results are displayed in Figure 11. The Pt contents of Pt/GCN, Pt/C (Vulcan XC-72R), and Pt/C(JM) calculated from the TGA curves are around 19.9, 19.8, and 20.1 wt.-%, respectively. Moreover, it can clearly be seen that the oxidation temperature for the Pt/GCN catalyst is higher than that of the Pt/C (Vulcan XC-72R) and Pt/C(JM) catalysts (by more than 200 °C) due to the higher crystallinity of the GCNs than of the carbon black. The above result further proves that the GCN support has better stability against oxidation than carbon black. It is known that the corrosion of carbon under oxidative conditions will lead to

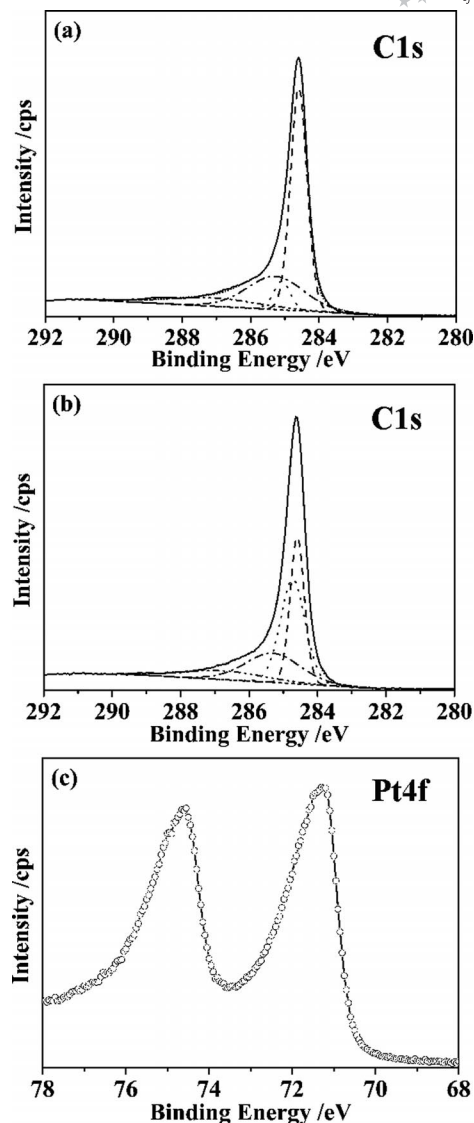


Figure 10. XPS of (a) C1s of the synthesized GCNs sample and (b) C1s and (c) Pt4f of the Pt/GCN catalyst.

a considerable reduction of the activity and durability of catalysts. Therefore, the synthesized GCNs could be used as advanced supports in DMFCs.

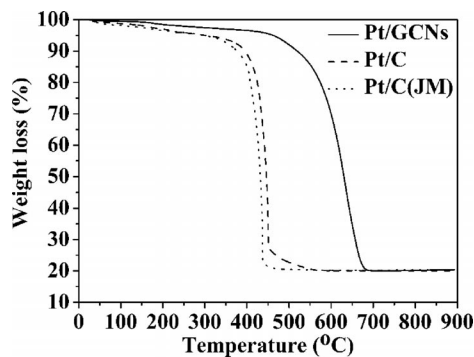


Figure 11. TG curves for the Pt/GCN, Pt/C (Vulcan XC-72R), and Pt/C(JM) catalysts under ambient oxygen. The Pt content is about 20 wt.-% for all of these catalysts based on weight loss.

Figure 12a shows the stabilized CVs obtained for the Pt/GCN, Pt/C (Vulcan XC-72R), and Pt/C(JM) catalysts in 1 M H₂SO₄ electrolyte at a scan rate of 50 mV/s. By using the hydrogen adsorption/desorption method described in the Exp. Sect., the electrochemical surface area (ESA) values deduced for the different catalysts are summarized in Table 1. Notably, the Pt/GCN catalyst has a high ESA value, much higher than those of the Pt/C (Vulcan XC-72R) and Pt/C(JM) catalysts. Thus, Pt exhibits high catalytic activity, and its use with GCNs in electrocatalytic supports has advantages.

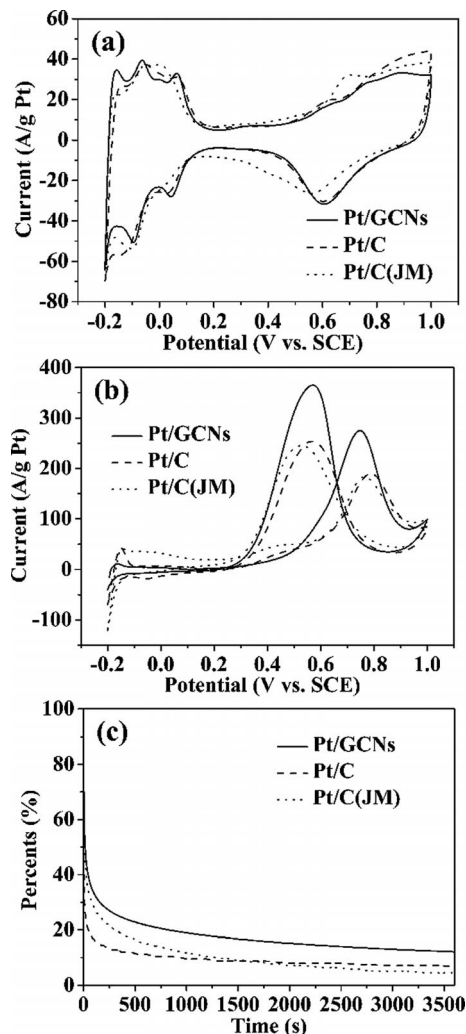


Figure 12. (a) Cyclic voltammograms for the Pt/GCN, Pt/C (Vulcan XC-72R), and Pt/C(JM) catalysts in a 1 M H₂SO₄ solution at a scan rate of 50 mV/s. (b) Cyclic voltammograms and (c) chronoamperometric curves for the oxidation of methanol with the Pt/GCN, Pt/C (Vulcan XC-72R), and Pt/C(JM) catalysts in 1 M CH₃OH and 1 M H₂SO₄ as electrolyte at a scan rate of 50 mV/s at room temperature.

The catalytic activity of Pt/GCN towards methanol electro-oxidation was investigated in 1 M CH₃OH and 1 M H₂SO₄ as electrolyte; Pt/C (Vulcan XC-72R) and Pt/C(JM) catalysts were also studied for comparison. The catalytic activity for methanol electro-oxidation is mainly evaluated by the onset potential, the peak potential, and the current

Table 1. Electrochemical activities towards methanol oxidation of Pt/GCN, Pt/C (Vulcan XC-72R), and Pt/C(JM) catalysts. J_m is the current density expressed per unit mass of Pt catalyst, and J_s is the current density expressed per unit surface area of Pt catalyst for methanol electro-oxidation ($J_s = J_m/\text{ESA}$).

Sample	Peak potential [V]	ESA [m ² /g Pt]	J_m [A/g Pt]	J_s [A/m ² Pt]
Pt/GCN	0.748	72.3	275	3.8
Pt/C	0.790	60.4	190	3.2
Pt/C(JM)	0.763	56.7	184	3.2

density. As can be seen from the CV curves shown in Figure 12b, the first methanol electro-oxidation peak potential in the forward scan is located at around 0.748 V for the Pt/GCN catalyst, which is much lower than that of 0.790 V for the Pt/C (Vulcan XC-72R) catalyst and 0.763 V for the Pt/C(JM), which indicates more favorable methanol oxidation with the Pt/GCN catalyst. Moreover, the Pt/GCN catalyst exhibits a much higher mass current density of 275 A/g Pt and a lower onset potential of 0.15 V in methanol electro-oxidation compared with the Pt/C (Vulcan XC-72R; 190 A/g Pt and 0.28 V) and Pt/C(JM) (184 A/g Pt and 0.24 V) catalysts, which indicates that the Pt/GCN catalyst exhibits excellent catalytic activity towards methanol electro-oxidation compared with the Pt/C (Vulcan XC-72R) and Pt/C(JM) catalysts. Moreover, the performance of the synthesized GCNs as support catalyst is much higher than that of CNTs and other reported graphitic carbon nanostructures (nanopipes and nanocoils).^[15,28,29] The durability of fuel cell catalysts is important for its practical application. Chronoamperometric tests over 3600 s for the catalysts were used to estimate the durability of the catalysts, and the results are displayed in Figure 12c. It can be seen that the residual currents for the Pt/GCN catalyst is 13% of its initial current density after 3600 s, which is much higher than that of the Pt/C (Vulcan XC-72R) (ca. 7%) and Pt/C(JM) (ca. 4%) catalysts. The results indicate the excellent stability of the Pt/GCN catalyst compared with Pt/C (Vulcan XC-72R) and Pt/C(JM). The above results demonstrate that the Pt/GCN catalyst has a high catalytic activity and excellent durability, which is important for the practical application of DMFCs.

Conclusions

GCNs with a large SSA have been prepared in high yield by a solid-state pyrolysis route using PAWBA-[Fe(CN)₆]³⁻ as the precursor. The synthesized GCNs exhibit high crystallinity, as shown by TEM, XRD, and Raman analyses. Based on a series of experiments, including TG, FTIR, Raman, and TEM analyses, a possible mechanism for the formation of the GCNs has been proposed as follows: The catalytic iron particles are surrounded by active carbon atoms derived from PAWBA during the pyrolytic process, and then the catalyst particles escape from the carbon nanocapsules with an increase in the pyrolytic temperature to give the GCNs. The synthesized GCNs were used as an electrocatalyst support to prepare a Pt/GCN catalyst with

Pt nanoparticles of 3–5 nm. The Pt/GCN catalyst exhibits a higher ESA, higher catalytic activity, and better durability towards methanol electro-oxidation than the Pt/C (Vulcan XC-72R support) and commercial Pt/C(JM) catalysts and is also superior to Pt nanoparticles deposited on other carbon forms such as CNTs.

Experimental Section

Preparation of the GCNs: In a typical synthesis, PAWBA ion-exchange resin (8 g) was added to a 0.08 M aqueous solution of $K_3[Fe(CN)_6]$ (115 mL), and the mixture was stirred for 24 h. After washing three times with water and drying at 100 °C, the corresponding ion-exchange resin–metal-ion composite was obtained, namely PAWBA– $[Fe(CN)_6]^{3-}$. Then the composite was carbonized under nitrogen at different temperatures (600–1100 °C) for 1 h. Subsequently, the prepared sample was treated with 10 wt.-% HCl at 90 °C for 8 h to remove catalyst particles. Afterwards, the samples were washed with distilled water until neutral to give the GCNs in a yield of approximately 1.1 g.

Preparation of the Pt/GCN Catalyst: Pt/GCN catalyst (20 wt.-%) was prepared by a traditional borohydride reduction method. In a typical synthesis, a certain quality of hexachloroplatinic(IV) acid was dissolved in deionized water, and the concentration was maintained at 0.002 M. Then the pH was adjusted to 8 by using 0.1 M NaOH solution, and the GCNs (0.2 g) were added. The suspension was treated with ultrasound for 0.5 h until uniformly mixed, and then excess $NaBH_4$ solution (0.15 g of $NaBH_4$ in 20 mL of deionized water) as the reducing agent was slowly added dropwise into the above solution, which was then stirred for 2 h. The solution was filtered, washed, and dried at 80 °C under vacuum to yield the Pt/GCN catalyst. In addition, Vulcan XC-72R supported catalyst (Pt/C, 20 wt.-% Pt) was also prepared according to the same procedure for comparison. A commercial Pt/carbon catalyst [Johnson Matthey, denoted as Pt/C(JM), 20 wt.-%] was also used as reference.

Characterization: X-ray diffraction (XRD) patterns were obtained with a Rigaku D/max-IIIb diffractometer by using $Cu-K\alpha$ ($\lambda = 1.5406 \text{ \AA}$) radiation. The accelerating voltage and the applied current were 40 kV and 20 mA, respectively. Transmission electron microscopy (TEM) experiments were performed with a JEM-2010 electron microscope (JEOL, Japan) with an acceleration voltage of 200 kV. Carbon-coated copper grids were used as the sample holders. Raman spectra were recorded with a Jobin Yvon HR 800 micro-Raman spectrometer at 457.9 nm. The laser beam was focused on the sample with a 50 \times objective. The laser intensity at the sample was kept below the threshold for any laser-induced changes in the Raman spectra and electrical transport characteristics. Thermogravimetric analysis was carried out by using an SDTQ600 instrument. FTIR spectra were recorded with a NICOLETIS10 spectrometer by using KBr pellets. XPS studies were carried out with a Kratos-AXIS UL TRA DLD instrument by using an $Al-K\alpha$ radiation source.

Electrochemical Measurements: Electrochemical experiments were performed with a three-electrode system by using a saturated calomel electrode (SCE) and Pt gauze as the reference and counter-electrode, respectively. A glass carbon (GC) electrode with a 4 mm diameter was used as the working electrode, which must be polished with 30 nm Al_2O_3 powder followed by washing with water and 2-propanol before testing. The catalyst (5 mg) and 5 wt.-% Nafion ionomer (50 μ L) were dispersed in 2-propanol (100 μ L). After the

catalyst ink had been mixed uniformly by using ultrasound, the ink (10 μ L) was dropped onto the GC electrode and left to dry. The electrochemical surface area (ESA) of platinum can be calculated from the cyclic voltammograms (CVs) recorded in 1 M H_2SO_4 electrolyte from the coulombic charges accumulated during hydrogen adsorption and desorption after correcting for the double-layer charging current according to Equation (1)^[30] in which Q_H is the electrical charge [mC] measured by the integration of the hydrogen adsorption and desorption region in the CVs between –0.2 V and 0.15 V, 0.21 mC/cm² is the electrical charge associated with monolayer adsorption of hydrogen on Pt, and [Pt] is the loading of Pt on the working electrode. The electrocatalytic activity and stability of the support catalyst for methanol electro-oxidation were measured in 1 M CH_3OH and 1 M H_2SO_4 as electrolyte. Before testing, nitrogen was bubbled through the electrolyte to remove oxygen. Electrochemical activity and stability were tested with a BAS100B electrochemical workstation.

$$ESA = \frac{Q_H}{0.21[Pt]} \quad (1)$$

Acknowledgments

We gratefully acknowledge the support of this research by the Key Program Projects of the National Natural Science Foundation of China (No. 21031001), the National Natural Science Foundation of China (No. 20971040, 21101061 and U1034003), the Cultivation Fund of the Key Scientific and Technical Innovation Project, the Ministry of Education of China (No. 708029) and the Youth Foundation of Heilongjiang Province of China (QC2010021).

- [1] S. Iijima, *Nature* **1991**, 354, 56–58.
- [2] L. Hu, D. S. Hecht, G. Grüner, *Chem. Rev.* **2010**, 110, 5790–5844.
- [3] G. Lota, K. Fic, E. Frackowiak, *Energy Environ. Sci.* **2011**, 4, 1592–1605.
- [4] P. Wu, N. Du, H. Zhang, J. Yu, D. Yang, *J. Phys. Chem. C* **2011**, 115, 3612–3620.
- [5] M. Pérez-Cabero, D. Kuvshinov, A. Guerrero-Ruiz, I. Rodríguez-Ramos, *Mater. Res. Bull.* **2008**, 43, 1737–1742.
- [6] Z. Kang, E. Wang, B. Mao, Z. Su, L. Gao, S. Lian, L. Xu, *J. Am. Chem. Soc.* **2005**, 127, 6534–6535.
- [7] W. Zhang, J. Hu, Y. Guo, S. Zheng, L. Zhong, W. Song, L. Wan, *Adv. Mater.* **2008**, 20, 1160–1165.
- [8] C. Wu, P. Wu, P. Lin, *J. Power Sources* **2010**, 195, 5122–5129.
- [9] C. Wu, X. Zhu, L. Ye, C. Ouyang, S. Hu, L. Lei, Y. Xie, *Inorg. Chem.* **2006**, 45, 8543–8550.
- [10] S. Kim, E. Shibata, R. Sergiienko, T. Nakamura, *Carbon* **2008**, 46, 1523–1529.
- [11] J. J. Niu, J. N. Wang, *J. Mater. Chem.* **2008**, 18, 5921–5926.
- [12] P. Kim, J. B. Joo, W. Kim, J. Kim, I. K. Song, J. Yi, *Catal. Lett.* **2006**, 112, 213–218.
- [13] Y. M. Chang, Y. C. Hsieh, P. W. Wu, *Diamond Relat. Mater.* **2009**, 18, 501–504.
- [14] X. Bo, J. Bai, J. Ju, L. Guo, *J. Power Sources* **2011**, 196, 8360–8365.
- [15] M. Sevil, C. Sanchís, T. Valdés-Solis, E. Morallón, A. B. Fierres, *Carbon* **2008**, 46, 931–939.
- [16] M. H. Teng, S. W. Tsai, C. I. Hsiao, Y. D. Chen, *J. Alloys Compd.* **2007**, 434–435, 678–681.
- [17] E. Ye, B. Liu, W. Y. Fan, *Chem. Mater.* **2007**, 19, 3845–3849.
- [18] P. Singjai, K. Wongwigkarn, Y. Laosiritaworn, R. Yimnirun, S. Maensiri, *Curr. Appl. Phys.* **2007**, 7, 662–666.

- [19] N. A. Katcho, E. Urones-Garrote, D. Avila-Brandé, A. Gomez-Herrero, S. Urbonaité, S. Csillag, E. Lomba, F. Agullo-Rueda, A. R. Landa-Canovas, L. C. Otero-Diaz, *Chem. Mater.* **2007**, *19*, 2304–2309.
- [20] Y. Huang, Y. Lin, C. Chen, *Mater. Chem. Phys.* **2011**, *127*, 397–404.
- [21] K. Chen, C. L. Wang, D. Ma, W. X. Huang, X. H. Bao, *Chem. Commun.* **2008**, *24*, 2765–2767.
- [22] Z. Chen, J. Wen, C. Yan, L. Rice, H. Sohn, M. Shen, M. Cai, B. Dunn, Y. Lu, *Adv. Energy Mater.* **2011**, *1*, 551–556.
- [23] L. Wang, C. Tian, B. Wang, R. Wang, W. Zhou, H. Fu, *Chem. Commun.* **2008**, *42*, 5411–5413.
- [24] G. He, Z. Yan, X. Ma, H. Meng, P. K. Shen, C. Wang, *Nano-scale* **2011**, *3*, 3578–3582.
- [25] E. D. Obiuztsova, M. Fujii, S. Hayashi, V. L. Kuznetsov, Y. V. Butenko, A. L. Chuvilin, *Carbon* **1998**, *36*, 821–826.
- [26] S. Stankovich, R. D. Piner, X. Chen, N. Wu, S. T. Nguyen, R. S. Ruoff, *J. Mater. Chem.* **2006**, *16*, 155–158.
- [27] H. S. Oh, H. Kim, *Adv. Funct. Mater.* **2011**, *21*, 3954–3960.
- [28] Y.-T. Kim, T. Mitani, *J. Catal.* **2006**, *238*, 394–401.
- [29] J. J. Wang, G. P. Yin, J. Zhang, Z. B. Wang, Y. Z. Gao, *Electrochim. Acta* **2007**, *52*, 7042–7050.
- [30] Y. C. Xing, *J. Phys. Chem. B* **2004**, *108*, 19255–19259.

Received: September 16, 2011

Published Online: January 18, 2012

The Nature of Spin Crossover and Coordination Core Distortion in a Family of Binuclear Iron(II) Complexes with Bipyridyl-Like Bridging Ligands

Galina S. Matouzenko,^{*,[a]} Erwann Jeanneau,^[b] Alexander Yu. Verat,^[a] and Yannick de Gaetano^[a]

Keywords: Iron / Ligand effects / Magnetic properties / Spin crossover / Binuclear complexes

The synthesis and characterization of two new binuclear compounds $[\text{Fe}(\text{dpia})(\text{NCS})_2]_2(\text{bpac}) \cdot n\text{CH}_3\text{OH}$ [$n = 0$ (**1**) and **2**], dpia = bis(2-picoly)amine, bpac = 1,2-bis(4-pyridyl)ethyne] are reported. The magnetic susceptibility measurements of the compounds revealed different types of magnetic behavior. Complex **1** displays a two-step spin crossover (SCO) that suggests the occurrence of a mixed [HS–LS] (HS = high spin, LS = low spin) pair at the plateau temperature (145 K), at which about 50 % of the complexes undergo a thermal spin conversion. The high-temperature step is very gradual, whereas the low-temperature step shows a first-order spin transition with a hysteresis width equal to 17 K. Compound **2** manifests a relatively abrupt one-step spin change with a narrow hysteresis of 4 K. The single-crystal X-ray structure of

1 was solved for the [HS–HS] complex at room temperature. Compound **2** was structurally characterized in both [HS–HS] and [LS–LS] spin states at 290 and 110 K. The magnetic and structural characteristics of **1** and **2** were compared with previously reported related binuclear compounds with 4,4'-bipyridine and 1,2-bis(4-pyridyl)ethene spacer ligands. This analysis confirms a recently proposed idea about the key role of the $[\text{FeN}_6]$ core structural distortions, which are caused by crystal packing and strain effects of terminal and/or bridging ligands, in the spin-crossover behavior of binuclear complexes. This study also revealed the predominant role of inter- vs. intramolecular interactions in the spin transition cooperativity.

Introduction

The design of new molecular compounds that exhibit spin-crossover (SCO) behavior is one of the most relevant issues in magnetic materials chemistry.^[1,2] The bistability between high-spin (HS) and low-spin (LS) electronic states implies a potential application of SCO compounds for information storage.^[3] Special attention has been paid to binuclear SCO compounds,^[1,4,5] which represent the simplest case of polynuclear species and for which particular effects due to covalently bridged metal centers can be expected. The first family of binuclear iron(II) SCO complexes was synthesized with the μ -bipyrimidine (bpym) bridging ligand.^[6] These compounds have been studied by a variety of experimental and theoretical methods.^[7–10] Further progress has been reached by the synthesis of new families of doubly pyrazolate- and triazolate-bridged diiron(II) SCO compounds.^[11–13] Extensive studies of these systems have revealed different types of magnetic behavior, such as one-

step [HS–HS] \leftrightarrow [LS–LS], two-step with a plateau [HS–HS] \leftrightarrow [HS–LS] \leftrightarrow [LS–LS], and partial (50%) [HS–HS] \leftrightarrow [HS–LS] spin transitions.^[5] The existence of the mixed [HS–LS] pair was unambiguously confirmed by Mössbauer spectroscopy with^[8] and without^[14,15] an external magnetic field. The only X-ray structural localization of the HS and LS sites in a mixed pair has been performed for a partial SCO complex,^[13] whereas all studies for two-step compounds at the plateau temperature resulted in an averaged centrosymmetric structure.^[15–18] These studies posed several problems of fundamental importance such as the intrinsic source of the three types of magnetic behavior and the cooperativity mechanism in binuclear compounds.^[4,5]

The general understanding of the origin of different types of SCO in binuclear complexes is an important challenge for the prediction of magnetic properties for new systems. Recently, the analysis of structural data for numerous binuclear complexes revealed the crucial role of ligand strain in the nature of SCO behavior.^[15] It has been concluded that the three types of SCO in binuclear compounds are conditioned by the degree of distortion of the $[\text{FeN}_6]$ octahedral geometry in different spin-state pairs, which is caused by both crystal packing and strain effects that arise from terminal and/or bridging ligands.^[18] A full one-step SCO can be observed for weakly constrained [HS–HS] species and for systems involving a sterically constrained zone,

[a] Laboratoire de Chimie (UMR CNRS and ENS-Lyon no 5182), École Normale Supérieure de Lyon, 46, allée d'Italie, 69364 Lyon cedex 07, France
Fax: +33-4-72728860
E-mail: Galina.Matouzenko@ens-lyon.fr

[b] Université Claude Bernard Lyon-1, Laboratoire des Multimatériaux et Interfaces (UMR CNRS no 5615), 69622 Villeurbanne cedex, France

Supporting information for this article is available on the WWW under <http://dx.doi.org/10.1002/ejic.201101178>.

common to both iron centers, that arises from a bridging ligand. The stabilization of the mixed [HS–LS] complex at the plateau temperature for the two-step or partial (50%) SCO results from an additional distortion of the HS site in the mixed pair. This extra distortion is basically specified by the ability of the ligand environment to perform transformations associated with the shortening of the Fe–N bond lengths and ordering of the N–Fe–N angles required for spin change to the LS state. The extent of the plateau is defined by a relative ligand field drop on the HS site in the mixed pair due to the extra distortion. In a partial SCO, compared with the two-step situation, the HS site in the mixed pair is highly distorted, which drastically weakens the ligand-field strength and this site loses the capacity for further spin change. A large original [FeN₆] distortion in the [HS–HS] complex leads to a reduction in the ligand-field strength and to HS state stabilization whatever the temperature. The novelty of this general approach, which is based on structural distortion criteria, consists of the analysis of *how* the structural changes are communicated in different spin-state isomers and *what* the consequences are for the three types of SCO observed for binuclear complexes.

This work has been undertaken to examine the relationship between strain-induced distortions and the SCO behavior in new binuclear compounds. In addition to recently reported binuclear SCO complexes with the bis-monodentate 4,4'-bipyridine (4,4'-bpy)^[15] and 1,2-bis(4-pyridyl)ethane (bpe)^[18] bridging units, two new binuclear SCO compounds [{Fe(dpia)(NCS)₂]₂(bpac)] (**1**) and [{Fe(dpia)(NCS)₂]₂(bpac)·2CH₃OH} (**2**) [dpia = bis(2-picoly)amine] with the 1,2-bis(4-pyridyl)ethyne (bpac) spacer ligand have been isolated. The new complexes show different types of SCO: **1** exhibits a two-step spin change, whereas **2** displays a relatively abrupt full one-step spin transition. Both compounds were characterized by single-crystal XRD. To examine the recently proposed SCO mechanism in binuclear compounds, we compared the structural characteristics of **1** and **2** and previously reported complexes.^[15,18] To gain further insight into the cooperativity mechanism in binuclear compounds, we analyzed the effects of inter- and intramolecular interactions on the cooperativity of spin change.

Results

Magnetic Susceptibility

The magnetic properties of **1** are presented in Figure 1 as a $\chi_M T$ (χ_M = molar magnetic susceptibility, T = temperature) vs. T plot. At 285 K, the magnitude of $\chi_M T$ is 6.66 cm³ mol^{−1} K, which corresponds to a quintet spin-state. This value varies slightly with decreasing temperature until 250 K and gradually decreases to 3.50 cm³ mol^{−1} K at ca. 145 K. Below 130 K, the $\chi_M T$ value descends abruptly to 0.30 cm³ mol^{−1} at 110 K. The residual paramagnetism (0.07 cm³ mol^{−1}) at 50 K is close to the expected temperature-independent paramagnetism value for singlet spin-state iron(II) complexes. The shape of the $\chi_M T$ vs. T curve shows

that the spin transition takes place in two steps that are separated by a short plateau centered at about 145 K at which 50% of complexes undergo a thermal spin conversion. The gradual high-temperature step is centered at 185 K. The low-temperature step displays a thermal hysteresis. The transition temperatures in the cooling and warming modes are $T_c \downarrow$ = 126 and $T_c \uparrow$ = 143 K, respectively, and the hysteresis width is equal to 17 K. Complex **1** exhibits a two-step SCO, which suggests the occurrence of the mixed [HS–LS] pair at the plateau temperature.

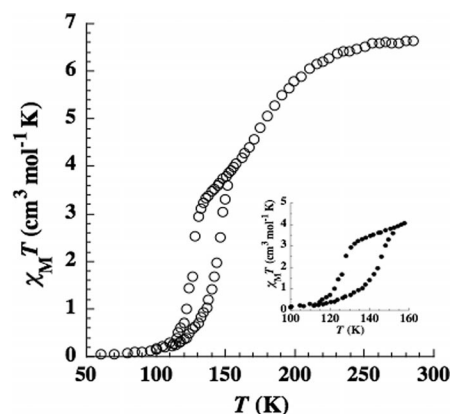


Figure 1. Thermal variation of $\chi_M T$ of **1**.

The variation of $\chi_M T$ vs. T for **2** is shown in Figure 2. At 290 K, the $\chi_M T$ value is 7.21 cm³ mol^{−1} K, which corresponds to a quintet spin-state. This value remains fairly constant with decreasing temperature until 200 K and then a relatively abrupt spin transition between 180 and 130 K occurs. Below 130 K, the $\chi_M T$ value slowly decreases to 0.16 cm³ mol^{−1} at 50 K, which is close to the expected value for LS iron(II) complexes. In the warming mode, the measurements revealed the presence of a thermal hysteresis effect. The observed transition temperatures are $T_c \downarrow$ = 150 and $T_c \uparrow$ = 154 K in the cooling and warming modes, respectively, and the hysteresis width is equal to 4 K. Complex **2** displays a relatively abrupt full one-step [HS–HS] ↔ [LS–LS] spin transition.

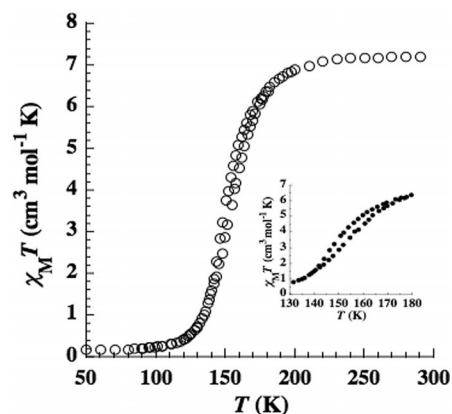


Figure 2. Thermal variation of $\chi_M T$ of **2**.

Description of the Structures of **1** and **2**

The single-crystal X-ray structure of **1** was determined for the [HS–HS] complex (293 K) and that of **2** for both [HS–HS] (290 K) and [LS–LS] (110 K) spin-state isomers. Compounds **1** and **2** crystallize in the monoclinic $C2/c$ ($Z = 4$) and $P2_1/n$ ($Z = 2$) groups, respectively (Table 3). Both

compounds consist of centrosymmetric binuclear units, in which the iron(II) atoms are linked by bpac (Figures 3 and 4). The midpoint of bpac in **1** and **2** coincides with the inversion center, and the asymmetric unit comprises half of a molecule. The unit cell of **2** also includes solvate methanol molecules. The coordination sphere of each iron(II) center contains three nitrogen atoms of the dpia ligand and two nitrogen atoms of the two NCS groups arranged in a *cis* configuration. The tridentate dpia ligand forms two five-membered chelate rings with an iron atom. Selected bond lengths and angles for **1** and **2** are given in Table 1.

Table 1. Selected bond lengths [Å] and angles [°] for **1** and **2**.^[a]

	1 293 K	2 290 K	2 110 K
Fe(1)–N(1)	2.109(5)	2.102(3)	1.957(2)
Fe(1)–N(2)	2.094(5)	2.082(3)	1.955(2)
Fe(1)–N(3)	2.192(4)	2.214(3)	1.988(2)
Fe(1)–N(4)	2.234(4)	2.218(3)	2.003(2)
Fe(1)–N(5)	2.222(4)	2.170(3)	1.956(2)
Fe(1)–N(6)	2.216(4)	2.234(2)	2.016(2)
N(1)–Fe(1)–N(2)	97.7(2)	96.5(1)	89.3(1)
N(1)–Fe(1)–N(3)	93.0(2)	94.4(1)	93.6(1)
N(1)–Fe(1)–N(4)	165.9(2)	168.6(1)	174.1(1)
N(1)–Fe(1)–N(5)	93.7(2)	97.1(1)	96.9(1)
N(1)–Fe(1)–N(6)	96.6(2)	92.4(1)	90.2(1)
N(2)–Fe(1)–N(3)	102.1(2)	93.2(1)	91.1(1)
N(2)–Fe(1)–N(4)	94.0(2)	89.5(1)	89.5(1)
N(2)–Fe(1)–N(5)	166.3(2)	166.4(1)	173.8(1)
N(2)–Fe(1)–N(6)	87.4(2)	89.6(1)	88.5(1)
N(3)–Fe(1)–N(4)	76.8(2)	75.5(1)	80.6(1)
N(3)–Fe(1)–N(5)	84.7(2)	86.3(1)	88.7(1)
N(3)–Fe(1)–N(6)	165.5(1)	172.3(1)	176.2(1)
N(4)–Fe(1)–N(5)	75.8(2)	77.2(1)	84.3(1)
N(4)–Fe(1)–N(6)	91.8(2)	97.4(1)	95.6(1)
N(5)–Fe(1)–N(6)	83.9(2)	89.3(1)	91.3(1)

[a] Estimated standard deviations in the least significant digits are given in parentheses.

[HS–HS] Structure of **1** (293 K)

In the [FeN₆] coordination core, the Fe–N distances are different and fall within the range 2.094(5)–2.234(4) Å (Table 1). The shortest Fe–N distances are formed by the two thiocyanate groups and the longest involves the secondary N4 atom. The average Fe–N distance is 2.178 Å. The values of the N–Fe–N angles (Table 1) between the adjacent and opposite atoms are in the range 75.8(2)–102.1(2)° and 165.5(1)–166.3(2)°, respectively, and show a strong deviation from the ideal O_h symmetry. The largest decrease from 90° is observed in the two five-membered chelate rings, which illustrates the steric constraints caused by the coordination of the tridentate dpia ligand. The CS group linked to the N2 atom is disordered over two positions with 0.5:0.5 occupancy (Figure 3). The NCS groups have nearly linear geometry [178.6(5)° for N1; 179(2) and 175(2)° for N2], whereas their Fe–N–C linkages are bent [168.3(5)° for N1; 163(1) and 173(2)° for N2]. The plane of the bpac ligand is

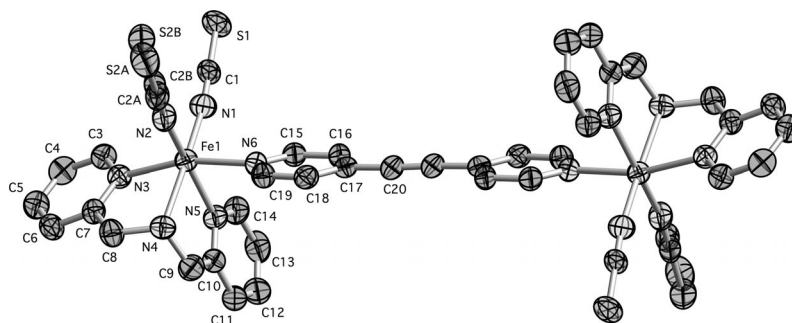


Figure 3. Molecular structure of **1** at 293 K. Ellipsoids enclose 30% probability. Hydrogen atoms are omitted for clarity.

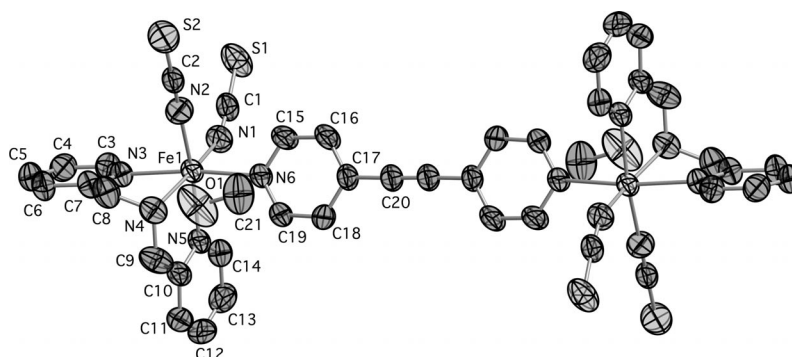


Figure 4. Molecular structure of **2** at 290 K. Ellipsoids enclose 30% probability. Hydrogen atoms are omitted for clarity.

slightly twisted relative to the Fe–N1–N3–N4–N6 coordination plane, which modifies the π -acceptor properties of the aromatic nitrogen atoms of bridging ligand. The Fe–Fe separation through the spacer ligand is 14.034(1) Å.

The crystal is formed from layers of molecules spreading in the [1 0 0] direction (Figure S1). The recurrent motif in a layer involves two ranges of binuclear molecules interlinked by intermolecular hydrogen bonding [N4–H4...S1 3.553(6) Å]. A similar H bond, which also plays an important role in SCO cooperativity, has been observed in [Fe-(bapbpy)(NCS)₂].^[19] The molecules in a layer are strongly bound by intermolecular π stacking interactions provided by several extremely short C...C contacts [up to 3.21(3) Å]. The molecules from the neighboring layers are also bound by several very short C...C contacts [up to 3.386(7) Å]. The intra- and interlayer intermolecular π stacking interactions are shown in Figure S2.

[HS–HS] Structure of **2** (290 K)

The structural parameters for the [FeN₆] core in the [HS–HS] structure of **2** (Table 1) are typical for iron(II) in the HS state. The Fe–N bond lengths vary from 2.082(3) to 2.234(2) Å, and the average Fe–N distance is 2.170 Å. The N–Fe–N angles are within the limits 75.5(1)–97.4(1)° and 166.4(1)–172.3(1)°. The largest N–Fe–N deviation from 90° is found in the two five-membered chelate rings formed by the dpia ligand. The two NCS groups have a nearly linear structure, however their Fe–N–C linkages are quite different. The Fe–N2–C2 linkage also has nearly linear geometry [173.2(3)°], whereas the Fe–N1–C1 linkage [151.8(3)°] exhibits a strong deviation from linearity. The bpac ligand plane is essentially twisted relative to the Fe–N1–N3–N4–N6 coordination plane, which can reduce the π acceptor properties of the N6 aromatic nitrogen atom. The Fe–Fe spacing through the bpac ligand is 14.091(1) Å.

The crystal packing (Figure S3) consists of alternate layers of binuclear molecules parallel to the *bc* plane. Each layer is formed from two sheets of molecules. The methanol molecules, located in the proximity of the neighbouring sheets, are involved in two extremely short intermolecular H bonds. The N4–H4...O1 [2.879(5) Å] hydrogen bond is arranged within a sheet, whereas the O1–H1...S1 [3.195(4) Å] hydrogen bond efficiently links the molecules from the neighboring sheets. In the sheets, the adjacent molecules are bound by π stacking interactions evidenced by short C...C intermolecular contacts [3.446(5) and 3.522(5) Å]. Several additional intermolecular C...C contacts [3.527(7)–3.582(7) Å] link the molecules from the neighboring sheets. Both S1 and S2 atoms of the two NCS groups participate in several short C...S intermolecular contacts [3.584(4)–3.775(4) Å] and link the molecules from the adjacent sheets.

[LS–LS] Structure (110 K) of **2**

The geometry of the [FeN₆] core is closer to *O_h* as a result of the HS→LS transition. The Fe–N bonds fall

within 1.955(2)–2.016(2) Å (Table 1), and the average Fe–N distance (1.979 Å) is reduced by 0.191 Å compared to the [HS–HS] structure. The N–Fe–N angles between the *cis* and *trans* nitrogen atoms are 80.6(1)–96.9(1)° and 173.8(1)–176.2(1)°, respectively. The two NCS groups retain a nearly linear structure, however the Fe–N–C linkages become less bent [161.0(2) and 172.6(2)° for the N1 and N2 linkages, respectively]. The intradimer Fe–Fe spacing is 13.735(1) Å.

The HS→LS transition is accompanied by a decrease of the unit cell volume of 146.4 Å³ (6.23%), which evidences high plasticity of the crystal. The anisotropy of the unit-cell contraction amounts to 0.94, 2.41, and 2.94% for the *a*, *b*, and *c* axes, respectively. The crystal packing and network of intermolecular interactions are similar to those observed at room temperature. However, the distances connected with the H bonds and intermolecular C...C and C...S contacts become shorter upon cooling, which shows the increased strength of the intermolecular interactions.

Discussion

Synthetic Approach

The design of new binuclear SCO compounds with desirable properties requires an understanding of the mechanisms that control the type and cooperativity of spin transition. The best way to search for the key factors responsible for these SCO characteristics is the analysis of structure–magnetic property correlations in a family of related compounds with systematic change just in the bridging or terminal ligand. Until recently, families of SCO binuclear compounds were based on the same bridging ligand, such as bipyrimidine (μ -bpym), pyrazolate (μ -bpypz), or triazolate (μ -bpytz), and the terminally bound ligands were varied. Most commonly, the compounds of these families were not systematically structurally characterized at different spin states, or the terminal ligands were too different in nature to be compared. These restrictions did not allow the performance of structure–property analysis. In this context, we intended to synthesize a family of binuclear compounds with variable bis-monodentate bridging units that feature similar structural and electronic properties, while retaining the other five positions in the [FeN₆] coordination core. We chose tridentate dpia and two NCS groups as integral terminal ligands and bipyridyl-like bridging ligands (4,4'-bpy, bpe, or bpac). We expected that such a variation would cause a slight change in the structural characteristics in a series of related compounds and their effect on the magnetic properties could be relatively easily identified.

With 4,4'-bpy, we isolated the two-step SCO binuclear complex [{Fe(dpia)(NCS)₂]₂(4,4'-bpy)]^[15] (**3**, Figure 5). Using the bpe ligand, we isolated three binuclear complexes [{Fe(dpia)(NCS)₂]₂(bpe)] \cdot *n*CH₃OH,^[18] which included two polymorphs **4** and **6** (*n* = 0) and a pseudopolymorph **5** (*n* = 2). These compounds display two-step (**4**), full one-step (**5**) SCO (Figures 5 and 6), and stable HS (**6**) behavior. The bpac-bridged pseudopolymorphs **1** and **2** also show different magnetic properties, namely, two-step (**1**) and one-

step (2) SCO. This family of binuclear compounds **1–6**, which have different bipyridyl-like bridging units, offers an excellent opportunity to analyze the correlations between the structural features and their different types of magnetic behavior.

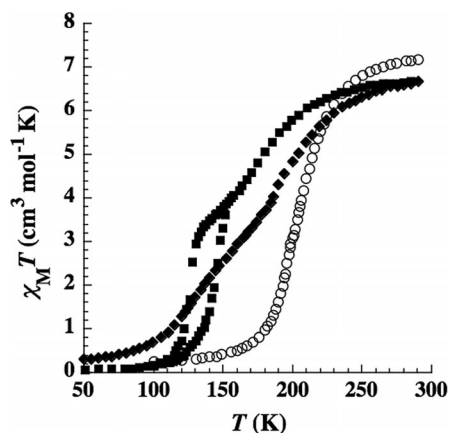


Figure 5. Thermal variation of $\chi_M T$ of **1** (■), **3** (○), and **4** (◆).

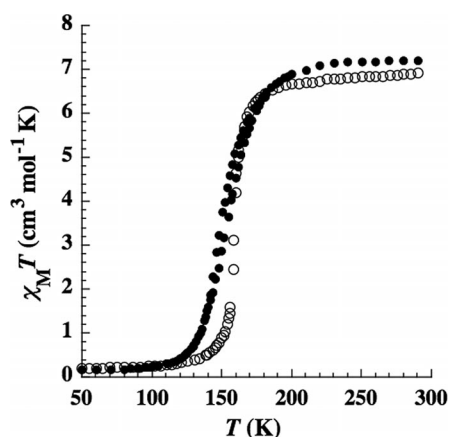


Figure 6. Thermal variation of $\chi_M T$ of **2** (●) and **5** (○).

Structure–Magnetic Property Correlations for **1–6**

Compounds **1–6** can be divided into two groups according to their different SCO behavior. In the first group, the SCO occurs in one step (**2** and **5**), whereas in the other

group the SCO has a two-step character (**1**, **3**, and **4**). We will analyze the two groups separately. The transition temperatures of **2** and **5** are close together: $T_c \downarrow = 150$ and $T_c \uparrow = 154$ K in the cooling and warming modes for **2** and 159 K for **5** (Figure 6). Our previous studies of families of mono-^[20] and binuclear^[18] polymorphic SCO compounds revealed that their magnetic properties are extremely sensitive to small structural variations in both the octahedral $[\text{FeN}_6]$ core geometry and the network of intermolecular cooperative interactions. Similar magnetic behavior assumes similarity of the structural features. At room temperature, both compounds have similar crystal structures (Figure S3). The binuclear molecules are bound by similar networks of intermolecular interactions that involve H bonding ($\text{N4–H4}\cdots\text{O1}$ and $\text{O1–H1}\cdots\text{S1}$) and short intermolecular $\text{C}\cdots\text{C}$ and $\text{C}\cdots\text{S}$ contacts. The distances connected with these intermolecular links are almost identical for both compounds. The molecular structures of **2** and **5**, which are composed of functionally similar chemical groups with the same relative arrangement around the metal centre, closely resemble each other. To estimate the degree of deviation of the $[\text{FeN}_6]$ geometry from the octahedron, several structural parameters were employed (Table 2). For the angular deviation, we used the values of the octahedral distortion parameter, Σ .^[21] This was calculated as the sum of the deviation of each of the 12 *cis* N–Fe–N angles from 90° and each of the three *trans* N–Fe–N angles from 180° . The $[\text{FeN}_6]$ core geometries of **2** and **5** display identical distortions (Table 2). Therefore, the similarity in the magnetic behavior of **2** and **5** can be attributed to the similarity of their structural characteristics. The one-step SCO compounds **2** and **5** exhibit less distorted $[\text{FeN}_6]$ core geometries. At the same time, this example also demonstrates that the magnetic properties may be insensitive to the difference in the electronic and structural features of the bridging ligands. The same trend is found for the two families of polymeric SCO compounds with bipyridine-like spacer ligands.^[22,23]

The two-step SCO complexes **1**, **3**, and **4** (Figure 5) also display similar molecular structures (Figure 3) and crystal packing (Figure S1) but slightly different networks of intermolecular interactions. The temperature of the plateaus ($T_{1/2}$), which separate the two steps, are in the order: $T_{1/2}(\mathbf{3}) > T_{1/2}(\mathbf{4}) > T_{1/2}(\mathbf{1})$ (Table 2), which reflects a decrease of the ligand-field strength. The structural determination was performed for the $[\text{HS–HS}]$ pair for **1** and for all spin-state

Table 2. Comparison of structural characteristics in the $[\text{HS–HS}]$ complexes of **1–6**.

	1	2	3	4	5	6 (Fe1 site)	6 (Fe2 site)
$T_{1/2}$ [K]	145	150/154	204	182	159	–	–
Fe–N range [Å]	2.094–2.234	2.082–2.234	2.068–2.236	2.089–2.248	2.093–2.239	2.085–2.289	2.106–2.220
Fe–N average [Å]	2.178	2.170	2.159	2.178	2.172	2.183	2.176
N–Fe–N (90°) range [$^\circ$]	75.8–102.1	75.5–97.4	76.4–98.4	75.9–101.8	75.1–98.0	72.9–101.7	76.3–100.6
Σ (90°) [$^\circ$]	80.3	63.6	68.1	80.5	65.8	88.1	65.1
N–Fe–N (180°) range [$^\circ$]	165.5–166.3	166.4–172.3	165.8–169.6	164.2–169.0	166.6–172.5	158.1–167.7	164.7–176.0
Σ (180°) [$^\circ$]	42.3	32.7	37.4	40.7	32.4	47.9	33.5
Fe–N–C (NCS) [$^\circ$]	168.3, 168.0 ^[a]	151.8, 173.2	167.5, 170.3	168.8, 160.2 ^[a]	148.2, 170.9	166.4, 170.4	156.2, 149.9
Fe–Fe separation [Å]	14.034	14.091	11.493	13.737	13.789	13.845	13.845

[a] Average value for one NCS group disordered over two positions.

isomers of **3** and **4**. Therefore, a full comparison of the structural data within the group can be performed for the [HS–HS] complexes. In all three compounds, the [FeN₆] core is formed from functionally identical chemical groups with the same relative arrangement around the metal centre. The average Fe–N distances in **1** and **4** are similar, but longer than those in **3**. The degree of angular deviation from octahedral geometry in three compounds, evidenced by Σ parameter values, is also different: less pronounced for **3** and more pronounced for **1** (Table 2). The increasing trend in the extent of the [FeN₆] distortion corresponds to the decrease in ligand-field strength, which leads to the order of the transition temperatures mentioned above. According to the proposed mechanism,^[15,18] the extent of the plateau in the two-step SCO is determined by the additional distortion of the HS site in the mixed [HS–LS] pair. The existence of the mixed [HS–LS] pair was unambiguously confirmed for **3** by routine Mössbauer spectroscopy without the application of a magnetic field.^[15] Unfortunately, the absence of structural data for the [HS–LS] pair for all three compounds does not allow the comparison of the HS site geometries in the mixed complexes. However, it is likely that the observed order of the HS site distortion in [HS–HS] is retained for the mixed [HS–LS] pairs of the three compounds. A more pronounced plateau is observed for **1**, which has the largest [FeN₆] core distortion, and the small core distortion in **3** results in a plateau that is reduced to a subtle inflexion point.

Examination of the whole family (Table 2) shows the different extent of the [FeN₆] distortion. This is evidenced by the Σ values from both 90 and 180°, which fall in the range 63.6–65.8 and 32.4–32.7°, respectively, for the one-step SCO compounds **2** and **5**, whereas for the two-step SCO compounds **1**, **3**, and **4**, they are within 68.1–80.5 and 37.4–42.3°, respectively. Furthermore, the smallest Σ values within the second group are observed for **3**, which displays spin change close to the borderline between one- and two-step SCO. The typical HS site FeI in **6** shows even higher Σ values (Table 2).^[24] In agreement with the proposed mechanism,^[15,18] the extent of the [FeN₆] core distortion for the two-step SCO complexes (**1**, **3**, and **4**) is intermediate between the one-step SCO compounds (**2** and **5**) and HS **6**.

The correlations between the quantitatively characterized distortions and different types of magnetic behavior are valid only for families of related SCO compounds with ligands that have similar electronic natures. The intramolecular steric constraint in the presented series results from the coordination of the terminal tridentate dpia ligand, which forms two fused, sterically strained, five-membered chelate rings with iron(II). Nevertheless, due to the presence of three additional monodentate ligands, the [FeN₆] core remains relatively flexible and, in principle, can be affected by crystal packing effects. It is important to recall that the one-step SCO compounds **2** and **5**, which have less distorted [FeN₆] cores, contain solvent molecules, whereas the more distorted two-step SCO compounds **1**, **3**, and **4** do not involve solvent molecules in the crystal lattice. Therefore, the variation of the [FeN₆] core distortion that leads to different

types of SCO in this family is related to the crystal packing modification by solvent inclusion. Solvent effects on SCO behavior, mainly focusing on cooperativity, are well documented.^[2f,25] This study demonstrates the role of solvent in the generation of intramolecular distortions that influence the type of SCO in binuclear complexes.

Cooperativity in 1–5

Compounds **1–5** display different SCO cooperativity, which has been estimated within the regular solution model^[26] (Supporting Information). It appears that the first transition [HS–HS]→[HS–LS] for **1** and **4** is less cooperative than that of **3** (Table S1). It is likely that similar cooperativity of the first transition [HS–HS]→[HS–LS] for **1** and **4** results from the similarities in the network of intermolecular cooperative interactions. Molecules of **1** and **4** in the [HS–HS] crystal lattice are linked by a similar 3D network of intermolecular interactions that comprise the N4–H4...S1 hydrogen bond (Figure S1) and the two modes of π stacking interactions (Figure S2). The distances that correspond to these intermolecular interactions are close for both compounds. Compound **3** also involves an extremely short [3.184(2) Å] intermolecular S1...S1 contact, which yields an infinite zigzag chain structure with close intra- and interdimer Fe–Fe separations [11.493(1) and 12.625(1) Å, respectively]. It could be suggested that this short contact, which leads to a quasipolymeric structure, is responsible for the stronger cooperativity of the high-temperature step for **3** relative to **1** and **4**. Certainly, the absence of such a S1...S1 contact in **1** and **4** is due to the different lengths of the 4,4'-bpy, bpe, and bpac bridging ligands. It is likely that the strong cooperativity in the low-temperature step for **1** results from a drastic reorganization of the network of intermolecular cooperative interactions at the plateau temperature. However, one can suppose that this reorganization occurs due to the appearance of the mixed pair, which is governed by intramolecular interactions. Unfortunately, attempts to perform structural analysis of **1** at the plateau failed because of crystal decomposition at this temperature.

The one-step SCO compound **2**, which also presents the hysteresis effect, was structurally characterized in the [HS–HS] and [LS–LS] forms. A comparison of the structures of both isomers did not reveal either a crystallographic phase transition or a sharp change in the crystal lattice parameters and/or topology of cooperative interactions. Upon cooling, the intermolecular distances connected with H bonding and π stacking are somewhat reduced, which shows the increased strength of the intermolecular interactions. Nevertheless, these minor changes do not usually give rise to a hysteresis effect. However, a large variation of the geometry of the Fe–N1–C1 linkage of one NCS group, which becomes less bent in the LS complex [151.8(3) and 161.0(2)° at 290 and 110 K, respectively], may indicate notable structural reorganization at intermediate temperatures.

It was previously proposed that cooperativity might be enhanced by the covalent linkage of metal centers by chemical bridges in polymeric or polynuclear structures.^[27] To elucidate the role of synergy of the intramolecular interactions through the spacer ligands and cooperative intermolecular interactions (H bonding, π stacking, van der Waals contacts) is not a trivial task. The effect of these two interactions could be more easily separated in a family of related compounds. In our study, we successfully synthesized two pairs of pseudopolymorphic modifications, namely, **1** and **2** with the bpac bridging ligand and **4** and **5** with the bpe spacer. The shapes of their magnetic curves (Figures 5 and 6) and fitting parameters (Supporting Information, Table S1 and Figure S4) show that the cooperativity of the spin change in each pair is different. It can be reasonably expected that the strength of intramolecular short-range interactions in each pseudopolymorphic pair is identical. Therefore, the difference in cooperativity in each pair can be attributed to the contributions from intermolecular cooperative interactions. It can be concluded that the overall cooperativity is mainly defined by intermolecular links, whereas the role of intramolecular links is minor. Indeed, examination of the data for known binuclear iron(II) compounds shows that they mostly display only a moderate cooperativity despite the presence of covalently linked metal centers. This conclusion agrees with our recent study of two families of SCO polymers,^[22,23] which demonstrated that the mere presence of a bridging unit that links the metal sites is not sufficient to build a highly cooperative SCO system.

Conclusions

The family of SCO binuclear systems offers a unique opportunity to analyze the correlations between their structural characteristics and magnetic behavior. The analysis described for $[\{\text{Fe}(\text{dpia})(\text{NCS})_2\}_2(\text{bpac})]$, its dimethanol solvate, and some previously reported complexes,^[15,18] revealed the crucial role of ligand strain on the nature of the SCO behavior. This study confirms the key role of the distortion of the $[\text{FeN}_6]$ octahedral geometry, which is caused by crystal packing and strain effects that arise from terminal and/or bridging ligands, in the generation of different types of magnetic behavior. This finding paves the way for the synthesis of new binuclear compounds with desired SCO behavior through the choice of bridging and terminal ligands. Furthermore, the examination of magnetic properties and the networks of intermolecular interactions in the crystal lattices of **1–5** demonstrated the synergy of intermolecular interactions (H bonding, π stacking, van der Waals contacts) to define the cooperativity of the spin transition and intramolecular interactions through the spacer.

Experimental Section

Chemistry: Synthesis of the Fe^{II} species was carried out with deoxygenated solvents under an inert atmosphere of N_2 using glovebox

techniques. Bis(2-picolyl)amine (dpia) was purchased from Aldrich. 1,2-bis(4-pyridyl)ethyne was prepared as described previously.^[28]

Synthesis of **1 and **2**:** A solution of KNCS (0.4 mmol) in MeOH (2 mL) was added to granules of $\text{FeSO}_4 \cdot 7\text{H}_2\text{O}$ (0.2 mmol) in MeOH (2 mL). The mixture was stirred for 15 min and filtered. A solution of bis(2-picolyl)amine (0.2 mmol) in MeOH (2 mL) was added dropwise to the filtrate with constant agitation, which resulted in the formation of a green-brown solution. After the addition of 1,2-bis(4-pyridyl)ethyne (0.1 mmol) in MeOH (1 mL), the reaction mixture was filtered, and the filtrate was left to stand overnight in a glovebox. Complexes **1** and **2** were obtained separately or as mixture of crystals, which were separated under microscope. Complex **1** was isolated as dark vinous-violet prismatic crystals, and **2** was obtained as dark red-brown druses. The crystals were collected by filtration, washed with methanol, and dried under vacuum. Crystals of **1** and **2** used for X-ray structure determination were selected from these samples; yield 50–60%. IR (KBr) for **1** and **2**: $\tilde{\nu} = 2068$ (for **1**) and 2073 cm^{-1} [for **2**, $\nu(\text{C}=\text{N})$]. For **1**: $\text{C}_{40}\text{H}_{34}\text{Fe}_2\text{N}_{12}\text{S}_4$ (922.72): calcd. C 52.07, H 3.71, N 18.22; found C 52.13, H 3.27, N 17.69. For **2**: $\text{C}_{42}\text{H}_{42}\text{Fe}_2\text{N}_{12}\text{O}_2\text{S}_4$ (986.81): calcd. C 51.12, H 4.29, N 17.03; found C 50.71, H 3.99, N 16.60.

Magnetic Measurements: Magnetic susceptibilities were measured from 20–300 K with a fully automated Manics DSM-10 susceptometer equipped with a TBT continuous-flow cryostat and an electromagnet operating at 1.6 Tesla. Data were corrected for magnetization of the sample holder and for diamagnetic contributions, estimated from the Pascal constants.

Solution and Refinement of the X-ray Structure: For **1**, data were collected with a Nonius Kappa CCD diffractometer using Mo radiation with COLLECT software.^[29] Reflection indexing, Lorentz-polarization correction, peak integration, and background determination were carried out with the DENZO^[30] program. Frame scaling and unit-cell parameter refinement were performed with the program SCALEPACK.^[30] The resulting set of hkl values was used for structure solution and refinement. A suitable crystal of **2** was selected and mounted in a Gemini kappa-geometry diffractometer (Agilent Technologies UK Ltd) equipped with an Atlas CCD detector and using Mo radiation ($\lambda = 0.71073 \text{ \AA}$). The intensities were collected at 100 and 290 K with the CrysAlisPro software.^[31] Reflection indexing, unit-cell parameter refinement, Lorentz-polarization correction, peak integration, and background determination were carried out with the CrysAlisPro software.^[31] An analytical absorption correction was applied using the modeled faces of the crystal.^[32] The structures were solved by direct methods with SIR97,^[33] and least-square refinement on F^2 was achieved with CRYSTALS software.^[34] All non-hydrogen atoms were refined anisotropically. The hydrogen atoms were all located in a difference map, but those attached to carbon atoms were repositioned geometrically. The H atoms were initially refined with soft restraints on the bond lengths and angles to regularize their geometry (C–H in the 0.93–0.98 range, N–H in the 0.86–0.89 range, and O–H equal to 0.82 \AA) and $U_{\text{iso}}(\text{H})$ (in the range 1.2–1.5 times U_{eq} of the parent atom), after which the positions were refined with riding constraints (Table 3). Compound **1** displayed solvent accessible voids in the unit cell where residual electron density was present, which was taken into consideration by using the SQUEEZE algorithm.^[35]

CCDC-846878 (for **1**), -846879 (for [HS–HS] **2**), and -846880 (for [LS–LS] **2**) contain the supplementary crystallographic data for this paper. These data can be obtained free of charge from The Cambridge Crystallographic Data Centre via www.ccdc.cam.ac.uk/data_request/cif.

Table 3. Crystallographic data for **1** and **2**.^[a]

	1	2	2
Spin state	HS–HS	HS–HS	LS–LS
Empirical formula	C ₄₀ H ₃₄ N ₁₂ S ₄ Fe ₂	C ₄₂ H ₄₂ N ₁₂ S ₄ O ₂ Fe ₂	C ₄₂ H ₄₂ N ₁₂ S ₄ O ₂ Fe ₂
<i>M</i>	922.75	986.86	986.86
<i>T</i> [K]	293	290	110
Crystal system	monoclinic	monoclinic	monoclinic
Space group	<i>C</i> 2/ <i>c</i>	<i>P</i> 2 ₁ / <i>n</i>	<i>P</i> 2 ₁ / <i>n</i>
<i>a</i> [Å]	20.974(1)	9.918(1)	9.825(1)
<i>b</i> [Å]	12.256(1)	17.249(2)	16.833(2)
<i>c</i> [Å]	20.713(1)	13.829(1)	13.423(2)
β [°]	114.326(2)	96.63(1)	96.96(1)
<i>V</i> [Å ³]	4851.6(2)	2350.0(4)	2203.6(5)
$\rho_{\text{calcd.}}$ [g cm ^{−3}]	1.263	1.395	1.487
<i>Z</i>	4	2	2
λ [Å]	0.71073	0.7107	0.7107
$\mu(\text{Mo–K}\alpha)$ [mm ^{−1}]	0.810	0.844	0.900
θ range [°]	2.0–25.2	3.6–29.6	3.5–29.5
Independent reflections	4302	6020	5388
Independent reflections with $I > 2\sigma(I)$	3280	4349	4542
Parameters	280	280	280
$R[F^2 > 2\sigma(F)^2]$	0.0740	0.0534	0.0431
$wR_2(F^2)$	0.2156	0.0765	0.0657

[a] Estimated standard deviations in the least significant digits are given in parentheses.

Supporting Information (see footnote on the first page of this article): Regular solution models of **1**–**5**, intra- and interlayer intermolecular π stacking interactions in **1**, crystal packing in the [HS–HS] structure of **2**, fitting parameters for magnetic curves.

Acknowledgments

We are grateful to the Agence Nationale de la Recherche (ANR) (NANOMOL project, grant to A. Yu. V. and Y. d. G.). This work was supported by the European Union (EU) (NE MAGMANET, grant number FP6-NMP3-CT-2005-515767). The authors are thankful to S. A. Borshch for valuable help.

- [1] *Spin Crossover in Transition Metal Compounds*, in: *Top. Curr. Chem* (Eds.: P. Gülich, H. A. Goodwin), **2004**, 233–235.
- [2] a) O. Kahn, *Molecular Magnetism*, VCH Publishers, New York, **1993**; b) P. Gülich, Y. Garcia, H. Spiering, in: *Magnetism: Molecules to Materials IV*, Wiley-VCH, Weinheim, Germany, **2002**, pp. 271–344; c) A. Bousseksou, G. Molnár, G. S. Matouzenko, *Eur. J. Inorg. Chem.* **2004**, 4353–4369; d) P. Gülich, P. J. van Koningsbruggen, F. Renz, *Struct. Bonding (Berlin)* **2004**, 107, 27–75; e) A. B. Gaspar, V. Ksenofontov, M. Serednyuk, P. Gülich, *Coord. Chem. Rev.* **2005**, 249, 2661–2676; f) J. A. Real, A. B. Gaspar, M. C. Muñoz, *Dalton Trans.* **2005**, 2062–2079; g) M. Sorai, M. Nakano, Y. Miyazaki, *Chem. Rev.* **2006**, 106, 976–1031; h) J. Kitchen, S. Brooker, *Coord. Chem. Rev.* **2008**, 252, 2072–2092; i) M. A. Halcrow, *Coord. Chem. Rev.* **2009**, 253, 2493–2514; j) B. Weber, *Coord. Chem. Rev.* **2009**, 253, 2432–2449.
- [3] a) O. Kahn, J.-P. Launay, *Chemtronics* **1988**, 3, 140–144; b) O. Kahn, J. Kröber, C. Jay, *Adv. Mater.* **1992**, 4, 718–728.
- [4] a) A. B. Gaspar, M. C. Muñoz, J. A. Real, *J. Mater. Chem.* **2006**, 16, 2522–2533; b) A. Bousseksou, G. Molnár, J. A. Real, K. Tanaka, *Coord. Chem. Rev.* **2007**, 251, 1822–1833.
- [5] K. S. Murray, *Eur. J. Inorg. Chem.* **2008**, 3101–3121.
- [6] J. A. Real, H. Bolvin, A. Bousseksou, A. Dworkin, O. Kahn, F. Varret, J. Zarembowitch, *J. Am. Chem. Soc.* **1992**, 114, 4650–4658.
- [7] a) V. Ksenofontov, A. B. Gaspar, J. A. Real, P. Gülich, *J. Phys. Chem. B* **2001**, 105, 12266–12271; b) G. Chastanet, C. Carbonera, C. Mingotaud, J.-F. Létard, *J. Mater. Chem.* **2004**, 14, 3516–3523.
- [8] a) V. Ksenofontov, H. Spiering, S. Reiman, Y. Garcia, A. B. Gaspar, N. Moliner, J. A. Real, P. Gülich, *Chem. Phys. Lett.* **2001**, 348, 381–386; b) A. B. Gaspar, V. Ksenofontov, H. Spiering, S. Reiman, J. A. Real, P. Gülich, *Hyperfine Interact.* **2002**, 144/145, 297–306; c) V. Ksenofontov, H. Spiering, S. Reiman, Y. Garcia, A. B. Gaspar, N. Moliner, J. A. Real, P. Gülich, *Hyperfine Interact.* **2002**, 141/142, 47–52.
- [9] a) A. Bousseksou, F. Varret, J. Nasser, *J. Phys. I (France)* **1993**, 3, 1463–1473; b) A. Bousseksou, J. Nasser, J. Linares, K. Boukheddaden, F. Varret, *Mol. Cryst. Liq. Cryst.* **1993**, 234, 269–274.
- [10] S. Zein, S. A. Borshch, *J. Am. Chem. Soc.* **2005**, 127, 16197–16201.
- [11] a) N. Suemura, M. Ohama, S. Kaizaki, *Chem. Commun.* **2001**, 1538–1539; b) K. Nakano, N. Suemura, S. Kawata, A. Fuyuhito, T. Yagi, S. Nasu, S. Morimoto, S. Kaizaki, *Dalton Trans.* **2004**, 982–988; c) K. Nakano, S. Kawata, K. Yoneda, A. Fuyuhito, T. Yagi, S. Nasu, S. Morimoto, S. Kaizaki, *Chem. Commun.* **2004**, 2892–2893; d) K. Yoneda, K. Adachi, S. Hayami, Y. Maeda, M. Katada, A. Fuyuhito, S. Kawata, S. Kaizaki, *Chem. Commun.* **2006**, 45–47.
- [12] a) B. A. Leita, B. Moubaraki, K. S. Murray, J. P. Smith, J. D. Cashion, *Chem. Commun.* **2004**, 156–157; b) S. R. Batten, J. Bjernemose, P. Jensen, B. A. Leita, K. S. Murray, B. Moubaraki, J. P. Smith, H. Toftlund, *Dalton Trans.* **2004**, 3370–3375; c) J. J. M. Amooore, C. J. Kepert, J. D. Cashion, B. Moubaraki, S. M. Neville, K. S. Murray, *Chem. Eur. J.* **2006**, 12, 8220–8227; d) C. J. Schneider, J. D. Cashion, B. Moubaraki, S. M. Neville, S. R. Batten, D. R. Turner, K. S. Murray, *Polyhedron* **2007**, 26, 1764–1772; e) J. J. M. Amooore, S. M. Neville, B. Moubaraki, S. S. Iremonger, J.-F. Létard, C. J. Kepert, *Chem. Eur. J.* **2010**, 16, 1973–1982.
- [13] M. H. Klingele, B. Moubaraki, J. D. Cashion, K. S. Murray, S. Brooker, *Chem. Commun.* **2005**, 987–989.
- [14] C. M. Grunert, S. Reiman, H. Spiering, J. Kitchen, S. Brooker, P. Gülich, *Angew. Chem.* **2008**, 120, 3039; *Angew. Chem. Int. Ed.* **2008**, 47, 2997–2999.
- [15] A. Yu. Verat, N. Ould-Moussa, E. Jeanneau, B. Le Guennic, A. Bousseksou, S. A. Borshch, G. S. Matouzenko, *Chem. Eur. J.* **2009**, 15, 10070–10082.

- [16] N. Ortega-Villar, A. L. Thompson, M. C. Muñoz, V. M. Ugalde-Saldivar, A. E. Goeta, R. Morena-Esparza, J. A. Real, *Chem. Eur. J.* **2005**, *11*, 5721–5734.
- [17] A. B. Gaspar, V. Ksenofontov, S. Reiman, P. Gütllich, A. L. Thompson, A. E. Goeta, M. C. Muñoz, J. A. Real, *Chem. Eur. J.* **2006**, *12*, 9289–9298.
- [18] G. S. Matouzenko, E. Jeanneau, A. Yu. Verat, A. Bousseksou, *Dalton Trans.* **2011**, *40*, 9608–9618.
- [19] a) S. Bonnet, M. A. Siegler, J. S. Costa, G. Molnár, A. Bousseksou, A. L. Spek, P. Gamez, J. Reedijk, *Chem. Commun.* **2008**, 5619–5621; b) S. Bonnet, G. Molnár, J. S. Costa, M. A. Siegler, A. L. Spek, A. Bousseksou, W.-T. Fu, P. Gamez, J. Reedijk, *Chem. Mater.* **2009**, *21*, 1123–1136.
- [20] G. S. Matouzenko, A. Bousseksou, S. Lecocq, P. J. van Koningsbruggen, M. Perrin, O. Kahn, A. Collet, *Inorg. Chem.* **1997**, *36*, 5869–5879.
- [21] a) P. Guionneau, C. Brigouleix, Y. Barrans, A. E. Goeta, J.-F. Létard, J. A. Howard, J. Gaultier, D. C. Chasseau, *C. R. Acad. Sci., Ser. IIC* **2001**, *4*, 161–171; b) P. Guionneau, M. Marchivie, G. Bravic, J. F. Létard, D. Chasseau, *Top. Curr. Chem.* **2004**, *234*, 97–128.
- [22] a) G. S. Matouzenko, G. Molnár, N. Bréfuel, M. Perrin, A. Bousseksou, S. A. Borshch, *Chem. Mater.* **2003**, *15*, 550–556; b) G. S. Matouzenko, M. Perrin, B. Le Guennic, C. Genre, G. Molnár, A. Bousseksou, S. A. Borshch, *Dalton Trans.* **2007**, 934–942.
- [23] a) C. Genre, G. S. Matouzenko, E. Jeanneau, D. Luneau, *New J. Chem.* **2006**, *30*, 1669–1674; b) C. Genre, E. Jeanneau, A. Bousseksou, D. Luneau, S. A. Borshch, G. S. Matouzenko, *Chem. Eur. J.* **2008**, *14*, 697–705.
- [24] Stabilization of the HS state at the Fe2 site of **6** results from strongly nonlinear FeNC groups (see ref.^[18]).
- [25] a) A. M. Greenaway, C. J. O'Connor, A. Schrock, E. Sinn, *Inorg. Chem.* **1979**, *18*, 2692–2695; b) F. Cecconi, M. Di Vaira, S. Modollini, A. Orlandini, L. Sacconi, *Inorg. Chem.* **1981**, *20*, 3423–3430; c) H. Toftlund, *Coord. Chem. Rev.* **1989**, *94*, 67–108; d) H. R. Chang, J. K. McCusker, H. Toftlund, S. R. Wilson, A. X. Trautwein, H. Winkler, D. N. Hendrickson, *J. Am. Chem. Soc.* **1990**, *112*, 6814–6827; e) J. A. Real, M. C. Muñoz, E. Andrés, T. Garnier, B. Gallois, *Inorg. Chem.* **1994**, *33*, 3587–3494; f) P. Gütllich, A. Hauser, H. Spiering, *Angew. Chem.* **1994**, *106*, 2109; *Angew. Chem. Int. Ed. Engl.* **1994**, *33*, 2024–2054; g) P. Gütllich, H. A. Goodwin, *Top. Curr. Chem.* **2004**, *233*, 1–47.
- [26] C. P. Slichter, H. G. Drickamer, *J. Chem. Phys.* **1972**, *56*, 2142.
- [27] a) O. Kahn, E. Codjovi, *Phil. Trans. R. Soc. A* **1996**, *354*, 359–379; b) O. Kahn, Y. Garcia, J.-F. Létard, C. Mathonière, *NATO ASI Ser., Ser. C* **1998**, *518*, 127–144.
- [28] M. Tanner, A. Ludi, *Chimia* **1980**, *34*, 23–24.
- [29] Nonius, *COLLECT*, Nonius BV, Delft, **1997–2001**.
- [30] Z. Otwinowski, W. Minor, *Methods Enzymol.* **1997**, *276*, 307–326.
- [31] *CrysAlisPro*, Agilent Technologies, version 1.171.34.49 (release 20-01-2011 CrysAlis171.NET) (compiled Jan. 20, **2011**, 15:58:25 h).
- [32] R. C. Clark, J. S. Reid, *Acta Crystallogr., Sect. A* **1995**, *51*, 887–897.
- [33] A. Altomare, M. C. Burla, M. Camalli, G. L. Cascarano, C. Giacovazzo, A. Guagliardi, A. Moliterni, G. Polidori, R. Rizzi, *J. Appl. Crystallogr.* **1999**, *32*, 115–119.
- [34] P. W. Betteridge, J. R. Carruthers, R. I. Cooper, K. Prout, D. J. Watkin, *J. Appl. Crystallogr.* **2003**, *36*, 1487.
- [35] P. van der Sluis, A. L. Spek, *Acta Crystallogr., Sect. A: Fundam. Crystallogr.* **1990**, *46*, 194.

Received: October 25, 2011

Published Online: January 23, 2012

Silver Melonates and Coordination Modes of the Multidentate $[\text{C}_6\text{N}_7(\text{NCN})_3]^{3-}$ Anion

Corinna Clauss,^[a] Uwe Böhme,^[a] Anke Schwarzer,^[a] and Edwin Kroke*^[a]

Keywords: N ligands / X-ray diffraction / Anions / Quantum chemical calculations / Silver

Three different silver melonates, $\text{Ag}_3[\text{C}_6\text{N}_7(\text{NCN})_3]\cdot\text{H}_2\text{O}$ (**2a**), $\text{Ag}_3[\text{C}_6\text{N}_7(\text{NCN})_3]\cdot 0.5\text{NH}_3$ (**2b**) and $\text{Ag}_3[\text{C}_6\text{N}_7(\text{NCN})_3]\cdot 2\text{C}_2\text{H}_8\text{N}_2$ (**2c**), and a nickel melonate, $\text{Ni}_3[\text{C}_6\text{N}_7(\text{NCN})_3]\cdot 10\text{NH}_3\cdot 6\text{H}_2\text{O}$ (**3**), have been synthesised by the reaction of potassium melonate with silver nitrate either in an aqueous solution (**2a**), aqueous ammonia solution (**2b**) or an aqueous solution of ethylenediamine (**2c**) and with nickel nitrate in an aqueous ammonia solution (**3**). The crystal structure of **2c** was determined by XRD [triclinic, $P\bar{1}$, $a = 7.5499(4)$, $b = 11.3438(6)$, $c = 12.5741(7)$ Å, $\alpha = 72.138(4)$, $\beta = 80.148(4)$, $\gamma = 75.945(4)^\circ$, $V = 984.90(9)$ Å³]. Silver atoms are coordinated to the terminal nitrogen atom of the cyanamide substituent as well as directly to the N atoms of the *s*-heptazine core. Complex **2c** crystallises in a layered structure. Adjacent Ag–melonate cation–anion units are connected by Ag–Ag interactions. The preferred coordination mode of metal ions at the

melonate anion has been considered by quantum chemical calculations. Natural atomic charges calculated for the four nonequivalent, nucleophilic N atoms of the $[\text{C}_6\text{N}_7(\text{NCN})_3]^{3-}$ anion are (a) –0.596, (b) –0.619, (c) –0.675 and (d) –0.644. The metal coordination found experimentally in the melonates correlates with these relatively small charge differences and with the hard-soft acid–base concept. However, (mono)protonation of the $[\text{C}_6\text{N}_7(\text{NCN})_3]^{3-}$ anion *exclusively* occurs at the terminal N atoms (b) of the *s*-heptazine core, which is indicated experimentally and theoretically. Silver melonates **2a**, **2b** and **2c** and nickel melonate **3** were further characterised by FTIR and ¹³C solid-state magic-angle spinning NMR spectroscopy, thermogravimetric/differential thermal analysis and elemental analysis. Solvent-free complexes **2a** and **2b**, i.e. $\text{Ag}_3[\text{C}_6\text{N}_7(\text{NCN})_3]$, are thermally stable up to 500 °C. In contrast, **2c** and **3** are thermally less stable.

Introduction

Interest in the synthesis, structure and application of *s*-heptazines^[1] has increased considerably over the last decade.^[2] Heptazine- and triazine-based graphitic CN_x materials chemically activate CO_2 ,^[3] act as metal-free photocatalysts^[4] and form networks with intercalation of lithium ions.^[5] Moreover, molecular heptazine derivatives have flame-retardant properties.^[6,7]

Among the few *s*-heptazine derivatives comprehensively characterised to date are melon,^[8] cyameluric acid,^[9,10] some cyameluric acid salts,^[11,12] esters^[13] and related polymers,^[14] which are based on the $[\text{C}_6\text{N}_7\text{O}_3]$ motif. Further *s*-heptazines have been derived from melem^[15] and cyameluric chloride.^[16,17] Asymmetrically substituted organic heptazine compounds have been reported.^[18,19]

Based on the work of Liebig and Gmelin in the 19th century, who synthesised melonates and other heptazine compounds and addressed themselves to identify their compositions with the analytical methods of their time,^[20,21] synthetic routes and proposed structures have been optimised, proved and completed by modern characterisation

methods.^[11,22] Several structures of so-called hydromelonates and melonates were assumed in the late 19th and early 20th centuries, but they did not reflect the high thermal stability and chemical inertness observed for heptazine compounds.^[23] Pauling and Sturdivant were the first to postulate the structure of a planar resonance-stabilised heptazine core C_6N_7 , which is in accordance with its observed properties.^[24] In 2003, the first structural determination of a melonate [potassium melonate (**1**)] was reported, which confirmed the arrangement of alternating sp^2 -hybridised carbon and nitrogen atoms in the heptazine core and that the –NCN substituents were cyanamide groups.^[22] Synthesis and structural determination of further alkali,^[25–27] alkaline earth^[28] and a Cu^{II} melonate^[29] followed to give further insights into the molecular structure and thermal behaviour of melonates as promising precursors for graphitic carbon nitrides.^[26–30] The crystal structures of the melonates revealed diverse modes of coordination, at which the outer nitrogen atoms of the heptazine nucleus and/or the two nitrogen atoms of the cyanamide sidearms are involved in coordination.

Herein we report the synthesis and characterisation of silver melonates synthesised either in distilled water $\{\text{Ag}_3[\text{C}_6\text{N}_7(\text{NCN})_3]\cdot\text{H}_2\text{O}$ (**2a**)}, aqueous ammonia solution $\{\text{Ag}_3[\text{C}_6\text{N}_7(\text{NCN})_3]\cdot 0.5\text{NH}_3$ (**2b**)} or aqueous ethylenediamine (EDA) solution $\{\text{Ag}_3[\text{C}_6\text{N}_7(\text{NCN})_3]\cdot 2\text{C}_2\text{H}_8\text{N}_2$ (**2c**)}. Additionally, a nickel melonate synthesised in aqueous am-

[a] Institut für Anorganische Chemie, TU Bergakademie Freiberg, Leipziger Str. 29, 09596 Freiberg, Germany
Fax: +49-3731-39-4058

E-mail: Edwin.Kroke@chemie.tu-freiberg.de

Supporting information for this article is available on the WWW under <http://dx.doi.org/10.1002/ejic.201101254>.

monia solution $\{Ni_3[C_6N_7(NCN)_3]_2 \cdot 10NH_3 \cdot 6H_2O\}$ (**3**) is presented. Only for **2c** was a product suitable for single-crystal X-ray analysis received. Its molecular structure was elucidated by XRD and shows a new coordination mode of the melonate species towards the metal ion. Quantum chemical calculations were performed to investigate the regioselective coordination observed at the melonate trianion by metal cations and by protonation.

Results and Discussion

Synthesis

A reaction of potassium melonate solution with silver ions was reported by Gmelin, which gave a white precipitate.^[20] In 1925, Burdick described the synthesis of hydromelonic acid via silver melonate by treating a sodium melonate solution with a silver nitrate solution.^[31] In the same publication, a less soluble silver melonate in liquid ammonia was reported whose composition was $Ag_3C_9N_{13} \cdot 6NH_3$.

We synthesised several silver melonates by mixing solutions of **1** with solutions of silver nitrate in a molar ratio of 1:3 either in water, aqueous ammonia or aqueous EDA solution. Only in aqueous EDA solution were pale pink single crystals suitable for a single-crystal XRD analysis isolated from the reaction mixture, which were **2c**. Otherwise, after separating, washing and drying, beige-coloured, poorly soluble powders were obtained with compositions that corresponded to **2a** and **2b**.

Upon irradiation with visible light, the surfaces of the powders darken, which is well known for many silver salts.^[32] However, elemental analysis of **2b** after storage in daylight showed only marginally decreased contents of carbon and nitrogen, and the C/N ratio remained constant at 0.57 (corresponding to a molar C/N ratio of 0.67). When the powders were stored in the dark, no colour change occurred.

Salts of hydromelonic acid were described by Gmelin.^[20] Almost 150 years later, transition metal melonates, which included nickel melonate, were precipitated by Finkelshtein et al. and investigated by vibrational spectroscopy.^[33] We prepared a nickel melonate by mixing stoichiometric amounts of solutions of potassium melonate and $Ni(NO_3)_2 \cdot 6H_2O$ in aqueous ammonia (5% solution). Pale violet crystals of **3** were obtained. FTIR spectroscopic analysis supported the proposed composition (see below), and powder XRD indicated that a crystalline product was obtained. However, various attempts to solve the structure were unsuccessful, which is related to the flexible coordination modes of the melonate anion as discussed below. Different metal–melonate interactions have been found in the structures of its complexes with K^+ ,^[22] Li^+ ,^[27] Cs^+ (Rb^+),^[26] Ca^{2+} ^[28] and Cu^{2+} .^[29] Fortunately, we were able to obtain single crystals of **2c**, which shows a new type of coordination.

Crystal Structure of **2c**

Crystals of **2c** were grown directly from the reaction mixture. Selected interatomic distances and angles are listed in

Table 1, and Table 2 summarises significant hydrogen bonds of the type $N-H \cdots N$. Crystallographic data and details of the structure refinement are given Table 3.

Table 1. Selected interatomic distances [Å] and angles [°] for **2c**.

Selected bond lengths for 2c			
Ag2–Ag3	3.1152(7)	Ag2–N16B ^[c]	2.142(5)
Ag1–N1	2.672(5)	Ag3–N6	2.200(5)
Ag1–N14	2.172(5)	Ag3–N11 ^[d]	2.306(5)
Ag1–N15 ^[a]	2.181(5)	Ag3–N17A	2.337(9)
Ag2–N4 ^[b]	2.113(4)	Ag3–N17B	2.200(12)
Ag2–N16A ^[c]	2.142(5)		
Selected bond angles for 2c			
N4–Ag2–N16A ^[b]	177.82(19)	N17B–Ag3–Ag2	107.5(5)
N14–Ag1–N15 ^[a]	172.57(17)	N6–Ag3–Ag2	71.98(13)
N4–Ag2–Ag3 ^[b]	100.03(13)	N17A–Ag3–Ag2	86.5(2)
N16B–Ag2–Ag3 ^[c]	80.54(14)		
N11–Ag3–Ag2 ^[d]	102.02(15)		

Symmetry codes: [a] $-1 + x, y, z$. [b] $2 - x, 1 - y, -z$. [c] $-x, -y, -z$. [d] $1 + x, -1 + y, z$.

Table 2. Intermolecular hydrogen bonds with distances r (D–H), d (H \cdots A), and D (D \cdots A) and the angle θ (D–H \cdots A) in **2c**.

	r [Å]	d [Å]	D [Å]	θ [°]
N17A–H17A \cdots N13 ^[a]	0.92	2.46	3.320(11)	155.7
N17B–H17D \cdots N13 ^[a]	0.92	2.25	3.125(14)	159.5
N14–H14A \cdots N13 ^[b]	0.92	2.46	3.226(6)	141.2
N15–H15A \cdots N12 ^[b]	0.92	2.57	3.355(7)	144.2
N16B–H16C \cdots N11 ^[b]	0.92	2.44	3.278(8)	152.0
N14–H14B \cdots N10 ^[c]	0.92	2.22	3.134(7)	173.8
N15–H15B \cdots N9 ^[d]	0.92	2.18	3.080(6)	166.5
N16A–H16A \cdots N11 ^[e]	0.92	2.37	3.278(8)	168.4
N16A–H16B \cdots N9 ^[f]	0.92	2.15	2.989(7)	151.1
N16B–H16D \cdots N9 ^[f]	0.92	2.09	2.989(7)	165.9
N17B–H17C \cdots N11 ^[b]	0.92	2.43	2.975(15)	117.9

Symmetry codes: [a] x, y, z . [b] $-x + 2, -y + 1, -z$. [c] $-x + 1, -y + 1, -z + 1$. [d] $-x + 2, -y, -z + 1$. [e] $-x + 2, -y + 1, -z$. [f] $x + 1, y, z - 1$.

Table 3. Metal–N interactions in the structurally analysed melonates.

Coordination Side	(a)	(b)	(c)	(d)	Ref.
$Li_3[C_6N_7(NCN)_3] \cdot 6H_2O$	–	–	X	X	[25]
$K_3[C_6N_7(NCN)_3] \cdot 5H_2O$	X	X	X	X	[21]
$Rb_3[C_6N_7(NCN)_3] \cdot 3H_2O$	X	X	X	X	[24]
$Cs_3[C_6N_7(NCN)_3] \cdot 3H_2O$	X	X	X	X	[24]
$Ca[HC_6N_7(NCN)_3] \cdot 7H_2O$	X	–	–	–	[26]
$Ca[HC_6N_7(NCN)_3] \cdot 7H_2O$	X	–	X	–	[26]
$[Cu(C_2H_8N_2)_3]_3[C_6N_7(NCN)_3] \cdot 4H_2O$	–	–	–	X	[27]
$Ag_3[C_6N_7(NCN)_3] \cdot 2C_2H_8N_2$	X	X	–	X	[a]

[a] This work.

Complex **2c** crystallises in the triclinic space group $P\bar{1}$ with one tri-*s*-triazine anion, three silver cations and two molecules of EDA in the asymmetric unit (Figure 1). The molecular shape of the heptazine core is best described by the planarity of the molecule, expressed by the root-mean-square deviation of all non-hydrogen atoms of 0.0229 Å. The bond lengths and angles are in accordance with those reported for other melonates and heptazine

compounds, and the inner C–N bonds (C2–N7, C4–N7, C6–N7) are significantly longer than the outer ones.^[6,7,11,13,16,18,19,22,26–29]

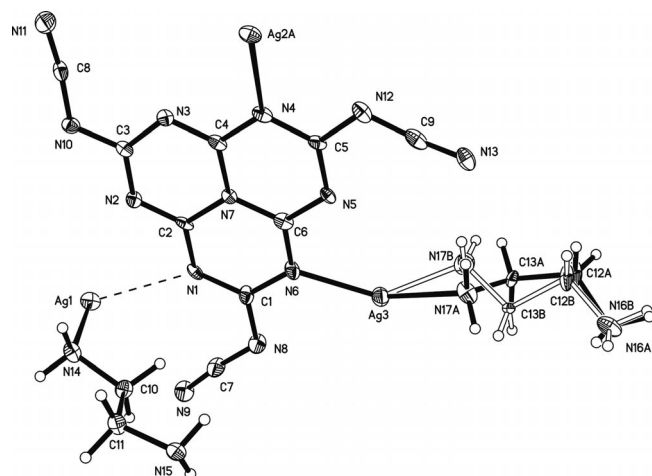


Figure 1. Asymmetric unit of **2c** with numbering scheme. The thermal displacement ellipsoids of the non-hydrogen atoms are drawn at the 50% probability level.

There are two types of silver atoms: Ag2 and Ag3 are directly connected to the heptazine core [2.113(4) and 2.200(5) Å, respectively], whereas Ag1 has a larger distance to the cyameluric nucleus [2.672(5) Å]. Ag1 and Ag2 are essentially coordinated in a linear fashion [N14–Ag1–N15 172.57(17)°; N4–Ag2–N16A 177.8(2)°]. In addition, Ag2 and Ag3 are connected by a d¹⁰–d¹⁰ interaction [3.1152(7) Å]. The formation of homoatomic interactions with distances similar to the respective intermetallic distances has been observed for a series of monovalent d¹⁰ cations (d¹⁰–d¹⁰ interactions). Whether it is a bonding interaction or not remains unclear.^[34] Ag3 has a trigonal-planar coordination environment and is bound to N6, N11 and N17B (Table 1), which come from the heptazine core (N6), the cyanamide/nitrile group (terminal N11) and the disordered EDA molecule (N17A/B). The inversion centre leads to a dimer of tri-*s*-triazine molecules connected through the Ag2–Ag3 contact (Figure 2). In contrast, Ag1 is coordinated in a linear fashion to N14 and N15 from EDA to generate a molecular strand in the crystal packing.

In contrast to copper melonate,^[29] the silver atom coordinates to two sites of the melonate molecule; firstly to the C₆N₇ core at N4 and N6 and secondly to the terminal cyanamide N11 atom.

The terminal N atoms are mainly involved in typical hydrogen bonds as depicted in Figure 3. Hence, several hydrogen bonds form a molecular, infinite network, which results in an alternating arrangement of the planar molecules (Table 2). Figure 3 shows this stacking limited to the C12–H12a⋯N8 interaction (B). The distance between the planes defined by two adjacent *s*-heptazine rings is 3.183 Å. A connection between the layers is implemented by an Ag–Ag contact (A). The Ag1–EDA strand shows a weak coordination to the heptazine core through the Ag1–N1 contact

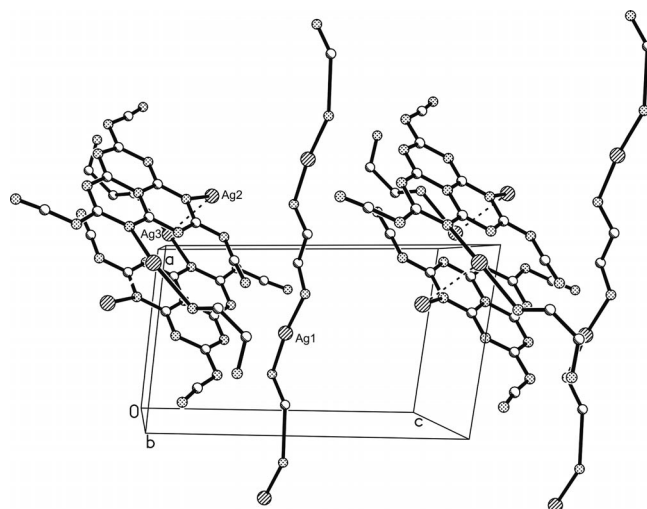


Figure 2. Packing diagram of **2c**, which illustrates the molecular strands generated by EDA and Ag1. Hydrogen atoms are omitted for clarity.

mentioned above. Due to the disorder of one EDA molecule, the N–H⋯N contacts of this molecule can be considered as weak.

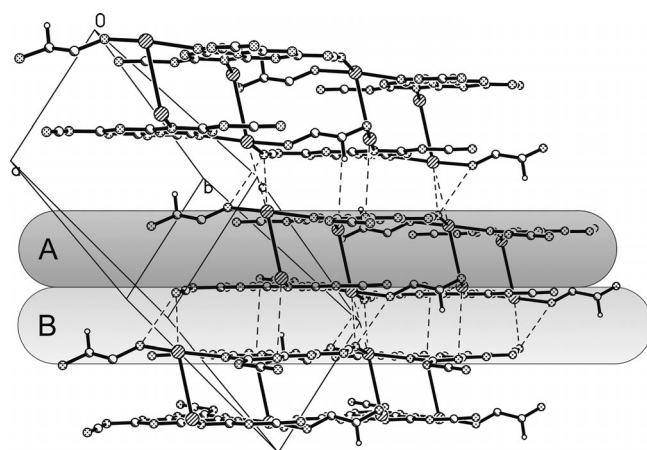


Figure 3. Packing diagram of **2c**, which indicates the layer structure connected through Ag2–Ag3 contacts and hydrogen bonds, e.g. C12–H12a⋯N8 interaction ($d = 2.894$ Å, $\theta = 123.8^\circ$). The Ag1–EDA–Ag1 strand and the hydrogen atoms are omitted for clarity.

Theoretical Considerations

The reactivity of ambident nucleophiles, such as NO₂[−], CN[−] and SCN[−], has been investigated in detail for over 50 years.^[35] The concept of charge- and frontier-controlled reactions was developed to explain experimental results.^[36] In this context, the melonate trianion considered represents a polydentate nucleophile with four different positions that are prone to metal coordination and/or protonation. These positions are (a) the sterically easily accessible nitrogen atom at the heptazine ring, (b) the sterically less accessible nitrogen atom at the heptazine ring, (c) the nitrogen atom of the cyanamide group bound to the heptazine ring and

(d) the terminal nitrogen atom (Figure 4). All other positions are symmetry equivalent to (a)–(d) due to the three-fold molecular symmetry. Positions (a) and (b) are equivalent in solution as shown by the ^{13}C NMR spectra of potassium and lithium melonate.^[22,27] The carbon atoms are not nucleophilic as they bear positive charges.

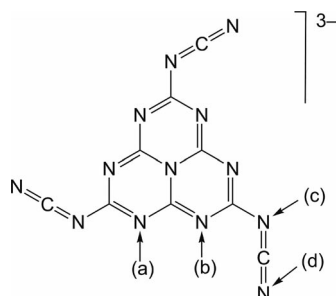


Figure 4. Positions available for electrophilic attack at the melonate trianion.

The X-ray structures of melonate derivatives show coordination at different positions. The silver ions in **2c** coordinate to positions (a), (b) and (d). The copper(II) ion coordinates to (d).^[29] The lithium ion coordinates to (c) and (d).^[27] Larger cations such as potassium,^[22] rubidium and cesium^[26] form irregular distorted polyhedra with nitrogen atoms from the melonate anion and further ligands. Multiple coordination sites of the melonate anion are involved in these cases (Table 3). The calcium ion coordinates to (a) and (c) of the protonated melonate.^[28] The proton in the protonated calcium derivative is located at (a).

To obtain an impression of the nucleophilic strength of the trianion under investigation natural atomic charges have been calculated. The values at the four nitrogen atoms are (a) -0.596 , (b) -0.619 , (c) -0.675 and (d) -0.644 . The highest negative charges are at (c) and (d). The softness of different cations has been estimated by Klopman^[36] on the basis of empty frontier orbital energies. These orbital energies are 2.33 eV for Ca^{2+} , 0.49 eV for Li^+ , 0.42 eV for H^+ , -0.55 eV for Cu^{2+} and -2.82 eV for Ag^+ . The calcium ion is the hardest, and the silver ion the softest ion in this series of electrophiles.

On the basis of these data it becomes understandable that the hard electrophile Li^+ coordinates at positions (c) and (d) in a charge-controlled interaction. The same holds true for Cu^{2+} , which is a harder electrophile than Ag^+ . The soft silver(I) ion coordinates at the less negatively charged positions (a) and (b). Furthermore, coordination to position (d) with a longer distance is present. If we consider the possible interactions with positions (a) and (b) on the basis of orbital control, we have to look for suitable donor orbitals in the melonate anion, which are able to interact with the silver ion. There are such orbitals with orbital energies of -2.52 eV (Figure 5). These are nearly ideally matched to the calculated orbital energy of Ag^+ given by Klopman (-2.82 eV). Therefore, we assume an orbital-controlled interaction in this case.

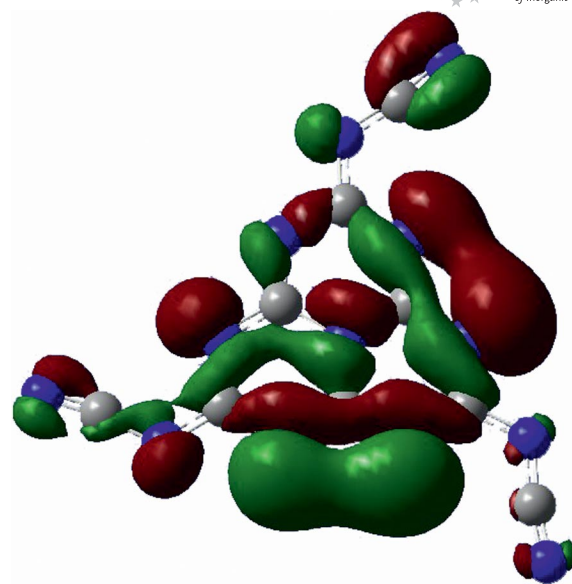


Figure 5. One of the three donor orbitals of the melonate anion at -2.52 eV, which are suitable for coordination of electrophiles at the *s*-heptazine core (isovalues are shown at $0.02 \text{ e}\text{\AA}^{-3}$).

The coordination mode of the calcium ion to positions (a) and (c) does not allow any conclusions to be drawn about charge- or orbital-controlled interactions. This leads to a drawback of the hard-soft acid–base (HSAB) concept: the discussion on the basis of hard and soft character of the electrophiles should be considered as a qualitative explanation. Numerous experimental facts have been omitted from the brief discussion above. These are, for instance, the influence of solvents and reaction conditions, the packing effects during crystallisation and the influence of further ligands at the electrophilic metal ions. The crystal structures mentioned here represent snapshots of the melonate derivatives. It could even be possible to find polymorphs of these compounds with coordination in other positions. Furthermore, it has recently been proposed to abandon the HSAB concept generally due to weak correlation with experimental facts.^[37]

The protonated melonate derivative described by Schnick et al.^[26] does not fit into the scheme of orbital- and charge-controlled reactivity as one would expect to coordinate the hard electrophile at the NCN group. Instead, it was found at the *s*-heptazine ring in position (a). A comparison of the total energies of the different protonated melonate derivatives (Figure 6) shows that position (a) yields the dianion with the lowest energy. Therefore, one should assume that the protonation proceeds under thermodynamic control.

In summary, the melonate anion shows very different coordination modes that depend on the electrophile. The nitrogen atoms of the cyano groups (c) and (d) are slightly more negatively charged than the ring nitrogen atoms (a) and (b). At the same time the nitrogen atoms (a) and (b) are stronger Brønsted bases than (c) and (d).

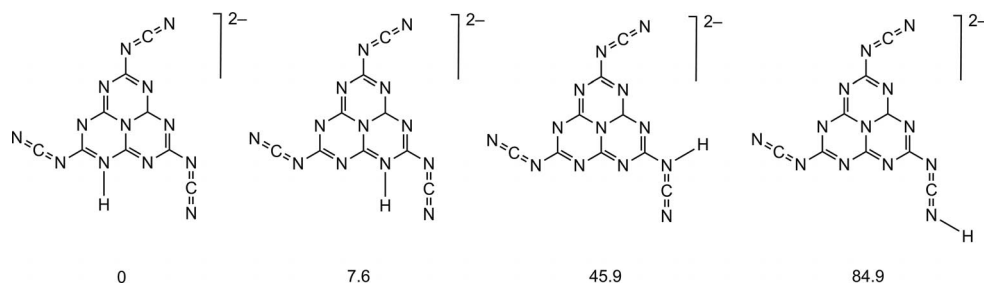


Figure 6. Calculated energy differences [kJ/mol] between isomers of the melonate dianion.

Spectroscopic Properties

FTIR spectra of **2a–2c** show the three typical bending and stretching vibrations of the cyameluric nucleus at 1650, 1447 and 795 cm^{-1} for **2a**, 1658, 1449 and 795 cm^{-1} for **2b** and 1632, 1434 and 791 cm^{-1} for **2c**. The sharp, broad band caused by the asymmetric NCN valence vibration of the NCN substituent is apparent in all the spectra. A shoulder that indicates a slight splitting of the energies of the NCN vibration is seen, which means that the equivalence of the three cyanamide substituents of the melonate anion is annulled by an unequal coordination within the cyanamide sphere. This is also shown in the crystal structure of **2c**. The respective asymmetric NCN vibrations emerge at 2180 (**2a**), 2170 (**2b**) and 2159 cm^{-1} (**2c**) and are shifted to lower wave numbers as a function of the solvent. Whereas **2a** and **2b** show only one broad band at 3190 and 3182 cm^{-1} , respectively, which are assigned to the OH and NH valence vibrations, the spectrum of **2c** is characterised by a broad band at 3440 and a sharper band at 3277 cm^{-1} , which indicate the existence of diverse inter- and intramolecular NH valence vibrations.

Figure 7 shows the FTIR spectrum of **3**. In addition to the bending and stretching vibrations of the cyameluric nucleus (1632, 1427 and 806 cm^{-1}), complete splitting of the asymmetric NCN valence vibration of the NCN substituent into two bands (2197 and 2143 cm^{-1}) is noticeable. The spectrum exhibits OH and NH valence vibrations (3341 cm^{-1}).

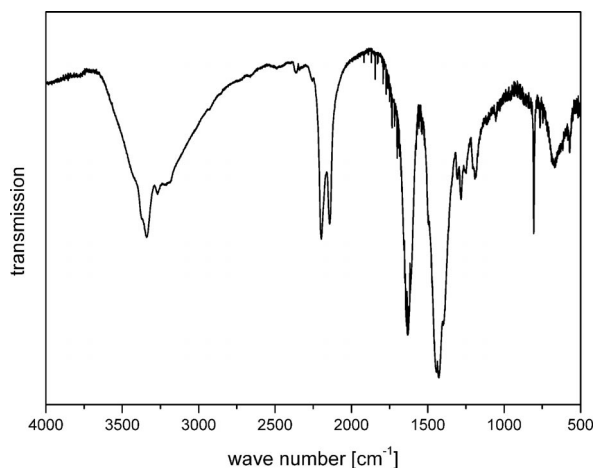


Figure 7. FTIR spectrum of **3**.

Solid-State ^{13}C NMR Studies

Complexes **2a–c** were characterised by solid-state ^{13}C magic-angle spinning (MAS) NMR (Figures 8, 9 and 10). The spectra of **2a** and **2b** look quite similar (Figure 8). All of the signals are broadened, which suggests less crystalline or amorphous products. The chemical shifts in the spectrum of **2a** are at $\delta = 119.85$ (cyanamide carbon atoms), 155.14 (inner heptazine carbon atoms) and 164.16 and 169.26 ppm (outer heptazine carbon atoms). The corresponding signals for **2b** appear at $\delta = 119.98$, 154.98 and 169.68 ppm.

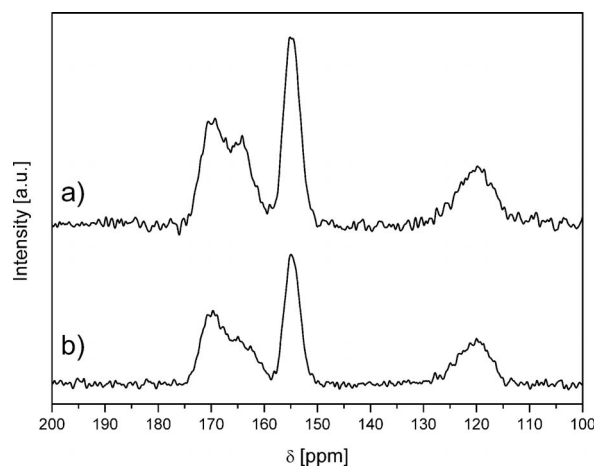
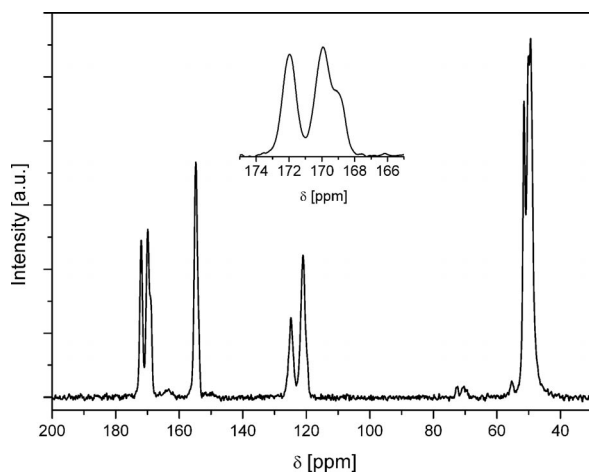
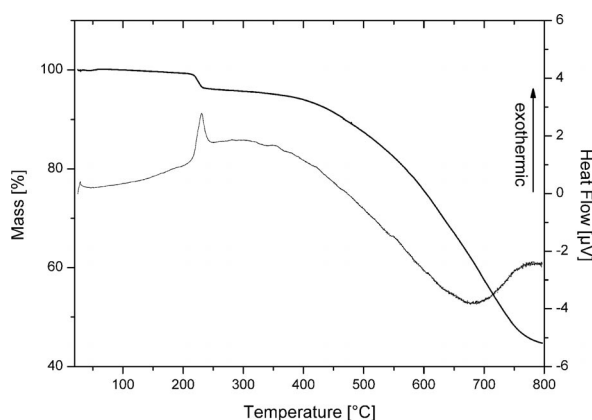


Figure 8. Cross-polarisation (CP) MAS ^{13}C NMR spectra of (a) **2a** and (b) **2b**.

The solid-state ^{13}C MAS NMR spectrum of **2c** is characterised by sharp bands, which is usual for crystalline solids (Figure 9). Signals for the EDA carbon atoms emerge at $\delta = 49.40$, 50.08 and 51.46 ppm. Two signals for cyanamide carbon atoms occur at $\delta = 121.04$ and 124.87 ppm with an intensity ratio of 2:1, which represent the modification of one cyanamide substituent by coordination of a silver atom to the terminal cyanamide nitrogen atom (Ag3–N11) contrary to two remaining cyanamide groups, which are less affected (see crystal structure). The three inner heptazine carbon atoms remain equivalent ($\delta = 154.77$ ppm). Due to dissymmetric coordination of silver atoms Ag1–Ag3 to the heptazine core, the outer heptazine carbon atoms (C1, C3, C5) give rise to signals at $\delta = 169.91$ ppm, which includes a shoulder at $\delta = 169.29$ and 171.96 ppm.

Figure 9. CP MAS ^{13}C NMR of **2c**.Figure 10. TG and DTA curves of **2c** (sample weight: 1.738 mg, heating rate: 5 K/min).

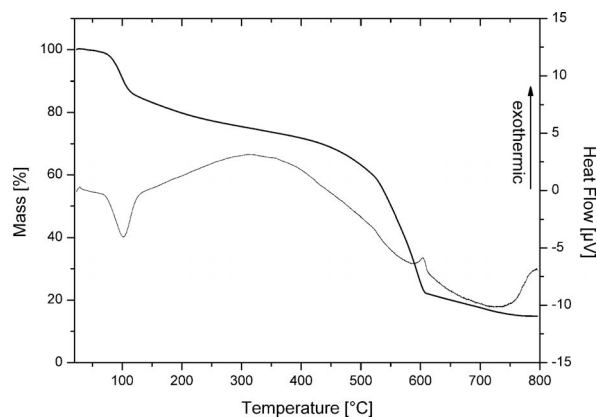
Thermal Properties

Complexes **2a–2c** were subjected to thermal analysis from 20 to 800 °C. Complex **2a** is characterised by a slight mass loss of 3.0% from 20 to 300 °C, which corresponds to one molecule of water (calcd. 2.9%), and is stable up to 500 °C. Afterwards it starts to decompose rapidly up to 750 °C. The overall mass loss of **2a** at 750 °C is 49.0%. From 750 to 800 °C, no further mass loss was observed; 51.0% of the initial mass remained, which corresponds to the silver (calcd. 51.2%). The thermogravimetric (TG) and differential thermal analysis (DTA) curves of **2b** resemble that of **2a**. The small mass loss of 1.6% from 20 to 150 °C correlates with the release of 0.5 equiv. NH_3 per molecule (calcd. 1.4%). The decomposition of **2b** starts at 500 °C and is finished at 730 °C. The overall mass loss was 49.0%. From 730 to 800 °C the mass remains constant at 51.0%, which corresponds to three silver atoms (calcd. 52.0%). The high thermal stability observed for silver melonate **2** $\{Ag_3[C_6N_7(NCN)_3]\}$ is well known for alkali and transition metal melonates^[22,26,27,29,30] and for other heptazine derivatives.^[11,15]

In contrast, the inclusion of EDA in **2c** leads to a different thermal behaviour. As depicted in Figure 10, the first

step of mass loss occurs at 210–255 °C, which is accompanied by a sharp exothermic signal in the DTA curve. The mass loss is 4.0%, which can be assigned to half a molecule of EDA per formula unit (calcd. 4.1%). From 300 to 800 °C, the mass decreases slightly and continuously. At 800 °C, the total mass loss is 55.2%. Hence, 44.8% of **2c** remained, and the silver content of **2c** is 44.1%. The small difference might be due to an as yet uncompleted decomposition within the measuring range. In summary, **2c** shows a somewhat lower thermal stability than other known melonates, which include **2a** and **2b**. For the EDA adduct of copper melonate,^[27] lower thermal stability was also observed.

The TG curve of **3** is characterised by two steps (Figure 11). Up to 400 °C, a mass loss of 26.9% occurs, which corresponds to the loss of ammonia and water (calcd. 26.9%). At 100 °C, a sharp endothermic signal in the DTA curve appears, which is associated with a rapid mass loss from 90 to 125 °C. A final rapid mass loss starts at 450 °C and is finished at 600 °C. Thus, **3** is thermally also somewhat less stable than **2a** and **2b**. From 600 to 800 °C, a slight mass loss is observed.

Figure 11. TG and DTA curves of **3** (sample weight: 3.438 mg, heating rate: 5 K/min).

In summary, TG data of **2a–c** and **3** show that melonates exhibit a high thermal stability up to 500 °C (**2a–b**) and become thermally less stable due to the influence of coordination with chelate ligands, such as EDA^[29] (**2c**) and ammonia (**3**), and by protonation of the heptazine nucleus.^[28]

Conclusions

This study investigated silver and nickel melonates synthesised either in water, aqueous ammonia or aqueous EDA. The spectroscopic and thermal properties of the products obtained were investigated. As expected, silver and nickel melonates show a high thermal stability in accordance with other melonate and *s*-heptazine derivatives. Complexing agents such as EDA decreased the thermal stability.

The crystal structure of an EDA-containing silver melonate **2c** comprises an asymmetric unit with one molecule of melonate, three silver atoms and two molecules of EDA.

The silver atoms show a new coordination mode with the melonate anions compared to Li, Ca or Cu^{II} melonates, which involve interaction with core N atoms in positions (a) and (b) and the terminal cyanamide N atom (d, Figure 4). Silver melonate **2c** crystallises in a layered structure with interlayer connection by Ag–Ag interactions and hydrogen bonds. The nickel melonate **3** is also crystalline, but its structure could not be solved from the experimental data available, which is attributed to the variable metal coordination of the melonate anion.

A qualitative explanation for the variability of the coordination of metal ions at the polydentate melonate trianion has been proposed by quantum chemical calculations. Based on the HSAB concept, it is expected that hard electrophiles coordinate at the NCN unit and soft electrophiles coordinate at the *s*-heptazine core of the anion, although the difference between the four different terminal N atoms (a), (b), (c) and (d) is very small, especially with respect to their charge distribution of –0.596, –0.619, –0.675 and –0.644, respectively. However, protonation of the melonate anion exclusively occurs at the peripheral N atoms of the C₆N₇ unit, which is analogous to the protonation of the cyamelurate anion and indicated by theoretical and experimental results.

Several research groups are focussed on the applications of *s*-heptazine-based carbon nitrides especially in catalysis. The results presented here might help to understand the catalytic activity of materials that contain the C₆N₇ nucleus. More comprehensive conclusions may be drawn if further (protonated) melonates and other *s*-heptazine derivatives are synthesised and structurally analysed.

Experimental Section

Starting Materials and Synthesis of Potassium Melonate Pentahydrate (1): Purification of the starting material (crude melon) and the synthesis of **1** are described in detail in the literature.^[22,27,29]

Synthesis of Ag₃[C₆N₇(NCN)₃]·H₂O (2a): AgNO₃ (512 mg, 3.01 mmol, Roth, >99.9%, p.a.) was dissolved in distilled water (25 mL) and added dropwise to a solution of **1** (500 mg, 1.01 mmol) in distilled water (50 mL). A microcrystalline beige precipitate was formed, which was separated by centrifugation, washed three times with distilled water and dried in a drying oven at 60 °C overnight. Yield: 600 mg (0.95 mmol, 94.5%). C₉H₂Ag₃N₁₃O (631.85): calcd. C 17.11, H 0.32, N 28.82; found C 17.01, H 0.43, N 28.75. IR (KBr): $\tilde{\nu}$ = 3190, 2181, 1650, 1447, 795 cm^{–1}. ¹³C MAS NMR (101 MHz): δ = 119.85 (C≡N), 155.14 (CN₃), 164.16 [C(NCN)N₂], 169.26 [C(NCN)N₂] ppm.

Synthesis of Ag₃[C₆N₇(NCN)₃]·0.5NH₃ (2b): The synthesis and purification of **2b** were performed according to the procedure described for **2a**. Compound **1** and AgNO₃ were dissolved in ammonia (5% aqueous solution), and a beige solid was obtained. Yield: 387 mg (0.62 mmol, 62.8%). C₉H_{1.5}Ag₃N_{13.5} (622.36): calcd. C 17.40, H 0.24, N 30.39; found C 16.99, H 0.40, N 29.63; found (after storage in daylight for one and a half months): C 16.86, H 0.44, N 29.55. IR (KBr): $\tilde{\nu}$ = 3182, 2170, 1658, 1449, 795 cm^{–1}. ¹³C MAS NMR (101 MHz): δ = 119.98 (C≡N), 154.98 (CN₃), 169.68 [C(NCN)N₂] ppm.

Synthesis of Ag₃[C₆N₇(NCN)₃]·2C₂H₈N₂ (2c): The synthesis and purification of **2c** were performed according to the procedure described for **2a**. Compound **1** and AgNO₃ were dissolved in ethylenediamine (5% aqueous solution, Sigma Aldrich, redist. 99.5+%), and a gray precipitate was obtained. Yield: 629 mg (0.86 mmol, 85.2%). C₁₃H₁₆Ag₃N₁₇ (734.04): calcd. C 21.27, H 2.20, N 32.45; found C 21.21, H 2.13, N 32.24. IR (KBr): $\tilde{\nu}$ = 3440, 3277, 2159, 1632, 1434, 791 cm^{–1}. ¹³C MAS NMR (101 MHz): δ = 49.40 [CH₂(NH₂)CH₂], 50.08 [CH₂(NH₂)CH₂], 51.46 [CH₂(NH₂)CH₂], 121.04 (C≡N), 124.87 (C≡N), 154.77 (CN₃), 169.91 [C(NCN)N₂], 171.96 [C(NCN)N₂] ppm.

Synthesis of Ni₃[C₆N₇(NCN)₃]·10NH₃·6H₂O (3): The synthesis and purification of **3** were performed according to the procedure described for **2a**. Ni(NO₃)₂·6H₂O (2.23 g, 7.67 mmol) was dissolved in ammonia (5% aqueous solution) and added dropwise to a solution of **1** (2.50 g, 5.12 mmol) in ammonia (5% aqueous solution). A pale violet, fine crystalline product was obtained. Yield: 2.23 g (2.15 mmol, 84.2%). C₁₈H₄₂N₃₆Ni₃O₆ (1035.06): calcd. C 20.89, H 4.1, N 48.73; found C 20.71, H 3.83, N 47.78. IR (KBr): $\tilde{\nu}$ = 3341, 2197, 2143, 1632, 1427, 807 cm^{–1}. The XRD pattern exhibits sharp signals, which indicates a crystalline product (Figure S4).

Crystal Structure Determination: Suitable crystals of **2c** were directly obtained from the reaction medium. Data collection was performed with a STOE IPDS-2 diffractometer (image plate) equipped with a low-temperature device [*T* = 100(2) K], with graphite-monochromated Mo-*K*_α radiation (λ = 0.71073 Å) by using ω and ϕ scans. Reflections were corrected for background, Lorentz and polarisation effects. Preliminary structure models were derived by direct methods,^[35] and the structures were refined by full-matrix least squares based on *F*² for all reflections using SHELXL.^[38] All hydrogen atoms were included in calculated positions and were refined as constrained to their bonding atoms. One EDA molecule

Table 4. Crystallographic and structure refinement data for **2c**.

2c	
Empirical formula	C ₁₁ H ₈ Ag ₂ N ₁₅ , C ₂ H ₈ AgN ₂
Formula mass	734.04
Colour	pale pink
Crystal system	triclinic
Space group	<i>P</i> $\bar{1}$
<i>a</i> [Å]	7.5499(4)
<i>b</i> [Å]	11.3438(6)
<i>c</i> [Å]	12.5741(7)
α [°]	72.138(4)
β [°]	80.148(4)
γ [°]	74.945(4)
<i>V</i> [Å ³]	984.90(9)
<i>Z</i>	2
<i>F</i> (000)	708
<i>D</i> _{calcd.} [g cm ^{–3}]	2.475
μ (Mo- <i>K</i> _α) [cm ^{–1}]	3.000
Data-collection temperature [K]	100(2)
θ limits [°]	1.71–27.00
<i>hkl</i> range	–8/9, \pm 14, \pm 16
No. of coll./unique refl.	23042/4287
<i>R</i> _{int}	0.0577
No. of refl. [<i>I</i> ≥ 2 σ (<i>I</i>)]	3368
No. of refined parameters	321
<i>R</i> 1(<i>F</i>) ^[a] / <i>wR</i> 2(<i>F</i> ²) (all data) ^[b]	0.0404/0.0948
<i>S</i> (goodness of fit on <i>F</i> ²) ^[c]	1.041
Final $\Delta\rho_{\max/\min}$ [e Å ^{–3}]	0.771/0.992

[a] $R1 = \sum ||F_o| - |F_c|| / \sum |F_o|$. [b] $wR2 = [\sum w(F_o^2 - F_c^2)^2 / \sum w(F_o^2)^2]^{1/2}$, $w = [\sigma^2(F_o^2) + (xP)^2 + yP]^{-1}$, where $P = [\text{Max}(F_o^2, 0) + 2F_c^2] / 3$. [c] $\text{GoF} = [\sum w(F_o^2 - F_c^2)^2 / (n_{\text{obs}} - n_{\text{param}})]^{1/2}$.

showed a disorder over two positions (56% and 44%). The crystal data and parameters pertinent to data collection and structure refinement are summarised in Table 4. CCDC-852826 contains the supplementary crystallographic data for this paper. These data can be obtained free of charge from The Cambridge Crystallographic Data Centre via www.ccdc.cam.ac.uk/data_request/cif.

Quantum Chemical Calculations: Quantum chemical calculations were carried out by using the Gaussian 03 series of programs.^[39] Geometries were fully optimised at DFT level by using Becke's three-parameter hybrid exchange functional and the correlation functional of Lee, Yang and Parr (B3LYP).^[40,41] Geometry optimisations and harmonic frequencies were calculated for all elements with the 6-311+G(d) basis set for the melonate trianion and 6-311+G(d,p) for the isomers of the melonate dianion.^[42] The local minima were characterised by zero imaginary frequencies. Energy differences between the isomers of the melonate dianion were calculated on the basis of the sum of electronic and zero-point energies. Natural charges of the melonate trianion were calculated with NBO 5.0.^[43] In order to obtain realistic orbital energies, the geometry optimisation and frequency calculation of the melonate trianion were repeated at the HF/6-311+G(d) level. The three-dimensional molecular orbital plot (Figure 4) was generated from this calculation with GaussView^[44] with a contour value of $0.02 \text{ e } \text{\AA}^{-3}$.

Spectroscopic and Thermal Characterisation: FTIR spectroscopy was performed at room temperature with a Nicolet 510-FTIR spectrometer in the range of $4000\text{--}400 \text{ cm}^{-1}$. TG/DTA data were recorded with a Seico Instrument (SSC/5200). The samples were heated under argon in a corundum crucible with heating rates of 5 K/min from room temperature to 800°C . Elemental analyses were measured by using a Vario Micro CHNS analyser. Solid-state NMR studies were performed with a conventional pulse spectrometer DSX Avance 400 (Bruker) with a rotation frequency of 10 kHz . Powder XRD was performed with a URD6 instrument with a $\text{Cu-K}\alpha$ X-ray source by using a secondary monochromator.

Supporting Information (see footnote on the first page of this article): FTIR spectra of **2a**, **2b** and **2c**; TG and DTA curves of **2a** (sample weight: 9.706 mg , heating rate: 5 K/min); TG and DTA curves of **2b** (sample weight: 5.362 mg , heating rate: 5 K/min); powder XRD pattern of **3**; orbital energies calculated with HF/6-311+G(d); spatial shape of frontier molecular orbitals (isovalue of $0.02 \text{ e } \text{\AA}^{-3}$). Degenerate orbitals are shown in one row.

Acknowledgments

The authors gratefully acknowledge the Deutsche Forschungsgemeinschaft (DFG project KR1739/20-1) for financial support. Dr. E. Brendler (Institute of Analytical Chemistry, TU Bergakademie Freiberg) is acknowledged for performing solid-state NMR measurements. Dipl.-Phys. G. Schreiber (Institute of Materials Science, TU Bergakademie Freiberg) is acknowledged for measuring the XRD pattern.

- [1] Synonyms for *s*-heptazine are tri-*s*-triazine, cyamelurine, 1,3,4,6,7,9,9b-heptaazaphenylene and 1,3,4,6,7,9-hexaazacyclo[333]azine.
- [2] E. Kroke, M. Schwarz, *Coord. Chem. Rev.* **2004**, *248*, 493–532.
- [3] F. Goettmann, A. Thomas, M. Antonietti, *Angew. Chem.* **2007**, *119*, 2773; *Angew. Chem. Int. Ed.* **2007**, *46*, 2717–2720.
- [4] a) X. Wang, K. Maeda, A. Thomas, K. Takanabe, G. Xin, J. M. Carlsson, K. Domen, M. Antonietti, *Nat. Mater.* **2008**, *7*, 76–80; b) X. Wang, K. Maeda, X. Chen, K. Takanabe, K. Domen, Y. Hou, X. Fu, M. Antonietti, *J. Am. Chem. Soc.* **2009**, *131*, 1680–1681.

- [5] a) E. Wirnhier, M. Döblinger, D. Gunzelmann, J. Senker, B. V. Lotsch, W. Schnick, *Chem. Eur. J.* **2011**, *17*, 3213–3221; b) M. J. Bojdys, J.-O. Müller, M. Antonietti, A. Thomas, *Chem. Eur. J.* **2008**, *14*, 8177–8182.
- [6] T. Saplinova, C. Lehnert, U. Böhme, J. Wagler, E. Kroke, *New J. Chem.* **2010**, *34*, 1893–1908.
- [7] T. Saplinova, V. Bakumov, T. Gmeiner, J. Wagler, M. Schwarz, E. Kroke, *Z. Anorg. Allg. Chem.* **2009**, *635*, 2480–2487.
- [8] B. V. Lotsch, M. Döblinger, J. Sehnert, L. Seyfarth, J. Senker, O. Oeckler, W. Schnick, *Chem. Eur. J.* **2007**, *13*, 4969–4980.
- [9] J. Wagler, N. E. A. El-Gamel, E. Kroke, *Z. Naturforsch. B* **2006**, *61*, 975–978.
- [10] A. Sattler, W. Schnick, *Z. Anorg. Allg. Chem.* **2006**, *632*, 1518–1523.
- [11] E. Horvath-Bordon, E. Kroke, I. Svoboda, H. Fueß, R. Riedel, N. Sharma, A. K. Cheetham, *Dalton Trans.* **2004**, 3900–3908.
- [12] A. Sattler, M. R. Budde, W. Schnick, *Z. Anorg. Allg. Chem.* **2009**, *635*, 1933–1939.
- [13] a) M. R. Schwarz, H. Ehrenberg, M. A. Kloc, E. Kroke, *Heterocycles* **2006**, *68*, 2499–2507; b) N. E. A. El-Gamel, L. Seyfarth, J. Wagler, H. Ehrenberg, M. Schwarz, J. Senker, E. Kroke, *Chem. Eur. J.* **2007**, *13*, 1158–1173.
- [14] N. E. A. El-Gamel, M. Schwarz, E. Brendler, E. Kroke, *Chem. Commun.* **2006**, 4741–4743.
- [15] B. Jürgens, E. Irran, J. Senker, P. Kroll, H. Müller, W. Schnick, *J. Am. Chem. Soc.* **2003**, *125*, 10288–10300.
- [16] E. Kroke, M. Schwarz, P. Kroll, E. Horvath-Bordon, B. Noll, A. Norman, *New J. Chem.* **2002**, *26*, 508–512.
- [17] S. Tragl, H.-J. Meyer, *Z. Anorg. Allg. Chem.* **2005**, *631*, 2300v2302.
- [18] A. Schwarzer, E. Kroke, *New J. Chem.* **2011**, *35*, 953–958.
- [19] A. Schwarzer, E. Kroke, *Chem. Commun.* **2010**, *46*, 2829–2831.
- [20] L. Gmelin, *Ann. Chim. Farm.* **1835**, *15*, 252–258.
- [21] a) J. Liebig, *Ann. Pharm.* **1834**, *10*, 1–47; b) J. Liebig, *Ann. Chem. Pharm.* **1844**, *50*, 337–363; c) J. Liebig, *Ann. Chem. Pharm.* **1855**, *95*, 257–282.
- [22] E. Horvath-Bordon, E. Kroke, I. Svoboda, H. Fuess, R. Riedel, *New J. Chem.* **2005**, *29*, 693–699.
- [23] a) E. Franklin, *J. Am. Chem. Soc.* **1922**, *44*, 486–509; b) P. Klason, *J. Prakt. Chem.* **1886**, *33*, 285–289; c) C. E. Redemann, H. J. Lucas, *J. Am. Chem. Soc.* **1939**, *61*, 3420–3425.
- [24] L. Pauling, J. H. Sturdivant, *Proc. Natl. Acad. Sci. USA* **1937**, *23*, 615–620.
- [25] A. Sattler, W. Schnick, *Eur. J. Inorg. Chem.* **2009**, *33*, 4972–4981.
- [26] S. J. Makowski, W. Schnick, *Z. Anorg. Allg. Chem.* **2009**, *635*, 2197–2202.
- [27] C. Clauss, J. Wagler, M. Schwarz, A. Schwarzer, E. Kroke, *Z. Anorg. Allg. Chem.* **2010**, *636*, 196–200.
- [28] S. J. Makowski, D. Gunzelmann, J. Senker, W. Schnick, *Z. Anorg. Allg. Chem.* **2009**, *635*, 2434–2439.
- [29] C. Clauss, H. Schmidt, A. Schwarzer, E. Kroke, *Z. Anorg. Allg. Chem.* **2011**, *637*, 2246–2251.
- [30] C. Clauss, M. Schwarz, E. Kroke, *Carbon* **2010**, *48*, 1137–1145.
- [31] W. L. Burdick, *J. Am. Chem. Soc.* **1925**, *47*, 1485–1490.
- [32] J. F. Hamilton, *Adv. Phys.* **1988**, *37*, 359–441.
- [33] A. I. Finkelshtein, S. G. Fedoruk, *Zh. Prikl. Spektrosk.* **1982**, *39*, 606–609.
- [34] M. Jansen, *Angew. Chem.* **1987**, *99*, 1136–1149.
- [35] See, for instance: a) N. Kornblum, R. A. Smiley, R. K. Blackwood, D. C. Iffland, *J. Am. Chem. Soc.* **1955**, *77*, 6269–6280; b) R. Gomper, *Angew. Chem.* **1964**, *76*, 412–423.
- [36] G. Klopman, *J. Am. Chem. Soc.* **1968**, *90*, 223–234.
- [37] H. Mayr, M. Breugst, A. R. Ofial, *Angew. Chem.* **2011**, *123*, 6598–6634.
- [38] G. M. Sheldrick, *Acta Crystallogr., Sect. A* **2008**, *64*, 112–122.
- [39] M. J. Frisch, G. W. Trucks, H. B. Schlegel, G. E. Scuseria, M. A. Robb, J. R. Cheeseman, J. A. Montgomery, T. Vreven, K. N. Kudin, J. C. Burant, J. M. Millam, S. S. Iyengar, J. Tomasi, V. Barone, B. Mennucci, M. Cossi, G. Scalmani, N. Rega,

- G. A. Petersson, H. Nakatsuji, M. Hada, M. Ehara, K. Toyota, R. Fukuda, J. Hasegawa, M. Ishida, T. Nakajima, Y. Honda, O. Kitao, H. Nakai, M. Klene, X. Li, J. E. Knox, H. P. Hratchian, J. B. Cross, C. Adamo, J. Jaramillo, R. Gomperts, R. E. Stratmann, O. Yazyev, A. J. Austin, R. Cammi, C. Pomelli, J. W. Ochterski, P. Y. Ayala, K. Morokuma, G. A. Voth, P. Salvador, J. J. Dannenberg, V. G. Zakrzewski, S. Dapprich, A. D. Daniels, M. C. Strain, O. Farkas, D. K. Malick, A. D. Rabuck, K. Raghavachari, J. B. Foresman, J. V. Ortiz, Q. Cui, A. G. Baboul, S. Clifford, J. Cioslowski, B. B. Stefanov, G. Liu, A. Liashenko, P. Piskorz, I. Komaromi, R. L. Martin, D. J. Fox, T. Keith, M. A. Al-Laham, C. Y. Peng, A. Nanayakkara, M. Challacombe, P. M. W. Gill, B. Johnson, W. Chen, M. W. Wong, C. Gonzalez, J. A. Pople, *Gaussian 03*, Revision C.02, Gaussian, Inc., Wallingford, CT, **2004**.
- [40] A. D. Becke, *J. Chem. Phys.* **1993**, *98*, 5648.
- [41] P. J. Stevens, F. J. Devlin, C. F. Chablowski, M. J. Frisch, *J. Phys. Chem.* **1994**, *98*, 11623.
- [42] R. Krishnan, J. S. Binkley, R. Seeger, J. A. Pople, *J. Chem. Phys.* **1980**, *72*, 650–654.
- [43] E. D. Glendening, J. K. Badenhoop, A. E. Reed, J. E. Carpenter, J. A. Bohmann, C. M. Morales, F. Weinhold, *NBO 5.0*, Theoretical Chemistry Institute, University of Wisconsin, Madison, **2001**.
- [44] *GaussView 5.0*, Gaussian Inc., Pittsburgh, **2008**.

Received: November 9, 2011

Published Online: January 13, 2012

Ca₂NiSn₂ – A Polymorphic Intermetallic Phase: Atomic and Electronic Structure as well as a Topological Description of the Phase Transition by a Sigmatropic-Type Rearrangement of Ni and Sn Atoms

Lisa Siggelkow,^[a] Viktor Hlukhyy,^[a] and Thomas F. Fässler^{*[a]}

Keywords: Tin / Intermetallic phases / ELF (Electron Localization Function) / Chemical bonding / Phase transitions

The synthesis and structural characterization of two polymorphic modifications of the intermetallic compound Ca₂NiSn₂ are described. The monoclinic modification *mC*-Ca₂NiSn₂ is obtained by arc melting and rapid cooling and forms two-dimensional Ni–Sn slabs that contain four- and six-membered rings. These nets are interconnected by Sn₂ dumbbells and thus 12-membered rings form between the slabs. The cavities of the resulting three-dimensional network are filled with Ca atoms. At annealing temperatures between 800 and 870 °C, an orthorhombic modification *oP*-Ca₂NiSn₂ forms. The two-dimensional Ni–Sn substructure contains Ni–Sn nets of four- and six-membered rings. Sn₂ dumbbells coordinate to these nets end-on to form additional five-membered Ni–Sn rings. The resulting slabs are separated by Ca atoms. Temperature-dependent synthesis and differential thermal

analysis experiments indicate that the monoclinic modification *mC*-Ca₂NiSn₂ is a metastable modification. Two approaches to the topological description of the phase transition are presented: 1) a conversion by a simple shift of ribbons of atomic layers and 2) a least-motion process describing the topology of the phase transformation by an electrocyclic mechanism through Ni–Sn bond scission and formation analogous to sigmatropic shifts known for organic molecules. The electronic structures and chemical bonding are discussed in terms of DFT calculations, including density of states, band structures and a topological analysis of the electron localization function, which revealed covalent Sn2–Sn2 bonds with partial π bonding of the Sn₂ dumbbells in *mC*-Ca₂NiSn₂ and a short Sn2–Sn3 contact with dominant lone-pair character at the terminal Sn2 atom in *oP*-Ca₂NiSn₂.

Introduction

The understanding of chemical bonding in intermetallic compounds is still far from our deep knowledge of chemical bonding in molecules in which generally the valence concept (8-*N* rule) applies and directed, localized bonds are dominant. The same ideas hold for Zintl phases, a subgroup of intermetallics, in which the assumption of a formal electron transfer from the more electropositive (e.g. alkali and alkaline earth metals) to the more electronegative component (p-block metals and semi-metals) leads to a salt-like description and the 8-*N* rule applies to the atoms of the anionic substructure. However, if transition metals are also involved, no concept exists for chemical bonding based on atom valency. Some recent examples have shown that intriguing clusters and low-dimensional substructures hint at an extension of the Zintl–Klemm concept (see for example, refs.^[1,2]). In this context p-block-rich compounds of the system *A/T/Tt* (*A* = alkali or alkaline earth metal, *T* = transition metal and *Tt* = tetrel) are at the borderline between semi-conducting Zintl phases and intermetallic compounds.

In particular, stannides and intermetallic Sn compounds display a wide range of structural and electronic properties, including interesting chemical bonding situations ranging from covalent to ionic bonding. The transition from Zintl phases to intermetallic phases has been described for binary alkali and alkaline earth metal stannides and plumbides.^[3] The structural diversity of binary and ternary intermetallic Sn compounds is summarized in ref.^[4] Only recently we showed that in the system *A*/Cu/Sn (*A* = Na, K, Rb, Cs), compounds with large binary anionic Sn@Cu₁₂@Sn₂₀ clusters exist, the stabilities of which are comprehensible based on a molecular description.^[1]

In this context we have investigated the phase systems *Ae*/Ni/Sn (*Ae* = alkaline earth metal), which show a variety of interesting Ni–Sn substructures. Until now, the intermetallic phases Ca₇Ni₄Sn₁₃^[5] and CaNi₄Sn₂^[6] have been described for the system Ca/Ni/Sn. In Ca₇Ni₄Sn₁₃ the main structural motifs are Ni–Sn channels, which are built up of alternate stacking of squares of Sn atoms and Ca-centred octagons of Sn and Ni atoms. These channels are connected through planar units of five Sn atoms to form a three-dimensional network. In CaNi₄Sn₂ the structure is constructed of a three-dimensional framework of Ni and Sn atoms with quasi-tetra and -octagonal channels along the *c* axis. The Ca atoms are situated within the quasi-octagonal channels.

[a] Department Chemie, Technische Universität München, Lichtenbergstr. 4, 85747 Garching, Germany

Supporting information for this article is available on the WWW under <http://dx.doi.org/10.1002/ejic.201101277>.

Our research of the Ca/Ni/Sn system led us to two new polymorphic modifications of the novel intermetallic phase Ca_2NiSn_2 . The monoclinic modification consists of a three-dimensional network of Ni and Sn atoms, which present interesting Sn–Sn contacts and will be denoted as *mC*- Ca_2NiSn_2 . The orthorhombic modification, denoted as *oP*- Ca_2NiSn_2 , clearly exhibits common structural features with respect to the crystal structure, the dimensionality being reduced by the formation of two-dimensional slabs. The electronic and crystal structures of these polymorphic modifications of Ca_2NiSn_2 are presented herein.

Results and Discussion

Crystal Structure of *mC*- Ca_2NiSn_2

The intermetallic compound *mC*- Ca_2NiSn_2 was synthesized by arc melting of the elements and consequent annealing at 700 °C and 750 °C. *mC*- Ca_2NiSn_2 crystallizes in the Zr_2CoSi_2 structure type.^[7] Its crystal structure was determined by single-crystal X-ray diffraction analysis and the unit cell parameters were refined by powder X-ray diffraction analysis: $C2/m$, $Z = 4$, $a = 11.138(2)$ Å, $b =$

$4.5638(8)$ Å, $c = 10.999(2)$ Å, $\beta = 117.85(2)^\circ$, $wR_2 = 0.068$ (all data).

The structure of *mC*- Ca_2NiSn_2 is shown in Figure 1. It can be seen that the Ni and Sn atoms form a three-dimensional network with the Ca atoms located in the cavities. Part b of Figure 1 presents distorted square ribbons of alternating Ni and Sn1 atoms ($^1_\infty[\text{Ni}_2\text{Sn}_2]$ ladder propagating along the b axis) that are interconnected through Sn1–Sn1 contacts with $d(\text{Sn1}–\text{Sn1}) = 3.177(1)$ Å resulting in six-membered $[\text{Ni}(\text{Sn1})_2\text{Ni}(\text{Sn1})_2]$ rings. The deviation of these rings from planarity towards a chair conformation is expressed by the small fold angle of $21.72(4)^\circ$, as shown in Figure 1 (c). The corrugated slabs are linked to each other by Sn2–Sn2 dumbbells [$d(\text{Sn2}–\text{Sn2}) = 2.934(1)$ Å] that are connected to the Ni atoms of neighbouring slabs. The resulting Ni–Sn2–Sn2–Ni unit has a *trans* conformation and a Ni–Sn2–Sn2 angle of $113.60(3)^\circ$. The observed Sn–Sn distances compare well with those found in β -Sn (3.02 and 3.18 Å). The Ni–Sn1 and Ni–Sn2 distances [$d(\text{Ni}–\text{Sn1}) = 2.580(1)$ Å, $d(\text{Ni}–\text{Sn1}) = 2.694(1)$ Å, $d(\text{Ni}–\text{Sn2}) = 2.633(1)$ Å] are in the same range as those observed in similar intermetallic compounds.^[6]

Crystal Structure of *oP*- Ca_2NiSn_2

The intermetallic compound *oP*- Ca_2NiSn_2 was synthesized by arc melting of the elements and consequent annealing at 800–870 °C. *oP*- Ca_2NiSn_2 crystallizes in a new structure type, which was determined by single-crystal X-ray analysis, and the unit cell parameters were refined by powder X-ray diffraction analysis: $Pmmn$, $Z = 4$, $a = 4.5992(3)$ Å, $b = 9.844(2)$ Å, $c = 10.9889(8)$ Å, $wR_2 = 0.048$ (all data).

The crystal structure of *oP*- Ca_2NiSn_2 is presented in Figure 2. The Ni and Sn atoms form two-dimensional Ni slabs separated by Ca atoms. Similarly to *mC*- Ca_2NiSn_2 , Figure 2 (b) shows that *oP*- Ca_2NiSn_2 contains distorted square Ni–Sn1 ribbons ($^1_\infty[\text{Ni}_2\text{Sn}_2]$ ladder) that are connected to form slabs through Sn1–Sn1 bonds [$d(\text{Sn1}–\text{Sn1}) = 3.140(1)$ Å]. The resulting six-membered $[\text{Ni}(\text{Sn1})_2\text{Ni}(\text{Sn1})_2]$ rings have a boat conformation with a small fold angle of $16.06(3)^\circ$, as shown in Figure 2 (c). In contrast, a chair conformation was observed for *mC*- Ca_2NiSn_2 (Figure 1, c). Focusing on these six-membered rings, a *trans*-type connection of the $^1_\infty[\text{Ni}_2\text{Sn}_2]$ ladders is observed in *mC*- Ca_2NiSn_2 , whereas in *oP*- Ca_2NiSn_2 a *cis*-type arrangement is present.

Furthermore, in *mC*- Ca_2NiSn_2 these two-dimensional arrangements are interconnected by Sn2 dumbbells that are connected at each end to one Ni atom of the neighbouring slabs. In contrast, in *oP*- Ca_2NiSn_2 , one atom of the Sn2 unit (Sn3) bridges two Ni atoms of two neighbouring $^1_\infty[\text{Ni}_2\text{Sn}_2]$ ladders within one slab and the second Sn atom (Sn2) of the dimer remains singly bonded to the Sn3 atom with a Sn2–Sn3 distance of $2.925(1)$ Å. The observed Sn–Sn distances compare well with those found in β -Sn (3.02 and 3.18 Å). As a consequence of the Sn2 unit being connected end-on to one slab, the $^1_\infty[\text{Ni}_2\text{Sn}_2]$ ladders are tilted towards

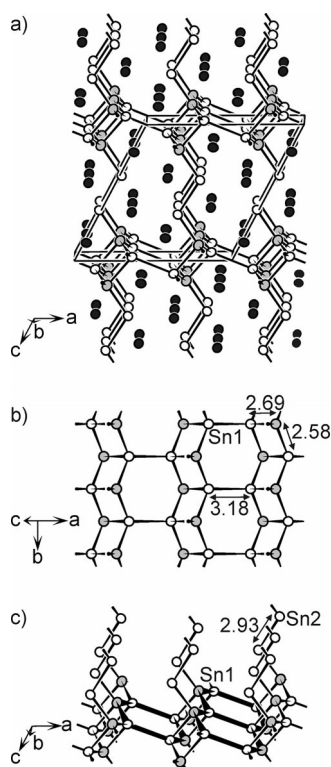


Figure 1. Crystal structure of *mC*- Ca_2NiSn_2 . a) Overview of the crystal structure, b) view of the Ni–Sn ladder interconnected by Sn1–Sn1 bonds to construct a two-dimensional slab (ab plane) and c) the 2D Ni–Sn slabs connected to a 3D network by Sn2–Sn2 dumbbells (view along the b axis). The Ni_2Sn_4 hexagons are pronounced, here being arranged in a chair conformation. The Ca, Sn and Ni atoms are drawn as black, white and grey spheres, respectively. The displacement ellipsoids are drawn at the 95% probability level. The atomic distances are given in Å.

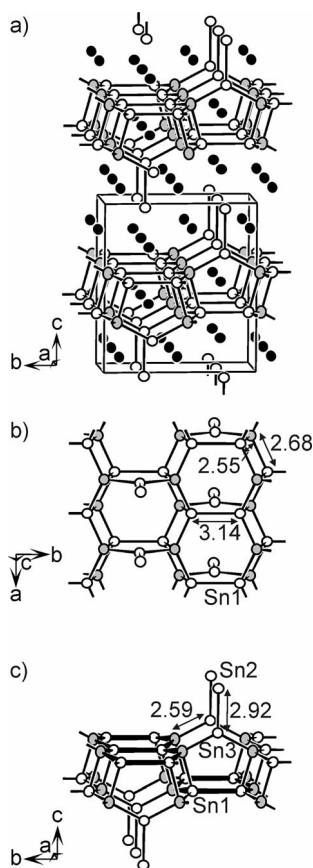


Figure 2. Crystal structure of *oP*-Ca₂NiSn₂. a) Overview of the structure, b) view along the stacking direction (*c* axis) and c) view along the *a* axis. The distorted square ¹_∞[Ni₂Sn₂] ribbons are connected through a Sn–Sn bond and one end of a Sn dumbbell. The Ni₂Sn₄ hexagons are pronounced, here being arranged in a boat conformation. The Ca, Sn and Ni atoms are drawn as black, white and grey spheres, respectively. The displacement ellipsoids are drawn at the 95% probability level. The atomic distances are given in Å.

each other and five-membered rings [Ni–Sn1–Sn1–Ni–Sn3] emerge between the ladders.

The shortest interslab Sn–Sn distance in *oP*-Ca₂NiSn₂ [*d*(Sn1–Sn2) = 4.542(1) Å] is certainly non-bonding, which underlines the two-dimensional character of the structure. The Ni–Sn distances are in the same range as observed in similar intermetallic compounds [*d*(Ni–Sn1) = 2.554(1) Å, *d*(Ni–Sn1) = 2.680(1) Å, *d*(Ni–Sn3) = 2.588(1) Å].

Related Crystal Structures

Structural motifs similar to those observed in *mC*-Ca₂NiSn₂ and *oP*-Ca₂NiSn₂ are found in various stannides in the systems *Re*,*Ae*/*T*/Sn (*Re* = rare earth metal, *Ae* = alkaline earth metal, *T* = transition metal). For example, the distorted square ¹_∞[Ni₂Sn₂] ladder is observed in the Ni–Pt substructure of NP–CePtSn^[8] (TiNiSi structure type,^[9] Figure 3, a). In NP–CePtSn, the ladders are directly connected to form a three-dimensional network with Ce atoms situated in the cavities.

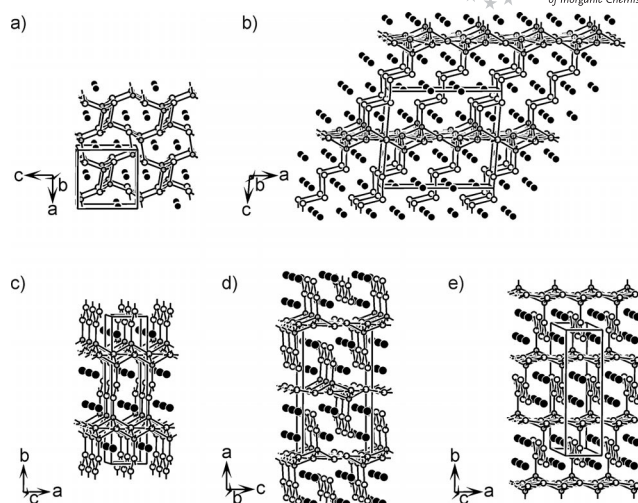


Figure 3. Crystal structures of a) NP–CePtSn,^[8] b) Ca₆Cu₂Sn₇,^[10] c) SrNiSn₂,^[12] d) Sm₂NiSn₄,^[13] and e) Yb₃CoSn₆.^[31] The alkaline earth and rare earth atoms are drawn as black spheres, the tetrel and transition-metal atoms as white and grey spheres, respectively.

In several examples, two-dimensional PbO-type slabs, in which square nets of Sn atoms are alternately capped above and below by Ni atoms, are connected by different arrangements of Sn atoms, just as the Ni–Sn slabs in *mC*-Ca₂NiSn₂ are interconnected by Sn₂ dumbbells. In Ca₆Cu₂Sn₇^[10] (Figure 3, b), the PbO-type slabs ²_∞[NiSn] are interconnected by Sn₄ zigzag chains to form a three-dimensional ³_∞[Cu₂Sn₇] network. The structures of polymorphic Ca₂NiSn₂ can furthermore be compared with SrNiSn₂ (CeNiSi₂ structure type,^[11] space group *Cmcm*, Figure 3, c)^[12] in which zigzag chains of the Sn atoms connect the PbO-type slabs ²_∞[NiSn] to form a three-dimensional network. Furthermore, Sm₂NiSn₄ (space group *Pnma*,^[13] Figure 3, d) has been described as an intermediate structure type between ZrSi₂^[14] and CeNiSi₂ and can be considered as a defective variant of the latter structure in which one half of the Ni atoms (arranged in rows) of the PbO-type slabs are missing. Consequently, the zigzag chains of the Sn atoms bind only to the Ni atoms of one slab and give rise to a two-dimensional Ni–Sn substructure. The removal of further Ni atoms leads to the Yb₃CoSn₆ structure^[15] (Figure 3, e) in which only a third of the positions of the transition metal are occupied. The Sn atoms of the connecting zigzag chains bind alternately along the chain to the Co atoms of the upper and lower slabs to form a three-dimensional Co–Sn substructure.

Topology of the Phase Transition of the Polymorphic Modifications of Ca₂NiSn₂

Even though distinct structural similarities are evident for the two polymorphic modifications of Ca₂NiSn₂, no group–subgroup relationship can be described. This indicates that the mechanism of the phase transition is reconstructive. This reconstructive phase transition is most likely

slow, which would explain the absence of a clearly defined exothermic peak in the differential thermal analysis (DTA). In the following paragraph, two pathways that topologically describe the transformation between the two Ni–Sn networks are presented.

The first path (Figure 4) is based on shifting ribbons, which are part of an atomic layer. Both structures can be described as being constructed of atomic layers of the formula Ca_2NiSn_2 (part a of Figure 4 presents the atomic layer at $y = 0$ and $y = 1/2$ in the ac plane for $mC\text{-Ca}_2\text{NiSn}_2$, part c presents the corresponding atomic layer at $x = 1/4$ and $x = 3/4$ in the bc plane for $oP\text{-Ca}_2\text{NiSn}_2$). The Ni–Sn and Sn–Sn bonds are highlighted. Parts of the Ni–Sn networks can be recognized in the atomic layers, such as the one-dimensional NiSn_2 chains in $mC\text{-Ca}_2\text{NiSn}_2$ (Figure 4, a) and five-membered Ni_2Sn_3 rings with a covalently *exo*-ring-bonded Sn atom in $oP\text{-Ca}_2\text{NiSn}_2$ (Figure 4, c). The next atomic layers complete the chains and rings of the Ni–Sn networks observed in $mC\text{-Ca}_2\text{NiSn}_2$ (Figure 4, b) and $oP\text{-Ca}_2\text{NiSn}_2$ (Figure 4, d), respectively. Furthermore, examination of the layers reveals that they can be split into ribbons. These are found in both crystal structures and are highlighted in Figure 4 (a, c). A shift of all atoms included in the central ribbon, highlighted in Figure 4 (a) for $mC\text{-Ca}_2\text{NiSn}_2$ (including the Ni atoms on the left side of this ribbon), leads to the formation of the five-membered rings shown in part c for $oP\text{-Ca}_2\text{NiSn}_2$.

In more detail, the phase transition includes changes in atomic layer stacking, which are indicated for the polyanionic Ni–Sn motifs in Figure 4 (b) for $mC\text{-Ca}_2\text{NiSn}_2$ and in part d for $oP\text{-Ca}_2\text{NiSn}_2$. In $mC\text{-Ca}_2\text{NiSn}_2$ the atomic layers shown in part a are stacked according to the sequence AA' . A and A' are identical layers with an offset of $x = 1/2$ and $y = 1/2$. For $oP\text{-Ca}_2\text{NiSn}_2$ the atomic layers shown in part c are analogously stacked according to the sequence BB' . B and B' are identical atomic layers, mapped onto each other by the inversion centre. Shifting the slabs in the atomic layer A and A' in $mC\text{-Ca}_2\text{NiSn}_2$, as described above, leads to a slightly distorted arrangement of the B and B' layers.

The second path to the shifting of the Ni–Sn bonds is shown in Figure 5. The phase transition discussed here is similar to the rearrangements that occur by electrocyclic mechanisms such as the sigmatropic shifts known for organic molecules. A larger section of the $mC\text{-Ca}_2\text{NiSn}_2$ structure in a projection along the b axis is presented in

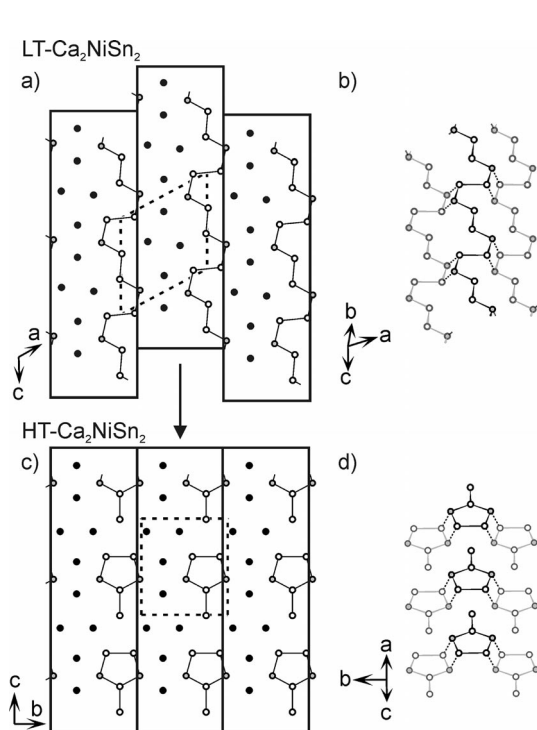


Figure 4. Description of the title compounds $mC\text{-Ca}_2\text{NiSn}_2$ and $oP\text{-Ca}_2\text{NiSn}_2$ in terms of atomic layers. a) Atomic layer in the ac plane of $mC\text{-Ca}_2\text{NiSn}_2$ (at $y = 0$ and $y = 1/2$), the Ni–Sn and Sn–Sn bonds are highlighted, b) the Ni–Sn chains of two layers (lower layer with grey bonds, upper layer with black bonds), c) atomic layer in the bc plane of $oP\text{-Ca}_2\text{NiSn}_2$ (at $x = 1/4$ and $x = 3/4$), the Ni–Sn and Sn–Sn bonds are highlighted, d) the Ni–Sn motifs of two layers (lower layer with grey bonds, upper layer with black bonds). To illustrate the relationship between the title compounds, ribbons within the atomic layers are highlighted in a) and c). The Ca, Sn and Ni atoms are drawn as black, white and grey spheres, respectively.

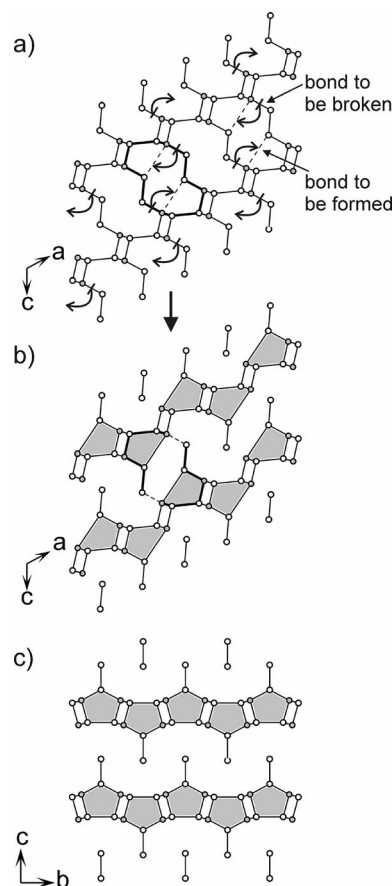
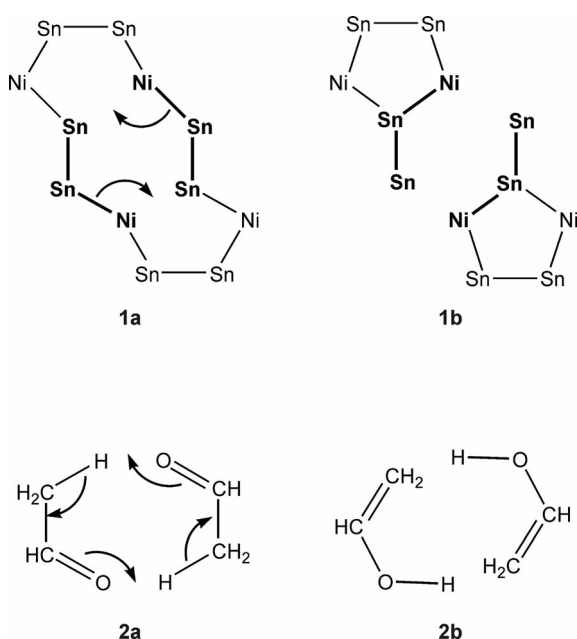


Figure 5. a, b) Projection along the b axis of $mC\text{-Ca}_2\text{NiSn}_2$. The positions of bond scission and bond formation (dashed lines, 5.2 Å) are indicated to topologically describe the phase transition from a molecular point of view. c) Projection along the a axis of $oP\text{-Ca}_2\text{NiSn}_2$. The Sn and Ni atoms are drawn as white and grey spheres, respectively.

Figure 5 (a). In analogy to an electrocyclic mechanism, the Ni–Sn bonds are shifted within the 12-membered ring as indicated in Figure 5 (a). As a result the 12-membered ring splits into two units with the topology of the above-mentioned five-membered ring with one *exo* cyclic ring bonded to a terminal Sn atom. The mechanism can even be seen to resemble an intermolecular keto/enol tautomerism, as shown in Scheme 1. Ni–Sn bond scission and formation according to **1a** leads to the two units in **1b**, just like C–H bond scission and O–H bond formation in the ketone **2a** lead to the two enols in **2b**. This, of course, remains a topological model because Ni–Sn bonds form over a distance of 5.2 Å. Nevertheless, this model shows that in addition to the shift of atomic layers, Ni–Sn bonds simultaneously form and split. After a “relaxation of the structure”, especially of the atoms of the ¹_∞[Ni₂Sn₂] ladder, the structure of *oP*-Ca₂NiSn₂ as shown in Figure 5 (c) results.



Scheme 1. Mechanism for the phase transition of *mC*-Ca₂NiSn₂ (**1a**) to *oP*-Ca₂NiSn₂ (**1b**) compared with the mechanism for the keto/enol tautomerism (**2**).

Chemical Bonding

When discussing the bonding in the two polymorphic modifications of Ca₂NiSn₂, some aspects relating to the crystal structure need to be considered. First, both compounds contain four bonded Sn1 atoms that participate in one Sn1–Sn1 bond and in three Sn1–Ni bonds. The Sn1–Sn1 distances are similar [$d(\text{Sn1–Sn1}) = 3.177(1)$ Å for *mC*-Ca₂NiSn₂ and $d(\text{Sn1–Sn1}) = 3.140(1)$ Å for *oP*-Ca₂NiSn₂]. Secondly, both compounds contain a Sn–Sn dumbbell with an even shorter bond length [$d(\text{Sn2–Sn2}) = 2.934(1)$ Å in *mC*-Ca₂NiSn₂ and $d(\text{Sn2–Sn3}) = 2.925(1)$ Å in *oP*-Ca₂NiSn₂]. This dumbbell is integrated into the crystal structure in different ways. In *mC*-Ca₂NiSn₂ both atoms of the dumbbell are involved in two bonds; each participates

in one Sn2–Sn2 bond and in one Sn2–Ni bond. In contrast, in *oP*-Ca₂NiSn₂ the Sn2 atom participates only in the Sn2–Sn3 bond whereas Sn3 is involved in three bonds, that is, in the Sn2–Sn3 bond and in two Ni–Sn3 bonds. All Ni atoms are involved in four bonds. Thus, the overall number of bonds within the two modifications does not change.

The crystal structures of the title compounds can be interpreted in terms of the Zintl concept if the Ni atoms as well as the Ca atoms are assigned a formal oxidation state of +II. The anionic Sn atoms consequently are all singly bonded to another Sn atom within a dumbbell and thus a charge of –III results for each Sn atom. The Sn atoms donate their lone pairs to the coordinated Ni ions. Such Ni–Sn bonds are well known in metalorganic complexes. For example, the complex Ni[Sn(*Nt*Bu)₂SiMe₂], which is obtained by the reaction of NiBr₂ and Me₂Si(*Nt*Bu)₂Sn in toluene, contains a Ni^{II}–Sn bond.^[16] The corresponding Ni–Sn distance [mean: 2.463(3) Å] is slightly shorter than the Ni–Sn distances observed in the title compounds.

To analyse the chemical bonding within the title compounds, paying particular attention to the different Sn–Sn bonds, we performed electronic structure calculations by using the Stuttgart TB-LMTO-ASA program.^[17] In the following, the total and partial density of states (DOS) curves, band structures, including fatbands, the electron localization function (ELF) and the crystal orbital Hamilton populations (COHP) will be discussed.

Information concerning the phase stability of the two polymorphs is given by the total energies determined in the TB-LMTO-ASA calculations, which show that at 0 K *oP*-Ca₂NiSn₂ is 31.51 kJ/mol (0.096 Ry) more stable than *mC*-Ca₂NiSn₂.

Electronic Structure of *mC*-Ca₂NiSn₂

The total DOS curve of *mC*-Ca₂NiSn₂ does not show any band gap at the Fermi level, which indicates metallic behaviour (see Figure S1 and Text S1 in the Supporting Information). In agreement with the three-dimensional character of the crystal structure, the band structure presents isotropic metallic properties (Figure 6 and Figure S3 in the Supporting Information). For a quantitative approach to the bond strength, the COHP curves and their descriptions are given in Figure S2 and Text S1, respectively. The values of the corresponding –iCOHP are given in Table 3. The high values observed for the Ni–Sn contacts (1.74–2.39 eV/bond) indicate covalent bonding. Similarly, high –iCOHP values are found for the Sn–Sn contacts. These vary with the bond length: for $d(\text{Sn2–Sn2}) = 2.934(1)$ Å, –iCOHP = 1.62 eV/bond, whereas for the longer distance $d(\text{Sn1–Sn1}) = 3.177(1)$ Å a significantly lower value of –iCOHP = 0.90 eV/bond is observed.

In Figure 7, two contour line diagrams for the electron localization function of *mC*-Ca₂NiSn₂ are presented. These two line diagrams correspond to the distinct planes outlined in Figure 7 (a): the *ac* plane through the Sn1–Sn1 and Sn2–Sn2 bonds (Figure 7, b) and the *bc* plane close to the Sn2–

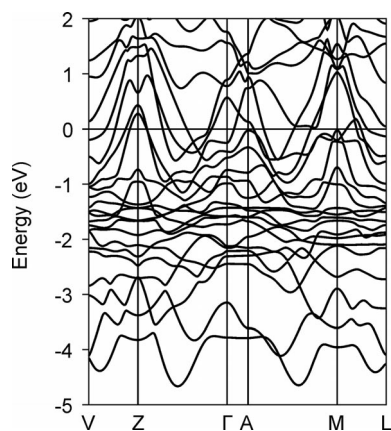


Figure 6. Bandstructures for *mC*-Ca₂NiSn₂. Information on the Brillouin zone of a base-centred monoclinic unit cell can be found in ref.^[32]

Sn2 bond (Figure 7, c). The examination of the Sn–Sn contacts shows the disynaptic valence basins below $\eta = 0.46$ for Sn1–Sn1 and below $\eta = 0.49$ for Sn2–Sn2 [(1) and (2) in Figure 7, b and c, respectively]. This is in accordance with the relatively short Sn1–Sn1 and Sn2–Sn2 distances as well as the high $-i\text{COHP}$ values. As seen in Figure 7 (c), for the Sn2–Sn2 contact the disynaptic valence basins are not situated directly on the bond, but one maximum is found on

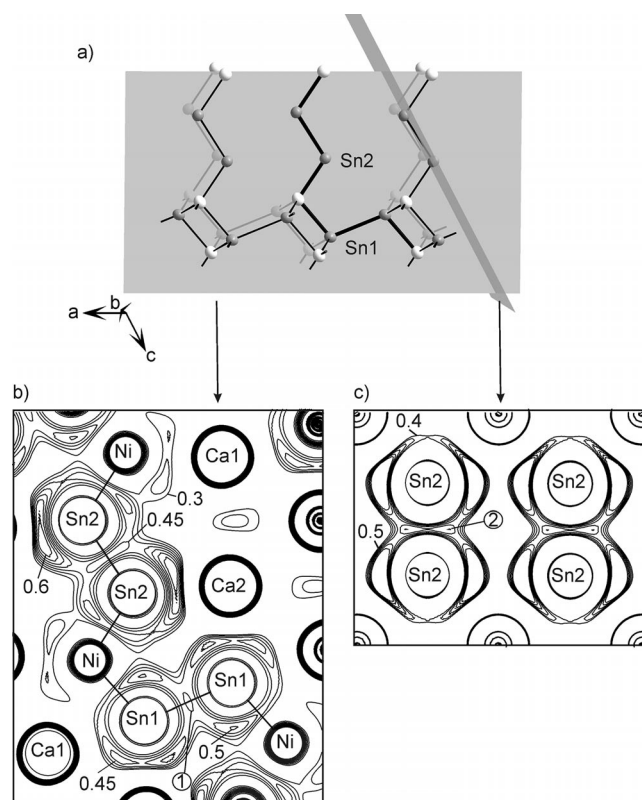


Figure 7. Contour line diagrams of the ELF in steps of b) 0.05 ($\eta = 0.3$ – 0.7) and c) 0.02 ($\eta = 0.4$ – 0.5) for *mC*-Ca₂NiSn₂. The sections correspond to the planes outlined in the structure in part (a): the *ac* plane (b) and the *bc* plane close to the Sn2–Sn2 bond (c). The bonds indicated in b) are highlighted in (a).

each side of the bond. This indicates the Sn2–Sn2 bond has π -bonding character. The fatbands of *mC*-Ca₂NiSn₂ given in Figure S3 reveal that all Sn *p* orbitals are associated with bands around E_F . Therefore partial π bonding due to the incomplete filling of anti-bonding π^* orbitals is anticipated. The monosynaptic valence basins of the Sn atoms are discussed in Text S2 and Figure S4 in the Supporting Information.

Electronic Structure of *oP*-Ca₂NiSn₂

The total DOS curve of *oP*-Ca₂NiSn₂ does not show any band gap at the Fermi level, which indicates metallic behaviour (see Figure S5 and Text S3 in the Supporting Information). The band structure of *oP*-Ca₂NiSn₂, including the fatbands of Sn1(*p_z*) and Ni(*d_{xz}*), is shown in Figure 8 and Figure S7 in the Supporting Information. The directions that are perpendicular to the ²_∞[NiSn₂] slabs ($\Gamma \rightarrow Z$, $T \rightarrow Y$ and $S \rightarrow R$) are marked with a grey background. The calculations on the electronic band structure reveal that, although no band crosses E_F along $\Gamma \rightarrow Z$ and $T \rightarrow Y$, a possible anisotropy is broken by two steep bands that cross E_F in the section $S \rightarrow R$. To assign these bands to their corresponding orbitals, a fatband analysis was performed in which bands are drawn with a thickness representative of the corresponding orbital contribution. The two bands that cross E_F in the section $S \rightarrow R$ are assigned to the Sn1(*p*), Ni(*d*) and Ca(*d*) orbitals. More precisely, the main contributions of these bands originate from the Sn1(*p_z*) and Ni(*d_{xz}*) orbitals, revealing an interaction between the Sn1 and Ni atoms along the *c* axis. Further contributions of these bands originate from Sn2(*p_z*) and Sn3(*p_z*), underlining the bonding interactions between Sn2 and Sn3.

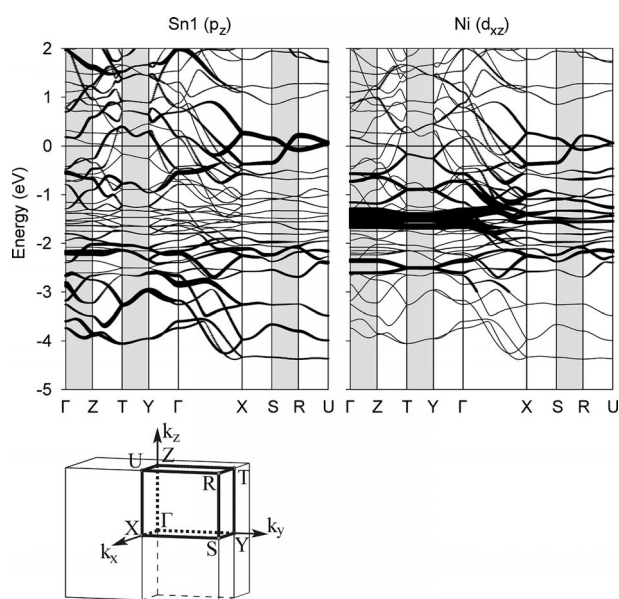


Figure 8. Band structure with fatbands for Sn1(*p_z*) and Ni(*d_{xz}*) in *oP*-Ca₂NiSn₂. The symmetry points in *k* space are given for the Brillouin zone shown.

Band structures of other intermetallic compounds containing Ni–Ge slabs have been discussed previously.^[18] For example, the calculation of the band structure of BaNi₂Ge, which contains rather flat ²_∞[Ni₂Ge] slabs, revealed anisotropic metallic properties: a band gap at E_F and relatively flat bands are observed in the directions perpendicular to the slabs, whereas metallic conductivity occurs parallel to the slabs. This anisotropy is broken in the case of Ca₄Ni₄Ge₃, which contains more puckered ²_∞[Ni₄Ge₃] slabs. A fatband analysis revealed that this is mainly due to the most exposed Ge atom.

For a quantitative approach to the bond strength, the COHP curves and the corresponding discussions are given in Figure S6 and Text S3 in the Supporting Information, respectively. The values of $-i\text{COHP}$ for the shortest distances Ni–Sn and Sn–Sn are given in Table 3. As observed for *mC*-Ca₂NiSn₂, high values are observed for the Ni–Sn contacts (1.64–2.40 eV/bond), which indicates covalent bonding. The $-i\text{COHP}$ values for the Sn–Sn contacts are also in good accord with those observed for *mC*-Ca₂NiSn₂: for the short Sn2–Sn3 contact [$d(\text{Sn2–Sn3}) = 2.925(1) \text{ \AA}$] $-i\text{COHP} = 1.67 \text{ eV/bond}$ is observed, for the longer Sn1–Sn1 contact [$d(\text{Sn1–Sn1}) = 3.140(1) \text{ \AA}$] $-i\text{COHP} = 0.88 \text{ eV/bond}$ is observed.

For a more pictorial view of the bonding situation, two contour line diagrams as well as a plot of the isosurface of the electron localization function (ELF) for *oP*-Ca₂NiSn₂ are presented in Figure 9. The two contour line diagrams correspond to the planes outlined in Figure 9 (a): the *bc* plane parallel to the Sn1–Sn1 and Sn2–Sn3 contacts (Figure 9, b) and the *ac* plane parallel to the Sn2–Sn3 contact. The plot of the isosurface in Figure 9 (d) is given for the Sn2–Sn3 contact at $\eta = 0.47$. Analysis of the Sn–Sn contacts shows a disynaptic valence basin below $\eta = 0.46$ for the Sn1–Sn1 bond in accord with the relatively short distance [$d(\text{Sn1–Sn1}) = 3.140(1) \text{ \AA}$] and high $-i\text{COHP}$ values [(1) in Figure 9, b]. Furthermore, in Figure 9 (b) an ellipsoid-shaped basin seems to appear between Sn2 and Sn3 below $\eta = 0.45$ in accord with the covalent bond length of $d(\text{Sn2–Sn3}) = 2.925(1) \text{ \AA}$ and high $-i\text{COHP}$ values. Nevertheless, close inspection of Figure 9 (c, d) reveals that no disynaptic valence basin exists between Sn3 and Sn2. Instead, the lone pairs of Sn3 (2) merge (Figure 9, c). This is illustrated by plots of the isosurface for the Sn2–Sn3 contact in Figure 9 (d) and in Figure S9. These findings are in strong contrast to the partial π bonding observed for the Sn2–Sn2 contact in *mC*-Ca₂NiSn₂. The analysis of the fatbands of *oP*-Ca₂NiSn₂ (Figure S7) reveals that the p_y orbitals of Sn2 and Sn3 are mainly associated with bands that are low-lying in energy (about -4 to -2 eV for Sn3 and -2 to -0.5 eV for Sn2) and that these mix very little with other orbitals. As these p_y orbitals correlate little with bands crossing E_F , the anti-bonding π^* orbitals are filled. Thus, the p_y orbitals have lone-pair character. Furthermore, lone-pair character is expected for the p_x orbitals, which reflects the geometry of the monosynaptic valence basin of Sn3 [(2), Figure 9, c]. The fatbands of the p_x orbitals of Sn2 and Sn3 reveal mixing at E_F parallel to the *b* axis ($Y \rightarrow \Gamma$ and $Z \rightarrow T$),

the bands being positioned above and below E_F . In summary, the topological analysis of the ELF indicates that the Sn2–Sn3 contact is mainly dominated by p lone pairs. The lone-pair character of p_y is confirmed by the fatband analysis. The monosynaptic valence basins of the Sn atoms are discussed in Text S3 and Figure S8 in the Supporting Information.

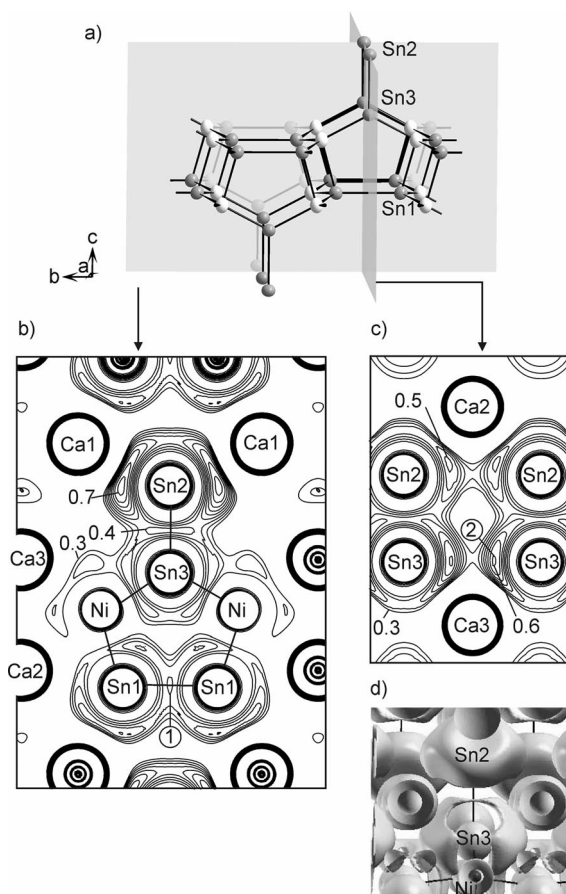


Figure 9. a) Structure of *oP*-Ca₂NiSn₂. Contour line diagrams of the ELF in steps of 0.05 ($\eta = 0.3$ – 0.7) for *oP*-Ca₂NiSn₂. The sections correspond to the planes outlined in the structure in part (a): the *bc* plane (b) and the *ac* plane including the Sn2–Sn3 contact (c). The bonds indicated in (b) are highlighted in (a). d) The isosurface at $\eta = 0.47$ is given for the Sn2–Sn3 contact viewed along the *b* axis.

Conclusions

Two new polymorphic modifications of the intermetallic compound Ca₂NiSn₂ have been synthesized. The crystal structures of the two modifications were determined by both powder and single-crystal X-ray diffraction analyses. The phase transition was analysed by annealing the samples at various temperatures. Supported by the calculated difference of the total energies, the results of the analysis of temperature-dependent syntheses indicate that the monoclinic *mC*-Ca₂NiSn₂ corresponds to a metastable modification and that the orthorhombic modification *oP*-Ca₂NiSn₂ is

thermodynamically more stable. The smaller volume and thus higher density of the metastable polymorph *mC*-Ca₂NiSn₂ (5.055 g/cm³) compared with *oP*-Ca₂NiSn₂ (5.023 g/cm³) is unusual. However, this phenomenon is not unheard of in tin chemistry; at low temperatures (below 13 °C) β-Sn is metastable even though it has a higher density (7.769 g/cm³) than α-Sn (5.769 g/cm³). This anomaly correlates with the formation of covalent directed bonds in α-Sn.

For the crystal structures of the two polymorphic modifications no group–subgroup relationship can be described. Consequently, the mechanism of the phase transition is most likely a reconstructive one. Nevertheless, similarities in the crystal structures are observed. In addition, two pathways to the description of the phase transition are given. First, examination of the atomic layers in both title compounds depicts the possibility of transforming one structure into the other by shifting ribbons of these atomic layers. The second path involves the shifting of Ni–Sn bonds. This is similar to rearrangements by electrocyclic mechanisms, such as the sigmatropic shift reactions known for organic molecules. As an example, the model of the phase transition can be compared with keto/enol tautomerism. Thus, the topological model of the sigmatropic rearrangement given here indicates a link between the solid-state chemistry of intermetallic compounds and the chemistry of rather simple organic molecules.

The chemical bonding of the title compounds is discussed in terms of DFT calculations performed with the TB-LMTO-ASA program. The DOS curves, band structures, including fatbands, and a topological analysis of the ELF are given and reveal covalent Sn1–Sn1 bonding for both compounds, covalent Sn2–Sn2 bonds with partial π bonding for the Sn₂ dumbbells in *mC*-Ca₂NiSn₂ and a short Sn2–Sn3 contact with dominant p lone pairs on the Sn2 and Sn3 atoms in *oP*-Ca₂NiSn₂.

Experimental Section

Syntheses: The starting materials for the synthesis of the two polymorphic modifications of Ca₂NiSn₂ were commercially available elements of high purity: ingots of calcium (Alfa Aesar, 99.3%), Ni wire (Alfa Aesar, 99.98%) and Sn pieces (Chempur, 99.999%). The Ca was distilled before use; Ni and Sn were used as provided. Stoichiometric amounts of the elements corresponding to a total mass of 0.7 g were used. Initially, the Ni wire and Sn pieces were fused by arc melting on a water-cooled copper hearth under argon (Mini Arc Melting System, MAM-1, Johanna Otto GmbH, placed in an argon-filled glovebox). After this, Ca was added and the arc melting was repeated at a lower current. The arc melting was repeated at least three times for each step and the sample was turned over after each melting to ensure homogeneity. Analysis of the sample after arc melting by powder X-ray diffraction revealed that the monoclinic modification (*mC*-Ca₂NiSn₂) was formed. In the next step, the regulus that was obtained after arc melting was sealed in a tantalum ampoule under argon. The tantalum ampoule was in turn enclosed under argon in a quartz ampoule. These quartz ampoules were then placed into a resistant furnace (LOBA, HTM Reetz GmbH) for tempering. Powder X-ray diffraction showed that the

phase *mC*-Ca₂NiSn₂ was preserved after tempering for 2 weeks at 700 and 750 °C, whereas tempering for 2 weeks at 800, 850 and 870 °C led to orthorhombic modification (*oP*-Ca₂NiSn₂). To test the reversibility of this phase transition, a sample of *oP*-Ca₂NiSn₂ was tempered for a month at 700 °C. The powder X-ray diffraction analysis showed that no *mC*-Ca₂NiSn₂ was formed. This suggests that either *mC*-Ca₂NiSn₂ is a metastable modification that transforms into *oP*-Ca₂NiSn₂ only above 800 °C or that below 750 °C the transformation from *oP*-Ca₂NiSn₂ to *mC*-Ca₂NiSn₂ is kinetically hindered. Because the shape of the regulus obtained from the arc-melting procedure changes upon heating to 900 °C, the melting point of the compound or of its decomposition products is reached at this temperature. Powder X-ray diffraction analysis of this sample heated at 900 °C reveals the presence of an unknown phase (main product) as well as CaSn and Ca₇Sn₆. Thus, peritectic decomposition of Ca₂NiSn₂ occurs between 870 and 900 °C.

In addition, the phase *mC*-Ca₂NiSn₂ was synthesized by sealing the regulus obtained after arc melting in a tantalum ampoule. The ampoule was then placed in a water-cooled sample chamber of an induction furnace (Hüttinger Elektronik, Freiburg, Typ TIG 2.5/300) and heated under flowing argon up to approximately 950 °C for 1 h and subsequently cooled within half an hour to approximately 800 °C and finally cooled down to room temperature in about 1 min by switching off the furnace.

No reaction of the samples with the crucible material was detected in any of the experiments. Single crystals with metallic lustre were isolated from the crushed samples.

Powder and Single-Crystal X-ray Diffraction Studies and Structure Refinement:

The purity of the sample was checked at room temperature by using a STOE STADI P powder diffractometer with Ge-monochromatized Cu-K α radiation ($\lambda = 1.54056 \text{ \AA}$). Data were recorded at room temperature within the 2θ range of 4–94° from a sample in a glass capillary (Fa. Hilgenberg, diameter: 0.1 mm, wall width: 0.01 mm). To reduce absorption, diamond powder was added to the sample. The powder X-ray diffraction pattern obtained from stoichiometric mixtures of the elements showed that the sample tempered in a resistance furnace at 750 °C contained mainly *mC*-Ca₂NiSn₂ in addition to small amounts of CaSn and at least one unknown phase. The sample tempered at 800 °C contained *oP*-Ca₂NiSn₂ and small amounts of an unknown phase. Both samples were sensitive to air and/or moisture. The lattice parameters of the title compounds (see Table 1) were obtained from least-squares fits of these powder X-ray diffraction data by using WinXPOW.^[19] The lattice parameters determined from the powder pattern and from single-crystal data varied by less than 0.1%. Comparison of the powder X-ray diffraction data of various samples indicated that Ca₂NiSn₂ is a line compound. All unit cell parameters as well as interatomic distances given in the article are derived from the powder data.

Single crystals of *mC*-Ca₂NiSn₂ were obtained in an induction furnace after heating the sample at 950 °C for 1 h and subsequent cooling within 30 min to approximately 800 °C and finally cooling to room temperature in about 1 min by switching off the furnace. The formation of crystals of *mC*-Ca₂NiSn₂ suggests that due to the short time of annealing (overall 1.5 h) neither the phase transition to *oP*-Ca₂NiSn₂ nor decomposition occurs. However, good quality single crystals were obtained besides other products by this procedure. Single crystals were fixed in a glovebox under the microscope on top of a glass fibre by using grease. These glass fibres were then inserted in a glass capillary (Fa. Hilgenberg, diameter: 0.5 mm, wall width: 0.01 mm), which was sealed by using a hot filament. Single crystals of *oP*-Ca₂NiSn₂ (sample tempered at

Table 1. Crystal data and structure refinement for *oP*-Ca₂NiSn₂ and *mC*-Ca₂NiSn₂.

Empirical formula	<i>mC</i> -Ca ₂ NiSn ₂	<i>oP</i> -Ca ₂ NiSn ₂
Formula mass [g/mol]	376.25	376.25
Space group	<i>C2/m</i> (12)	<i>Pmmm</i> (59)
<i>Z</i>	4	4
Unit cell dimensions (from powder, at 293 K)		
<i>a</i> [Å]	11.138(2)	4.5992(3)
<i>b</i> [Å]	4.5638(8)	9.844(2)
<i>c</i> [Å]	10.999(2)	10.9889(8)
β [°]	117.85(2)	
<i>V</i> [Å ³]	494.4(1)	497.5(1)
Calculated density [g/cm ³]	5.055	5.023
Absorption coefficient [mm ⁻¹]	15.673	15.574
<i>F</i> (000)	672	672
Crystal size [mm ³]	0.06 × 0.05 × 0.05	0.07 × 0.05 × 0.04
θ range [°]	3.7–32.7	3.7–32.9
<i>hkl</i> range	±16, −6 < <i>k</i> < 5, ±16	± 6, −15 < <i>k</i> < 11, −15 < <i>l</i> < 16
Reflections collected	4749	4724
Independent reflections	954 (<i>R</i> _{int} = 0.043)	1009 (<i>R</i> _{int} = 0.035)
Reflections with <i>I</i> ≥ 2σ(<i>I</i>)	804 (<i>R</i> _σ = 0.028)	842 (<i>R</i> _σ = 0.027)
Data/parameters	954/32	1009/36
GOF on <i>F</i> ²	1.209	1.082
Final <i>R</i> indices with <i>I</i> > 2σ(<i>I</i>)		
<i>R</i> ₁	0.027	0.023
<i>wR</i> ₂	0.060	0.042
<i>R</i> indices (all data)		
<i>R</i> ₁	0.034	0.031
<i>wR</i> ₂	0.068	0.048
Extinction coefficient	0.0168(7)	0.0047(3)
Largest diff. peak and hole [e/Å ³]	1.90/−1.83	1.92/−1.37

850 °C) proved to be stable enough to be measured in air. Hence, they were fixed on top of a glass fibre in air by using nail polish. Single-crystal intensity data was collected at room temperature by using an Oxford Diffraction Xcalibur3 diffractometer with graphite-monochromatized Mo-*K*_α radiation ($\lambda = 0.71073$ Å). Empirical absorption corrections were applied to the data.^[20] The atomic positions were deduced from an automatic interpretation of direct methods with SHELXS-97.^[21] The structures were refined by using SHELXL-97 (full-matrix least-squares on *F*_o²)^[22] with anisotropic atomic displacement parameters for all atoms. As a check for the correct composition, the occupancy parameters of both compounds were refined in a separate series of least-squares cycles. All sites were fully occupied and kept fixed during the last refinement cycles (free refinement of the occupancy parameters led to deviations of no more than 2%). All relevant crystallographic data for the data collection and evaluation are listed in Table 1. Positional parameters and selected interatomic distances are listed in Tables 2 and 3. The anisotropic displacement parameters are given in Table S1 and Table S2 in the Supporting Information.

Further details on the crystal structure investigation(s) may be obtained from the Fachinformationszentrum Karlsruhe, 76344 Eggenstein-Leopoldshafen, Germany (fax: +49-7247-808-666; e-mail: crysdata@fiz-karlsruhe.de), on quoting the depository number CSD-423439 (for *mC*-Ca₂NiSn₂) and -423440 (for *oP*-Ca₂NiSn₂).

After single-crystal X-ray measurement the single crystals were analysed with a JEOL SEM 5900LV scanning electron microscope. A qualitative EDX analysis of well-shaped single crystals reveals the presence of all three elements Ca, Ni and Sn. No impurity elements heavier than sodium were observed.

Table 2. Atomic coordinates and equivalent isotropic displacement parameters (10³ Å²) for *mC*-Ca₂NiSn₂ and *oP*-Ca₂NiSn₂.

Atom	Wyckoff pos.	<i>x</i>	<i>y</i>	<i>z</i>	<i>U</i> _{eq}
<i>mC</i> -Ca ₂ NiSn ₂					
Ca1	4i	0.4985(2)	0	0.1666(2)	14(1)
Ca2	4i	0.3129(2)	0	0.3911(2)	15(1)
Ni	4i	0.7780(1)	0	0.1478(1)	15(2)
Sn1	4i	0.1605(1)	0	0.0618(1)	13(1)
Sn2	4i	0.0128(1)	0	0.3732(1)	13(1)
<i>oP</i> -Ca ₂ NiSn ₂					
Ca1	4e	1/4	0.5593(1)	0.1351(1)	15(1)
Ca2	2b	1/4	3/4	0.4493(2)	13(1)
Ca3	2b	1/4	3/4	0.7835(2)	14(1)
Ni	4e	1/4	0.0181(1)	0.6315(1)	15(2)
Sn1	4e	1/4	0.0905(1)	0.3965(1)	13(1)
Sn2	2a	1/4	1/4	0.0086(1)	14(1)
Sn3	2a	1/4	1/4	0.7424(1)	13(1)

Thermal Analysis: The thermal analyses (DTA) were carried out in the temperature range 25–950 °C using custom-made niobium containers for the sample and as reference crucible (Netzsch DSC 404C). The niobium crucibles were loaded with about 100 mg of a powdered sample of *mC*-Ca₂NiSn₂ containing small amounts of CaSn. The crucibles were then closed by pressing the niobium in the upper part of the crucible using a pipe tong and subsequent welding. The DTA curves were recorded under a continuous flow of argon (50 mL/min) to prevent corrosion of the crucibles at high temperatures. After the DTA experiments, the crucibles were opened in the glove-box and the products were again analysed by

Table 3. Interatomic distances calculated with the lattice parameters taken from the X-ray powder data and the corresponding integrated crystal orbital Hamilton populations (–iCOHPs) at E_F in mC -Ca₂NiSn₂ and oP -Ca₂NiSn₂. All distances within the first coordination spheres are listed.

		Distance [Å]	–iCOHP [eV/bond]			Distance [Å]	–iCOHP [eV/bond]
<i>mC</i> -Ca ₂ NiSn ₂							
Ca1	Sn2	3.1715(9) (2 ×)		Ca2	Sn1	3.202(2) (1 ×)	
	Ni	3.215(2) (1 ×)			Sn2	3.255(2) (1 ×)	
	Sn1	3.2404(9) (2 ×)			Sn2	3.2576(9) (2 ×)	
	Ni	3.288(1) (2 ×)			Sn2	3.316(1) (2 ×)	
	Sn1	3.383(2) (1 ×)			Ni	3.398(2) (2 ×)	
	Ni	3.390(2) (1 ×)			Ca2	3.712(3) (1 ×)	
	Sn1	3.426(1) (2 ×)			Ca1	3.890(2) (1 ×)	
	Ca1	3.681(3) (1 ×)			Ca1	3.935(2) (1 ×)	
Sn1	Ni	2.5801(5) (2 ×)	2.39	Sn2	Ni	2.633(1) (1 ×)	2.19
	Ni	2.6943(9) (1 ×)	1.74		Sn2	2.9335(8) (1 ×)	1.62
	Sn1	3.1769(9) (1 ×)	0.90				
<i>oP</i> -Ca ₂ NiSn ₂							
Ca1	Sn1	3.229(2) (1 ×)		Ca3	Ni	3.123(2) (2 ×)	
	Sn3	3.2595(7) (2 ×)			Sn2	3.242(1) (2 ×)	
	Sn2	3.347(2) (1 ×)			Sn1	3.4153(8) (4 ×)	
	Sn2	3.3623(8) (2 ×)			Ca2	3.673(3) (1 ×)	
	Ni	3.4684(9) (2 ×)		Sn1	Ni	2.5544(4) (2 ×)	2.40
	Ca1	3.755(3) (1 ×)			Ni	2.6797(7) (1 ×)	1.64
	Ca3	3.919(1) (3 ×)			Sn1	3.1397(9) (1 ×)	0.88
	Ca2	3.930(2) (1 ×)					
Ca2	Sn3	3.119(1) (2 ×)		Sn2	Sn3	2.9247(7) (1 ×)	1.67
	Sn1	3.2599(7) (4 ×)					
	Ni	3.313(2) (2 ×)		Sn3	Ni	2.5880(8) (2 ×)	2.30
	Ni	3.3599(7) (4 ×)					

powder X-ray diffraction. The thermodiagrams were evaluated with the Netzsch Proteus software.^[23] Six cycles of heating to 930 °C and cooling to room temperature at a heating rate of 5 °C/min were performed. The first heating showed several endothermic peaks in the range of 820–891 °C. In subsequent cycles the peaks became less intense and no peaks were observable after the fourth cycle. Powder X-ray diffraction after the experiment revealed that Ca₂NiSn₂ peritectically decomposes to CaSn, Ca₇Sn₆ and an unknown phase, in agreement with the experiments in the resistant furnace described before. No peak in the DTA experiment can be assigned to the mC -Ca₂NiSn₂/ oP -Ca₂NiSn₂ transition.

Electronic Structure Calculations: The electronic structure calculations were performed with the linear muffin-tin orbital (LMTO) method in the atomic sphere approximation (ASA) by using the tight-binding (TB) program TB-LMTO-ASA.^[17] The exchange-correlation term was calculated within the local density approximation (LDA) and parametrized according to von Barth and Hedin.^[24] The radii of the muffin-tin and empty spheres were determined according to the method of Jepsen and Andersen.^[25] The basis set of short-range^[26] atom-centred TB-LMTOs contained s and d valence functions for Ca, s and d valence functions for Ni and s and p valence functions for Sn. Ca 4p as well as Sn 5d and 4f orbitals were included by using a down-folding technique.

The analysis of the chemical bonding was based upon partial and total DOS curves, plots of the crystal orbital Hamilton populations (COHPs),^[27] band structures with fatbands and contour line diagrams of the ELF.^[28–30] From COHP analyses, the contribution of the covalent part of a particular interaction to the total bonding energy of the crystal can be obtained. All COHP curves are presented in the following format: positive values are bonding, nega-

tive values are anti-bonding. In the fatband analysis the atomic orbital character is represented as a function of the band width.

Supporting Information (see footnote on the first page of this article): Tables of atomic displacement parameters, discussion of the electronic structure and topological analysis of the ELF, the total and partial DOS curves, the COHP and –iCOHP curves, band structures including fatbands, contour line diagrams of the ELF, isosurfaces of the ELF of oP -Ca₂NiSn₂.

- [1] S. Stegmaier, T. F. Fässler, *J. Am. Chem. Soc.* **2011**, *133*, 19758.
- [2] L. Siggelkow, V. Hlukhyy, B. Wahl, T. F. Fässler, *Eur. J. Inorg. Chem.* **2011**, 4012.
- [3] T. F. Fässler, S. Hoffmann, *Z. Kristallogr.* **1999**, *214*, 722.
- [4] R. Pöttgen, *Z. Naturforsch. B: J. Chem. Sci.* **2006**, *61*, 677.
- [5] D. A. Vennos, M. E. Badding, F. J. Disalvo, *J. Less-Common Met.* **1991**, *175*, 339.
- [6] V. Hlukhyy, F. Raif, P. Claus, T. F. Fässler, *Chem. Eur. J.* **2008**, *14*, 3737.
- [7] J. P. Jarmoljuk, L. A. Lysenko, *Dopov. Akad. Nauk Ukr. RSR Ser. A* **1978**, 376.
- [8] Y. Yamaguchi, J. Sakurai, F. Teshima, H. Kawanaka, T. Takabatake, H. Fujii, *J. Phys. Condens. Matter* **1990**, *2*, 5715.
- [9] C. B. Shoemaker, D. P. Shoemaker, *Acta Crystallogr.* **1965**, *18*, 900.
- [10] Z. M. Sun, S. O. Xia, Y. Z. Huang, U. M. Wu, J. G. Mao, *Inorg. Chem.* **2005**, *44*, 9242.
- [11] O. P. Bodak, E. I. Gladyshevskii, *Sov. Phys. Crystallogr.* **1970**, *14*, 859.
- [12] V. Hlukhyy, S. Eck, T. F. Fässler, *Inorg. Chem.* **2006**, *45*, 7408.
- [13] Z. M. Sun, D. C. Pan, X. W. Lei, J. G. Mao, *J. Solid State Chem.* **2006**, *179*, 3378.
- [14] V. Naray-Szabo, *Z. Kristallogr.* **1937**, *97*, 223.

- [15] X. W. Lei, G. H. Zhong, M. J. Li, J. G. Mao, *J. Solid State Chem.* **2008**, *181*, 2448.
- [16] M. Veith, A. Müller, L. Stahl, M. Notzel, M. Jarczyk, V. Huch, *Inorg. Chem.* **1996**, *35*, 3848.
- [17] M. v. Schilfgarde, T. A. Paxton, O. Jepsen, O. K. Andersen, G. Krier, *The Stuttgart Tight-Binding LMTO-ASA program*, v. 4.7, Max-Planck-Institut für Festkörperforschung, Stuttgart, Germany, **1998**.
- [18] L. Siggelkow, V. Hlukhyy, T. F. Fässler, *Z. Anorg. Allg. Chem.* **2010**, *636*, 1870.
- [19] *STOE, WinXPOW*, v. 2.08, STOE & Cie GmbH, Darmstadt, Germany, **2003**.
- [20] *CrysAlis RED, Scale3/ABSPACK*, v. 1.171.33.34d, Oxford Diffraction, Poland Sp. z o. o., **2009**.
- [21] G. M. Sheldrick, *SHELXS-97 – Program for the Determination of Crystal Structures*, University of Göttingen, Germany, **1997**.
- [22] G. M. Sheldrick, *SHELXL-97 – Program for Crystal Structure Refinement*, University of Göttingen, Germany, **1997**.
- [23] *Proteus – Thermal Analysis*, version 4.3.1, NETZSCH-Gerätebau GmbH, Selb, Germany, **2004**.
- [24] U. v. Barth, L. Hedin, *J. Phys. Chem. C* **1972**, *5*, 1629.
- [25] O. Jepsen, O. K. Andersen, *Z. Phys. B* **1995**, *97*, 35.
- [26] O. K. Andersen, O. Jepsen, *Phys. Rev. Lett.* **1984**, *53*, 2571.
- [27] R. Dronskowski, P. E. Blochl, *J. Phys. Chem.* **1993**, *97*, 8617.
- [28] A. D. Becke, K. E. Edgecombe, *J. Chem. Phys.* **1990**, *92*, 5397.
- [29] T. F. Fässler, *Chem. Soc. Rev.* **2003**, *32*, 80.
- [30] A. Savin, R. Nesper, S. Wengert, T. F. Fässler, *Angew. Chem. Int. Ed. Engl.* **1997**, *36*, 1809.
- [31] G. Venturini, B. Malaman, *J. Less-Common Met.* **1990**, *167*, 45.
- [32] M. P. Ruzsai, N. V. Kudryavt, *Russ. Phys. J.* **1974**, 934.

Received: November 16, 2011

Published Online: January 12, 2012

Diene Dissolution of the Heavier Alkaline Earth Metals

Olaf Michel,^[a,b] Hiroshi Kaneko,^[c] Hayato Tsurugi,^[c] Koji Yamamoto,^[c]
Karl W. Törnroos,^[b] Reiner Anwander,^{*[a]} and Kazushi Mashima^{*[c]}**Keywords:** Alkaline earth metals / Barium / Calcium / Strontium / Structure elucidation / Organometallic complexes / Arenes / Diene ligands

Alkaline and alkaline earth metals are efficiently activated in the presence of aromatic hydrocarbons ("potassium–naphthalene", "magnesium–anthracene") or (substituted) 1,3-dienes to produce well-defined organometallic complexes. In this study, mononuclear diene complexes of calcium, strontium, and barium have been synthesized by utilizing tailor-made 1,3-dienes. Complexes $[M(2,3\text{-dimethyl-1,4-ditolyl-1,3-butadiene})(\text{thf})_4]$ ($M = \text{Ca}, \text{Sr}$), $[\text{Ca}(2,3\text{-dimethyl-1,4-dinaphthyl-1,3-butadiene})(\text{thf})_4]$, and $[\text{Ba}(2,3\text{-dimethyl-1,4-}$

$\text{bis}(2,4\text{-dimethylphenyl-1,3-butadiene})(\text{thf})_4]$ were isolated and fully characterized including X-ray structure analyses. Whereas the calcium- and strontium-dienes show an approximate metallacyclo-3-pentene coordination, barium(II) as the largest nonradioactive metal(II) cation reveals metallacyclo-2,4-heptadiene bonding in the solid state. It is further shown that barium(II) can accommodate eight thf molecules as evidenced in the dicationic complex $[\text{Ba}(\text{thf})_8][\text{B}(\text{C}_6\text{F}_5)_4]_2$, obtained from the reaction of barium–diene with trityl borate.

Introduction

Direct reaction of alkaline earth metals with conjugated unsaturated hydrocarbons can give access to highly reactive organometallic compounds, as exemplified by the crystallographically authenticated $[\text{Mg}(\text{anthracene})(\text{thf})_3]$.^[1] The latter "organically solvated" magnesium has the ability to serve not only as a dinucleophile but also as a source of atomic magnesium with applications as a powerful reducing agent and in metal-based hydrogen-storage materials.^[2] The discovery in 1967 by Ramsden^[3] that magnesium also readily reacts with simple 1,3-dienes such as isoprene spurred further research activities in this field,^[4] thereby resulting in the isolation of well-defined 1:1 adducts $[\text{Mg}(\text{diene})(\text{thf})_x]$ with myrcene, 1,3-butadiene, or 2,3-dimethyl-1,3-butadiene.^[5,6] The first X-ray structural evidence of a metal–diene complex was provided in 1982 for $[\text{Mg}(s\text{-cis-PhCH=CH-CH=CHPh})(\text{thf})_3]$ featuring a 2-butene-1,4-diyl ligand with two Mg–alkyl σ bonds.^[7] Crucially, phenyl substituents at 1,4-positions considerably increased the solubility of the resulting complex in thf, at the same time counteracting

oligomerization of the diene moiety. Later, the utilization of such magnesium–diene compounds was extensively studied for diene ligand transfer/exchange reactions,^[8] the stereospecific oligomerization of isoprene,^[9] and organic transformations,^[10] for example.

The chemical understanding of the heavier alkaline earth elements has attracted much interest, true to Schlosser's statement, "The individuality of the metal involved is the most crucial parameter for orienting any fine-tuning of organometallic reactions".^[11] Accordingly, Rieke and co-workers utilized the corresponding calcium–diene compounds (via "highly reactive calcium" obtained from CaI_2 and preformed lithium biphenylide), which exhibited enhanced stereospecificity and regioselectivity in dialkylation reactions of α,ω -alkylene dihalides and dichlorosilanes.^[12] In 1994, Mashima and Nakamura et al. presented the first X-ray structure determination of 1,3-diene complexes of the heavier alkaline earth metals calcium and strontium, $[\text{M}(2,3\text{-dimethyl-1,4-diphenyl-1,3-butadiene})(\text{thf})_4]$ ($M = \text{Ca}, \text{Sr}$).^[13] Whereas the presence of two methyl groups further enhanced the solubility, simultaneously counteracting the formation of oligomeric species, the solid-state structures revealed a η^4 coordination of the *s-cis*-oriented diene ligand.^[14] The C–H coupling constants of the CH–M resonances suggested an almost tetrahedral (sp^3) hybridization, and hence a metallacyclo-3-pentene (dialkyl) rather than a η^4 -diene structure in solution, in accordance with the solid-state structure. Herein, we report on the synthesis of organo-alkaline-earth complexes of calcium, strontium, and barium by utilizing tailor-made 1,3-diene ligands, thus allowing us to isolate and crystallographically characterize the first barium–diene complex.

[a] Institut für Anorganische Chemie,
Eberhard Karls Universität Tübingen
Auf der Morgenstelle 18, 72076 Tübingen, Germany
Fax: +49-7071-29-2436
E-mail: reiner.anwander@uni-tuebingen.de

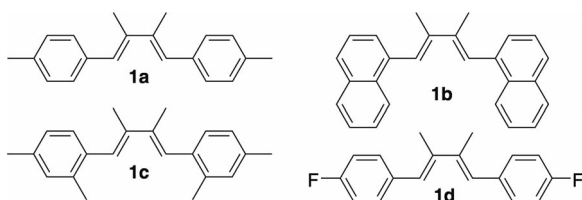
[b] Department of Chemistry, University of Bergen,
Allégaten 41, 5007 Bergen, Norway

[c] Department of Chemistry,
Graduate School of Engineering Science,
Osaka University, Toyonaka, Osaka 560-8531, Japan
Fax: +81-6-6850-6245
E-mail: mashima@chem.es.osaka-u.ac.jp

Supporting information for this article is available on the
WWW under <http://dx.doi.org/10.1002/ejic.201101342>.

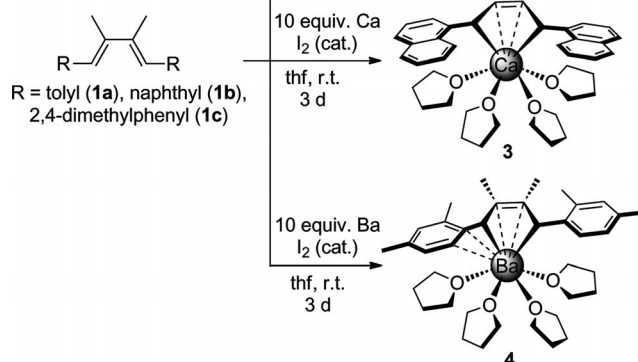
Results and Discussion

For preparing diene complexes of the heavier alkaline earth metals (Ca, Sr, Ba), we envisaged a small library of differently functionalized 1,3-butadiene ligands bearing electron-withdrawing and electron-donating substituents (Scheme 1).



Scheme 1. 1,3-Dienes under study.

Treatment of 2,3-dimethyl-1,4-ditolyl-1,3-butadiene (**1a**) with an excess amount of calcium or strontium in thf in the presence of catalytic amounts of iodine yielded a dark red solution (Scheme 2). Upon separating the clear supernatant from unreacted alkaline earth metal and concentrating the solution to a quarter of its volume, dark red single crystals of $[M(2,3\text{-dimethyl-1,4-ditolyl-1,3-butadiene})(\text{thf})_4]$ [$M = \text{Ca}$ (**2a**), Sr (**2b**)] were formed in over 60% yield at -40°C . The solid-state structures of **2a** and **2b** revealed a η^4 -coordination mode for the diene ligand and the additional coordination of four molecules of thf (Scheme 2, Figure 1). The $M\text{-C}$ distances average 2.643 \AA (**2a**) and 2.796 \AA (**2b**). The larger strontium seems to additionally interact with the phenyl substituents as suggested by close $\text{Sr-C}(\textit{ipso})$ contacts [**2b**, av. 3.270 \AA ; **2a**, $3.450(4)$ and $3.460(4)\text{ \AA}$]. This pronounced bending of the phenyl groups toward the strontium center is also evident from the torsion angles C8-C5-C2-C3 and C17-C14-C3-C2 of 139.5 and 126.7° , respectively (**2a**, 162.1 and 167.1°). The C-C bond lengths clearly evidence a charge relocation according to a butadiene \rightarrow 2-butene-1,4-diyl(metallacyclo-3-pentene) coordination shift.



Scheme 2. Synthesis of complexes **2a**, **2b**, **3**, and **4**.

^1H and ^{13}C NMR spectra recorded in $[\text{D}_8]\text{thf}$ corroborate this coordination mode by displaying $M\text{-CH}$ signals shifted considerably to higher field (**2a**: ^1H : 3.20 ppm ; ^{13}C : 70.9 ppm ; **2b**: ^1H : 3.38 ppm ; ^{13}C : 73.5 ppm) relative to proligand **1a** (^1H : 6.78 ppm ; ^{13}C : 125.0 ppm) (cf. Figures S1–S3 in the Supporting Information).

2,3-Dimethyl-1,4-dinaphthyl-1,3-butadiene (**1b**, Scheme 1) gave a dark blue diene complex with calcium, $[\text{Ca}(2,3\text{-dimethyl-1,4-dinaphthyl-1,3-butadiene})(\text{thf})_4]$ (**3**, Scheme 2). The solid-state structure of the thf-soluble bis-organocalcium compound **3** (Figure 2) shows an asymmetrically η^4 -coordinated diene ligand forming one additional close $M\text{-C}(\textit{ipso})$ contact of $3.164(3)\text{ \AA}$ with the naphthyl substituent. The chemical shifts of the $M\text{-CH}$ group (^1H : 4.53 ppm ; ^{13}C : 73.0 ppm) match the corresponding ones in **2a** and **2b**, thereby corroborating the partial σ -bond character of the $M\text{-C}$ bonds.

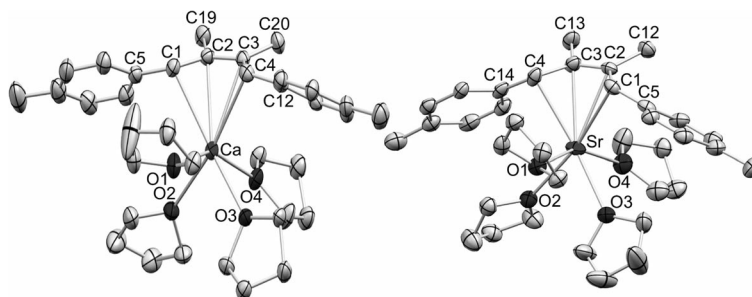


Figure 1. Molecular structures of compound **2a** (left) and **2b** (right; one molecule of cocrystallized thf is not shown) with 50% probability ellipsoids; H atoms are omitted for clarity. Selected bond lengths [\AA] and angles [$^\circ$]: **2a**: Ca-C1 $2.598(3)$, Ca-C2 $2.692(3)$, Ca-C3 $2.696(3)$, Ca-C4 $2.586(3)$, $\text{Ca}\cdots\text{C5}$ $3.450(4)$, $\text{Ca}\cdots\text{C12}$ $3.460(4)$, C1-C2 $1.461(5)$, C2-C3 $1.393(5)$, C3-C4 $1.479(5)$; C1-Ca-C2 $32.0(1)$, C1-Ca-C3 $56.0(1)$, C1-Ca-C4 $68.0(1)$, C1-C2-C3 $121.2(3)$, C1-C2-C19 $117.9(3)$, C4-C3-C2 $120.4(3)$, C4-C3-C20 $119.1(3)$. **2b**: Sr-C1 $2.704(3)$, Sr-C2 $2.871(3)$, Sr-C3 $2.869(3)$, Sr-C4 $2.738(3)$, $\text{Sr}\cdots\text{C5}$ $3.287(4)$, $\text{Sr}\cdots\text{C14}$ $3.252(4)$, C1-C2 $1.456(4)$, C2-C3 $1.389(4)$, C3-C4 $1.476(4)$; C1-Sr-C2 $30.08(8)$, C1-Sr-C3 $52.96(9)$, C1-Sr-C4 $65.7(1)$, C1-C2-C3 $122.1(3)$, C1-C2-C12 $118.9(3)$, C4-C3-C2 $122.3(2)$, C4-C3-C13 $119.2(3)$.

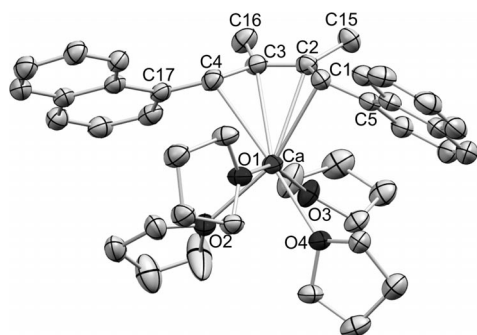


Figure 2. Molecular structure of compound **3** with 50% probability ellipsoids; H atoms are omitted for clarity. CocrySTALLIZED thf (3 molecules) are not shown. Selected bond lengths [Å] and angles [°]: Ca–C1 2.607(3), Ca–C2 2.804(2), Ca–C3 2.847(3), Ca–C4 2.687(3), Ca–C5 3.164(3), Ca–C17 3.496(3), C1–C2 1.479(4), C2–C3 1.383(4), C3–C4 1.479(4); C1–Ca–C2 31.45(9), C1–Ca–C3 54.63(9), C1–Ca–C4 67.97(10), C1–C2–C3 122.7(2), C1–C2–C15 117.5(2), C4–C3–C2 121.7(2), C4–C3–C16 118.8(2).

Although the formation of barium–diene complexes from barium metal and proligands **1a** and **1b** was indicated by a dark red solution and low-intensity signals in the NMR spectra (high amount of unreacted proligand), isolable complexes were not obtained.^[15] In contrast and luckily, the 2,3-dimethyl-1,4-bis(2,4-dimethylphenyl)-1,3-butadiene proligand **1c** afforded an isolable barium–diene complex. According to Scheme 2, treatment of **1c** with an excess amount of barium metal in thf with catalytic amounts of iodine gave a dark purple solution, from which dark purple single crystals of {Ba[2,3-dimethyl-1,4-bis(2,4-dimethylphenyl)-1,3-butadiene](thf)₄} (**4**) could be harvested in moderate yield.

The solid-state structure of barium complex **4** revealed an unprecedented η^6 coordination of the unsaturated hydrocarbon (Figure 3), arising from an η^4 coordination of the diene unit (C1–C4) and an η^2 coordination of the *ipso*-carbon (C7) and α -carbon (C8) atoms of the xylyl moiety. The Ba–C bond lengths range from 2.937(2) to 3.137(2) Å, being similar to the Ba–C(alkyl) bond lengths in, for example, [{Ba(AlEt₄)₂]_n] (av. Ba–CH₂ bond length 3.125 Å), or [{Ba(GaEt₄)₂(tol)]₂] [Ba–CH₂ bond lengths ranging from 2.934(5) to 3.158(5) Å].^[16] The NMR spectra displaying the

expected shift of the Ba–CH signals to higher field (**4**: ¹H: 3.83 ppm; ¹³C: 77.7 ppm; **1c**: ¹H: 6.77 ppm; ¹³C: 125.7 ppm) are in accordance with the formation of a metallacyclo-2,4-heptadiene.

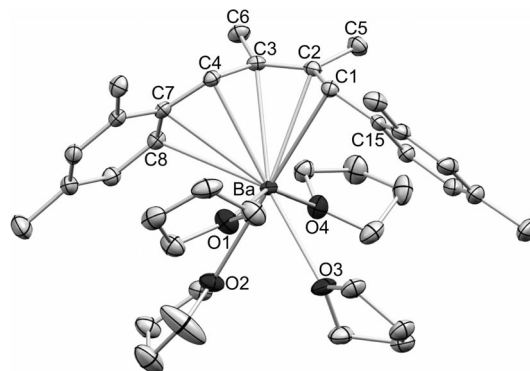


Figure 3. Molecular structure of compound **4** with 50% probability ellipsoids; H atoms are omitted for clarity. Selected bond lengths [Å] and angles [°]: Ba–C1 2.942(2), Ba–C2 3.022(2), Ba–C3 3.026(2), Ba–C4 2.937(2), Ba–C7 3.110(2), Ba–C8 3.137(2), Ba–C15 3.279(2), C1–C2 1.462(2), C2–C3 1.381(2), C3–C4 1.467(2); C1–Ba–C2 28.34(5), C1–Ba–C3 49.03(5), C1–Ba–C4 59.06(5), C1–Ba–C7 85.73(5), C1–Ba–C8 105.56(5), C1–C2–C3 121.2(2), C1–C2–C5 119.0(2), C4–C3–C2 121.2(2), C4–C3–C6 118.0(2).

Not surprisingly, phenyl groups carrying substituents with a strong inductive effect imply an unfavorable electronic environment: any significant activation of calcium, strontium, and barium did not occur with 2,3-dimethyl-1,4-bis(*p*-fluorophenyl)-1,3-butadiene (**1d**, Scheme 1), which means that only the proligand could be recovered from the reaction mixtures.

Preliminary reactivity studies of compound **4** were carried out toward trityl tetrakis(pentafluorophenyl)borate (trityl borate). The equimolar reaction did not yield the envisaged single-cationized abstraction product [Ba{CH(R)–C(Me)=C(Me)CH(R)–CPh₃}] [B(C₆F₅)₄] (R = 2,4-dimethylphenyl), but the ion-separated dicationic complex {[Ba(thf)₈][B(C₆F₅)₄]₂} (**5**) (Figure 4). Compound **5** represents the first structurally characterized octa-thf metal cation, complementing the series [M(thf)₆]²⁺ (e.g., {[Mg(thf)₆][AlMe₄]₂}^[17] and {[Ca(thf)₆][BPh₄]₂}^[18]) and [M(thf)₇]²⁺ (e.g., {[M(thf)₇]

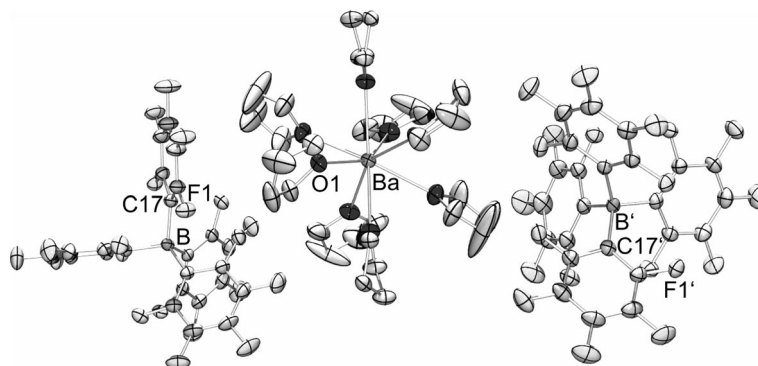


Figure 4. Molecular structure of compound **5** (two molecules of cocrySTALLIZED thf are not shown) with 50% probability ellipsoids; H atoms are omitted for clarity. Selected bond lengths [Å]: Ba–O1 2.765(2), B–C17 1.654(3).

[BPh₄]₂) (M = Sm, Sr)^[19] and {[Sm(thf)₇][Zn₄(μ₂-SePh)₆(SePh)₄]}.^[20] The barium center in complex **5** adopts a square antiprismatic coordination geometry.

Furthermore, protonolytic ligand exchange was evidenced by treating compound **4** with silanol HOSi(O*t*Bu)₃ (2 equiv.). A rapid reaction was indicated by an instantaneous color change from purple to slightly yellowish. After filtration and removal of the solvent, the yellow solution gave an oily residue, which was analyzed by NMR spectroscopy. The signals could be assigned to homoleptic {Ba[OSi(O*t*Bu)₃]₂} and the protonated 2-butene-1,4-diyl ligand R'CH₂-C(Me)=C(Me)-CH₂R' [**6**, R' = 2,4-dimethylphenyl; ¹³C: 37.1 ppm (CH₂); see also Figure S4 in the Supporting Information].

Conclusion

Tailor-made substituted 1,3-butadienes react with the heavier alkaline earth metals including barium to produce thf-soluble metal–diene complexes. The large barium(II) metal center accommodates the unsaturated hydrocarbyl ligand in an unprecedented η⁶ coordination. Preliminary investigations of the reactivity behavior of the barium–diene complex revealed the feasibility of alkyl abstraction and alkyl protonolysis protocols, clearly demonstrating that diene complexes of the heavier alkaline earth metals are potential reagents for providing a highly reactive mononuclear metal source.

Experimental Section

General Procedures: All operations were performed with rigorous exclusion of air and water, using standard Schlenk, high-vacuum, and glovebox techniques (MBraun MBLab; <0.1 ppm O₂, <0.1 ppm H₂O). Hexane, toluene, and thf were purified by using Grubbs columns (MBraun SPS, solvent purification system) and stored in a glovebox. [D₆]Benzene and [D₈]thf were obtained from Aldrich, degassed, dried with Na for 24 h, and filtered. HOSi(O*t*Bu)₃ and [Ph₃C][B(C₆F₅)₄] were purchased from Aldrich and used as received. The NMR spectra of air- and moisture-sensitive compounds were recorded by using J. Young valve NMR spectroscopy tubes at 25 °C on a Bruker-BIOSPIN-AV500 (5 mm BBO) instrument, and a Bruker-AVIII-400 (5 mm QNP) instrument. ¹H and ¹³C shifts were referenced to internal solvent resonances and reported in parts per million relative to TMS. Elemental analyses were performed on an Elementar Vario MICRO. Reliable elemental analyses were difficult to obtain for complexes **2a**, **2b**, and **3**. This is a well-known problem in alkaline earth metal chemistry.^[21] IR spectra were recorded on a Thermo Scientific Nicolet 6700 FTIR spectrometer using a DRIFT cell equipped with KBr windows, for which the samples were mixed with KBr powder (80% in weight), or on a JascoFT/IR-230 spectrometer using Nujol mulls sandwiched between NaCl plates. The spectra were recorded in 256 scans (DRIFT) or 32 scans (NaCl plates) at ambient temperature in the range of 4000 to 400 cm^{−1} with a spectral resolution of 2 cm^{−1}. High-resolution mass spectra were recorded on a JEOL JMS-700 instrument and EI mass spectra were recorded on a Finnigan TSQ 70 mass spectrometer.

General Procedure for the Synthesis of Substituted 1,3-Butadienes: Proligands **1a**, **1b**, **1c**, and **1d** were synthesized according to the

literature procedure described for 2,3-dimethyl-1,4-diphenyl-1,3-butadiene.^[22] Accordingly, a 1 L Schlenk flask was charged with Mg chips and Et₂O (200 mL). The mixture was cooled to 0 °C and benzyl chloride (diluted with Et₂O, 100 mL) was added dropwise under vigorous stirring. The Grignard solution was warmed to ambient temperature, stirred for another 2 h, and the crude reaction mixture was cannulated into a round-bottom flask. The solution was cooled to −20 °C and a solution of 2,3-dibutanedione in Et₂O (30 mL) was added slowly. The reaction mixture was allowed to stir for 24 h at ambient temperature. A saturated NH₄Cl solution (150 mL) was added slowly and the organic phase was dried with Na₂SO₄, filtered, and the solvent was removed under reduced pressure. The 2,3-dimethyl-1,4-diaryl-2,3-ol was dissolved in acetic anhydride and acetyl chloride and stirred under reflux for 3 h. Cooling to 0 °C afforded white crystals of the substituted 1,3-butadienes.

Diene 1a: Following the procedure described above, Mg (5.00 g, 0.205 mol), 4-methylbenzyl chloride (20 g, 0.14 mol), 2,3-dibutanedione (3.4 mL, 3.37 g, 0.039 mol), acetic anhydride (13.86 mL, 15.0 g, 0.147 mol), and acetyl chloride (13.59 mL, 15.0 g, 0.064 mol) yielded **1a** (70%, 7.34 g, 0.028 mol). IR (KBr): $\tilde{\nu}$ = 3080 (m), 3047 (s), 3021 (s), 2962 (s), 2916 (s), 2859 (s), 2731 (vw), 1920 (m), 1803 (w), 1735 (w), 1648 (m), 1609 (m), 1562 (m), 1506 (vs), 1438 (s), 1400 (s), 1367 (s), 1182 (m), 1112 (s), 1093 (m), 1032 (s), 941 (s), 878 (s), 866 (s), 845 (s), 817 (s), 768 (m), 707 (m), 630 (w), 552 (w), 510 (s), 407 (m) cm^{−1}. ¹H NMR (500 MHz, [D₈]thf, 25 °C): δ = 7.20 [m, 8 H, CH(Ar)], 6.78 (s, 2 H, CH), 2.36 (s, 6 H, CH₃), 2.14 (s, 6 H, CH₃) ppm. ¹³C NMR (125 MHz, CDCl₃, 25 °C): δ = 136.4 [C(Ar)], 133.9 [C(Ar)], 133.8 [C(Ar)], 127.2 [C(Ar)], 126.6 [C(CH₃)], 125.0 (CH), 18.4 (CH₃), 13.1 (CH₃) ppm. HRMS (EI): *m/z* calcd. for C₂₀H₂₂ 262.1722; found 262.1697.

Diene 1b: Following the procedure described above, Mg (3.50 g, 0.144 mol), 1-(chloromethyl)naphthalene (23.6 g, 0.133 mol), 2,3-dibutanedione (3.1 mL, 3.07 g, 0.036 mol), acetic anhydride (13.86 mL, 15.0 g, 0.147 mol), and acetyl chloride (13.59 mL, 15.0 g, 0.191 mol) yielded **1b** (54%, 6.49 g, 0.019 mol). IR (KBr): $\tilde{\nu}$ = 3054 (s), 3000 (s), 2941 (s), 2869 (m), 1927 (w), 1829 (w), 1791 (w), 1737 (m), 1712 (m), 1592 (s), 1506 (vs), 1454 (m), 1386 (s), 1269 (m), 1215 (m), 1142 (w), 1016 (m), 979 (vw), 782 (vs), 699 (vw), 622 (vw), 569 (w), 481 (w), 428 (m) cm^{−1}. ¹H NMR (500 MHz, CDCl₃, 25 °C): δ = 8.18–7.41 [m, 14 H, CH(Ar)], 3.56 (s, 2 H, CH), 2.16 (s, 6 H, CH₃) ppm. ¹³C NMR (100 MHz, [D₈]thf, 25 °C): δ = 139.8 [C(CH₃)], 136.0 [C(Ar)], 134.0 [C(Ar)], 132.3 [C(Ar)], 128.3 [C(Ar)], 127.0 [C(Ar)], 126.7 [C(Ar)], 125.6 [C(Ar)], 125.5 [C(Ar)], 125.4 [C(Ar)], 125.0 [C(Ar)], 15.6 (CH₃) ppm. HRMS (EI): *m/z* calcd. for C₂₆H₂₂ 334.1722; found 334.1707.

Diene 1c: Following the procedure described above, Mg (3.33 g, 0.137 mol), 2,4-dimethylbenzyl chloride (10 mL, 10.6 g, 0.069 mol), 2,3-dibutanedione (1.79 mL, 1.77 g, 0.021 mol), acetic anhydride (9.24 mL, 10.0 g, 0.098 mol), and acetyl chloride (9.06 mL, 10.0 g, 0.127 mol) yielded **1c** (63%, 3.83 g, 0.013 mol). IR (KBr): $\tilde{\nu}$ = 3002 (s), 2962 (m), 2941 (s), 2917 (vs), 2728 (vw), 1922 (w), 1800 (w), 1737 (w), 1714 (w), 1604 (w), 1489 (vs), 1422 (s), 1370 (m), 1246 (w), 1206 (w), 1161 (w), 1086 (m), 1037 (m), 1000 (w), 941 (w), 866 (s), 821 (m), 815 (m), 777 (vw), 637 (w), 590 (w), 564 (m), 536 (m), 466 (m), 442 (w) cm^{−1}. ¹H NMR (400 MHz, [D₈]thf, 25 °C): δ = 7.03 [m, 6 H, CH(Ar)], 6.77 (s, 2 H, CH), 2.32 (s, 6 H, CH₃), 2.25 (s, 6 H, CH₃), 2.02 (s, 6 H, CH₃) ppm. ¹³C NMR (100 MHz, [D₈]thf, 25 °C): δ = 137.9 [C(Ar)], 136.1 [C(Ar)], 136.0 [C(Ar)], 134.9 [C(Ar)], 130.3 [C(Ar)], 129.2 [C(Ar)], 126.0 [C(CH₃)], 125.7 (CH), 20.3 (CH₃), 19.1 (CH₃), 14.8 (CH₃) ppm. MASS (EI): *m/z* calcd. for C₂₂H₂₆ 290.2; found 290.3.

Diene 1d: Following the procedure described above, Mg (2.25 g, 0.093 mol), 4-fluorobenzyl chloride (10 mL, 12.17 g, 0.084 mol), 2,3-dibutanedione (2.43 mL, 2.41 g, 0.028 mol), acetic anhydride (9.24 mL, 10.0 g, 0.098 mol), and acetyl chloride (9.06 mL, 10.0 g, 0.127 mol) yielded **1d** (60%, 4.54 g, 0.017 mol). ^1H NMR (500 MHz, CDCl_3 , 25 °C): δ = 7.30–7.27 [m, 4 H, $\text{CH}(\text{Ar})$], 7.09–7.05 [m, 4 H, $\text{CH}(\text{Ar})$], 6.75 (s, 2 H, CH), 2.11 (s, 6 H, CH_3) ppm. ^{13}C NMR (125 MHz, CDCl_3 , 25 °C): δ = 162.7 [$\text{C}(\text{Ar})$], 134.6 [$\text{C}(\text{Ar})$], 130.9 [$\text{C}(\text{CH}_3)$], 126.2 [$\text{C}(\text{Ar})$], 115.0 (CH), 15.6 (CH_3) ppm. ^{19}F NMR (376 MHz, CDCl_3 , 25 °C): δ = –115.9 ppm.

Complex 2a: Diene **1a** (260 mg, 1.0 mmol) and Ca metal (600 mg, 14.14 mmol) were mixed in thf (10 mL) and catalytic amounts of iodine (0.05 mmol) were added. The reaction mixture was allowed to stir for 3 d at ambient temperature. After centrifugation, the supernatant dark red solution was filtered and concentrated under reduced pressure. Dark red crystals of **2a** were obtained at –35 °C (68%, 400 mg, 0.68 mmol) suitable for X-ray diffraction analysis. IR (Nujol): $\tilde{\nu}$ = 2723 (vw), 1596 (s), 1421 (m), 1351 (m), 1285 (s), 1193 (w), 1170 (vs), 1107 (vw), 1030 (vs), 994 (m), 925 (w), 879 (m), 804 (m), 777 (w), 722 (vw), 703 (vw), 654 (w), 634 (w) cm^{-1} . ^1H NMR (400 MHz, $[\text{D}_8]\text{thf}$, 25 °C): δ = 6.39 [d, $J_{\text{H,H}}$ = 8.49 Hz, 4 H, $\text{CH}(\text{Ar})$], 6.10 [d, $J_{\text{H,H}}$ = 7.47 Hz, 4 H, $\text{CH}(\text{Ar})$], 3.65 (m, 16 H, thf), 3.20 (br., 2 H, CH), 2.00 (s, 6 H, CH_3), 1.96 (s, 6 H, CH_3), 1.81 (m, 16 H, thf) ppm. ^{13}C NMR (100 MHz, $[\text{D}_8]\text{thf}$, 25 °C): δ = 138.9 [$\text{C}(\text{CH}_3)$], 136.2 [$\text{C}(\text{Ar})$], 128.2 [$\text{C}(\text{Ar})$], 116.9 [$\text{C}(\text{Ar})$], 113.00 [$\text{C}(\text{Ar})$], 70.9 (CH), 67.2–65.9 (thf), 25.4–23.9 (thf), 19.8 (CH_3), 15.6 (CH_3) ppm.

Complex 2b: Diene **1a** (100 mg, 0.38 mmol) and Sr metal (800 mg, 9.13 mmol) were mixed in thf (10 mL) and catalytic amounts of iodine (0.05 mmol) were added. The reaction mixture was allowed to stir for 3 d at ambient temperature. After centrifugation, the supernatant dark red solution was filtered and concentrated under reduced pressure. Dark red crystals of **2b** were obtained at –35 °C (45%, 110 mg, 0.17 mmol) suitable for X-ray diffraction analysis. IR (Nujol): $\tilde{\nu}$ = 2724 (vw), 1597 (m), 1377 (s), 1297 (m), 1169 (m), 1104 (vw), 1075 (vw), 1034 (m), 986 (w), 918 (vw), 878 (w), 799 (w), 776 (w), 722 (w), 664 (vw) cm^{-1} . ^1H NMR (500 MHz, $[\text{D}_8]\text{thf}$, 25 °C): δ = 6.20–6.18 [m, 4 H $\text{CH}(\text{Ar})$], 5.81 [d, $J_{\text{H,H}}$ = 8.17 Hz, 4 H, $\text{CH}(\text{Ar})$], 3.52–3.47 (m, 16 H, thf), 3.38 (br., 2 H, CH), 1.81 (s, 6 H, CH_3), 1.76 (s, 6 H, CH_3), 1.68–1.62 (m, 16 H, thf) ppm. ^{13}C

NMR (125 MHz, $[\text{D}_8]\text{thf}$, 25 °C): δ = 143.4 [$\text{C}(\text{CH}_3)$], 127.2 [$\text{C}(\text{Ar})$], 126.4 [$\text{C}(\text{Ar})$], 126.0 [$\text{C}(\text{Ar})$], 111.3 [$\text{C}(\text{Ar})$], 106.3 [$\text{C}(\text{Ar})$], 73.5 (CH), 65.1–64.4 (thf), 23.3–22.1 (thf), 17.6 (CH_3) ppm.

Complex 3: Diene **1b** (100 mg, 0.33 mmol) and Ca metal (180 mg, 4.49 mmol) were mixed in thf (10 mL) and catalytic amounts of iodine (0.05 mmol) were added. The reaction mixture was allowed to stir for 3 d at ambient temperature. After centrifugation, the supernatant dark red solution was filtered and concentrated under reduced pressure. Dark red crystals of **3** were obtained at –35 °C (55%, 120 mg, 0.182 mmol) suitable for X-ray diffraction analysis. ^1H NMR (500 MHz, $[\text{D}_8]\text{thf}$, 25 °C): δ = 8.01 [d, $J_{\text{H,H}}$ = 8.31 Hz, 2 H, $\text{CH}(\text{Ar})$], 7.20 [d, $J_{\text{H,H}}$ = 8.01 Hz, 2 H, $\text{CH}(\text{Ar})$], 7.01 [t, $J_{\text{H,H}}$ = 7.40 Hz, 2 H, $\text{CH}(\text{Ar})$], 6.87–6.80 [m, 4 H, $\text{CH}(\text{Ar})$], 6.11 [d, $J_{\text{H,H}}$ = 7.66 Hz, 2 H, $\text{CH}(\text{Ar})$], 5.84 [d, $J_{\text{H,H}}$ = 8.02 Hz, 2 H, $\text{CH}(\text{Ar})$], 4.53 (br., 2 H, CH), 3.66–3.60 (m, 16 H, thf), 2.12 (s, 6 H, CH_3), 1.82–1.75 (m, 16 H, thf) ppm. ^{13}C NMR (125 MHz, $[\text{D}_8]\text{thf}$, 25 °C): δ = 140.7 [$\text{C}(\text{CH}_3)$], 135.7 [$\text{C}(\text{Ar})$], 126.8 [$\text{C}(\text{Ar})$], 125.7 [$\text{C}(\text{Ar})$], 124.5 [$\text{C}(\text{Ar})$], 122.8 [$\text{C}(\text{Ar})$], 122.0 [$\text{C}(\text{Ar})$], 120.4 [$\text{C}(\text{Ar})$], 117.8 [$\text{C}(\text{Ar})$], 73.0 (CH), 65.5–64.1 (thf), 23.7–22.1 (thf), 20.5 (CH_3) ppm.

Complex 4: Diene **1c** (150 mg, 0.57 mmol) and Ba metal (5 equiv., 393 mg, 2.86 mmol) were mixed in thf (10 mL) and catalytic amounts of iodine (0.05 mmol) were added. The reaction mixture was allowed to stir for 3 d at ambient temperature. After centrifugation, the supernatant solution was filtered and concentrated. Dark purple crystals of **4** (60%, 0.34 mmol) suitable for X-ray diffraction analysis were obtained at –40 °C. IR (KBr): $\tilde{\nu}$ = 2962 (s), 2918 (s), 2871 (s), 2718 (vw), 1597 (s), 1470 (vs), 1367 (m), 1285 (s), 1236 (m), 1166 (w), 1032 (m), 875 (m), 815 (m), 721 (m), 613 (m), 541 (m) cm^{-1} . ^1H NMR (400 MHz, $[\text{D}_8]\text{thf}$, 25 °C): δ = 7.19–6.94 [m, 3 H, $\text{CH}(\text{Ar})$], 6.45–6.40 [m, 3 H, $\text{CH}(\text{Ar})$], 3.83 (br., 2 H, CH), 3.67–3.61 (m, thf), 2.01 (s, 9 H, CH_3), 1.91 (s, 9 H, CH_3), 1.82–1.76 (m, thf) ppm. ^{13}C NMR (100 MHz, $[\text{D}_8]\text{thf}$, 25 °C): δ = 141.4 [$\text{C}(\text{CH}_3)$], 130.7 [$\text{C}(\text{Ar})$], 126.3 [$\text{C}(\text{Ar})$], 124.1 [$\text{C}(\text{Ar})$], 120.0 [$\text{C}(\text{Ar})$], 77.7 (CH), 67.2–65.9 (thf), 25.4–23.9 (thf), 21.4 (CH_3), 19.6 (CH_3), 17.9 (CH_3) ppm. $\text{C}_{38}\text{H}_{58}\text{BaO}_4$ (716.20): calcd. C 63.73, H 8.16; found C 64.15, H 7.53.

Complex 5: Compound **4** (50 mg, 0.07 mmol) was suspended in toluene (5 mL) and $[\text{Ph}_3\text{C}][\text{B}(\text{C}_6\text{F}_5)_4]$ (67 mg, 0.07 mmol) was added. The mixture turned bright yellow and a few drops of thf were

Table 1. Crystallographic data for complexes **2a**, **2b**, **3**, **4**, and **5**.

	2a	2b	3	4	5
Formula	$\text{C}_{36}\text{H}_{54}\text{CaO}_4$	$\text{C}_{40}\text{H}_{62}\text{O}_5\text{Sr}$	$\text{C}_{54}\text{H}_{78}\text{CaO}_7$	$\text{C}_{38}\text{H}_{58}\text{BaO}_4$	$\text{C}_{88}\text{H}_{80}\text{B}_2\text{BaF}_{40}\text{O}_{10}$
M_r	590.87	710.55	879.24	716.17	2216.47
Crystal system	monoclinic	monoclinic	monoclinic	monoclinic	monoclinic
Space group	$P2_1/n$	$P2_1/c$	$P2_1/n$	$P2_1/n$	$C2/c$
a [Å]	8.491(4)	17.203(9)	12.855(7)	9.6540(3)	19.6571(9)
b [Å]	26.944(12)	8.916(5)	26.281(14)	29.4712(10)	16.7434(8)
c [Å]	14.794(7)	25.134(14)	14.819(8)	12.9968(4)	27.8161(13)
α [°]	90.00	90.00	90.00	90.00	90
β [°]	95.513(6)	99.239(5)	100.667(6)	105.1410(10)	96.9791(18)
γ [°]	90.00	90.00	90.00	90.00	90
V [Å ³]	3369(3)	3805(4)	4920(5)	3569(2)	9087.2(7)
Z	4	4	4	4	4
$F(000)$	1288	1520	1528	1496	4456
T [K]	113	113.1	113(2)	123(2)	113.1(2)
$\rho_{\text{calcd.}}$ [g cm ^{–3}]	1.165	1.240	1.187	1.333	1.620
μ [mm ^{–1}]	0.221	1.455	0.178	1.149	0.577
$R_1(\text{obsd.})^{[a]}$	0.0860	0.0622	0.0804	0.0273	0.0476
$wR_2(\text{all})^{[b]}$	0.2125	0.1747	0.2420	0.0641	0.1330
$S^{[c]}$	1.033	1.064	1.071	1.031	0.917

[a] $R_1 = \Sigma(|F_o| - |F_c|)/\Sigma|F_o|$, $F_o > 4\sigma(F_o)$. [b] $wR_2 = \{\Sigma[w(F_o^2 - F_c^2)^2]/\Sigma[w(F_o^2)^2]\}^{1/2}$. [c] $S = [\Sigma w(F_o^2 - F_c^2)^2/(n_o - n_p)]^{1/2}$.

added. The clear solution was filtered and concentrated under reduced pressure. Cooling to -35°C afforded crystals of **5** in moderate yield (60%, 0.02 mmol). IR (Nujol): $\tilde{\nu}$ = 1644 (vw), 1513 (w), 1377 (s), 1276 (vw), 1086 (m), 1033 (w), 980 (m), 873 (vw), 774 (w), 756 (w), 725 (w), 699 (w), 683 (vw), 661 (vw), 605 (vw), 574 (vw) cm^{-1} . ^{13}C NMR (125 MHz, $[\text{D}_8]\text{thf}$, 25°C): δ = 127.4 (BPh), 126.1 (BPh), 124.1 (BPh) ppm. ^{19}F NMR (376 MHz, $[\text{D}_8]\text{thf}$, 25°C): δ = -132.8 , -164.3 , -168.9 ppm. $\text{C}_{80}\text{H}_{64}\text{B}_2\text{BaF}_{40}\text{O}_8$ (2072.25): calcd. C 46.37, H 3.11; found C 46.77, H 3.19.

Crystallographic Data Collection and Refinement: Crystals of **2a**, **2b**, **3**, **4**, and **5** were grown by standard techniques from saturated solutions using $\text{thf}/-35^{\circ}\text{C}$ (**2a**, **2b**, **3**, **4**) and toluene/ $\text{thf}/-35^{\circ}\text{C}$ (**5**). Suitable single crystals for X-ray structure analyses were selected in a glovebox and coated with Paratone-N (Hampton Research) and fixed on a glass fiber. X-ray data for compounds **2a**, **2b**, **3**, and **5** were collected on a Rigaku Mercury CCD system. Data collection for **4** was done on a Bruker SMART 2 K CCD diffractometer using graphite-monochromated $\text{Mo-K}\alpha$ radiation (λ = 0.71073 \AA) performing 182° ω scans in four orthogonal ϕ positions. Raw data were collected using program SMART,^[23] and integrated and reduced with program SAINT.^[24] Corrections for absorption effects were applied with SHELXTL and/or SADABS.^[25] The structures were solved by direct methods and refined with standard difference Fourier techniques. All plots were generated using the program ORTEP-3.^[26] Further details of the refinement and crystallographic data are listed in Table 1.

CCDC-837559 (for **2a**), -837560 (for **2b**), -837561 (for **3**), -837562 (for **4**), and -837563 (for **5**) contain the supplementary crystallographic data for this paper. These data can be obtained free of charge from The Cambridge Crystallographic Data Centre via www.ccdc.cam.ac.uk/data_request/cif.

Supporting Information (see footnote on the first page of this article): NMR spectra of compounds **1a**, **2a**, $\{\text{Ba}[\text{OSi}(\text{O}t\text{Bu})_3]_2\}$, and **6**.

Acknowledgments

We thank the Norwegian Research Council (project number 182547/I30) and the Global-COE Osaka (short-term internship) for financial support.

- [1] a) B. Bogdanović, N. Janke, C. Krüger, R. Mynott, K. Schlichte, U. Westeppe, *Angew. Chem.* **1985**, *97*, 972–974; *Angew. Chem. Int. Ed. Engl.* **1985**, *24*, 960–961; b) L. M. Engelhardt, S. Harvey, C. L. Raston, A. H. White, *J. Organomet. Chem.* **1988**, *341*, 39–51.
- [2] a) B. Bogdanović, *Angew. Chem.* **1985**, *97*, 253–264; *Angew. Chem. Int. Ed. Engl.* **1985**, *24*, 262–273; b) B. Bogdanović, S. Liao, M. Schwickardi, P. Sikorsky, B. Spliethoff, *Angew. Chem.* **1980**, *92*, 845–846; *Angew. Chem. Int. Ed. Engl.* **1980**, *19*, 817–819; c) H. Bönnemann, B. Bogdanović, R. Brinkmann, D.-W. He, B. Spliethoff, *Angew. Chem.* **1983**, *95*, 749–750; *Angew. Chem. Int. Ed. Engl.* **1983**, *22*, 728.
- [3] H. E. Ramsden, US-Pat. 3354190, **1967**.
- [4] a) M. Yang, K. Yamamoto, N. Otake, M. Ando, K. Takase, *Tetrahedron Lett.* **1970**, *11*, 3843–3846; b) M. Yang, M. Ando, K. Takase, *Tetrahedron Lett.* **1971**, *12*, 3529–3532; c) Y. Nakano, K. Natsukawa, H. Yasuda, H. Tani, *Tetrahedron Lett.* **1972**, *13*, 2833–2836.
- [5] For a review, see: A. Nakamura, K. Mashima, *J. Organomet. Chem.* **2004**, *689*, 4552–4563.
- [6] a) S. Akutagawa, S. Otsuka, *J. Am. Chem. Soc.* **1976**, *98*, 7420–7421; b) K. Fujita, Y. Ohnuma, H. Yasuda, H. Tani, *J. Organomet. Chem.* **1976**, *113*, 201–213; c) H. Yasuda, Y. Kajihara, K. Mashima, K. Nagasuna, K. Lee, A. Nakamura, *Organometallics* **1982**, *1*, 388–396.
- [7] Y. Kai, N. Kanehisa, K. Miki, N. Kasai, K. Mashima, H. Yasuda, A. Nakamura, *Chem. Lett.* **1982**, *11*, 1277–1280.
- [8] For examples, see: a) A. Scholz, A. Smola, J. Scholz, J. Loebel, H. Schuman, K.-H. Thiele, *Angew. Chem.* **1991**, *103*, 444–445; *Angew. Chem. Int. Ed. Engl.* **1991**, *30*, 435–436; b) K. Mashima, Y. Matsuo, H. Fukumoto, K. Tani, H. Yasuda, A. Nakamura, *J. Organomet. Chem.* **1997**, *545–546*, 549–552; c) G. Erker, T. Mühlenbernd, R. Benn, A. Ruffinška, *Organometallics* **1986**, *5*, 402–404; d) G. Erker, T. Mühlenbernd, A. Ruffinška, R. Benn, *Chem. Ber.* **1987**, *120*, 507–519.
- [9] For examples, see: a) H. Yasuda, Y. Nakano, K. Natsukawa, H. Tani, *Macromolecules* **1978**, *11*, 586–592; b) H. Lehmkuhl, J. Čulikovic, H. Nehl, *Justus Liebigs Ann. Chem.* **1973**, 666–691.
- [10] For examples, see: a) R. D. Rieke, *Science* **1989**, *246*, 1260–1264; b) H. Xiong, R. D. Rieke, *J. Org. Chem.* **1989**, *54*, 3247–3249; c) H. Xiong, R. D. Rieke, *Tetrahedron Lett.* **1991**, *32*, 5269–5272; d) R. D. Rieke, H. Xiong, *J. Org. Chem.* **1991**, *56*, 3109–3118; e) H. Xiong, R. D. Rieke, *J. Am. Chem. Soc.* **1992**, *114*, 4415–4417; f) M. S. Sell, H. Xiong, R. D. Rieke, *Tetrahedron Lett.* **1993**, *34*, 6011–6012.
- [11] *Organometallics in Synthesis. A Manual* (Ed.: M. Schlosser), Wiley, Chichester, U.K., **1994**.
- [12] T.-C. Wu, H. Xiong, R. D. Rieke, *J. Org. Chem.* **1990**, *55*, 5045–5051.
- [13] K. Mashima, H. Sugiyama, N. Kanehisa, Y. Kai, H. Yasuda, A. Nakamura, *J. Am. Chem. Soc.* **1994**, *116*, 6977–6978.
- [14] For a review on bonding features of metal–diene complexes, see: H. Yasuda, K. Tatsumi, A. Nakamura, *Acc. Chem. Res.* **1985**, *18*, 120–126.
- [15] The 1,3-dienes under study did not produce any isolable complexes with ytterbium or samarium.
- [16] O. Michel, K. W. Törnroos, C. Maichle-Mössmer, R. Anwender, *Chem. Eur. J.* **2011**, *17*, 4964–4967.
- [17] O. Michel, C. Meermann, K. W. Törnroos, R. Anwender, *Organometallics* **2009**, *28*, 4783–4790.
- [18] S. Harder, S. Feil, T. Repo, *Chem. Eur. J.* **2002**, *8*, 1991–1999.
- [19] a) W. J. Evans, M. A. Johnston, M. A. Greci, T. S. Gummshamer, J. W. Ziller, *Polyhedron* **2003**, *22*, 119–126; b) J. Langer, S. Kriech, H. Görls, G. Kreisel, W. Seidel, M. Westerahausen, *New J. Chem.* **2010**, *34*, 1667–1677.
- [20] M. Berardini, T. J. Emge, J. G. Brennan, *Inorg. Chem.* **1995**, *34*, 5327–5334.
- [21] M. Gillett-Kunnath, W. Teng, W. Vargas, K. Ruhlandt-Senge, *Inorg. Chem.* **2005**, *44*, 4862–4870.
- [22] F. Xi, C. P. Lillya, W. Bassett Jr., O. Vogl, *Monatsh. Chem.* **1985**, *116*, 401–412.
- [23] SMART, version 5.054, Bruker AXS Inc., Madison, WI, USA, **1999**.
- [24] SAINT, version 6.45a, Bruker AXS Inc., Madison, WI, USA, **2003**.
- [25] SHELXTL, version 6.14, Bruker AXS Inc., Madison, WI, USA, **2003**; G. M. Sheldrick, SADABS, version 2008/1, University of Göttingen, Germany, **2006**.
- [26] Ortep-3: L. J. Farrugia, *J. Appl. Crystallogr.* **1997**, *30*, 565.

Received: November 30, 2011

Published Online: January 13, 2012